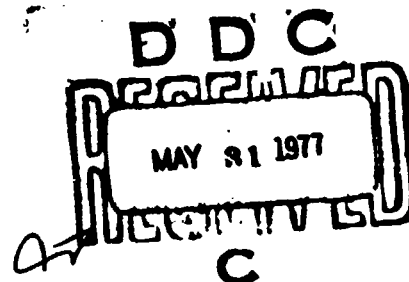ADA040029

AD

AMMRC CTR 77-9

NOISE ABATEMENT AND INTERNAL VIBRATIONAL ABSORPTION IN POTENTIAL STRUCTURAL MATERIALS

February 1977

DDC

MAY 31 1977

C

L. Kaufman, S. A. Kulin, P. P. Neshe

ManLabs, Inc.
21 Erie Street
Cambridge, Massachusetts 02139

Final Report   Contract Number DAAG46-74-C-0048

Sponsored by: Defense Advanced Research Project; Agency
              ARPA Order No. 2555

Program Code No. A 13719
Effective Date of Contract: 30 November 1973
Contract Expiration Date: 31 December 1976
Amount of Contract: $635,452.00
Contract Period Covered by Report: 30 November 1973 to
                                    31 December 1976

Prepared for

ARMY MATERIALS AND MECHANICS RESEARCH CENTER
Watertown, Massachusetts 02172

REPORT DOCUMENTATION PAGE		READ INSTRUCTIONS BEFORE COMPLETING FORM
1. REPORT NUMBER AMMRC CTR-77-9	2. GOVT ACCESSION NO.	3. RECIPIENT'S CATALOG NUMBER
4. TITLE (and Subtitle) NOISE ABATEMENT AND INTERNAL VIBRATIONAL ABSORPTION IN POTENTIAL STRUCTURAL MATERIALS.		5. TYPE OF REPORT & PERIOD COVERED FINAL REPORT. 30 Nov 1973 - 31 Dec 1976
		6. PERFORMING ORG. REPORT NUMBER
7. AUTHOR(s) L. Kaufman, S. A. Kulin, P. P. Neshe		8. CONTRACT OR GRANT NUMBER(s) DAAG46-74-C-0048 ARPA Order-2555
9. PERFORMING ORGANIZATION NAME AND ADDRESS ManLabs, Inc. 21 Erie Street Cambridge, Massachusetts 02139		10. PROGRAM ELEMENT, PROJECT, TASK AREA & WORK UNIT NUMBERS D/A Project: ARPA 2555 AMCMS Code: 690000.21.10846 Agency Accession: DOE 4778
11. CONTROLLING OFFICE NAME AND ADDRESS Army Materials and Mechanics Research Center Watertown, Massachusetts 02172		12. REPORT DATE FEBRUARY 1977
		13. NUMBER OF PAGES 239
14. MONITORING AGENCY NAME & ADDRESS(if different from Controlling Office) 237p.		15. SECURITY CLASS. (of this report) Unclassified
		15a. DECLASSIFICATION/DOWNGRADING SCHEDULE

16. DISTRIBUTION STATEMENT (of this Report)

Approved for public release; distribution unlimited.

17. DISTRIBUTION STATEMENT (of the abstract entered in Block 20, if different from Report)

See Block 20

D D C

MAY 31 1977

18. SUPPLEMENTARY NOTES

19. KEY WORDS (Continue on reverse side if necessary and identify by block number)

Vibration damping	Iron-cobalt alloys
Sound transmission	Internal friction
Titanium-nickel alloys	Copper-aluminum-nickel alloys

20. ABSTRACT (Continue on reverse side if necessary and identify by block number)

Sponsored by: Defense Advanced Research Project Agency, ARPA Order No.2555
Program Code No. A13719
Effective Date of Contract: 30 November 1973
Contract Expiration Date: 31 December 1976
Amount of Contract: $635,452.00
Contract Period Covered by Report: 30 November 1973 to 31 December 1976

DD FORM 1 JAN 73 1473   EDITION OF 1 NOV 65 IS OBSOLETE

215470

ABSTRACT

Efforts were directed toward identifying potential structural materials which combine high strength with damping characteristics in the audible range. Cobalt-iron alloys with additions of aluminum and manganese, copper-aluminum-nickel alloys, iron-chromium-aluminum alloys, titanium-nickel alloys, and several commercial steel compositions have been investigated. The range of yield strengths and loss factors which are attainable exceed currently available commercial materials.

Measurements of the enthalpy of transformation in a thermoelastic Cu-Al-Ni alloy has been conducted over a range of grain size and sample size to assess the stored elastic strain energy. Studies of the magnetic domain wall configuration in a cobalt-iron alloy have been carried out to evaluate the contribution of domains to damping in this alloy.

The hull of a one-sixth scale dynamic model of an armoured personnel carrier was fabricated from a high-damping iron-chromium-aluminum alloy and was evaluated over a range of vibrational frequencies simulating operation. A torpedo propeller was cast from a high damping cobalt-iron alloy and evaluated in underwater vibration tests.

FOREWORD

TABLE OF CONTENTS

LIST OF TABLES

LIST OF TABLES (continued)

Page

8. NET ENTHALPY CHANGE FOR THE $\beta_1 \to \gamma_1'$ TRANSFOR-
MATION IN SINGLE-CRYSTAL AND POLYCRYSTALLINE
SAMPLES OF Cu-14^W/oAl-3^W/o Ni........................ 167

9. NET ENTHALPY CHANGE FOR THE $\beta_1 \to \gamma_1'$ TRANSFOR-
MATION IN NON-PLATED AND Ni-PLATED SAMPLES
OF Cu-14^W/oAl-3^W/o Ni.............................. 172

10. CHEMICAL THERMODYNAMIC QUANTITIES FOR
Cu-14Al-3Ni CALCULATED FROM CALORIMETRY DATA
OF SINGLE-INTERFACE TRANSFORMATIONS................ 175

11. THE EFFECT OF Mn AND Fe ADDITIONS OF THE
GRAIN SIZE OF Cu-14^W/oAl............................ 200

LIST OF FIGURES

LIST OF FIGURES (continued)

Page

LIST OF FIGURES (continued)

LIST OF FIGURES (continued)

LIST OF FIGURES (continued)

LIST OF FIGURES (continuted)

LIST OF FIGURES (continued)

Page

LIST OF FIGURES (continued)

Page

LIST OF FIGURES (continued)

LIST OF FIGURES (continued)

I. INTRODUCTION

This introduction cites all the salient results of this program and has been written specifically for those requiring a less detailed exposition.

A. Structural materials capable of reducing noise and vibration are generally not considered in the initial design of military systems. In the past, noise suppressors, such as acoustic absorbers (and even ear plugs) have been added-on after the initial design simply because structural alloys with good damping capacity have been unavailable. The present research program has demonstrated that at least two such damping alloys exist Fe(14w/oCr) and Co(19w/oFe) and that when these alloys replaced structural components in two military systems, significant noise reduction was achieved. (1-5)*

B. Initially this program sought new structural alloys with high damping capacity at audible frequencies (20-4000 hertz) and attempted to understand the damping mechanism. In addition, the yield strength, Young's Modulus, cost, and fabrication factors were considered in order to show that these alloys were attractive for military systems. Finally, the two most promising alloys were tested in military systems: 1.) The Fe-Cr alloy in a 1/6 scale model of an armoured personnel carrier (M113). 2.) The CoFe alloy in a torpedo propeller.

C. Novel damping alloys such as Nitinol (Ni-Ti) and copper-aluminum-nickel (both of which derive their damping characteristics from thermoelastic martensite transformations and commercial damping alloys such as NIVCO (Co-Ni-Ti-Al) (6) and INCRAMUTE (Cu-Mn-Al) (7-10) (whose damping depends upon magnetic interactions) have been available for a number of years, but they all have serious shortcomings. The first two are only useful over a small temperature range of a few degrees and are difficult to fabricate while NIVCO

---

* Underscored numbers in parentheses denote references.

has a fairly low damping capacity and INCRAMUTE exhibits poor
corrosion resistance. In the present program, a family of CoFe
and FeCr alloys (with some Mn and Al additions) which could be
heat treated to yield very high damping characteristic have
been synthesized. Although the atomic mechanism leading to
the high damping capacity is not clear, it appears that a com-
bination of magnetic and crystal structure factors play a role.
These alloys have been cast, forged, cold worked, fabricated
into rod and cold rolled into foil suggesting a variety of
applications.

   D. Figure 1 is a bar graph comparing the damping capacity
(loss factor) and 0.2 percent offset yield strength for various
damping alloys. NIVCO and INCRAMUTE were supplied by commercial
vendors although the NIVCO required a further 15% reduction in
thickness by cold rolling to optimize its properties. The
Co-Fe, Co-Fe-Mn, Co-Fe-Al, and Fe-Cr-Al alloys were annealed
samples fabricated for this study. All data in Figure 1 were
taken at 25°C. The loss factors were measured at 200 hertz by
the so called "resonant dwell" method (described in detail later
in the report), employing a cantilevered beam at a peak stress of
2000 psi. While it is known that many materials show increased
damping capacity at higher stress levels and in some cases
show marked frequency dependence at low frequencies ($\sim$1 hertz),
this study has been confined to audible frequencies and to
medium stress levels (500-2000 psi).

   E. The Co-Fe alloys [80Co-20Fe], when modified with either
a 2.5 w/o Al addition or a 4 w/o Mn addition, demonstrated
(Figure 1) that one can achieve a wide range of strength and
damping albeit the two properties are inversely related.
However, to assess the practical considerations of these alloys
in military systems, one must also determine the temperature
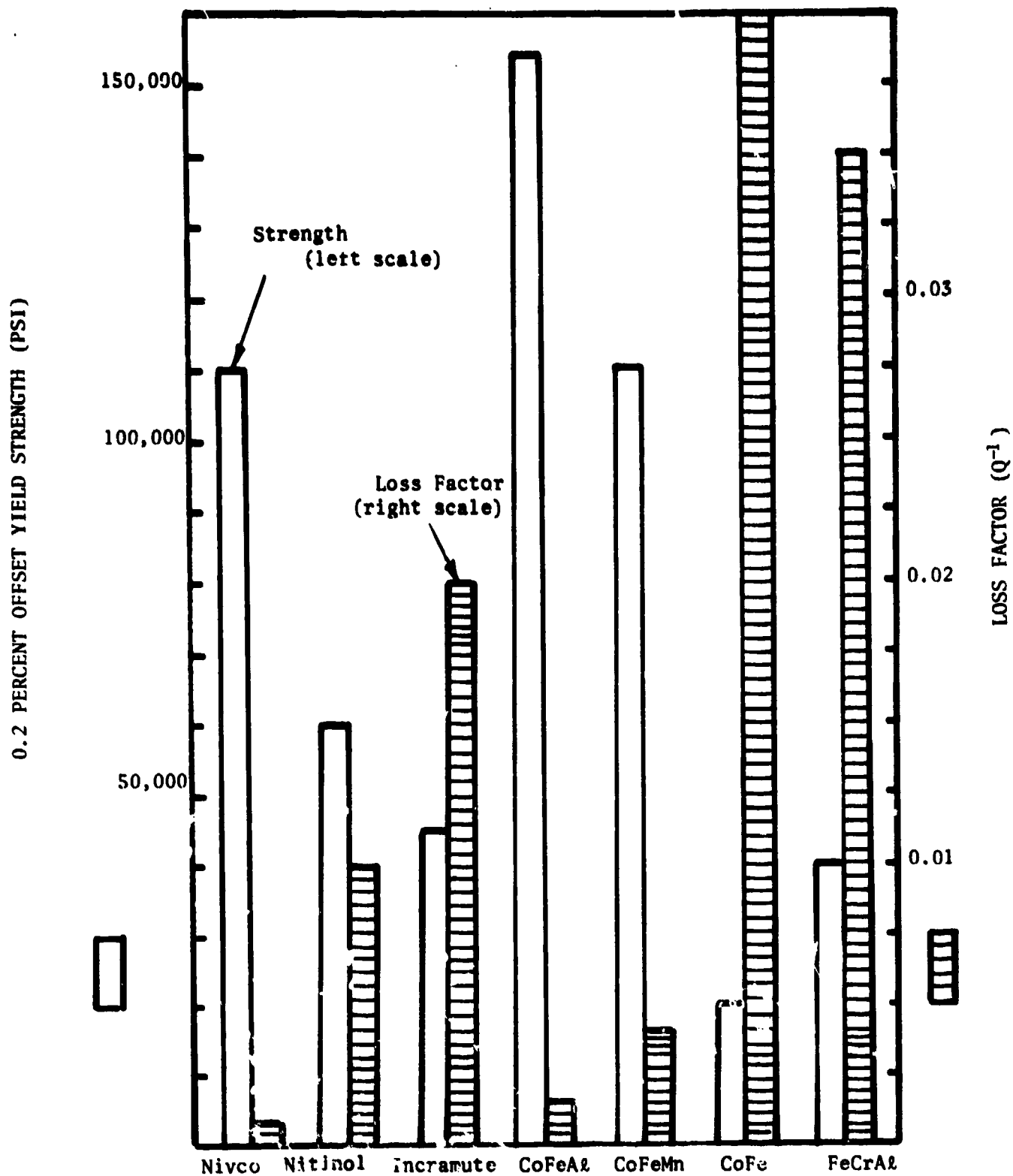
Figure 1. Comparison of Loss Factors (right scale) and
Yield Strengths (left scale) at 25°C, 150-
250 Hertz (cps) and 2000 psi peak stress.
The loss factors for structural steel and
aluminum are too small to be seen on this scale.

dependence of the damping as shown in Figure 2. Only the Fe-Cr and Co-Fe alloys show high damping over a significant temperature range.

F. The Fe-Cr alloys Fe (15 w/o Cr 3 w/o Al) and Fe (14 w/o Cr .05 w/o C) simulating both a commercial Japanese damping alloy and a type 405 stainless steel are promising corrosion resistant alloys with strengths from 37000 to 42000 psi and temperature independent loss factors of .015 to .035. They can be produced relatively inexpensively (up to 80 cents per pound).

G. Measurements of the loss factor of the Co-Fe and Fe-Cr alloys in a saturating magnetic field lead decrease the loss factor by approximately 50% suggesting that the magnetic domain walls only partly account for the loss factors. A measurement of the loss factor in Co-Fe at 500 psi and 2000 psi stress levels shows an increase in the loss factor from .02 to .04 which is consistent with some previous work indicating the loss factor is proportional to the square root of the stress.

H. Since the Surgeon-Generals office has identified the (aluminum) armored personnel carrier (M113) as producing a potential health hazard to its occupants due to the high interior noise level (>120db) and since BBN has carried out noise level measurements on a 1/6 scale aluminum model; it was decided to fabricate a second 1/6 scale model using the Fe-Cr damping alloy for the exterior hull. A photo of the model is shown in Figure 3 and in Figure 4 are shown the comparative results of the interior sound level measurements at various frequencies for vehicle speeds of 6 and 50 mph. There is very little difference at the low speed (where the noise level is not a problem) but, at the higher speed differences of as much as 10 db are observed.

-4-
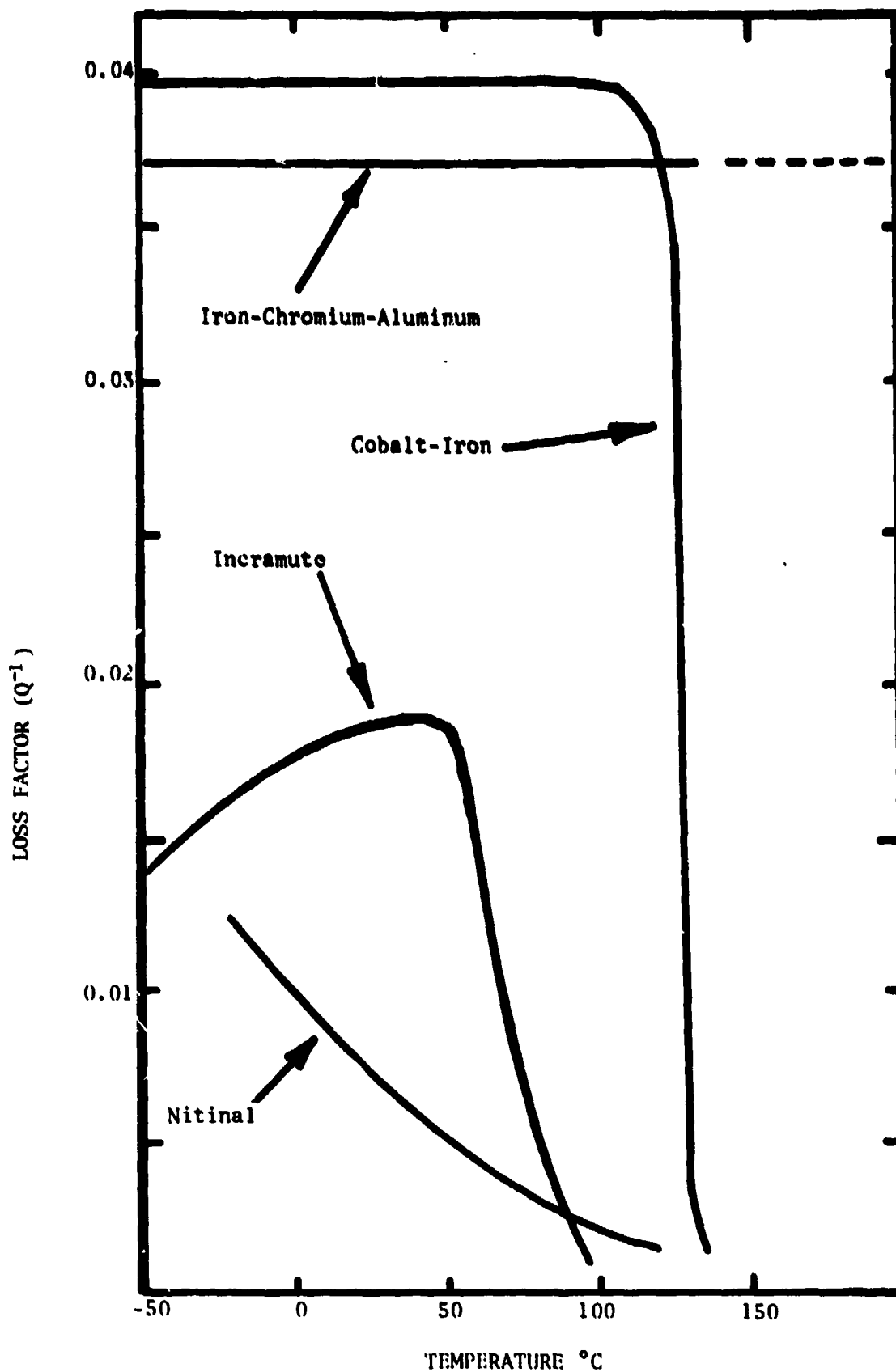
Figure 2. Comparison of the Loss Factor for various
alloys as a function of Temperature at a
Frequency of 200 Hertz and a Stress of
2000 psi.

-5-
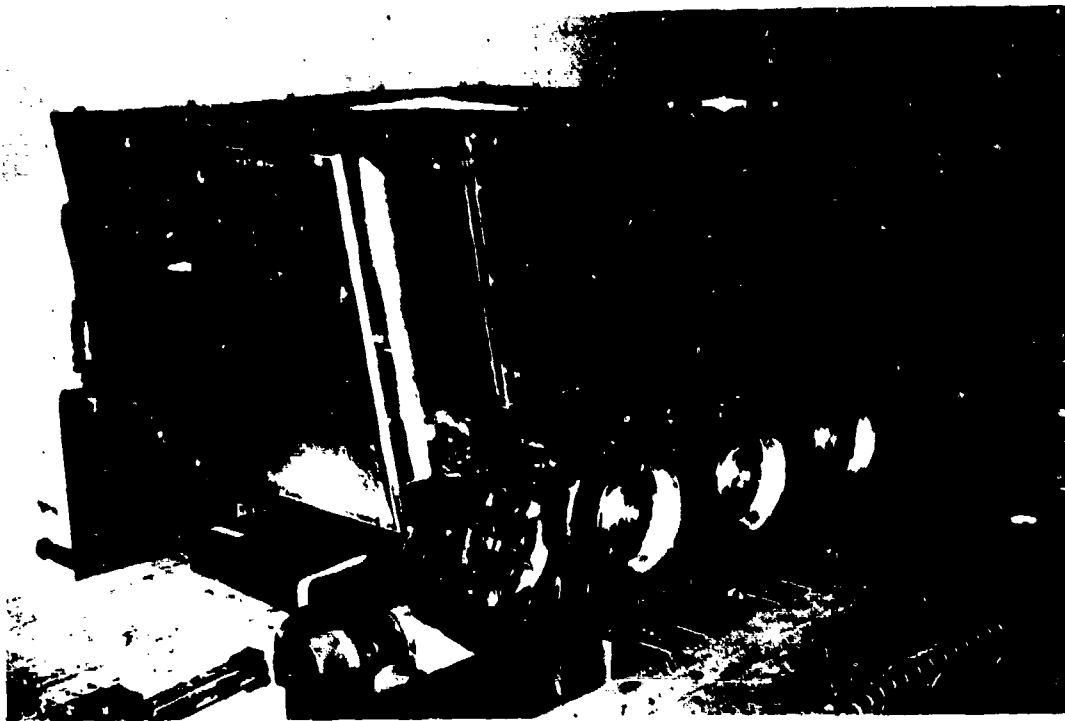
Figure 3a. Aluminum Scale Model M-113 Vehicle, Front
View on Motor Driven Steel Belt Running
Surface.

-6-
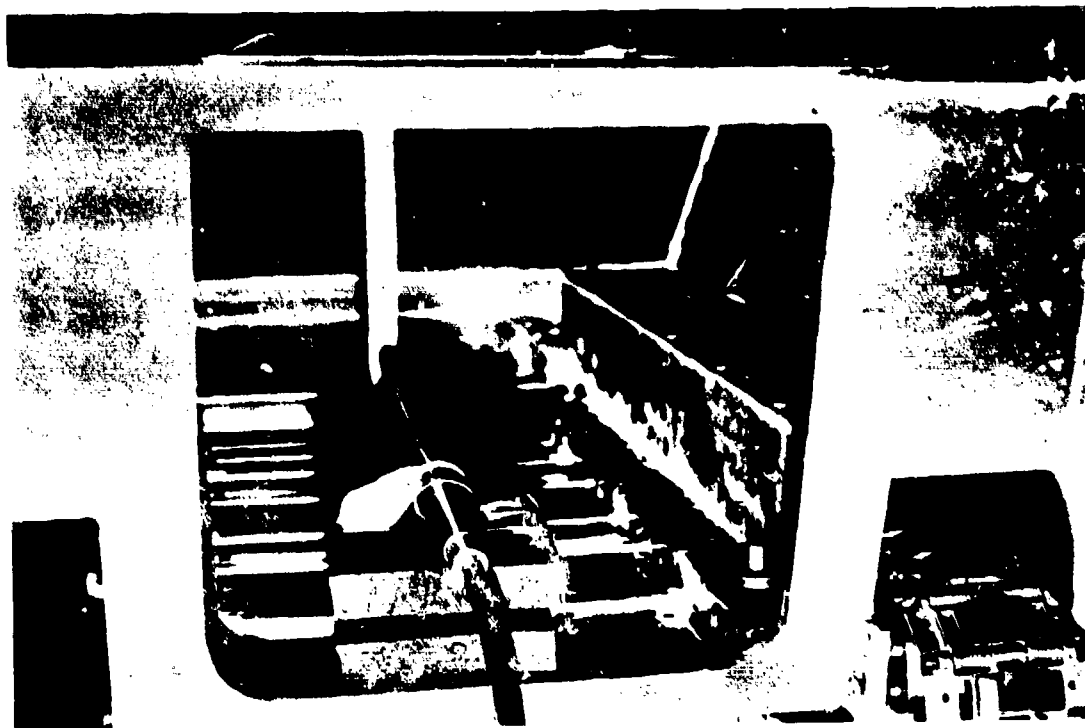
Figure 3b.   Iron-Chromium-Aluminum Alloy M-113 Vehicle,
Aft View, With "Soft Mounted" Microphone.
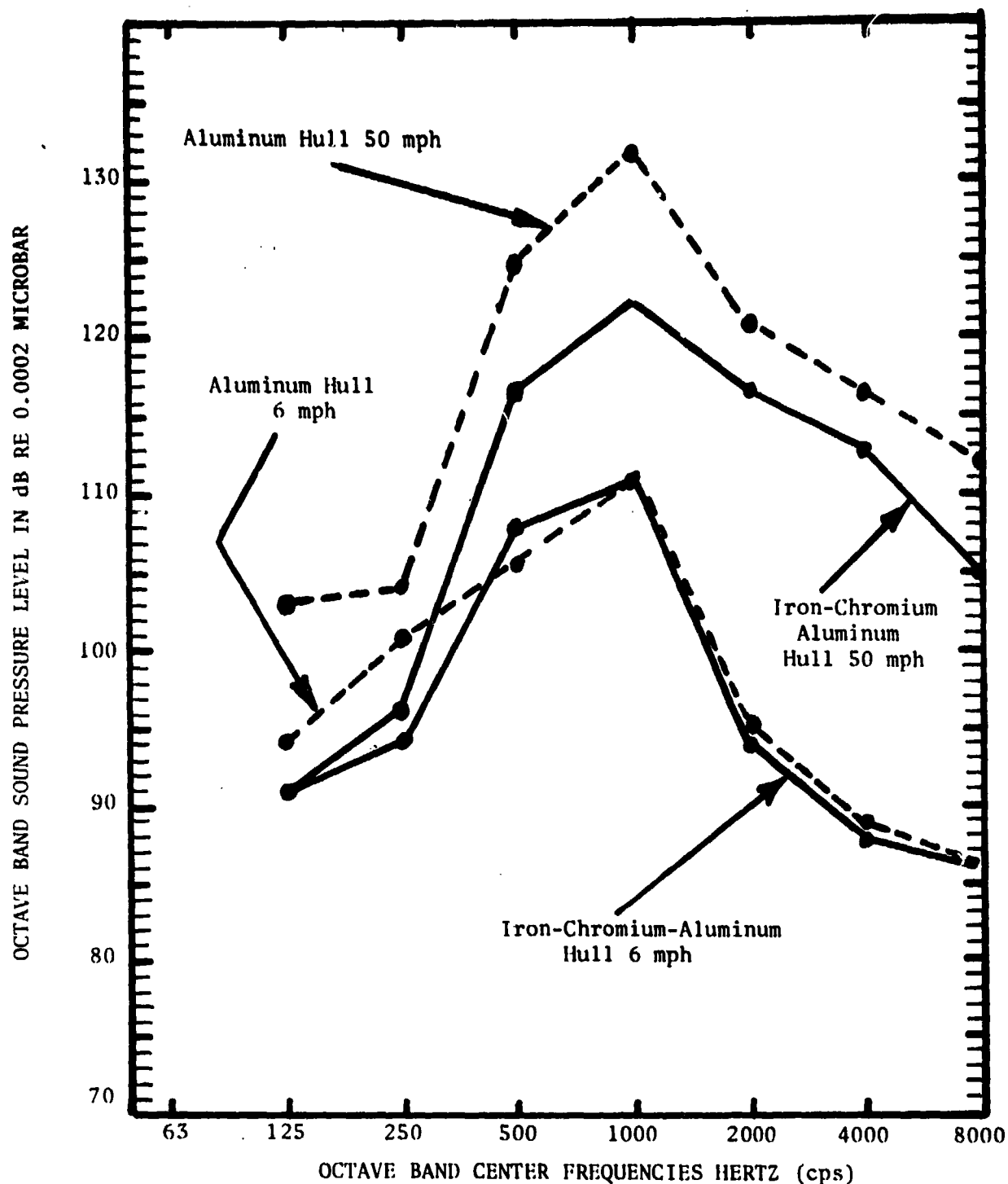
Figure 4. Interior Sound Levels, Aluminum and Iron-Chromium
Aluminum Hulls on One-Sixth Scale Model M-113
Vehicles at Forward Speeds of 6 and 50 mph.
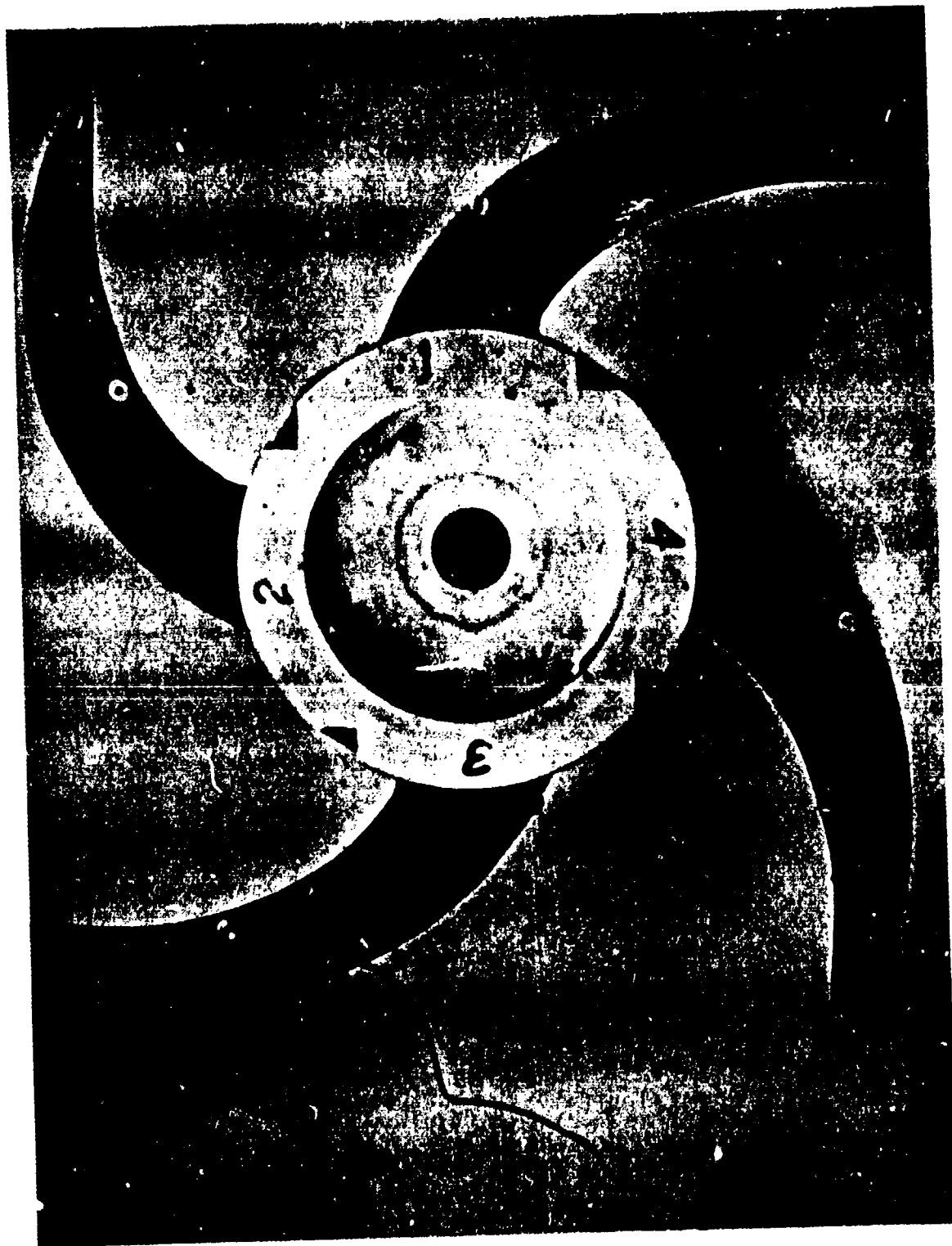
Figure 5.   Propeller with Accelerometer and Pads (Cobalt-Iron Alloy).
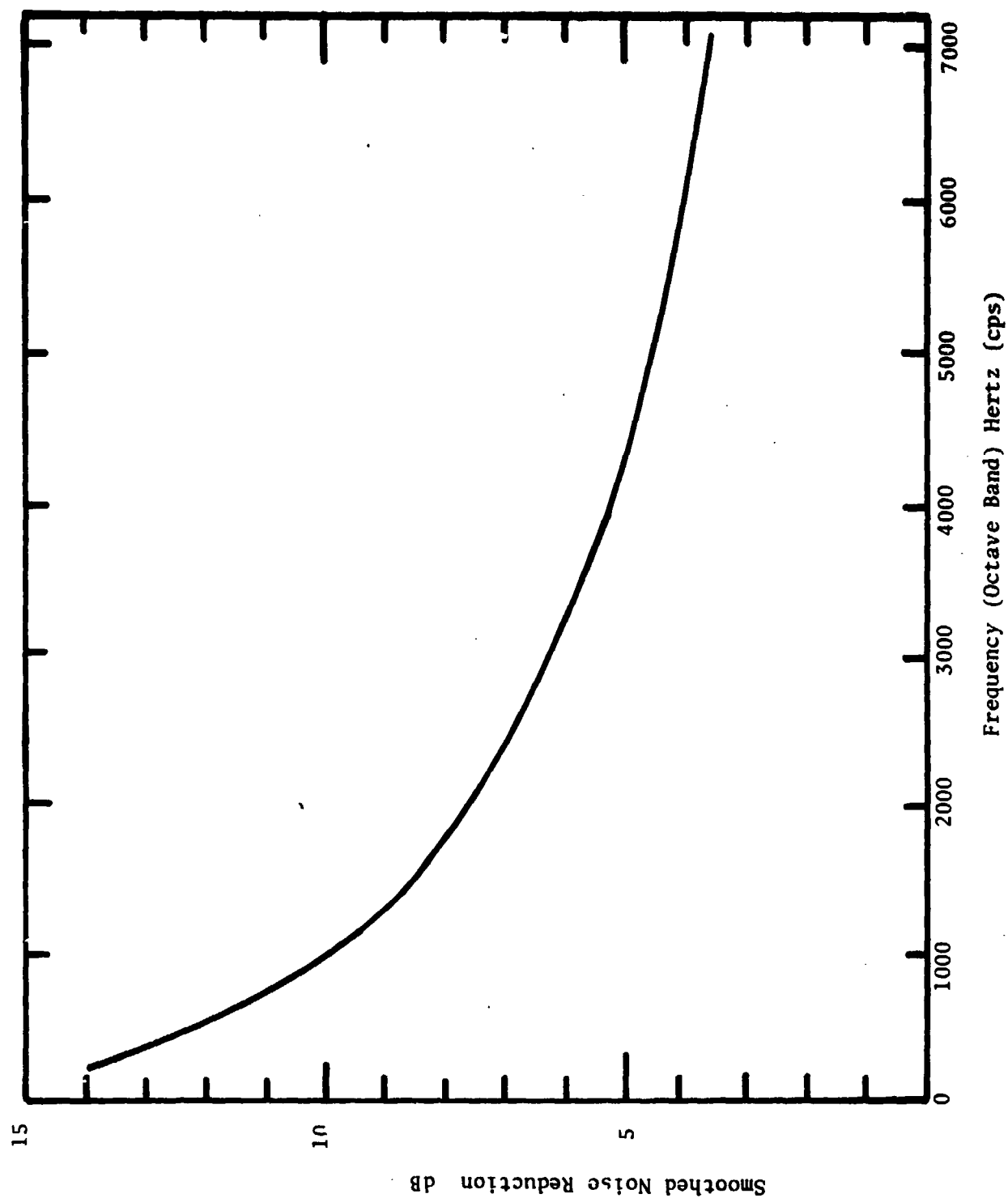
Figure 6. Smoothed Noise Reduction Curve for Cobalt-Iron Alloy Propeller Blades Relative to Aluminum Blades.

-10-

I. A second recognized military noise problem arises
from the induced vibration of the aluminum propellers used in
torpedo propulsion. In Figure 5 is shown such an aluminum
propeller. An identical propeller was fabricated (cast and
finish-machined) from the Co-Fe alloy and tested under water
by BBN. The results are given in Figure 6 and again show
significant reductions in transmitted sound levels ($\sim$10 db).

J. These results indicate that the Fe-Cr and Co-Fe
damping alloys are worthy of further development. Specific
work projects might include;

1. Some basic research to establish the atomic
    damping mechanism.

2. Testing in both torsion bars and tank treads
    on the M-113.

3. Optimization studies of these alloys with
    respect to strength, damping, armor capabilities
    etc.

4. Incorporation into other underwater systems.

K. It is likely that such structural damping alloys will
find use in many non-military products since noise suppression
is very fashionable.

L. The basic mechanisms by which ..orational energy is
absorbed by a thermoelastic martensitic transformation have
been studied in detail in Cu-Al-Ni alloys. The energy

-11-

absorbing mechanisms are found to be highly repeatable around M_s - that is, the damping capacity does not readily deteriorate. The damping is due to the motion of specific crystal defects which are inherent to the martensitic transformation - in particular, the motion of stress-induced martensite-parent around M_s, and martensite-martensite, and twin-twin interfaces below M_s have been shown to cause the major portion of the damping. See Figure 107. Further investigation is warrented in thermoelastic martensites to examine the characteristics of high damping, elastic energy storage, and repeatability.

II. DESCRIPTION OF THE EXPERIMENTAL METHODS FOR MEASURING DAMPING

The methods employed for characterizing the loss factor of the metals and alloys investigated in this program are based on the resonance dwell technique. Resonance measurements of loss factors have been discussed by Heine (11) and Cremer, Heckl and Ungar (12). The specific "Resonance Dwell Apparatus" employed in this study was designed and built at Bolt, Beranek and Newman and incorporated a flexible temperature range of operation between -100°C and +300°C. This feature permitted evaluation of the candidate alloys over a range of temperatures where change in behavior could be observed. Measurement of the specimen loss factor, g_s, as a function of temperature, stress level, frequency, (and in some cases magnetic field) provided a direct means for characterizing the damping behavior.

The resonance dwell technique is a forced vibration method of indirectly determining the loss factors of simple structural elements by measuring their response to excitation at a modal frequency (11-12). For a thin beam, where the mode and dynamic stress distributions are well known, the specific damping capacity of the material (energy dissipated per unit volume in one stress cycle at a given peak stress divided by 2π times the peak potential energy in the unit volume at the same stress) may be inferred from the determined loss factor.

In this test, the specimen loss factor in a mode (usually the fundamental) is determined from the resonant amplification factor, or Q, of the specimen in that mode. The mechanical Q of a

-13-

vibrating system is defined in terms of a characteristic deflection δ of the system due to distributed exciting forces proportional to the inertia forces of the mode in question. The amplification factor at resonance is

$$Q = \frac{\delta_{res}}{\delta_0} \tag{1}$$

where δ_0 is the deflection due to the distributed exciting force being applied statically and δ_{res} is the deflection when the same pattern of forces is applied in simple harmonic motion at the modal natural frequency. The relationship between Q, the specimen loss factor g_s, and the logarithmic decrement ζ of a single-degree-of-freedom system is

$$\zeta = \frac{\pi}{Q} = \pi g_s \tag{2}$$

$$Q^{-1} = g_s \tag{3}$$

The advantages of the resonance dwell method are: first, the ratio δ_0/δ_{res} for a properly designed specimen is dependent only upon the damping in the specimen; second, the vibration amplitude δ_{res} may be maintained at any constant level so that specimen damping may be determined as a function of a well-defined stress history; and third, because nothing is attached directly to the vibrating specimen extraneous energy losses are minimized.

The method for ensuring that the beam specimen is excited at a mode is straightforward. The apparatus is constructed in such a way that the specimen acts as a vibration absorber placed on an excited single degree-of-freedom supporting system (see Figure 7). At a natural frequency of the beam, the response of the supporting system is minimized. The frequency of the response minimum, and hence of the beam mode, can therefore be determined by monitoring the acceleration of the supporting system.

A sketch of the apparatus is shown in Figure 8. A cantilever beam specimen of a test material is clamped to a bar which

-14-
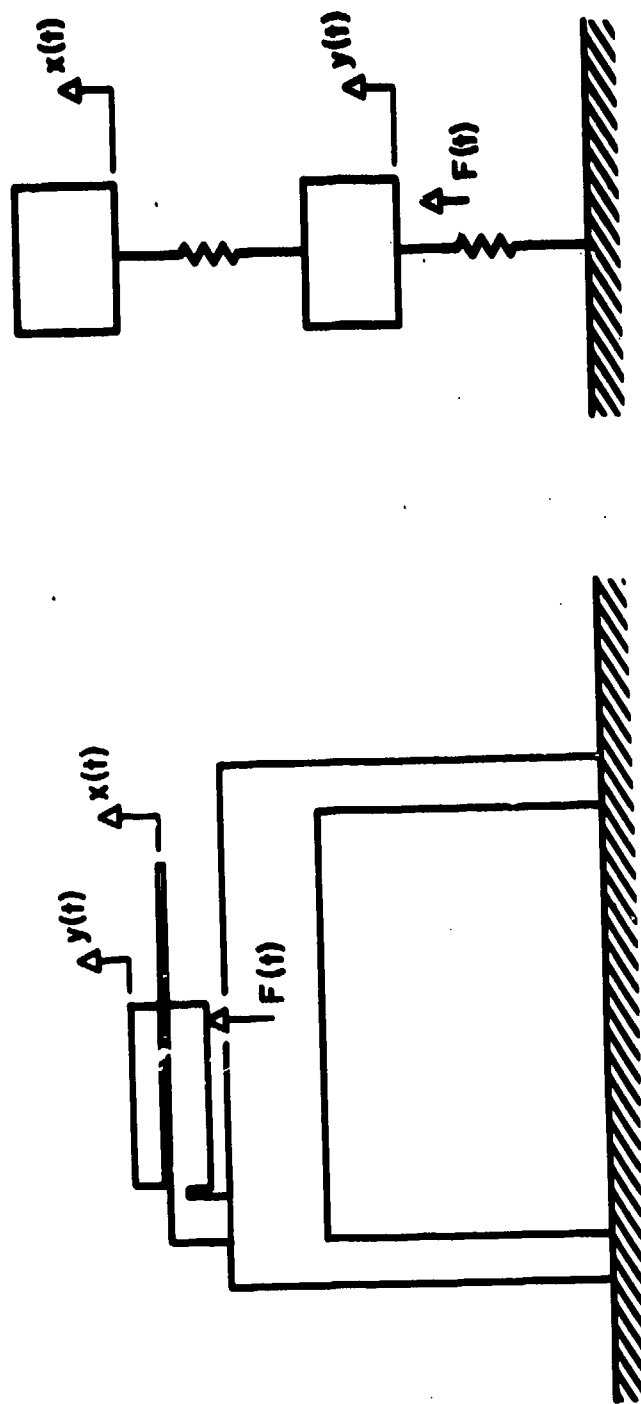
FIGURE 7. AN EXCITED MECHANICAL SYSTEM WITH A RESONANT VIBRATION ABSORBER (EQUIVALENT TO THE RESONANT DWELL DAMPING APPARATUS).

-15-
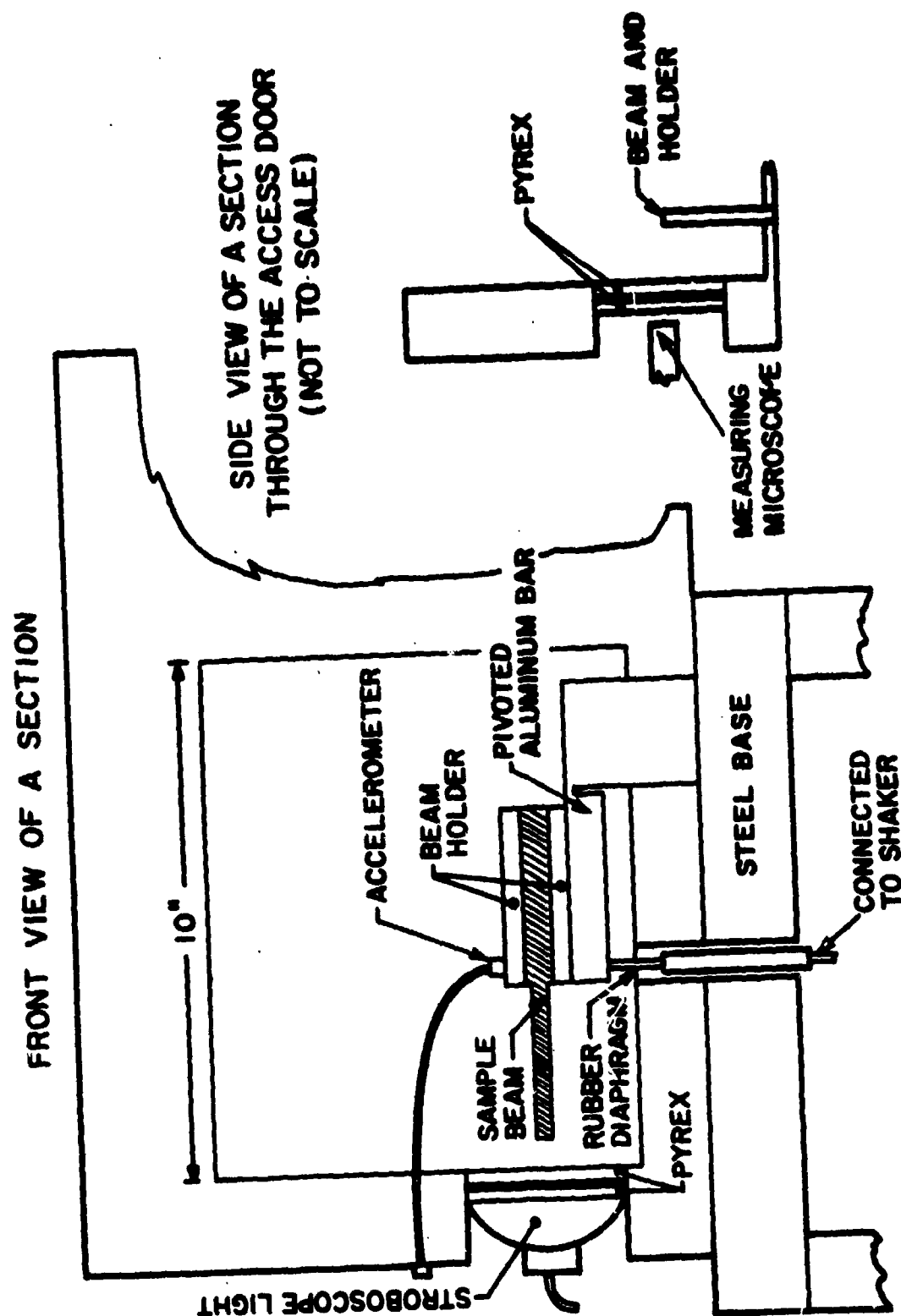
Figure 8. Sketch of the Resonant Dwell Apparatus and Enviromental Chamber. The Sample is Cross Hatched and can be seen in Figure 9.

-16-

is connected at one end to an electromagnetic shaker and the other to a heavy base. The thickness of the bar at the base end has been reduced by a saw cut to provide a pivot around which the remainder of the bar can rotate when excited by the shaker. Figure 9 shows the configuration of a typical reed-type test beam.

The shaker is connected to the bar by a rod which passes through a hole in the base. The hole is sealed by a rubber diaphragm which keeps the gases that are used for temperature control from leaking out of the chamber.

Control of the temperature of the test beam is provided by a commercially available environmental chamber that has been modified to provide some viewing ports. The chamber can be raised to a temperature of over 600°F by air that is blown over electric heaters. It can be cooled to -100°F by allowing carbon dioxide to expand through the chamber.

The base shown in Figure 8 may be placed on any convenient solid surface, such as a laboratory table. Excitation of the base by the shaker reaction is minimized by the large mass of the base and by supporting the body of the shaker on a jack which passes between the legs of the base. The jack provides some isolation of the shaker from the table. The isolation can be improved by supporting the shaker on a "bridge" that is tied to the floor. Measurements of the acceleration of the base showed the present configuration to be adequate.

The response of the supporting system [y(t) in Figure 7] to shaker excitation is measured with an accelerometer mounted on the bar at the root of the specimen. Specimen response [x(t) in Figure 7] is measured optically with a low power microscope with a retical.

Figure 10 shows a block diagram of the electronic instrumentation that is used in conjunction with the resonance dwell apparatus. Only two electronic measurements are required--identification of the resonant frequency of the test beam, and accelero-
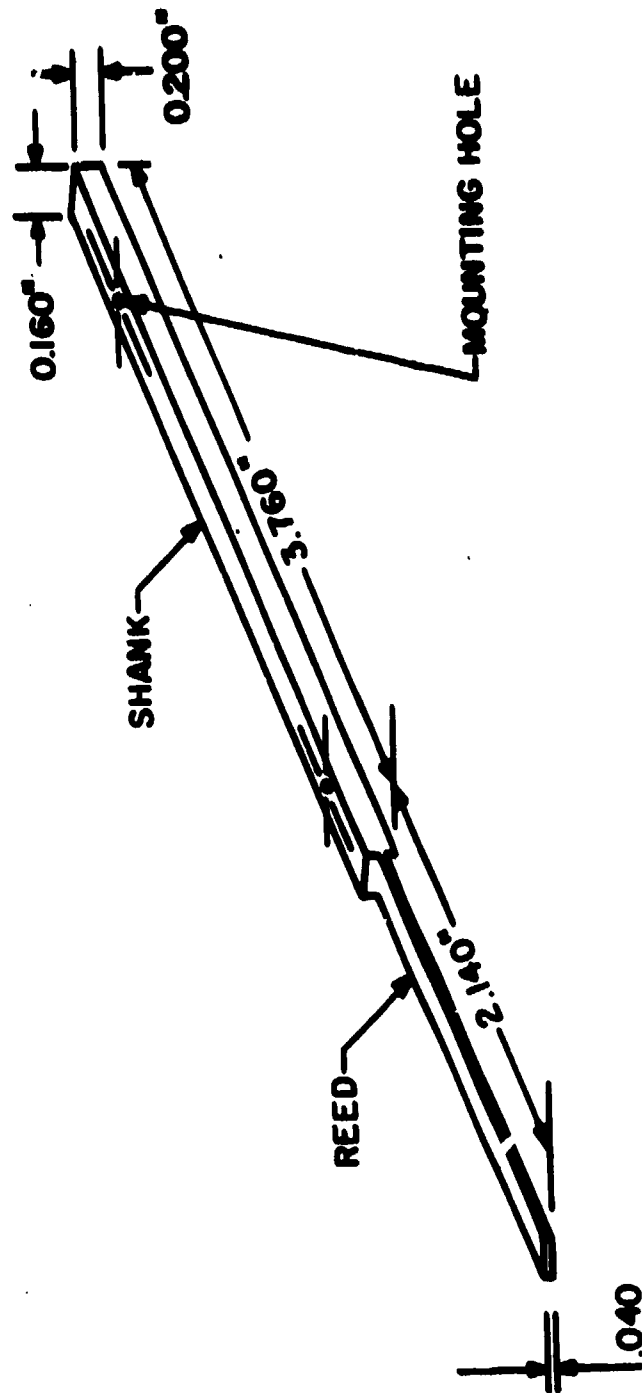
FIGURE 9. SPECIMEN DESIGN FOR MEASURING DAMPING CAPACITY.

-18-
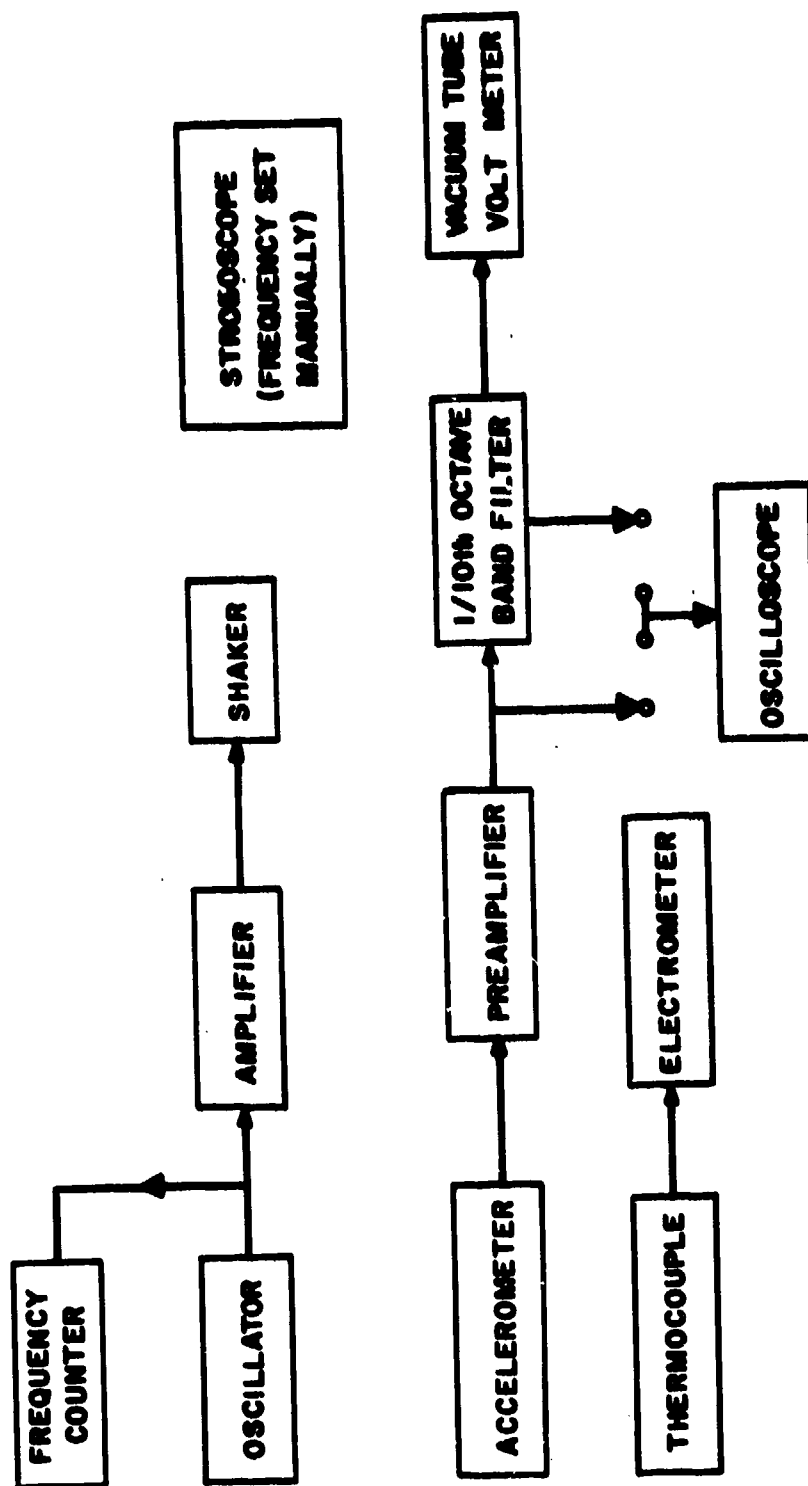
FIGURE 10. BLOCK DIAGRAM OF ELECTRONIC INSTRUMENTATION FOR RESONANT DWELL DAMPING MEASUREMENTS.

-19-

meter output. The remaining measurement is the nonelectronic optical measurement of displacement of the beam tip. That measurement is facilitated by the "stop-action" feature of a stroboscope light that is set to flash at nearly the same frequency as the frequency of the mechanical oscillation of the test beam. Figure 11 shows a photograph of the environmental chamber and the associated electronics.

The response of a test beam in the resonant dwell apparatus can be described by the following mathematics. For cantilever beams in their fundamental mode of vibration, tip amplitudes as a function of peak stress and specimen natural frequency are given by

$$y_{t,DA} = 3.63 \left(\frac{\sigma_p}{f_n} \right) \frac{1}{\sqrt{E\rho}} \tag{4}$$

where $y_{t,DA}$ = peak to peak amplitude (in.), σ_p = maximum stress (psi), f_n = specimen design natural frequency (Hz), E = Young's Modulus (psi), and ρ = material density (lb/in^3). The fundamental natural frequency of a cantilever beam of length L (in.) and thickness h (in.) is

$$f_n = \frac{1}{2\pi} \left(\frac{1.8751}{L} \right)^2 h \left(\frac{32E}{\rho} \right)^{1/2} \tag{5}$$

The working equation relating the specimen loss factor g_s and root acceleration a_0, fundamental specimen frequency f_n, and beam tip double amplitude $y_{t,DA}$ is

$$g_s = 0.083 \ (1 + 0.2L) \ \frac{a_0}{f_n^2} \ \frac{1}{y_{t,DA}} \tag{6}$$

where a_0 is the bar acceleration in in./sec^2 measured by the accelerometer at the frequency f_n (the response minimum). The latter is the measured resonance frequency determined by observing a maximum amplitude. The amplitude, $y_{t,DA}$ is determined visually.

Each beam specimen may be run at the frequencies of modes higher than the fundamental. In practice, however, the highest

-20-
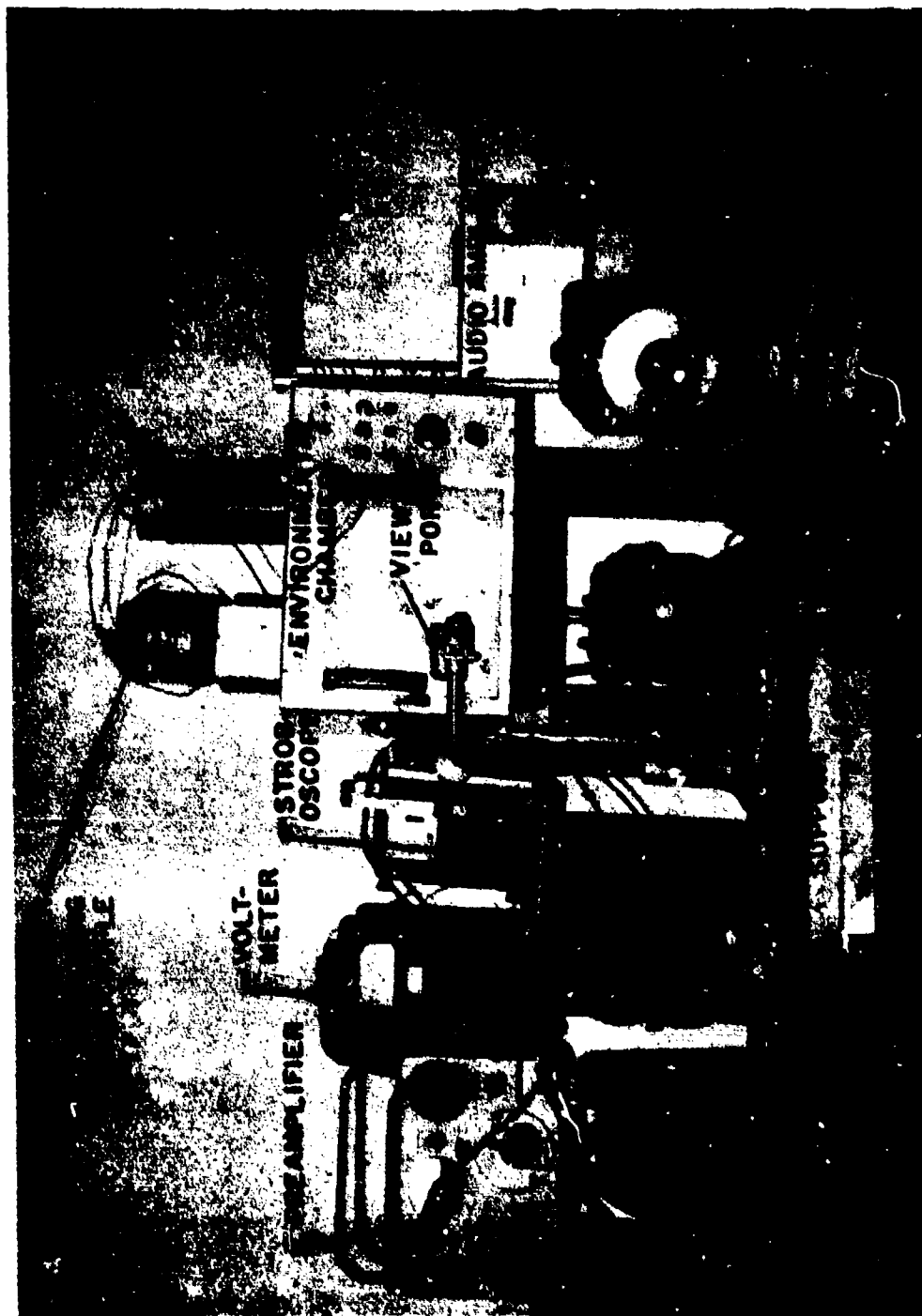
FIGURE 11. PHOTOGRAPH OF THE ENVIRONMENTAL CHAMBER AND ELECTRONICS COMPRISING THE RESONANT DWELL APPARATUS.

-21-

useful mode is usually the second (though for specially designed specimens the third might be used), because the tip amplitude for a given stress becomes very small with increasing frequency and because the force required for the excitation of a given stress increases with both mode number as well as frequency. For example, a force higher by a factor of more than 3 is required to excite a 10,000 psi peak stress in a specimen with a 650 Hz second mode than for a specimen designed to have a 650 Hz first mode even though the tip amplitudes required are the same for the two specimens.

The formulas equivalent to Equations 4 and 5 for the second mode are

$$f_2 = \frac{1}{2\pi} \left(\frac{4.6941}{L}\right)^2 h\left(\frac{32E}{\rho}\right)^{1/2} \tag{7}$$

and

$$g_{s,2} = 0.045 \ (1 + 0.056L) \ \frac{a_0}{f_2^2 y_{t,DA}} \tag{8}$$

The measurements described in this section were obtained with a nickel-titanium reed-type sample like the specimen shown in Figure 9. The test specimen was prepared by standard heat treatment and temperature cycling 70 times between -90°C and +65°C.

Preliminary measurements of the temperature distribution within the test volume of the commercial temperature chamber revealed that the temperature was not uniform, and the temperature at a given point in the chamber varied with time for a fixed setting of the temperature control. Therefore, it was necessary to measure the temperature of the test specimen by attaching an iron-constantan thermocouple to its surface (near the root of the beam).

These measurements also showed that the specimen loss factor of the Nitinol test beam depended on the amplitude of vibration of the tip of the beam at a fixed temperature at which the higher loss factors were exhibited. In addition, the value of the loss factor and the relationship between the loss factor or

-22-

tip amplitude at a given temperature depended on the past history
of the temperature changes. That is, the damping properties at a
given temperature were not necessarily the same when the sample was
cooling as when it was heating.

The resonant frequency of the test beam varied as the tip
amplitude and temperature were changed. Some of the change in loss
factor with changing tip amplitude may have been caused by the ac-
companying frequency change, and not by the amplitude change. How-
ever, the changes in resonant frequency were small. The resonant
frequency of the test beam was between 150 Hz and 200 Hz for the
entire range of temperature and tip amplitude covered during the
tests.

Figure 12 shows that the specimen loss factor determined
from the observations of the test specimen was not a function of
tip displacement for the higher temperatures where lower values
of loss factor were observed. Figure 12 also shows that the mea-
sured specimen loss factor was a relatively strong function of tip
displacement at the lower temperatures where high specimen loss
factors were measured.

The strain-independence of the loss factor at 77°F would
seem to rule out dislocation motion and magnetic domain motion as
the mechanisms that generate the observed loss factor since those
mechanisms are predicted to be stress (and therefore strain) depen-
dent (10). Of the known mechanisms for generating internal friction
in metals, theory predicts that only thermal diffusion is indepen-
dent of stress (ibid). Substitution of the values of the thermal
coefficients for the test sample into the equation to predict the
sample loss factor due to thermal diffusion yielded a value which
is an order of magnitude lower than the constant value in Figure
12. Therefore, the loss factor measured at 77°F does not reflect
the internal friction level characteristic of thermal diffusion.
However, it may be possible to obtain this magnitude of damping
by thermoelastic martensitic behavior. It seem unlikely that
the equipment gave extraneous high readings at 77°F,

-23-
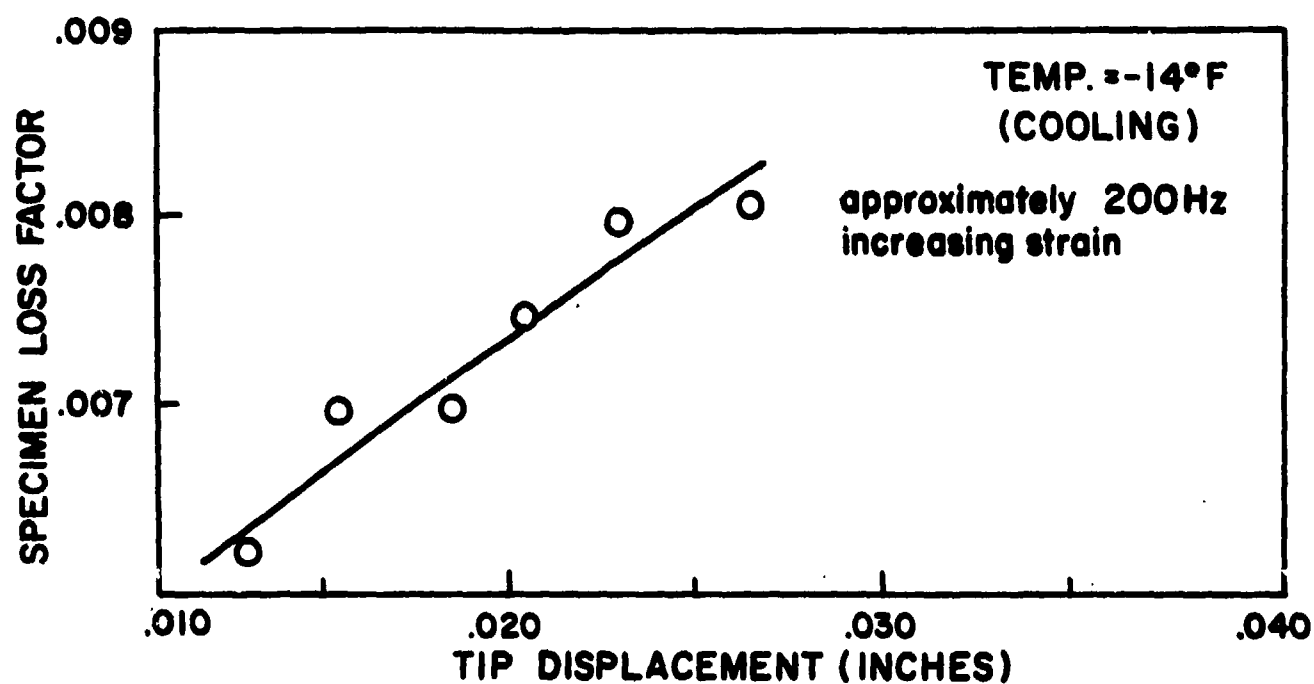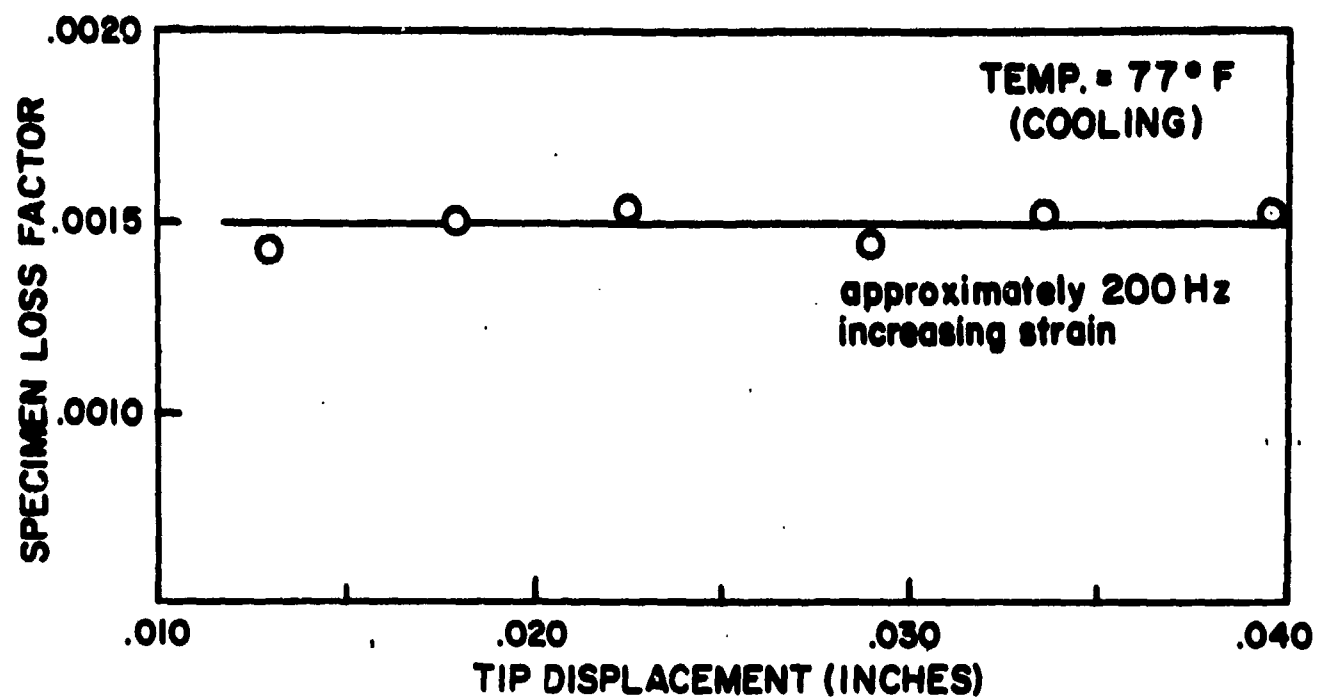
FIGURE 12. AMPLITUDE-DEPENDENCE OF THE SPECIMEN LOSS FACTOR
OF NICKEL-TITANIUM SAMPLE NUMBER V4609-80.

since readings an order of magnitude lower (in agreement with thermal diffusion theory) were obtained above 100°F.

A number of graphs like those shown in Figure 12 were used to pick off the specimen loss factor corresponding to a constant tip displacement (zero to peak) of .02 in. for various temperatures. It was necessary to use separate graphs for heating sequences and cooling sequences. The value of the loss factor depended slightly on the strain sequence (increasing or decreasing strain). Straight lines were fit through the points on the graphs like those in Figure 12. Curved lines may have been equally appropriate. The straight line provided better definition of the temperature dependence of the damping factor than was obtained before any attempt was made to plot the damping factors at constant tip amplitude.

Figure 13 shows the specimen loss factors determined from observations of the nickel-titanium test specimen. The curve reveals some apparent hysteresis in the damping properties of the specimen--the specimen loss factors effective at temperatures near 80°F appeared to be different for the cooling and heating cycles. Relatively small errors in the measured output of the thermocouple attached to the root of the test beam could have contributed to the apparent hysteresis. If portions of the test beam were not at the same temperature that was measured at the root of the beam, there might have been apparent hysteresis generated by the non-uniform temperature of the beam.

The point that lies well above the curve in Figure 13 was determined from observations of the test sample that were made on a different day from the observations that yielded most of the other points in the figure. That point provides some evidence that the response of the test sample depended on the past history of the sample, which is consistent with the observed temperature hysteresis of the damping properties of the test sample.

Laboratory measurements showed that the internal damping of mechanical vibrations of a Nitinol test beam was unusu-

-25-
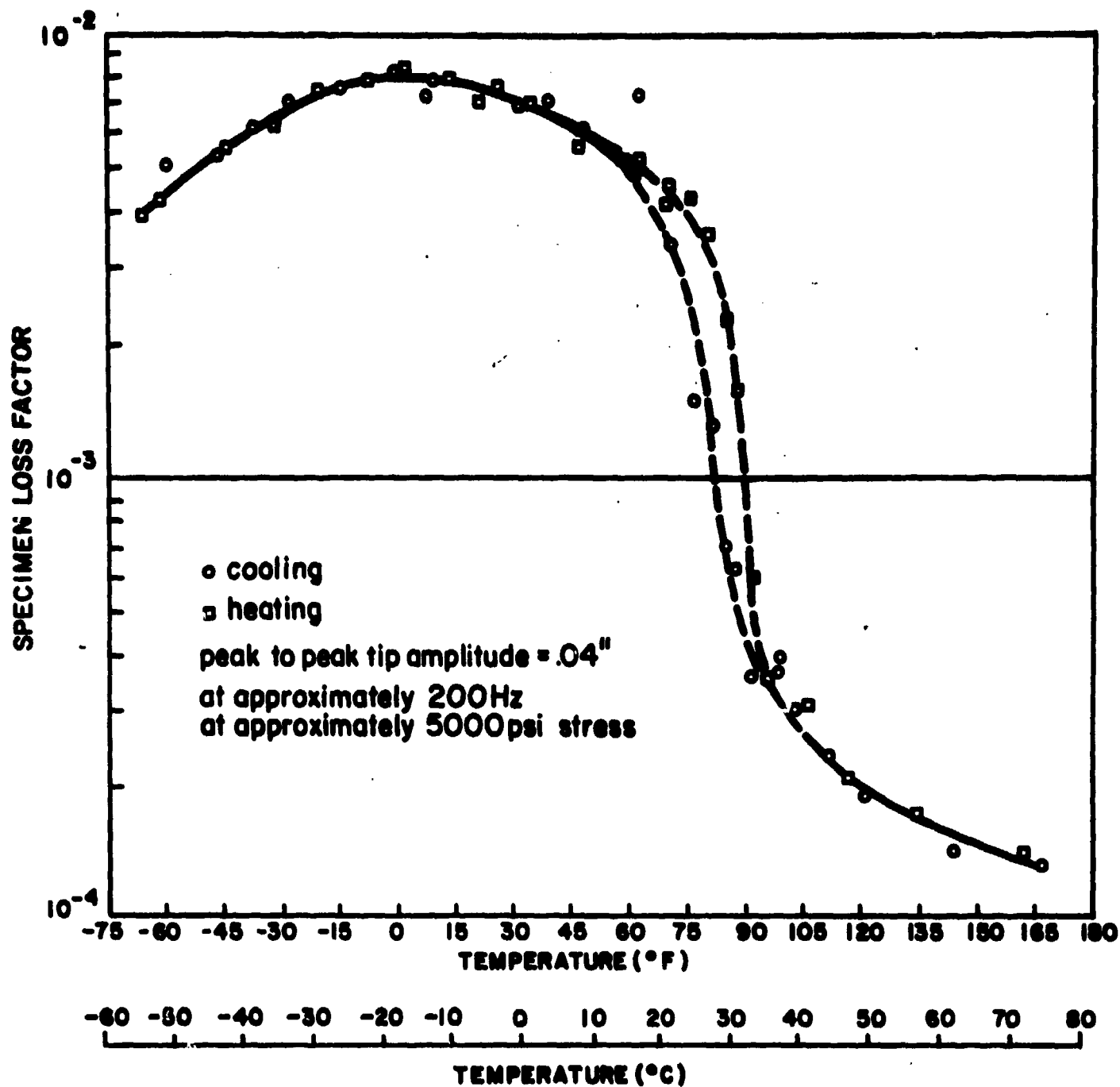
FIGURE 13. TEMPERATURE-DEPENDENCE OF THE SPECIMEN LOSS FAC-
TOR OF NICKEL-TITANIUM SAMPLE NUMBER V4609-80
(AT CONSTANT TIP AMPLITUDE).

ally high at temperatures below about 80°F. The specimen loss fac-
tor approached .01 near 0°F at about 200 Hz and about 5000 psi
stress. The value for the loss factor is more typical of built-up
composite structures than homogeneous samples (13,14). The values
of the loss factor determined from the measurements depended on
temperature, past history of temperature, the amplitude of the tip
of the vibration test reed, possibly upon the resonant frequency
of the test beam, and slightly upon the strain history of the
test beam. (Examination of Figure 47 (page 71) will show that
the low temperature behavior is associated with the low strength
due to ease of twin formation. A discussion of the mechanisms
for damping in thermoelastic martensite is given on page 182 ff).

III. MEASUREMENT OF TRANSFORMATION, DAMPING AND STRENGTH
CHARACTERISTICS OF A 55Ni-45Ti ALLOY AND 83Cu-14Al-3Ni
ALLOYS

1. Resistivity of Nitinol

A substantial portion of the effort in the initial
phase of this program was directed toward establishing whether
the damping phenomenon observed in NiTi is directly related
to the onset of a transformation or if it occurs in a tempera-
ture range above M_s where "atomic shuffles" are thought to
take place. In order to test the latter hypothesis it was
decided to perform simultaneous measurements of the electri-
cal resistance and acoustic emission of NiTi samples as a
function of temperature. The measurements were conducted on
the standard "reed" samples (Figure 9) which BBN requires for
measurements of damping capacity as a function of temperature.
The resistivity of a typical NiTi 55 w/o alloy is shown in
Figure 14 as a function of temperature cycling through the
transition range. Simultaneous metallographic and resistance
measurements do not disclose actual formation of the daughter
or martensite phase in the region where the resistance increases.
This is where the "atomic shuffles" are supposed to take place.
In order to determine if these "soft mode displacements" lead
to enhanced damping, specimens were temperature cycled many
times to obtain a well defined resistivity peak. The peak
in the cooling curve represents the M_s temperature as defined
by the temperature at which the first observable surface relief
forms on cooling (15-17).

The present results obtained by BBN indicate that the
increase in damping capacity begins in the temperature regime
above M_s corresponding to the region of increasing electrical
resistivity during cooling of the NiTi alloy.

In order to perform the above experiments, a precision
electrical resistivity apparatus was constructed using the
double Kelvin Bridge principle. This apparatus uses an L&N
type K-3 potentiometer, a standard cell, constant voltage supply, a

-28-
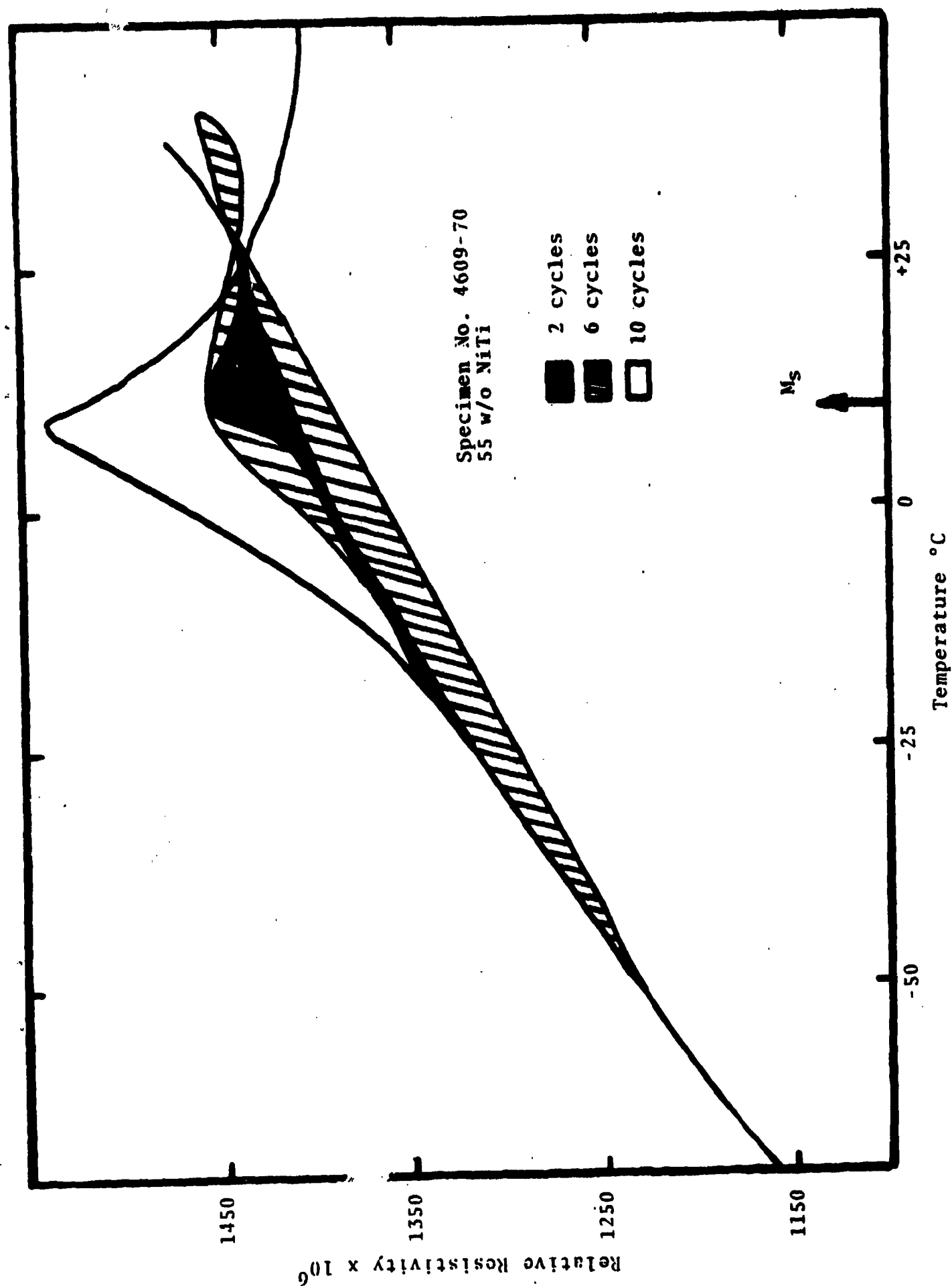
Figure 14. Electrical Resistivity versus Temperature for a 55 w/o NiTi Alloy as a Function of Number of Temperature Cycles.
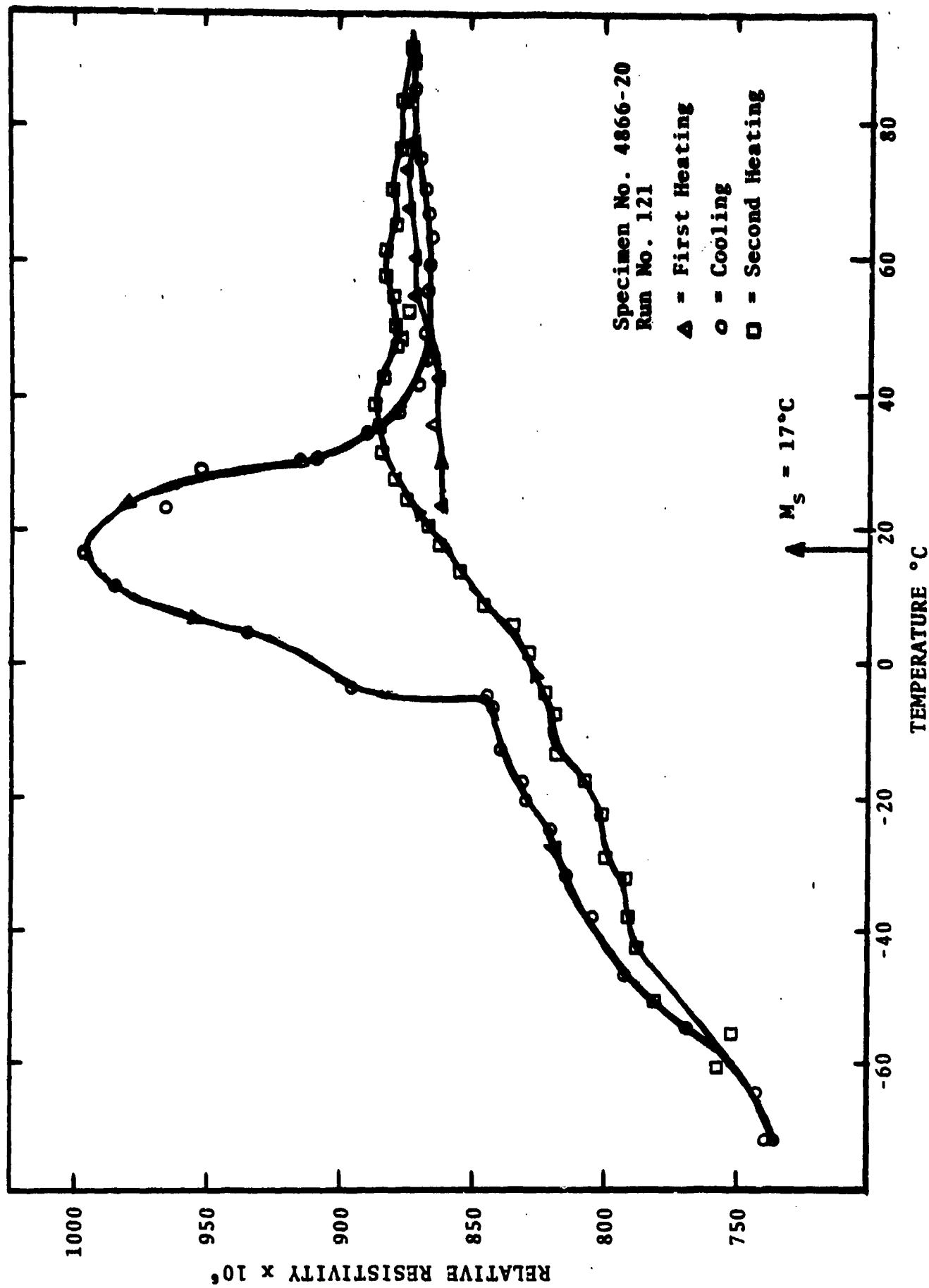
Figure 15. Electrical Resistivity versus Temperature for a 55 w/o NiTi Alloy as a Function of Temperature after 76 cycles between -65°C and +90°C.

regulated power supply, a L&N resistance standard and a L&N D.C. null detector. The precision of measurement obtained is of the order of 1×10^{-6} ohm-cm.

An acoustic apparatus was designed and constructed to yield information as to the types of martensitic transformations occuring, i.e. burst phenomena, thermoelastic, etc. This equipment uses a wire hook-up from a crystal transducer to the specimen. Standard amplifier and loud speaker are connected to the transducer. In addition, an Esterline Angus high speed recorder was connected so that a permanent record could be made of the acoustic emissions from the specimen during temperature cycling through the temperature range of interest. No acoustic emissions have been observed to date in experiments performed on NiTi samples as cycled through the "soft-mode" and the martensitic transformation temperature ranges. In contrast, much acoustic activity was detected during transformation in experiments using 70 Fe-30 Ni alloys in which "burst-type" martensitic transformation is known to occur (18). The above experiments indicate that the mechanism of martensitic transformation in the highly damping NiTi alloys is of the thermo-elastic mode.

In order to establish a stable transformation behavior as a baseline treatment for samples to be treated prior to various measurements, multiple temperature cycles between -65°C and +90°C were employed. The cycling treatment consisted of immersion in a Dow Corning 200-10CS/Dry Ice mixture held at -65°C and a second Dow Corning 200-10CS bath at 90°C. A ten-minute cycle is employed in this treatment. Figure 15 shows the resistance-temperature curve obtained after seventy-six cycles. Since these characteristics are well defined, a treatment of 50-70 cycles was selected as the basis for preparation of specimens to be evaluated by calorimetry, damping and Young's modulus measurements over the -65°C to 90°C temperature range.

A second series of experiments designed to evaluate the effects of cold work on the transformation characteristics was

- 31 -

carried out. These studies were conducted by heat treating strips of 55 w/o NiTi (4866) by annealing at 790°C for thirty minutes, quenching in water and cycling between -65°C and +90°C fifty times. Following this treatment the electrical resistance of the 190 mil x 250 mil x 5.5 inch strip was measured as a function of temperature. Figure 16 shows the results of this test. Subsequently, the strip was deformed by rolling at room temperature. This treatment was followed by a second set of fifty temperature cycles between -65°C and +90°C. Finally the resistance-temperature characteristics were measured again. Three levels of deformation were employed in this series of tests. These corresponded to 3.2%, 7% and 15.2%. The resultant measurements (obtained on three different bars) are shown in Figures 17-19. These curves show that deformation in the 0-7% range broadens the temperature range of the transformation while 15% deformation seems to obscure the change of resistance with transformation or eliminate the transformation entirely. These test bars were examined by determining their damping characteristics so that the effect of deformation on damping could be evaluated. The results have been combined to determine the optimum treatment which can be employed to achieve attractive damping and strength characteristics.

Due to the difficulty in machining NiTi specimens, it was decided to determine the possible usefulness of a flat-type specimen as compared with the standard reed-type specimens employed for damping capacity measurements in the BBN Resonant Dwell Apparatus. Specimens of each type were fabricated and were temperature cycled (up to seventy-six cycles) to yield stable temperature resistivity curves prior to measurement of damping capacity as a function of temperature by BBN. The results of the damping studies on the flat-type specimens did not compare favorably with the standard reed-type samples. As a consequence, the latter configuration was employed exclusively. The transformation characteristics of the 55 w/o NiTi alloy (i.e. 55 w/o Ni-45 w/o Ti) were redetermined at tensile stresses of 1275 and 5484 respectively. Figures 20 through 22 show the results of runs numbered 124, 130 and 131. Identical samples of the 55 w/o Ni-45 w/o Ti alloy were an-

- 32 -
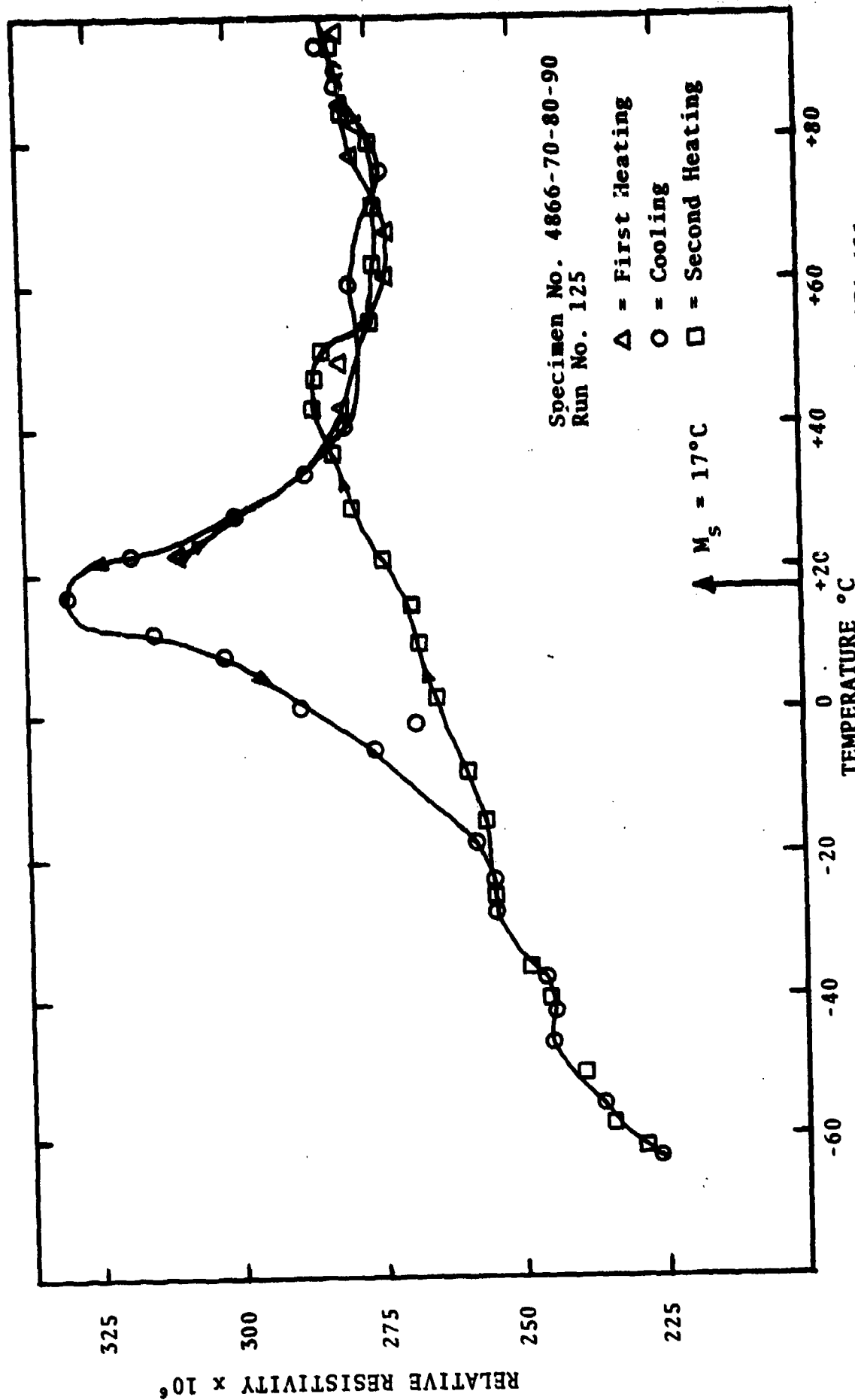
Figure 16. Electrical Resistivity versus Temperature for a 55 w/o NiTi Alloy as a Function of Temperature after 50 cycles between -65°C and +90°C.

Specimen No. 4866-70-80-90
Run No. 125

Δ = First Heating
O = Cooling
□ = Second Heating

M_s = 17°C

TEMPERATURE °C

RELATIVE RESISTIVITY x 10⁶

- 33 -
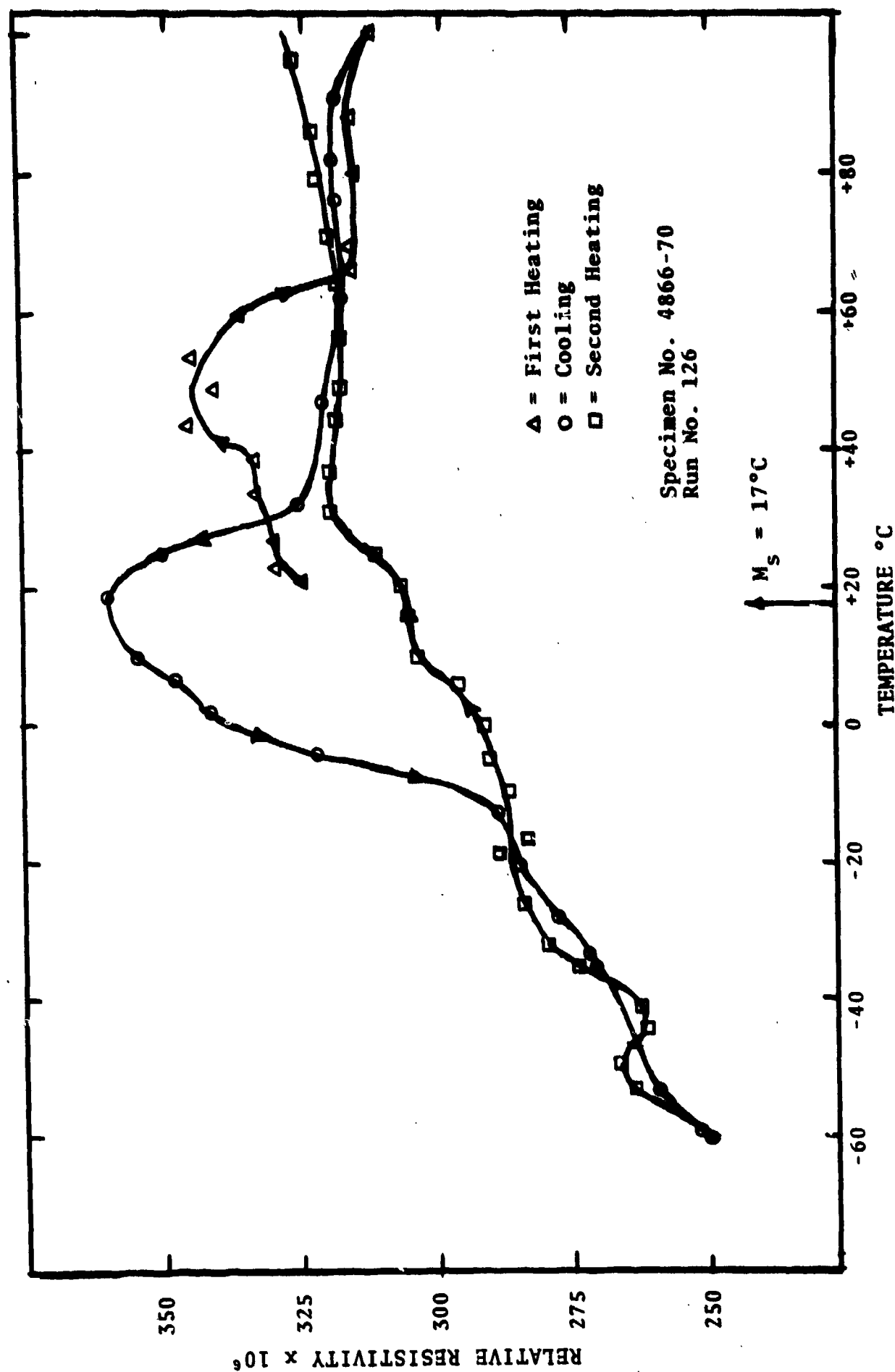
Figure 17. Electrical Resistivity versus Temperature for a 55 w/o NiTi Alloy as a Function of Temperature after 3.2% deformation by rolling followed by 50 cycles between -65°C and +90°C.

- 34 -
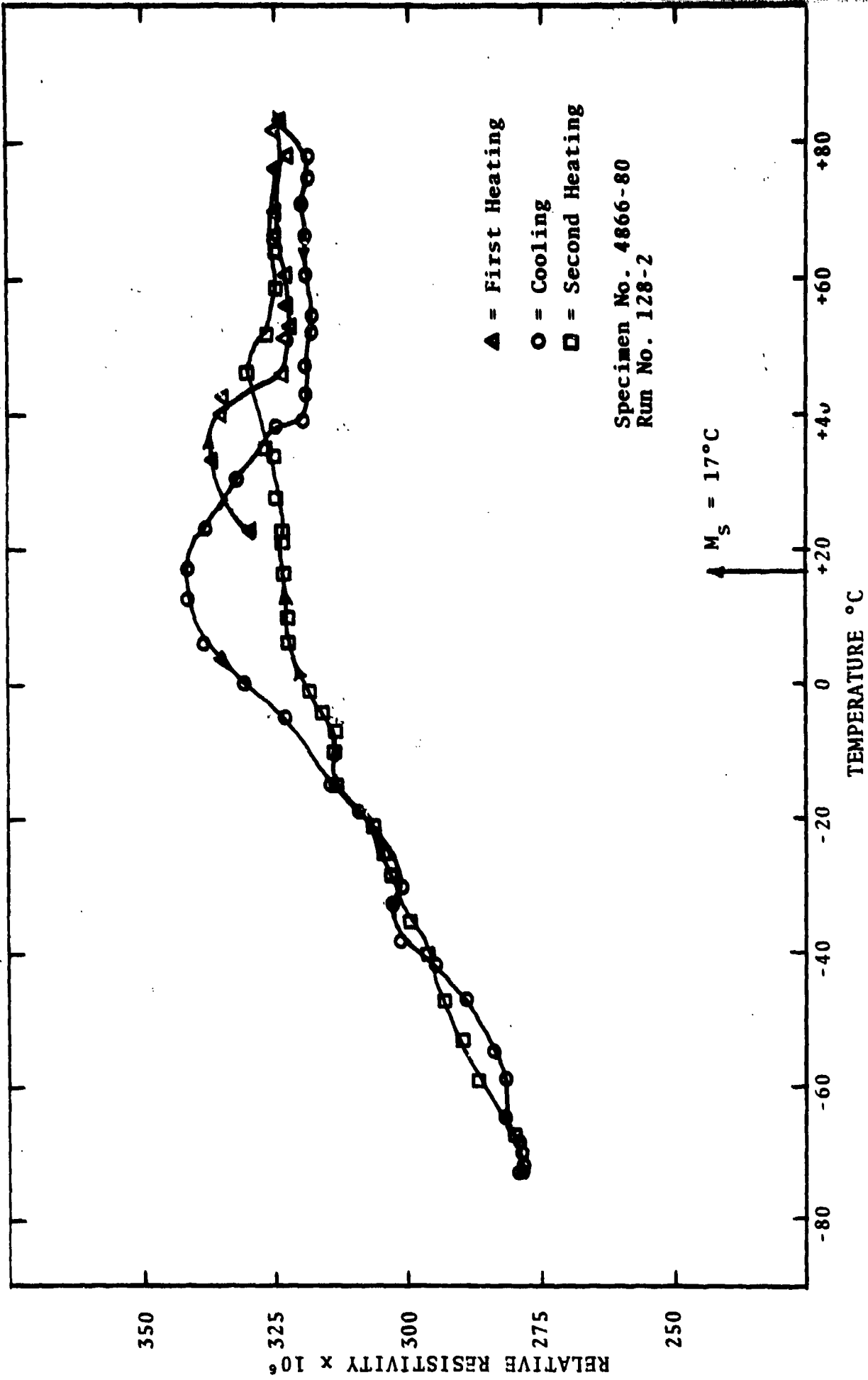
Figure 18. Electrical Resistivity versus Temperature for a 55 w/o NiTi Alloy as a Function of Temperature after 7% deformation by rolling followed by 50 cycles between -65°C and +90°C.

▲ = First Heating

O = Cooling

□ = Second Heating

Specimen No. 4866-80
Run No. 128-2

M_s = 17°C

TEMPERATURE °C

RELATIVE RESISTIVITY x 10⁶

- 35 -
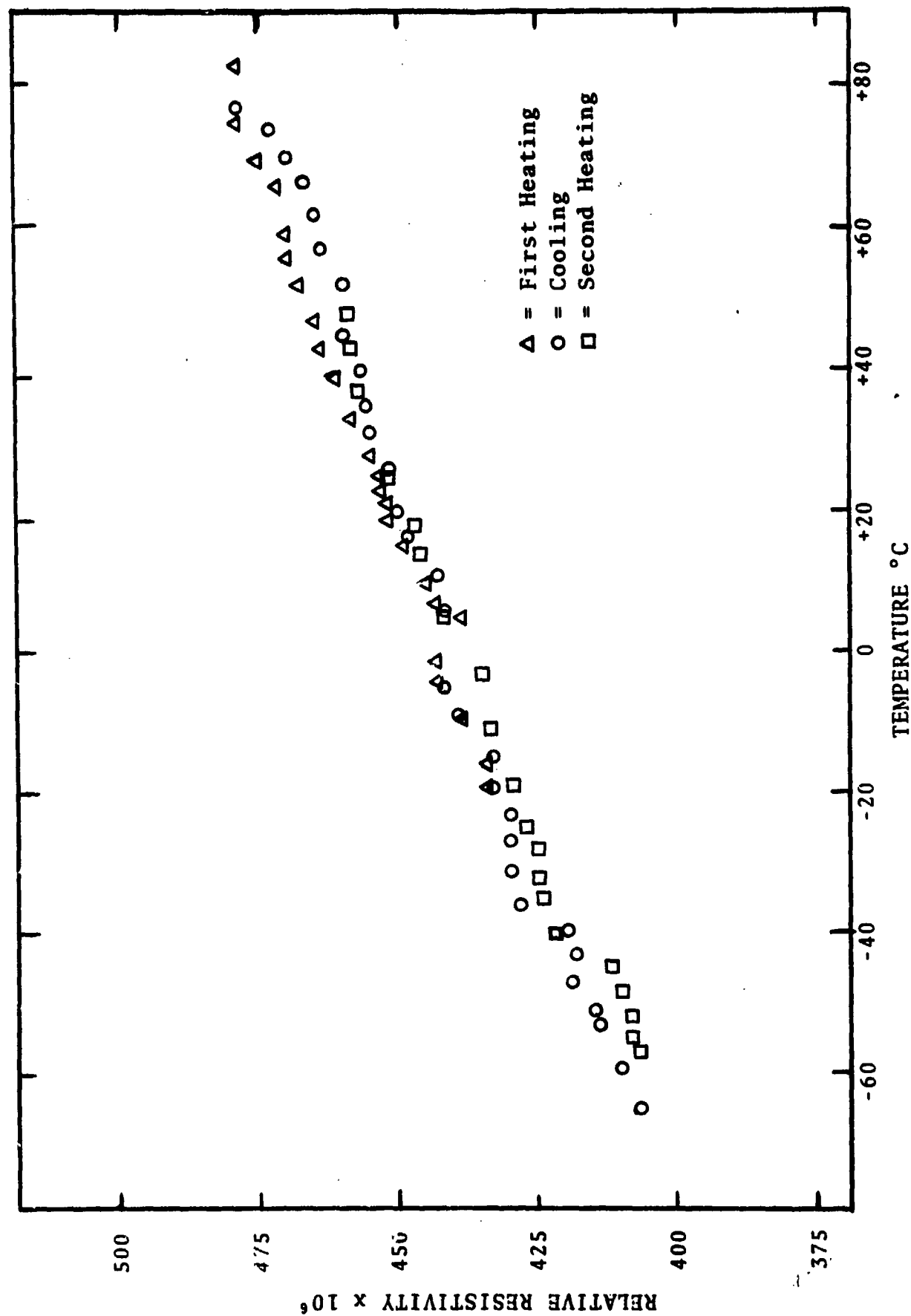
Figure 19. Electrical Resistivity versus Temperature for a 55 w/o NiTi Alloy as a Function of Temperature after 15% deformation by rolling followed by 50 cycles between -65°C and +90°C.
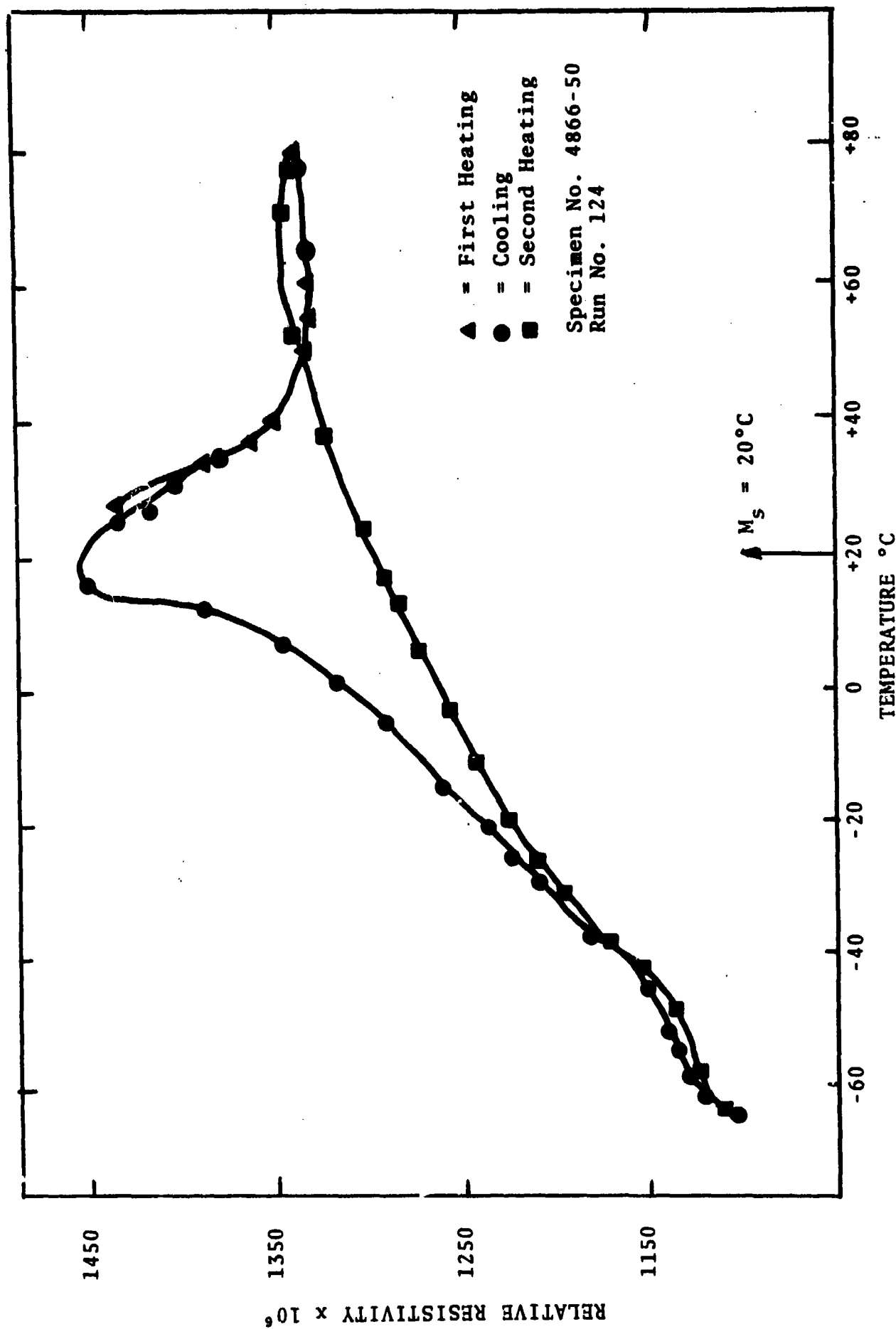
Figure 20. Electrical Resistivity versus Temperature for a 55 w/o Ni-45 w/o Ti Alloy after 50 cycles between -65°C and +90°C.

- 37 -
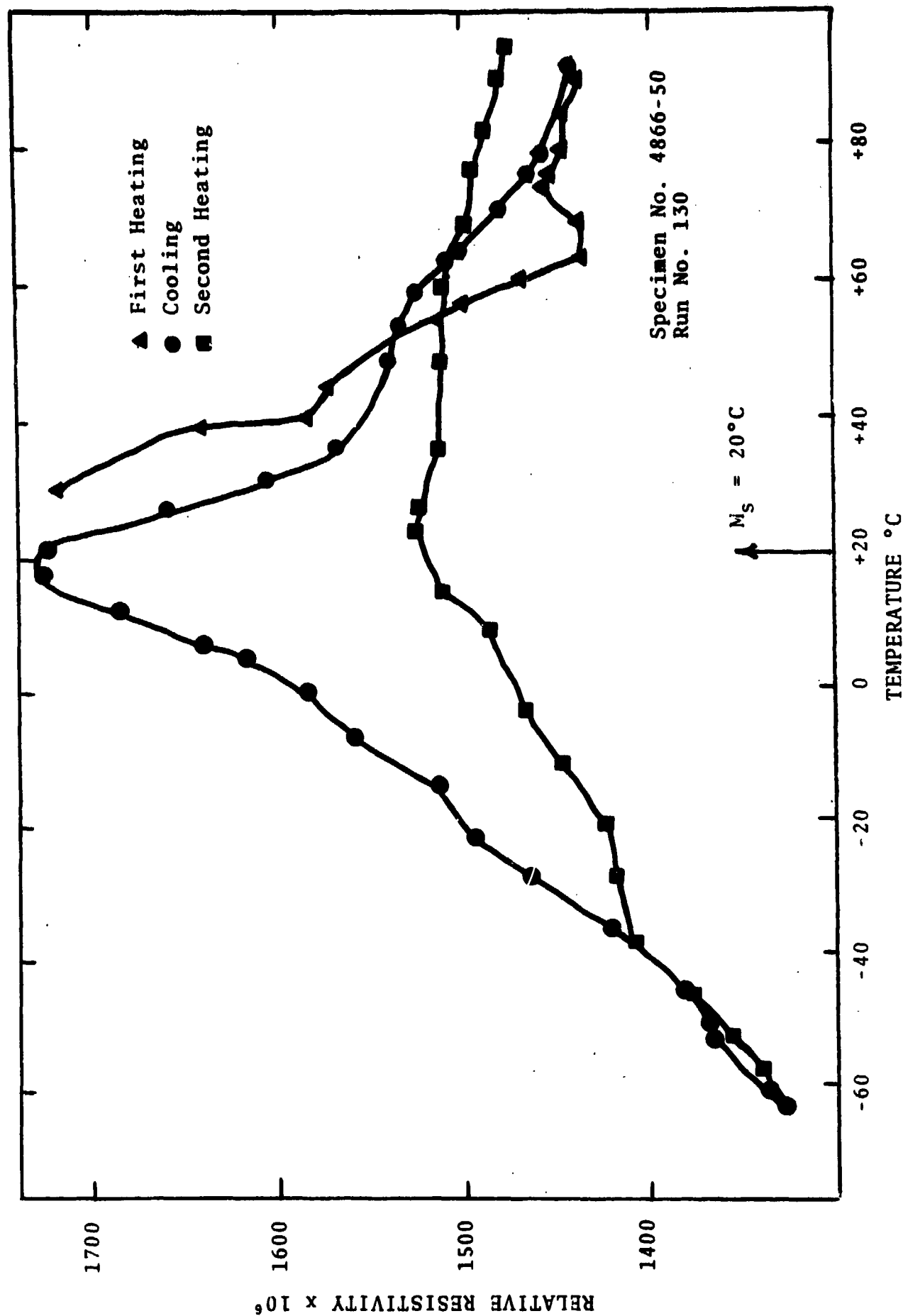
Figure 21. Electrical Resistivity versus Temperature for a 55 w/o Ni-45 w/o Ti Alloy after 50 cycles between -65°C and +90°C. Tensile Stress of 1275 psi Applied during Measurement.
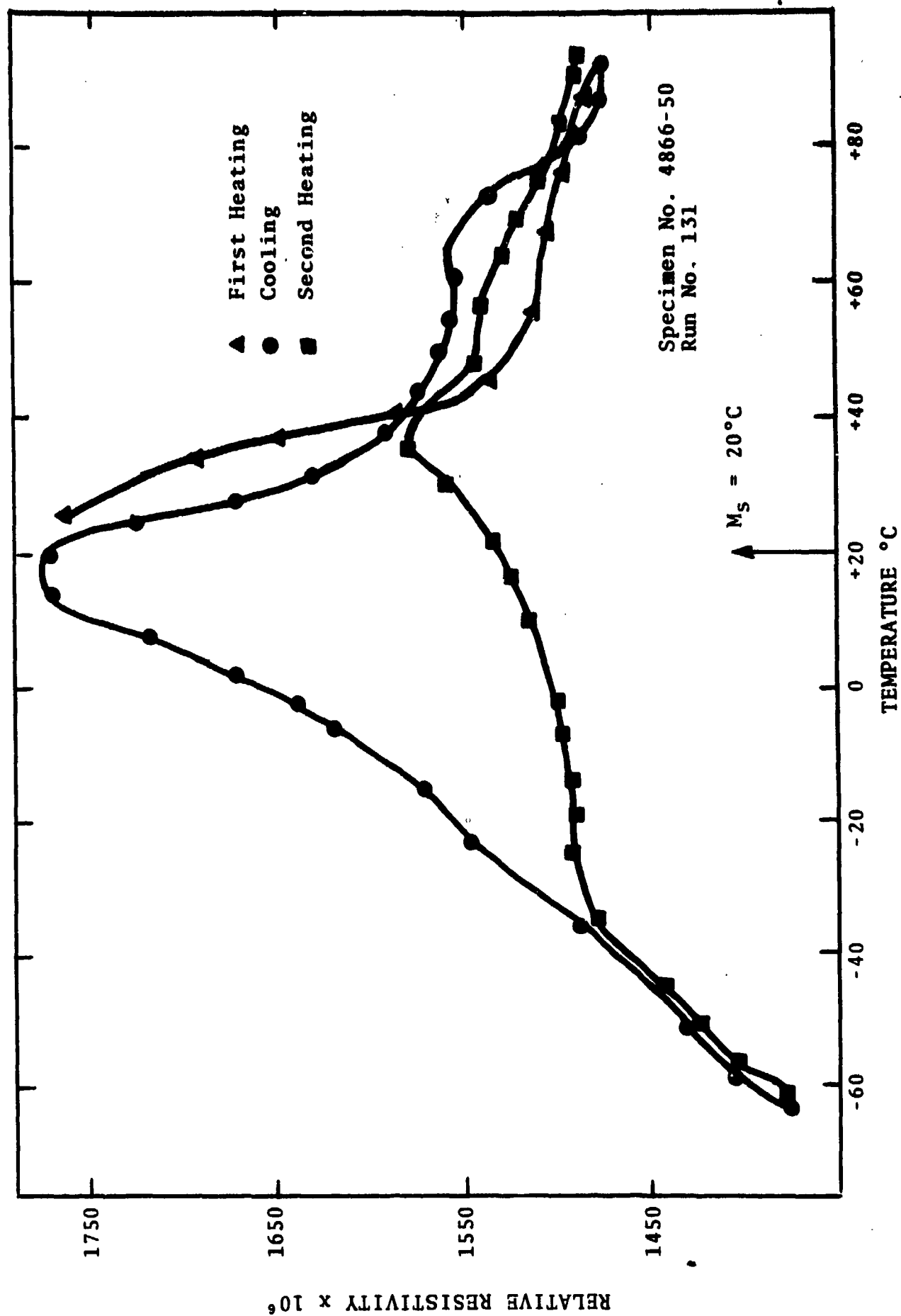
Figure 22. Electrical Resistivity versus Temperature for a 55 w/o Ni-45 w/o Ti Alloy after 50 cycles between -65°C and +90°C. Tensile Stress of 5484 psi Applied during Measurement.

First Heating
Cooling
Second Heating

Specimen No. 4866-50
Run No. 131

$M_S = 20°C$

TEMPERATURE °C

RELATIVE RESISTIVITY x 10^6

nealed and run through fifty temperature cycles between -65°C and +90°C. Figure 20 shows the resistivity-temperature curve obtained on a sample with no applied tensile load. The resistivity peak occurs at about +20°C, in good general agreement with the results obtained for samples of this alloy which were run earlier as shown in Figures 2 and 3. Figures 21 and 22 show the resistivity-temperature curves obtained on the companion samples while tensile loads corresponding to stress levels of 1275 and 5484 psi respectively were applied. No appreciable shift in M_s was observed.

2. Damping in Nitinol.

The BBN resonant dwell apparatus generates damping (Q^{-1}) versus temperature curves. The applied bending stress is between 1 and 10 ksi, and the frequency is between 100 and 1000 Hz. Experimentally, it was found that the damping varies with the cycling of the temperature-control unit, but the quality of the measurements could be improved significantly by determing the damping isothermally versus strain amplitude (tip deflection). This involves measuring the resonant frequency and the accelerometer output as a function of controlled tip displacement. Over the range of tip displacement y_t the acceleration a_o and the resonant frequency f_n of the sample are each nearly linear functions of y_t which increases confidence in the values of a_o, and f_n as shown in Figure 23. The damping, Q^{-1}, is nearly independent of bending stress y_t at low values of Q^{-1} but increases with y_t at larger values as illustrated in Figure 24.

"Isothermal" curves of f_n and a_o versus y_t were taken on both cooling and heating; values of f_n and a_o were selected for y_t = 0.040 in. and used to calculate Q^{-1} (Equation 6). All specimens were first heated to well above M_s, held for 15-30 minutes, then slowly cooled to the temperature at which the measurement was to be made, and held for 15 to 20 minutes to insure thermal equilibrium. The f_n versus y_t and a_o versus y_t data were taken by increasing y_t in a stepwise fashion at the given temperature. Each of these "isothermal" curves yields one point on the damping versus temperature plots, and since only comparatively few of these measurements can be made each day, compatibility of measurements taken on different

-40-
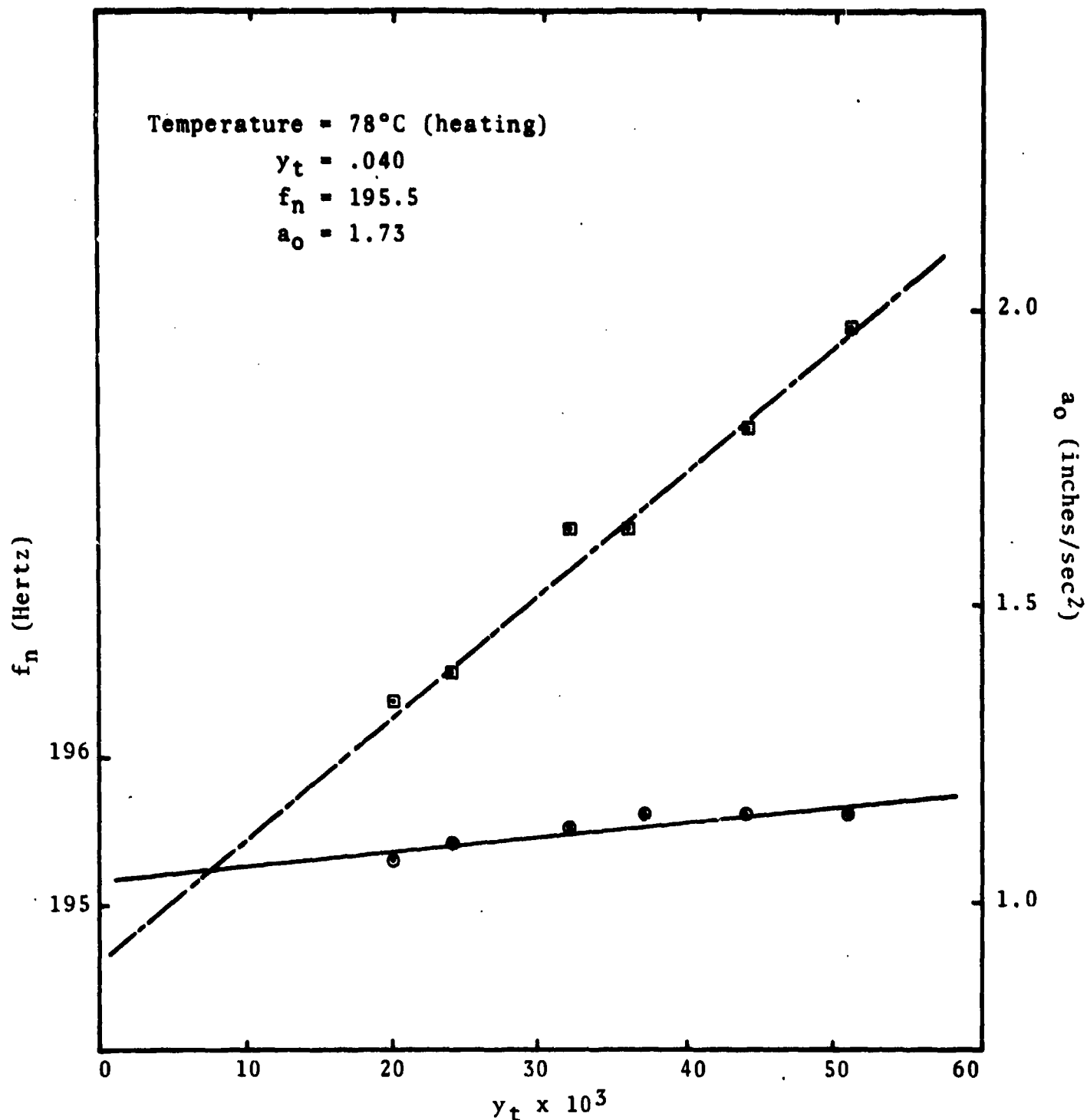
Figure 23. Sample resonant frequency (f_n) and acceleration (a_o) as a function of tip deflection (y_t) at a temperature of 78°C for a sample of 55w/oNi-45w/oTi.

- 41 -
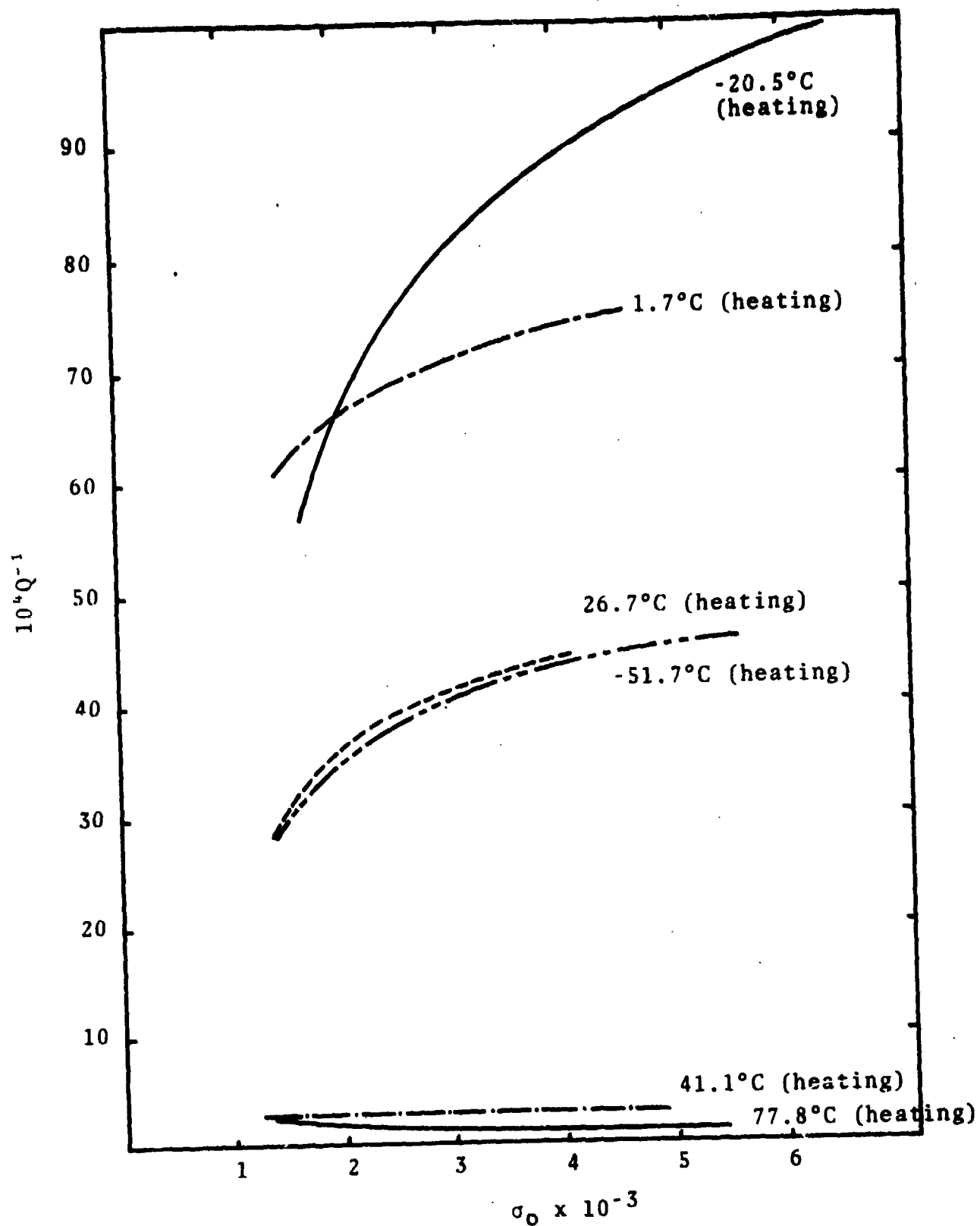
Figure 24. Specimen damping factor (g_s) as a function of maximum bending stress (σ_0) at various temperatures for a sample of 55w/oNi-45w/oTi.

days had to be determined. The agreement was found to be good. Figure 25 is a plot of damping versus temperature data for specimens with different stress and thermal histories. Figure 26 shows the curves for specimens during heating and cooling. There is a small hysteresis.

The dynamic Young's modulus of NiTi, measured at 180Hz, was determined as a function of temperature by noting the variation in resonant frequency. These results, together with data on the change in electrical resistance and heat capacity, measured in a differential thermal calorimeter, are shown as a function of temperature in Figure 27.

On cooling, the marked increase in the damping capacity and the decrease in Young's modulus set in at the same temperature (approximately 45°C). The increases in electrical resistance and heat capacity also start together, but at a temperature (approximately 25°C) which is some 20°C lower than the temperature at which the modulus and damping start their increase. The M_S of this alloy is, however, indicated by the peak in the resistivity curve on cooling, and this occurs at about 5°C. The damping thus seems to increase significantly before M_S is reached (in the unstressed sample) and this may result from (1) stress-induced martensite (i.e. the stress-induced raising of M_S), (2) premartensitic effects in the alloy, or (3) a combination of both. (c/f Section VII).

In initial tests of NiTi alloys, the cantilever beam portion of the sample deformed (i.e. it both twisted and bent) during testing. The cause of this deformation was believed to be connected with the "shape memory" of this material. More specifically, the machining and heat treating operations combined to cause the NiTi samples to bend and twist as the sample transformed while the temperature was lowered to effect a martensitic (or reverse) transformation. The bending and twisting of the sample is deleterious to testing using the resonance dwell apparatus because of the change in stress distribution associated with the deformation. In order to avoid macro-deformation associated with the transformation,

-43-
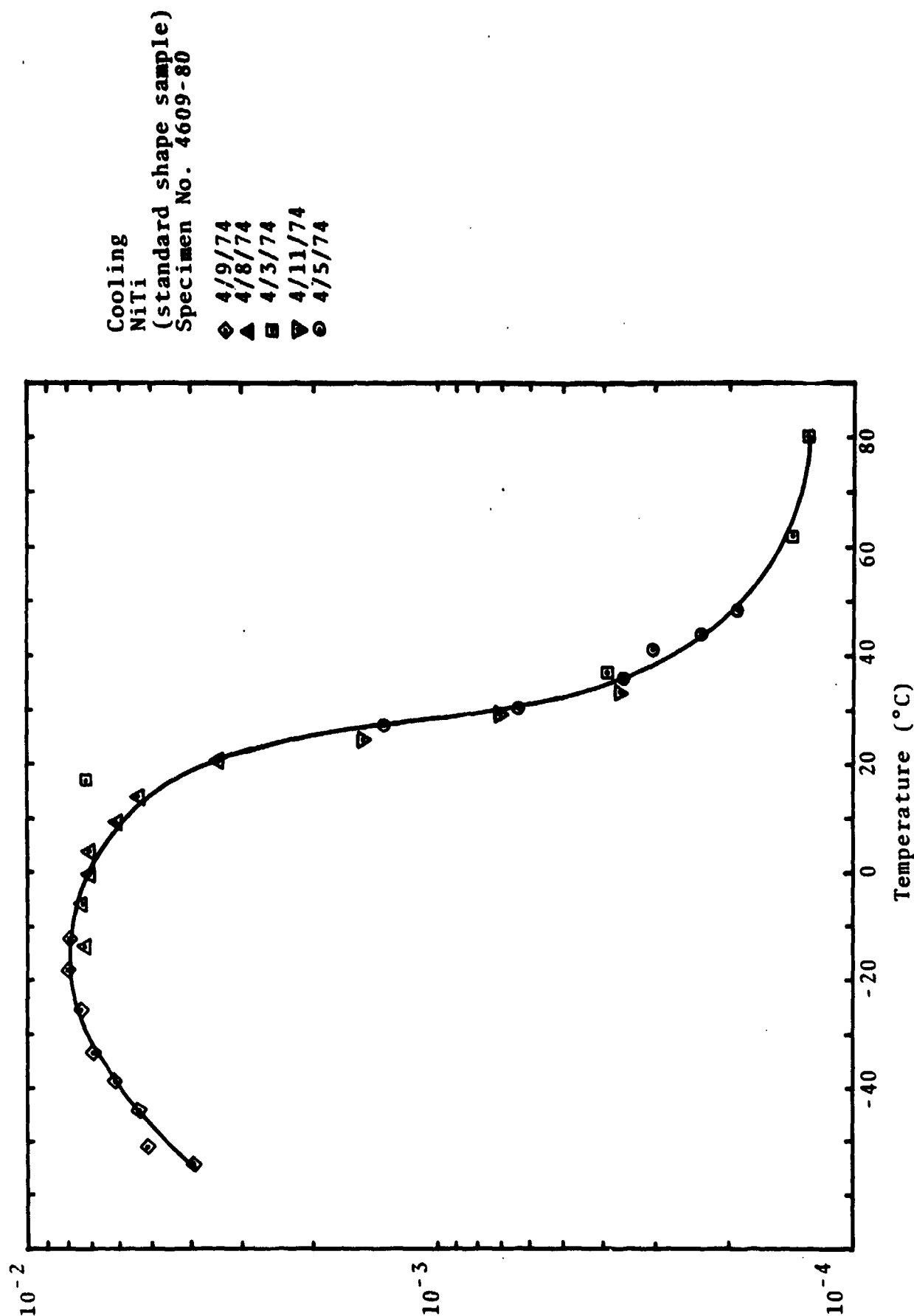
Figure 25. Specimen damping factor (g_s) as a function of temperature on cooling (for a constant $y = 0.040$ in.) for a sample of 55 w/o Ni-45 w/o Ti.
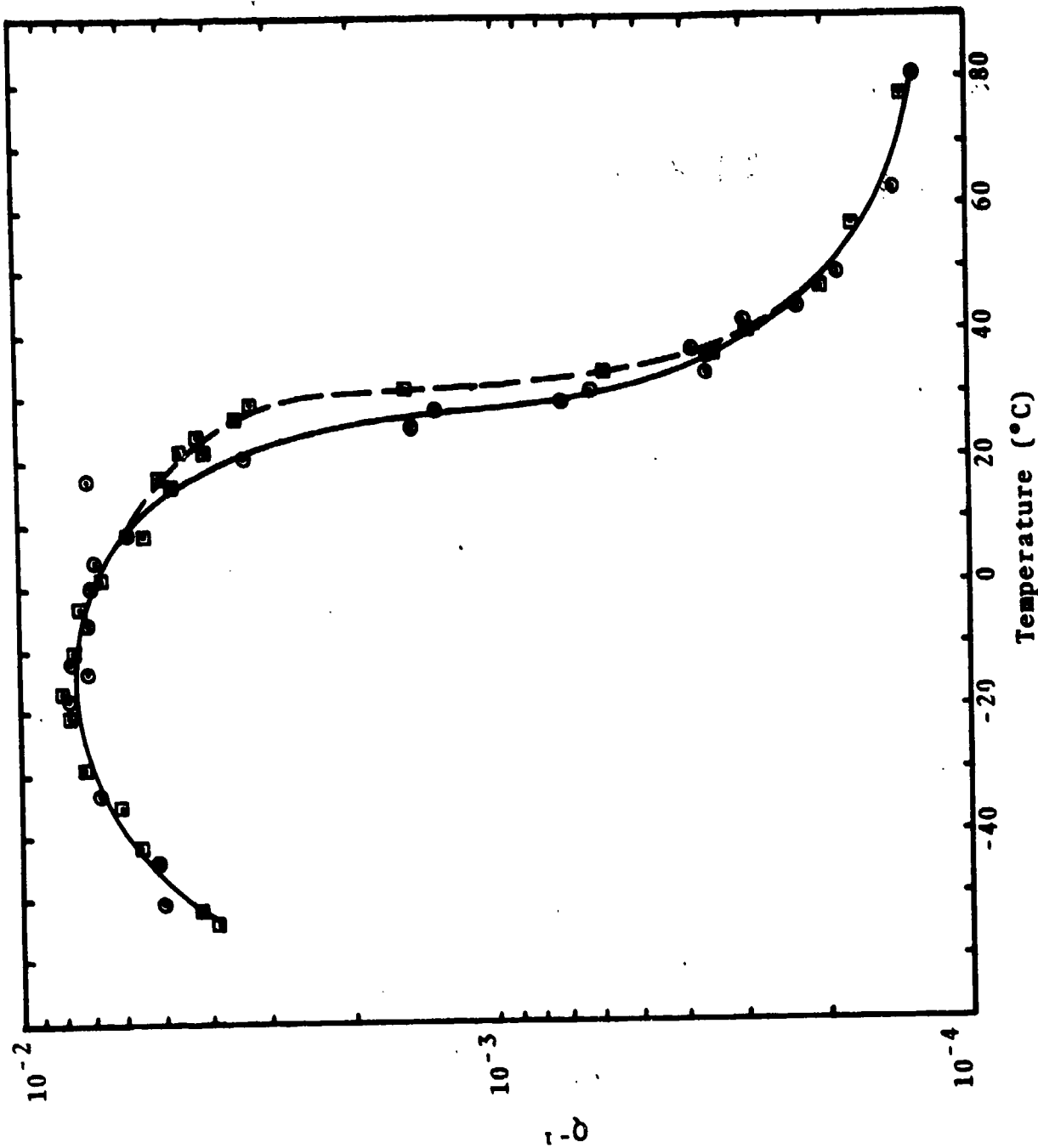
Figure 26. Specimen damping factor (g_s) as a function of temperature on both heating and cooling for a sample of 55 w/o Ni-45 w/o Ti.
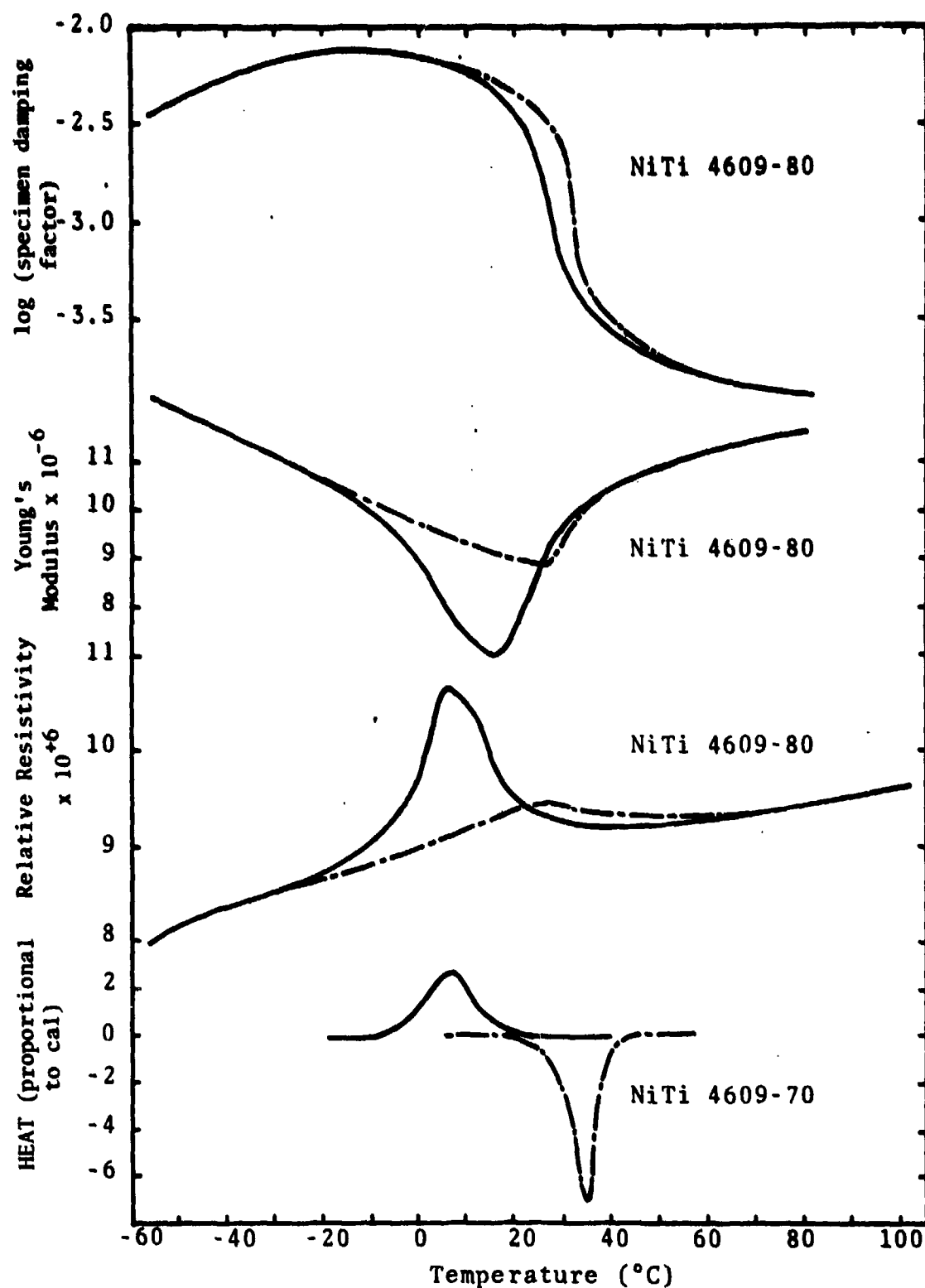
Figure 27. Specimen damping factor, Young's modulus, relative resistivity and heat evolved as a function of temperature for the same series (4609) of 55w/oNi-45w/oTi.

the samples were heat treated with the intention of putting a straight untwisted beam into the "memory" of the sample. To do this, the NiTi specimen was fixed in an appropriately shaped steel clamping device, put into a furnace at 800°C, allowed to come to equilibrium and then water quenched. The quenched samples were then thermally cycled (through their M_s temperatures) approximately seventy-five times before damping tests were performed on these samples.

The damping tests on samples V-4866-40 and V-4866-60 (55 w/o Ni-45 w/o Ti) are shown in Figures 28 and 29. The cooling curves are shown as solid lines and the dashed lines indicate the heating curves. The two figures show curves which are similar to each other. Upon cooling both of the samples showed a significant increase in damping by 40°C, the damping continued to rise to a maximum at about 22°C. The damping then more or less levels to an approximately constant value. On heating, the damping curve basically follows the same path as the cooling curve except that the maximum is reduced and there is a hysteresis effect. That is, the damping remains high to a temperature above that where the damping first increased on cooling.

During the tests on samples V-4866-40 and -60, the beams deformed slightly so that the memory was not entirely "straight." Figures 28 and 29 can be compared with Figure 30 which shows the damping curve of sample 4866-40 before the effort to straighten the beam. In this test the beam deformed significantly, but as shown in the figure, the basic shape and position (with respect to temperature) of the curve is the same as the curves from the (approximately) "straight memory" samples.

An important point which was necessary to clarify was the location of the martensite start temperature (M_s) in relation to the damping curve. The resistivity curve of a 4866 sample (thermally cycled through M_s seventy-five times) indicates the M_s is at about 20°C. However, there was a question as to how much the (vibratory) stress applied by the resonant dwell apparatus

-47-
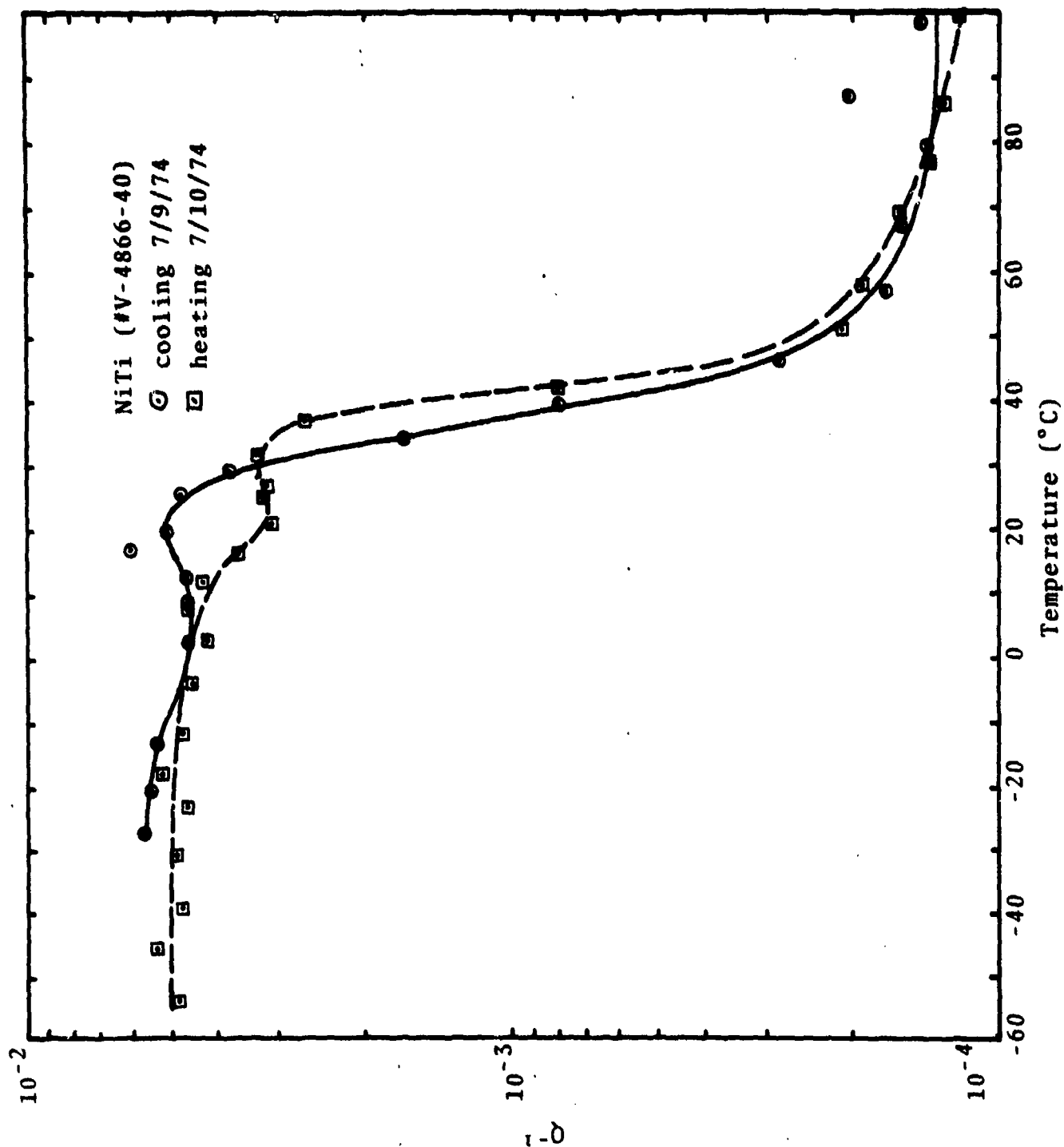
Figure 28. Damping behavior of NiTi alloy 4866 (sample no. 40) heat treated such that cantilever beam sample remains undeformed throughout the test. Composition 55 w/o Ni-45 w/o Ti.
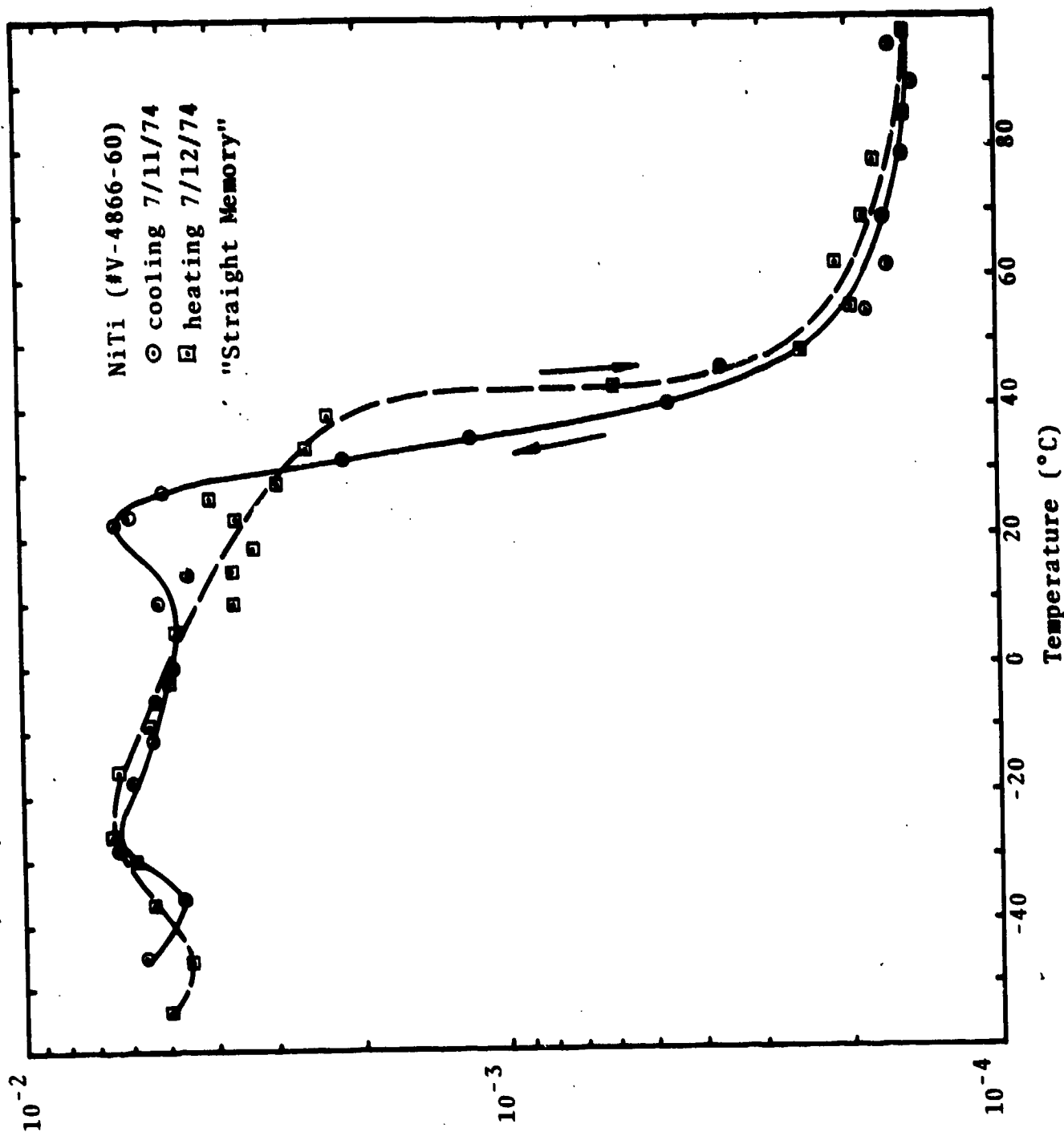
Figure 29. Damping behavior of NiTi alloy 4866 (sample no. 60) heat treated such that the cantilever beam sample remains undeformed throughout the test. Composition 55w/oNi-45w/oTi.

-49-
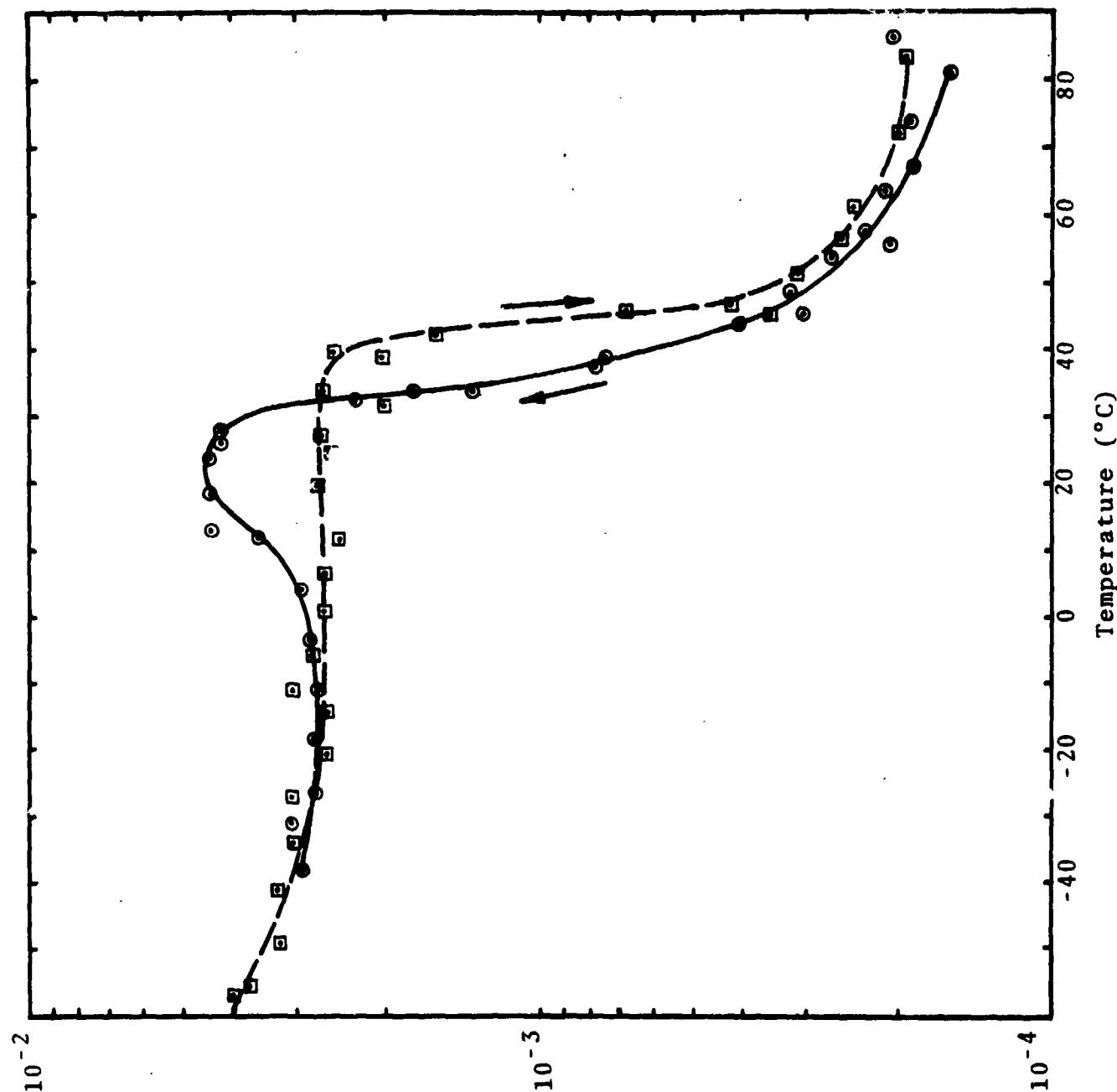
Figure 30. Damping behavior of NiTi alloy 4866 (sample no. 40)
prior to straightening heat treatment. Composition
.55 w/o Ni-45 w/o Ti.

might raise the M_s temperature. In order to obtain a reasonable estimate of how M_s is affected by the stress (applied by the testing apparatus), the resistivity of a sample of V-4866 NiTi material was measured with a dead load of 1275 psi and 5485 psi (the maximum stress applied in the damping test). These tests showed that M_s (indicated by the temperature at the peak in resistivity) was not shifted (see Figures 20-22). The conclusion of the damping and resistivity measurements is that the damping increases significantly (that is, some 20°C) before M_s is reached. This suggests that the damping increase upon cooling is initially (in the 40°C to 20°C range) caused by premartensitic phenomena. It is also of interest to note that the dynamic Young's modulus (i.e., the modulus measured at the resonant frequency of the sample) has a minimum near the same temperature that the damping is at a maximum. (Note also the anomalous positive slope of the modulus above M_s). The curves for damping, Young's modulus, and resistivity versus temperature are shown in Figure 31 for sample #4866-40. The cooling curves (solid lines) of each property have extrema at approximately the same temperature. Also, viewing the heating curves (dashed lines), extrema are again found at about the same temperature.

It is apparent that the damping reamins at a high level even after M_f (approximately -10°C) has been reached. Thus the mechanism which causes the high damping (up to 20°C) is probably distinct from the mechanism which causes the high damping from 20°C to -45°C. In order to gain further information about the mechanisms causing damping, a thermal-tensile stage for a light microscope was constructed. The stage was tested over the temperature range of -50°C to +60°C. The stage was constructed in order to observe the behavior of the sample when a stress is applied and subsequently removed at various temperatures. Samples of V-4866 NiTi were polished (both mechanically and electrolytically) and observed in the stage (with no applied stress) as the temperature was lowered from 60°C to -50°C.

-51-
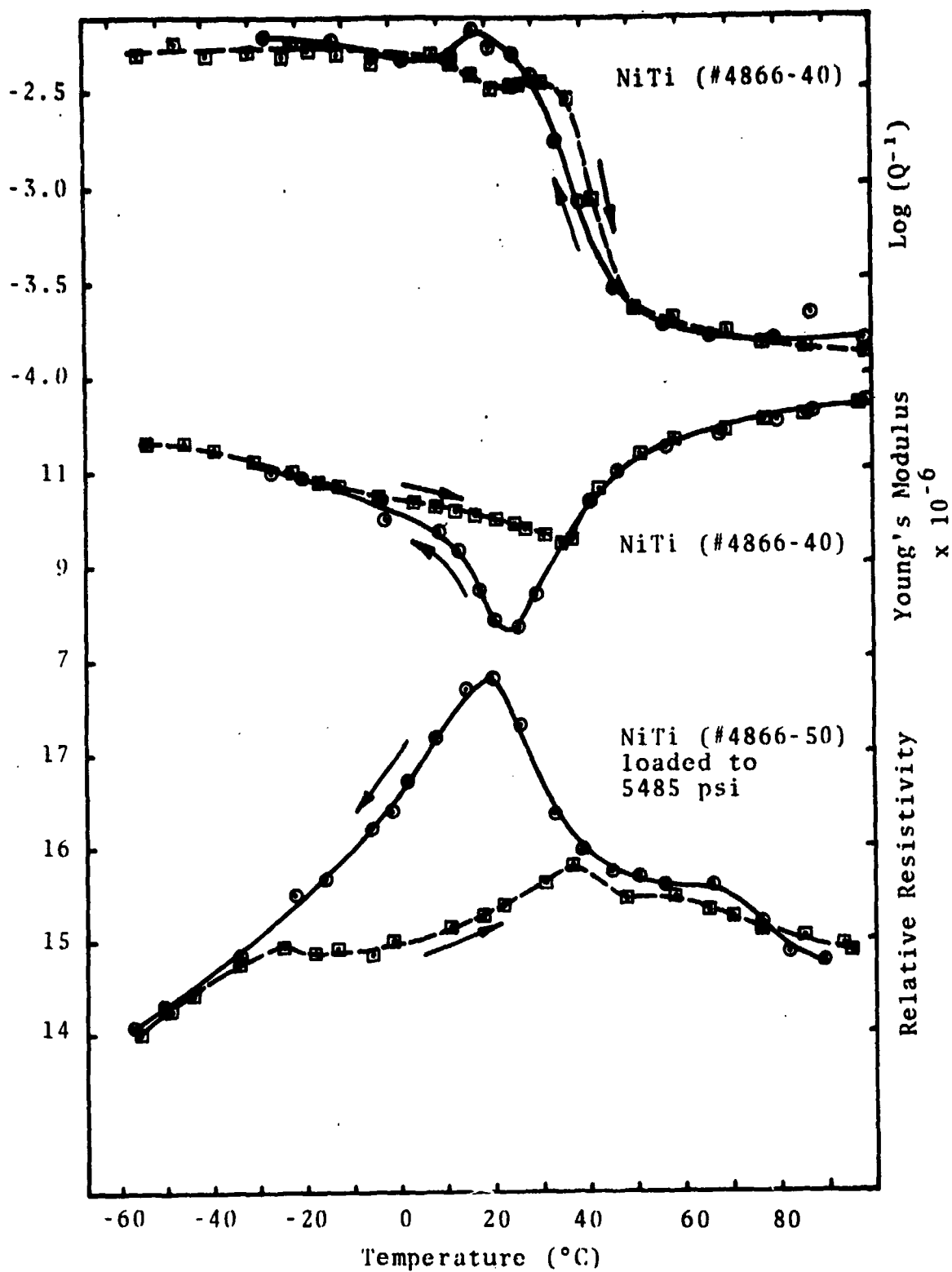
Figure 31. Damping behavior, Young's modulus, and
electrical resistivity as a function of
temperature for NiTi alloy 4866.
(55 w/o Ni-45 w/o Ti)

No surface relief caused by the martensite was noted in these samples.

In order to evaluate the effects of cold working on the loss factor, Q^{-1}, a series of samples were cold worked and then machined into reeds. These were subsequently cycled eighty times between -90°C and +100°C and measured over the range -60°C to +80°C. Figures 32-37 show the results for Q^{-1} versus T and the dynamic Young's modulus versus temperature. The general features of these curves are similar to those shown earlier in Figure 27. However, the results obtained for the sample which received 15% reduction do not show the maxima and minima exhibited by the other curves.

3. Damping in Cu-Al-Ni

The damping behavior of 83 w/o Cu-14 w/o Al-3 w/o Ni are measured by preparing samples of this alloy in the single crystal and polycrystalline forms. The initial results were obtained on a polycrystalline sample. Figure 38 shows these results disclosing rather high loss factors. However, subsequent examination showed that the sample exhibited some cracks which may have contributed to the damping. Consequently, several single crystals of this material were prepared and the measurements repeated.

Samples of Cu-14.0Al-3.0Ni and Cu-14.1Al-3.0Ni have been run on a differential thermal calorimeter at AMMRC. Critical results indicate that the M_s of the sample can be determined quite well by calorimetry. Small samples (approximately 20mg) indicated that the $\beta_1 \to \gamma_1$ martensitic reaction occurs in a very narrow temperature range--less than 0.07°C between the M_s and M_f for the samples tested (indicating from measurements made at the slowest rate of temperature change allowed on the machine used). Larger samples (approximately 120mg) showed a difference of approximately 5.0°C between M_s and M_f. This may be the effect that the bulk characteristics of the larger sample have on the thermoelastic transformation. In both large and small samples there is an appreciable difference between A_s and A_f (about 15°C) and the heat liberated versus temperature curve exhibits a significant amount of struc-

-53-
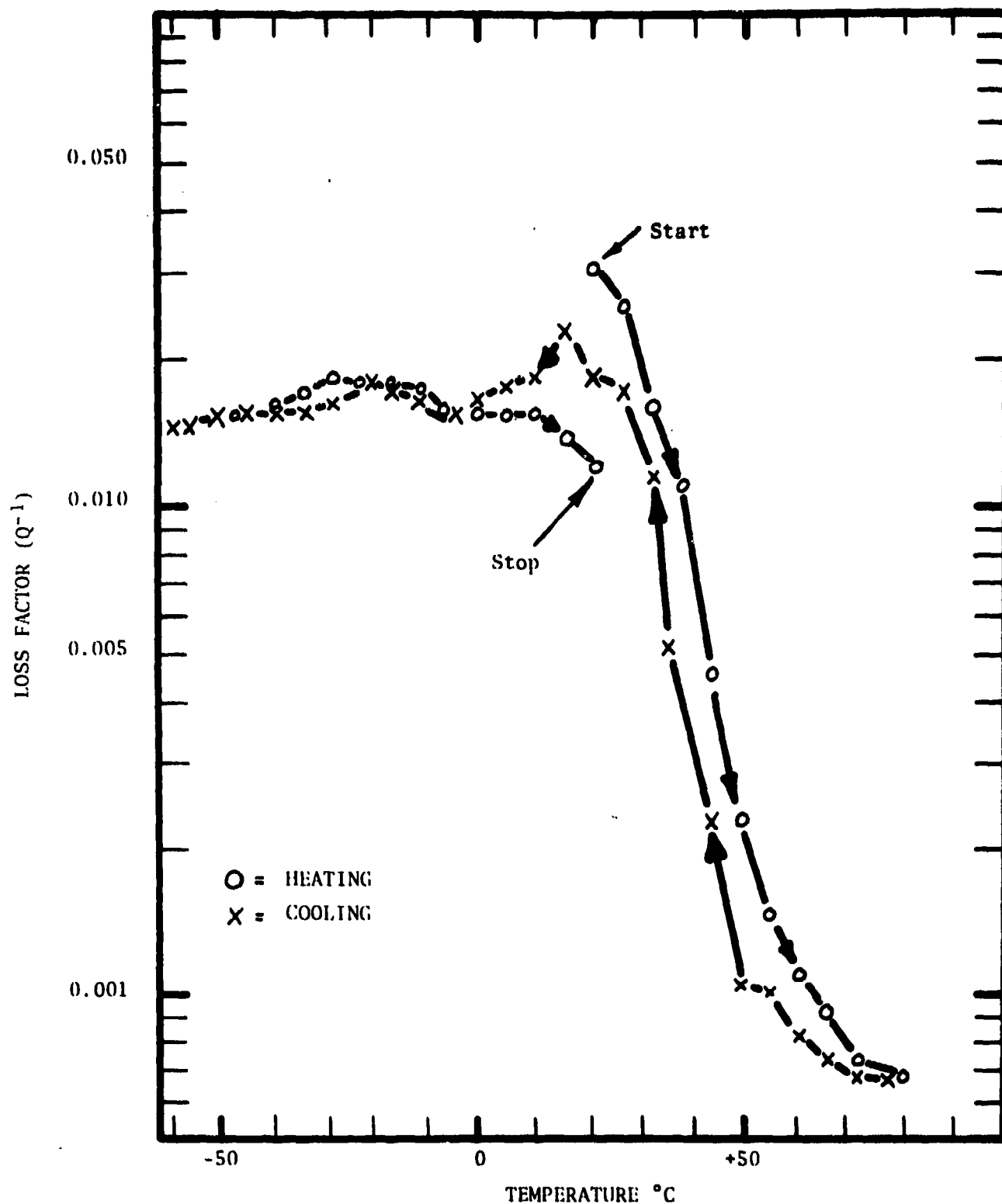
Figure 32. Loss Factor vs. Temperature Curve for a Sample of
55 w/o Ni-45 w/o Ti measured at 160-190 Hertz and a Stress
of 2000 psi. The sample was cycled 80 times between -90°C
and +100°C prior to testing. The final cycle ended by
heating from -90°C to 25°C. The M_s is at +17°C.

-54-
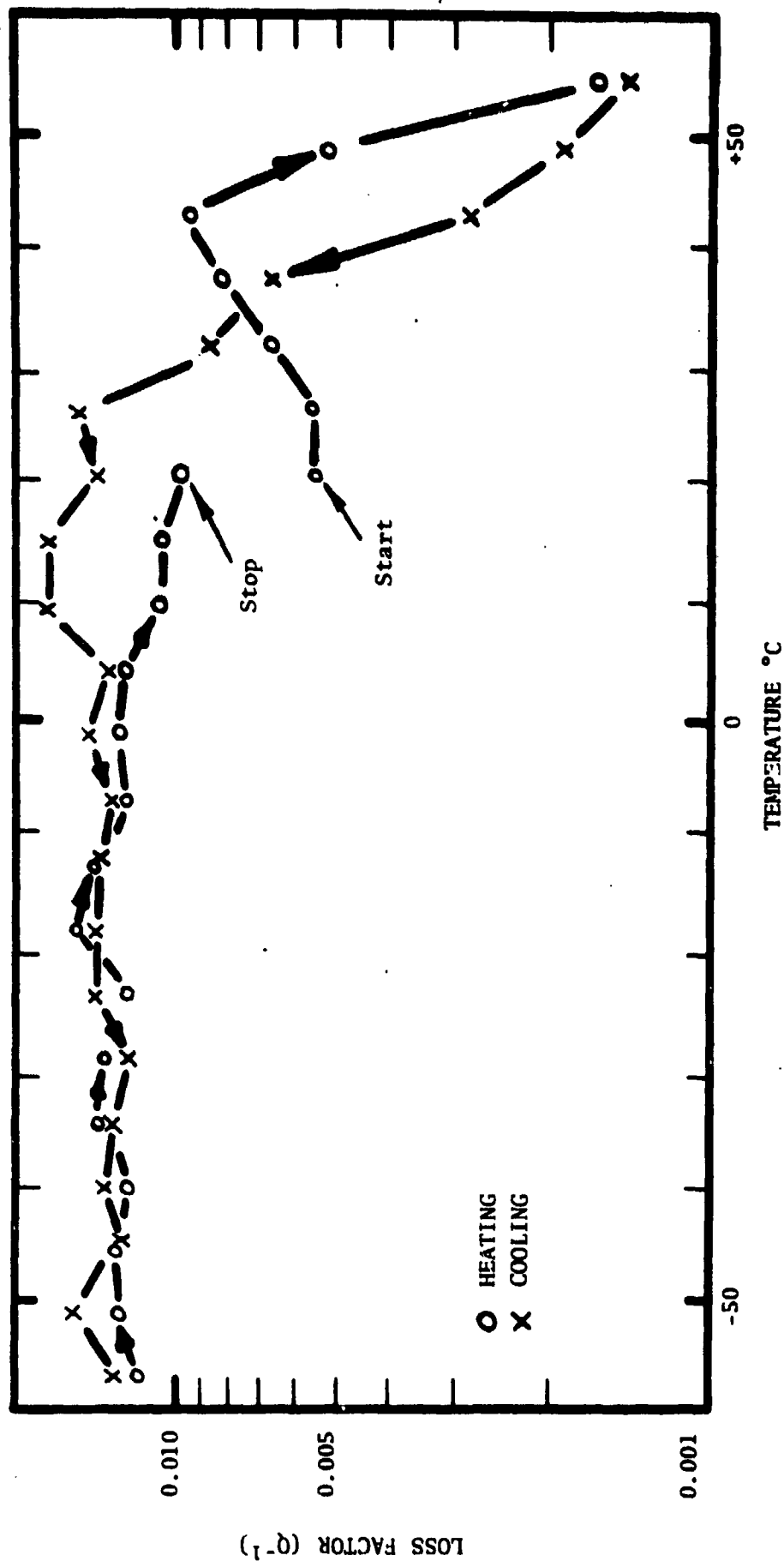
Figure 33. Loss Factor vs. Temperature Curve for a Sample of 55 w/o Ni-45 w/o Ti measured at 145-175 Hertz and a Stress of 2000 psi. The sample was deformed 3.2% by rolling and cycled 80 times between -90°C and +100°C prior to testing. The final cycle ended by heating from -90°C to 25°C. The alloy exhibits an M_s near +17°C in the annealed state.
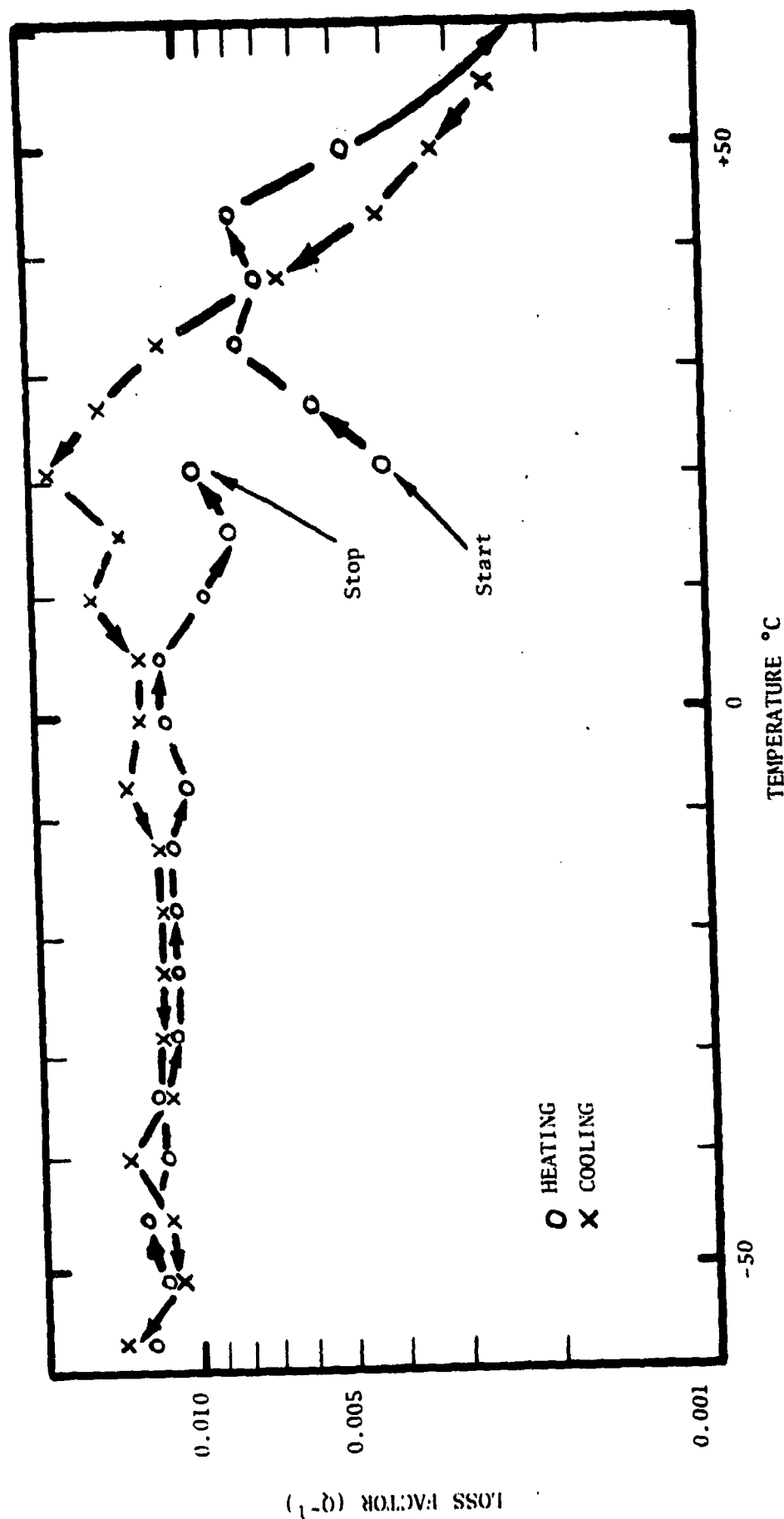
Figure 34. Loss Factor vs. Temperature Curve for a Sample of 55 w/o Ni-45 w/o Ti measured at 170-190 Hertz and a Stress of 2000 psi. The sample was deformed 7% by rolling and cycled 80 times between -90°C and +100°C prior to testing. The final cycle ended by heating from -90°C to 25°C. The alloy exhibits an N_s near +17°C in the annealed state.
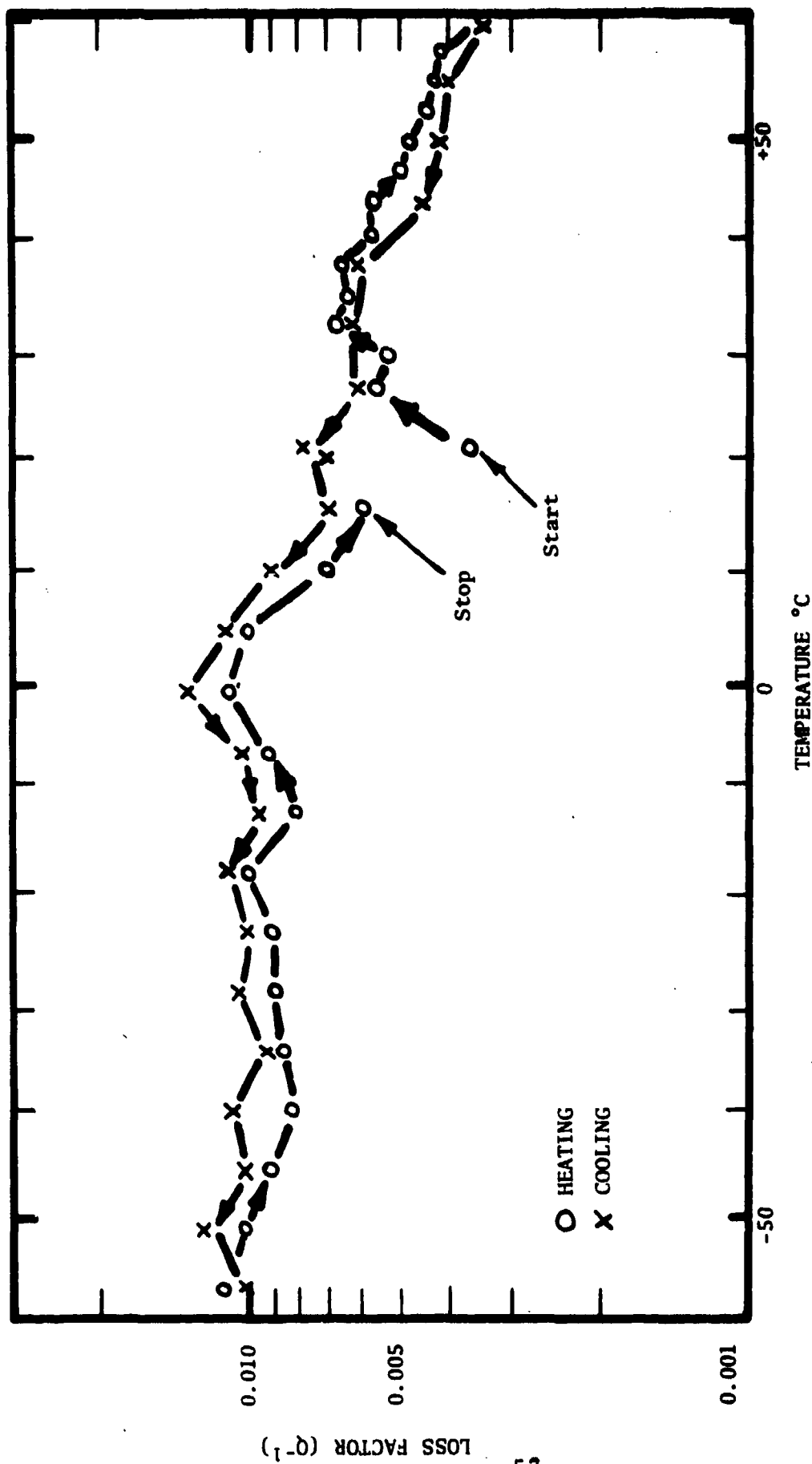
Figure 35. Loss Factor vs. Temperature Curve for a Sample of 55 w/o Ni-45 w/o Ti measured at 155-170 Hertz and a Stress of 2000 psi. The sample was deformed 15% by rolling and cycled 80 times between -90°C and +100°C prior to testing. The final cycle ended by heating from -90°C to 25°C. The alloy exhibits an M_s near +17°C in the annealed state.
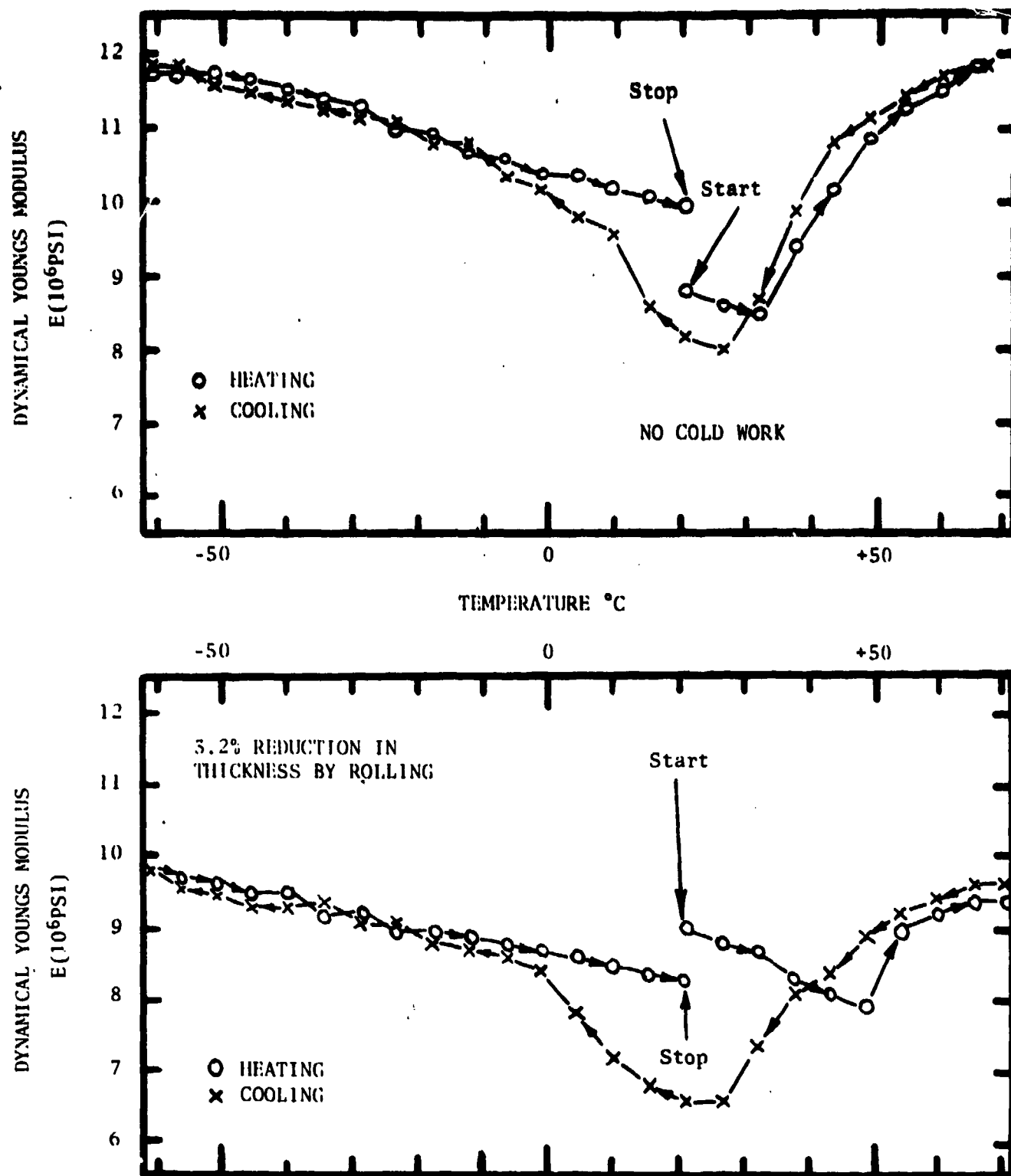
Figure 36. Dynamical Youngs Modulus vs. Temperature for 55 w/o Ni-45 w/oTi measured at 145-190 Hertz at a Stress of 2000 psi. The lower sample was deformed 3.2% by rolling prior to 80 cycles between -90°C and +100°C before testing. The final cycle ended by heating from -90°C to 25°C. The M_s is at +17°C.
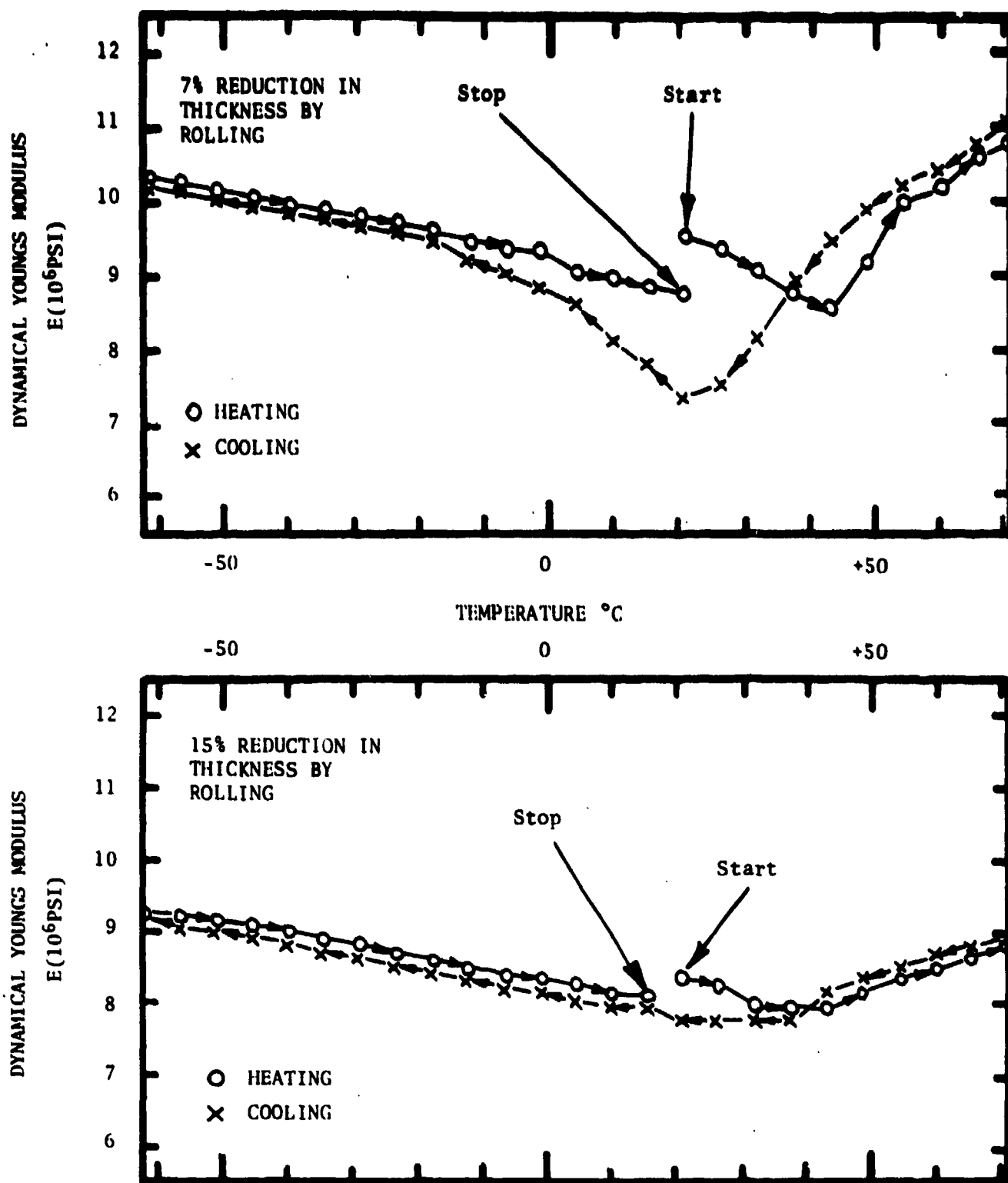
Figure 37. Dynamical Youngs Modulus vs. Temperature for 55 w/o Ni-45 w/o Ti measured at 155-190 Hertz at a Stress of 2000 psi. Both samples were deformed by rolling prior to 80 cycles between -90°C and +100°C before testing. The final cycle ended by heating from -90°C to 20°C. The M_s is at +17°C.

-59-
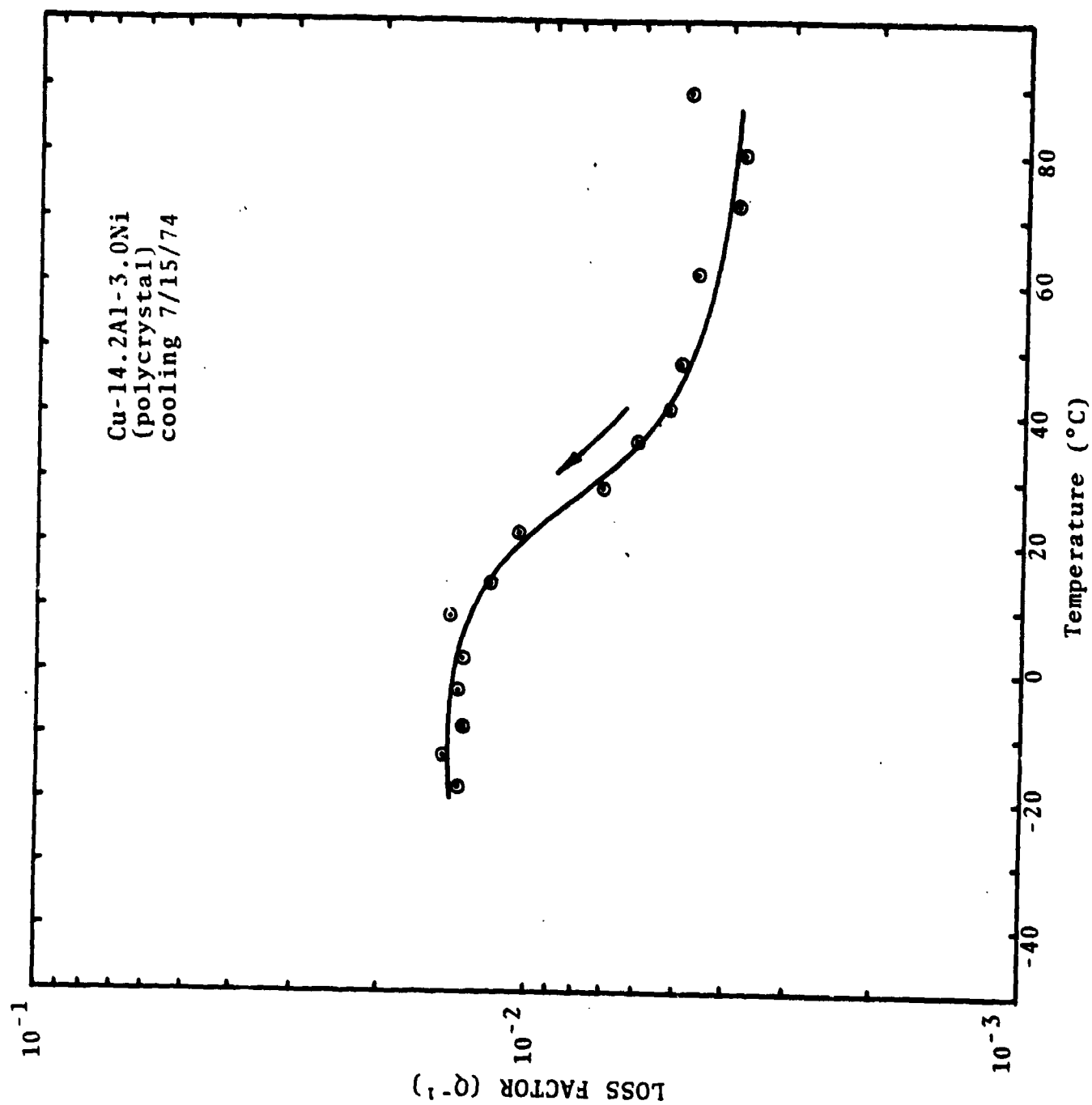
Figure 38. Damping behavior of polycrystalline Cu-14.2 w/o Al-3.0 w/o Ni (thermoelastic alloy).

Cu-14.2Al-3.0Ni
(polycrystal)
cooling 7/15/74

Temperature (°C)

LOSS FACTOR (Q⁻¹)

-60-

ture. The complexity of the transformation curves will be better understood after further optical study of the transformations.

Samples of Cu-14.0Al-3.0Ni single crystals have been polished and optically examined. The reported color change has been observed to occur in the transformation of $\beta_1' \rightarrow \gamma_1'$ (β_1 is an ordered BCC phase and is copper-red in color; γ_1' is basically an ordered HCP structure and is a yellowish-gold in color). A sample of the β_1 (parent) phase was transformed under an optical microscope by adding liquid nitrogen to the glass dish holding the sample. The martensite phase was seen to grow into the parent phase in a slow (thermoelastic) manner. The martensite plates were seen to retract in a similar manner when the sample was reheated above A_s. A thermal recycling of the $\beta_1 \cdot \gamma_1'$ transformation indicated that the microstructure did not have a "memory." The lack of a "microstructural memory" may be due to the rapid and erratic manner in which the sample was thermally cycled.

In order to gain some idea of possible mechanisms which contribute to high damping in the thermoelastic alloys, a simple stressing device was constructed. A Cu-Al-Ni sample was stressed about 200 psi in compression and observed simultaneously under a low-power light microscope. As the sample was stressed, twins could be seen to appear and to increase in length and number as the stress was increased. These same twins disappeared immediately upon the release of the stress. The interface between the γ_1' martensite and the β_1 parent phase was allowed to move upon the application of an applied stress. The amount of γ_1' increased with the applied stress. After the stress was removed, the $\gamma_1' \rightarrow \beta_1$ interface retracted slightly, but did not fully recover its original unstressed position.

Figures 39 and 40 show the results of Loss Factor and Dynamic Modulus versus temperature measurements on single crystal samples of the Cu-Al-Ni alloy. The loss factor is quite high below the M_s temperature. However, the alloy exhibits a very low modulus and the loss factor drops off rapidly above +50°C.

-61-
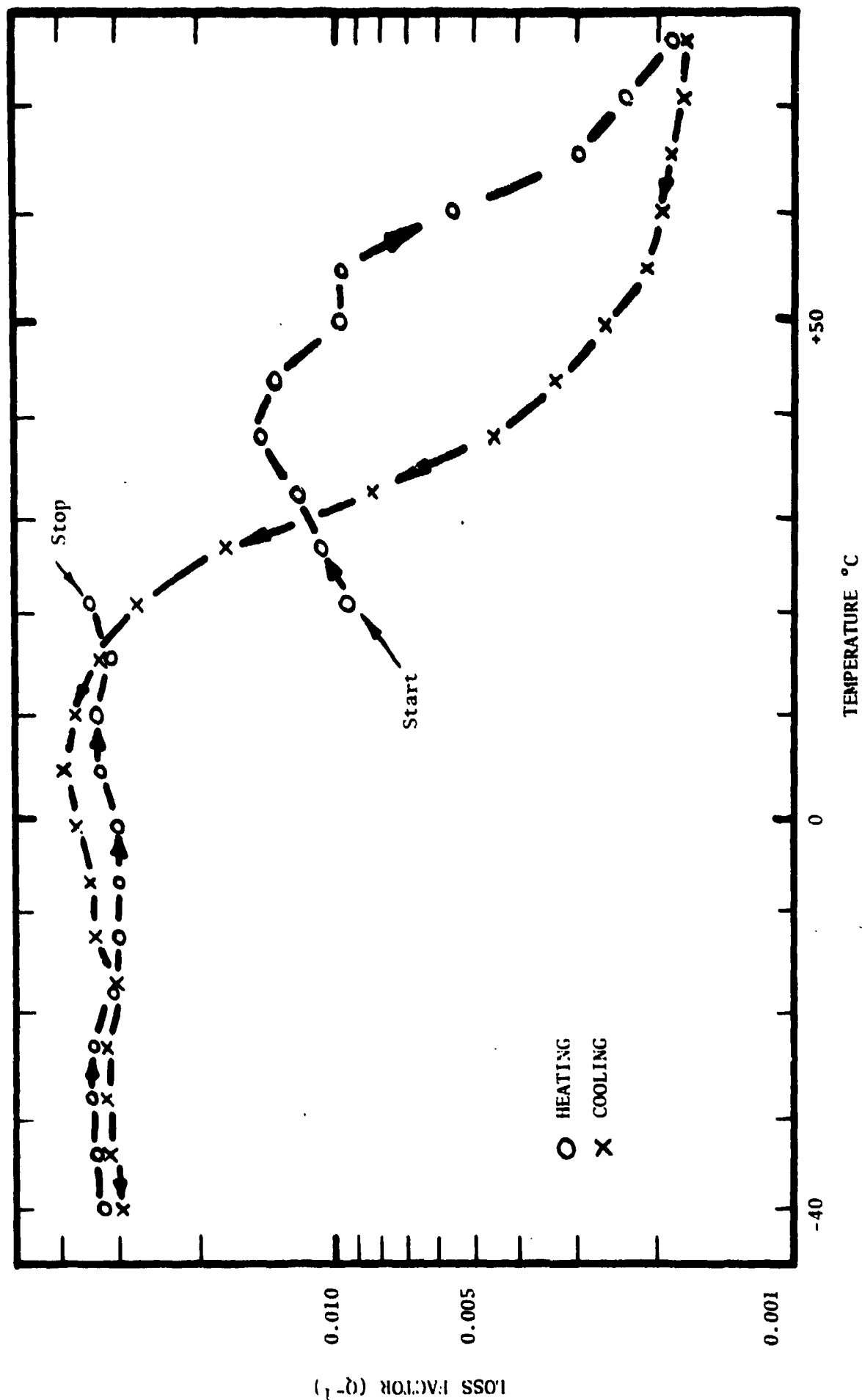
Figure 39. Loss Factor vs. Temperature Curve for a Single Crystal Sample of Cu-14.2 w/o Al-3.0 w/o Ni measured at 115-150 Hertz and a stress of 2000 psi. The M_s temperature for this material is approximately +10°C.

-62-
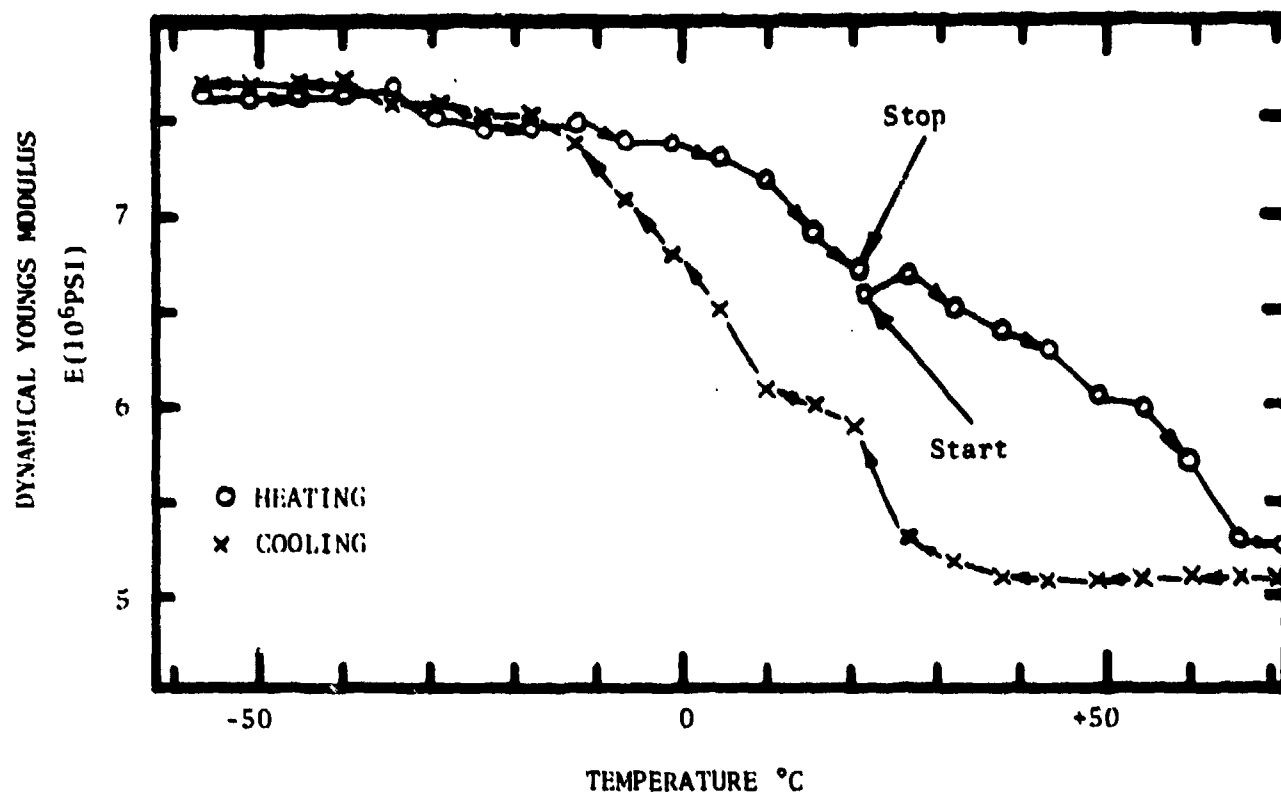
Figure 40. Dynamical Youngs Modulus vs. Temperature Curve for a Single
Crystal Sample of Cu-14.2 w/o Al-3.0 w/o Ni measured at
115-150 Hertz. The M_S temperature for this material is
approximately +10°C.

-63-

4. Yield/Strength of Nitinol.

A series of experiments were carried out to evaluate the
strength levels attainable in the 55 w/o NiTi alloy in the temper-
ature range where high damping levels could be achieved. As a
first step, annealed samples were exposed to fifty temperature cy-
cles between -65°C and +90°C and then tested at +83°C, +20°C, 0°C
and -74°C in tension. Figures 41-44 show the stress-strain curves
obtained from these tests. The 0.2 percent offset strain yield
strength is indicated in each case. This heat of the 55 w/o Ni-
45 w/o Ti alloy (4866) exhibits an M_s at +17°C after multiple cycl-
ing as can be seen in Figures 15, 16, 17 and 18. Thus the +83°C
and +20°C tensile tests correspond to temperatures above M_s while
the 0°C and -74°C tests correspond to temperatures below M_s. The
latter give low yield strengths near 20,000 psi. However, at
20°C, yield strengths in the 47000-55000 psi range are attained.
The stress-strain curves shown in Figures 41-44 were obtained on
samples which were cycled fifty times between -65°C and +90°C. In
each case, the final step was heating from -65°C to room tempera-
ture before tensile testing. Figures 45-46 show the results
obtained when the final cycle consists of cooling from 100°C to
room temperature. In this case, lower strength levels are
obtained.

Figure 47 is a composite representation of the damping,
electrical resistivity, and 0.2% offset yield strength data as a
function of temperature. Although heats 4609 and 4866 are both
55Ni-45Ti, the M_s temperatures are slightly different being 7°C and
17°C respectively. As a consequence, the yield strength data
(taken on heat 4866) have been displaced by -10°C. Nevertheless,
the composite data shown in Figure 47 shows that in the tempera-
ture range above M_s, high damping values near 5×10^{-3} and strengths
in the vicinity of 47000-55000 psi can be obtained simultaneously.
Since the effect of plastic deformation is to broaden the transfor-
mation range (i.e. see Figures 17 and 18) it is quite likely that
the temperature range where high strength and high damping factors
can be obtained simultaneously will be increased by deformation.
Moreover, the strength levels will undoubtedly be higher than

-64-
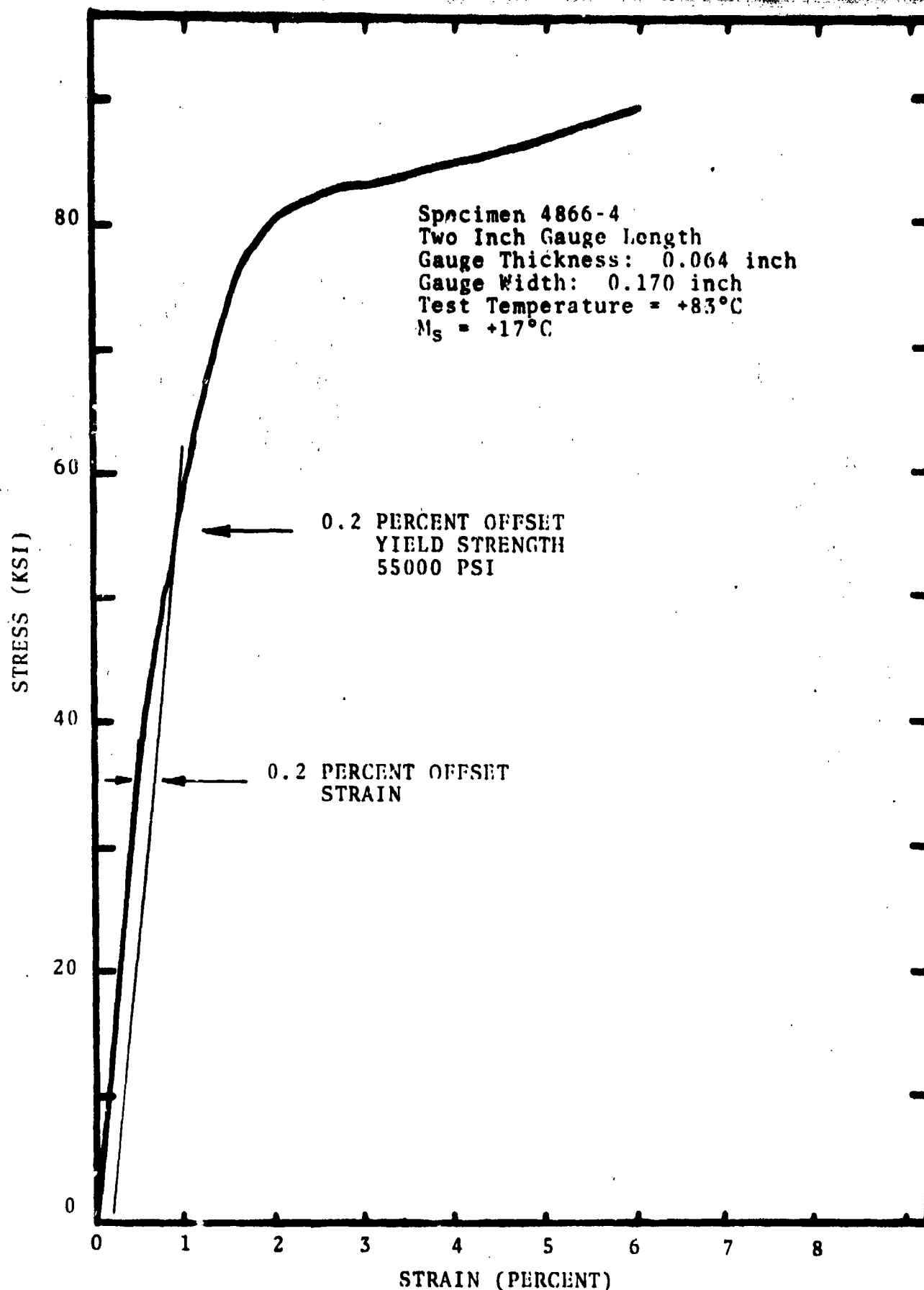
Figure 41. Stress-strain curve for 55 w/o Ni-45 w/o Ti Alloy at +83°C after 50 temperature cycles between -65°C and +90°C. The final step was heating from -65°C to 25°C.

-65-
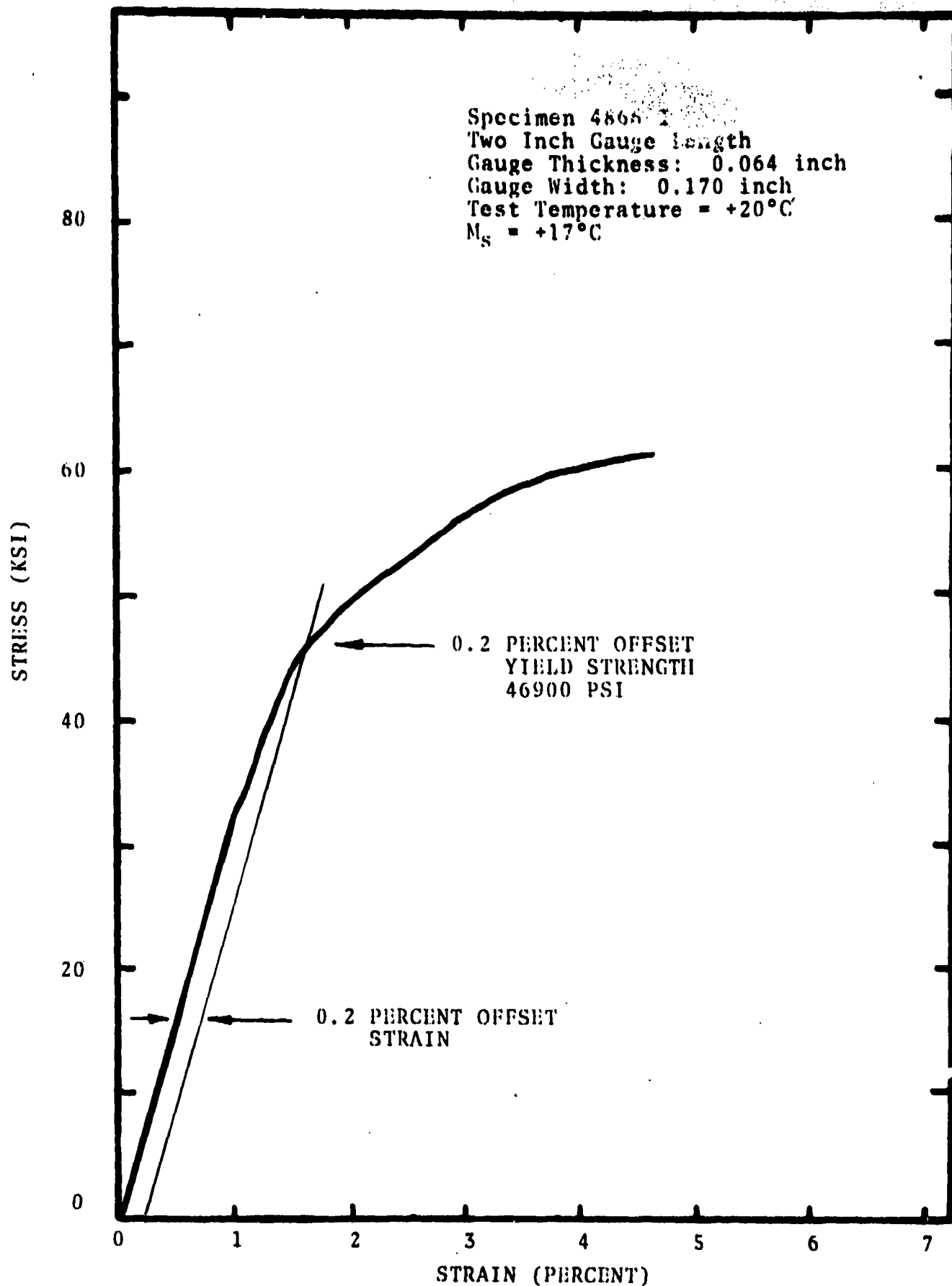
Figure 42. Stress-strain curve for 55 w/o Ni-45 w/o TI Alloy at +20°C after 50 temperature cycles between -65°C and +90°C. The final step was heating from -65°C to 25°C.
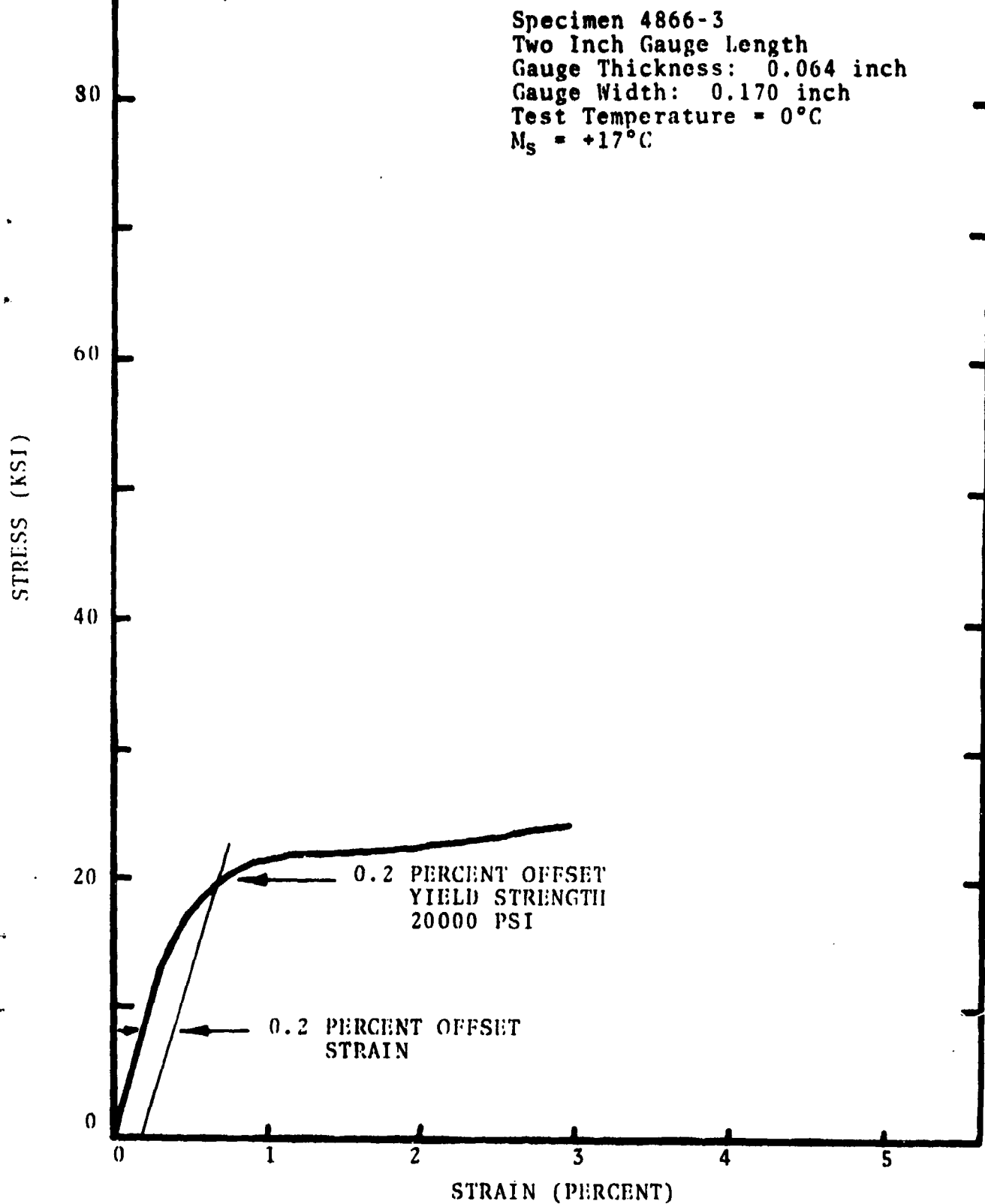
Figure 43. Stress-strain curve for 55 w/o Ni-45 w/o Ti Alloy
at 0°C after 50 temperature cycles between -65°C
and +90°C. The final step was heating from -65°C
to 25°C.
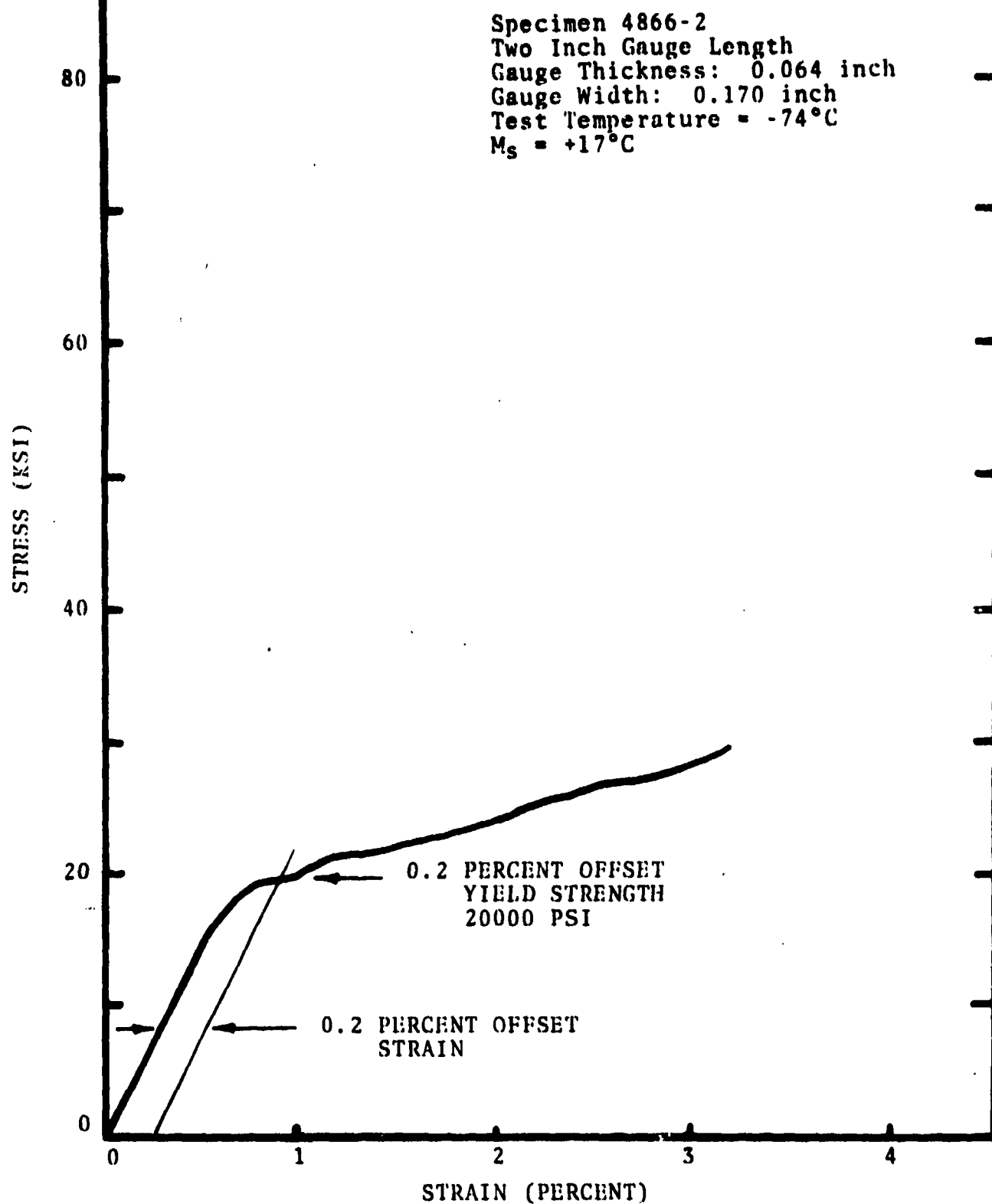
Figure 44. Stress-strain curve for 55 w/o Ni-45 w/o Ti Alloy at -74°C after 50 temperature cycles between -65°C and +90°C. The final step was heating from -65°C to 25°C.

Specimen: 4866-V-8
Two Inch Gauge Length
Gauge Thickness: 0.064 inch
Gauge Width: 0.168 inch
Test Temperature: 40°C
M_s = +17°C

80

60

STRESS (KSI)

APPARENT ELASTIC
LIMIT 19500 PSI

40

0.2 PERCENT OFFSET
YIELD STRENGTH 31400 PSI

Sample was cycled 80 times
between -90°C and +100°C.
The final step was cooling
from 100°C to 25°C.

20

1.0   2.0

STRAIN (PERCENT)
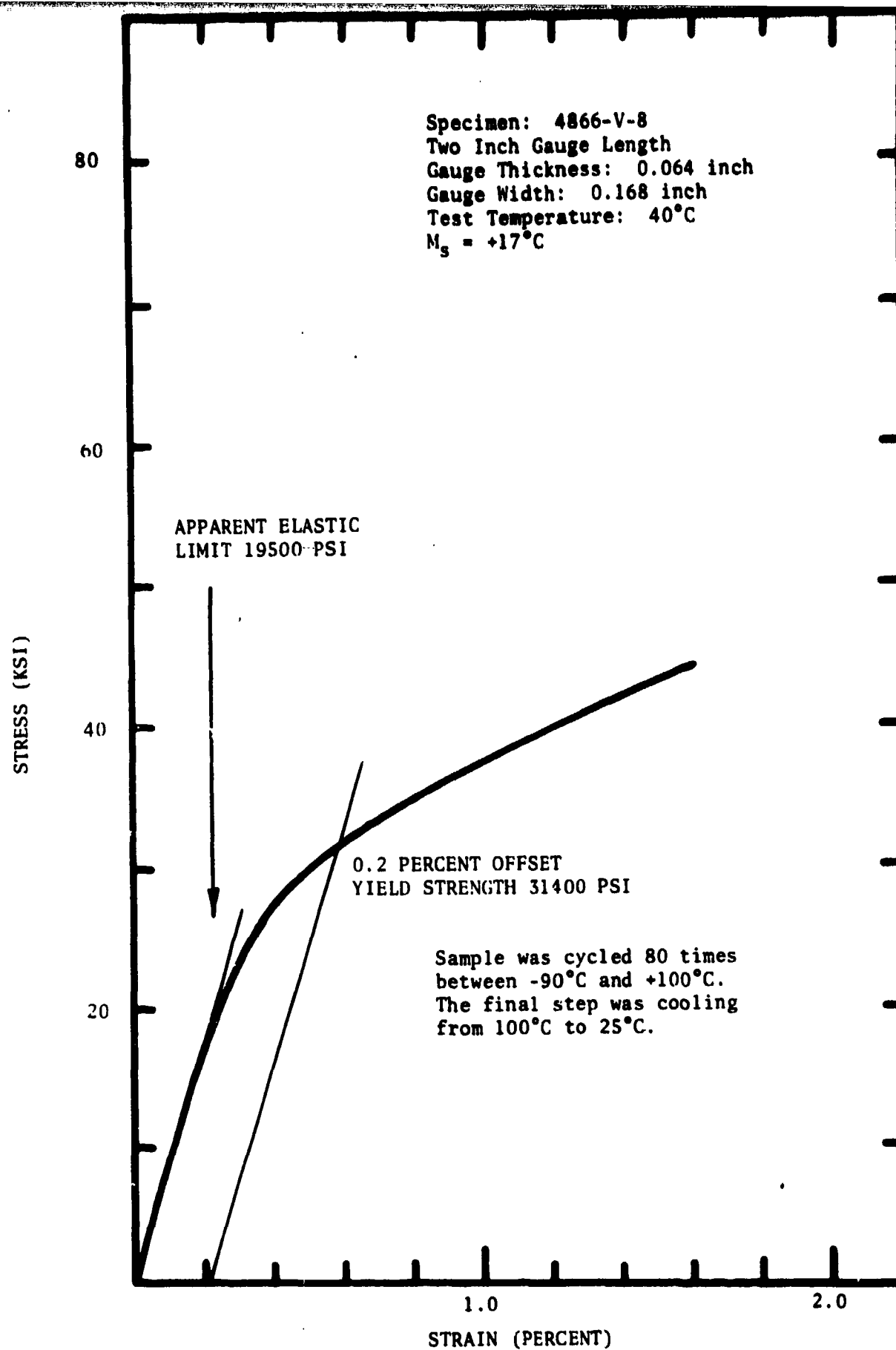
Figure 45. Stress-Strain Curve for 55 w/o Ni-45 w/o Ti at 40°C
after Cycling.

-69-
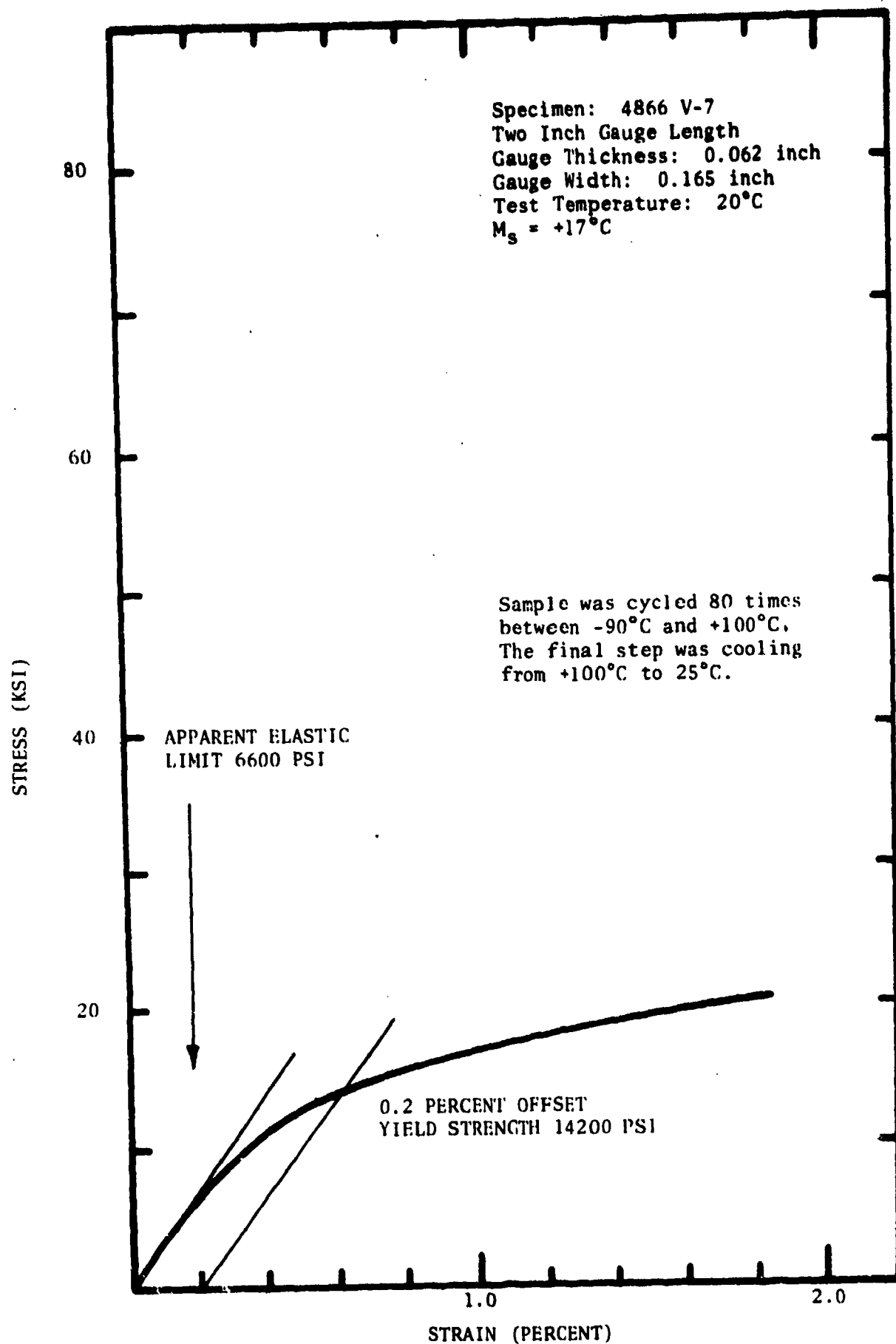
Figure 46. Stress-Strain Curve for 55 w/o Ni-45 w/o Ti at 20°C after Cycling.

-70-
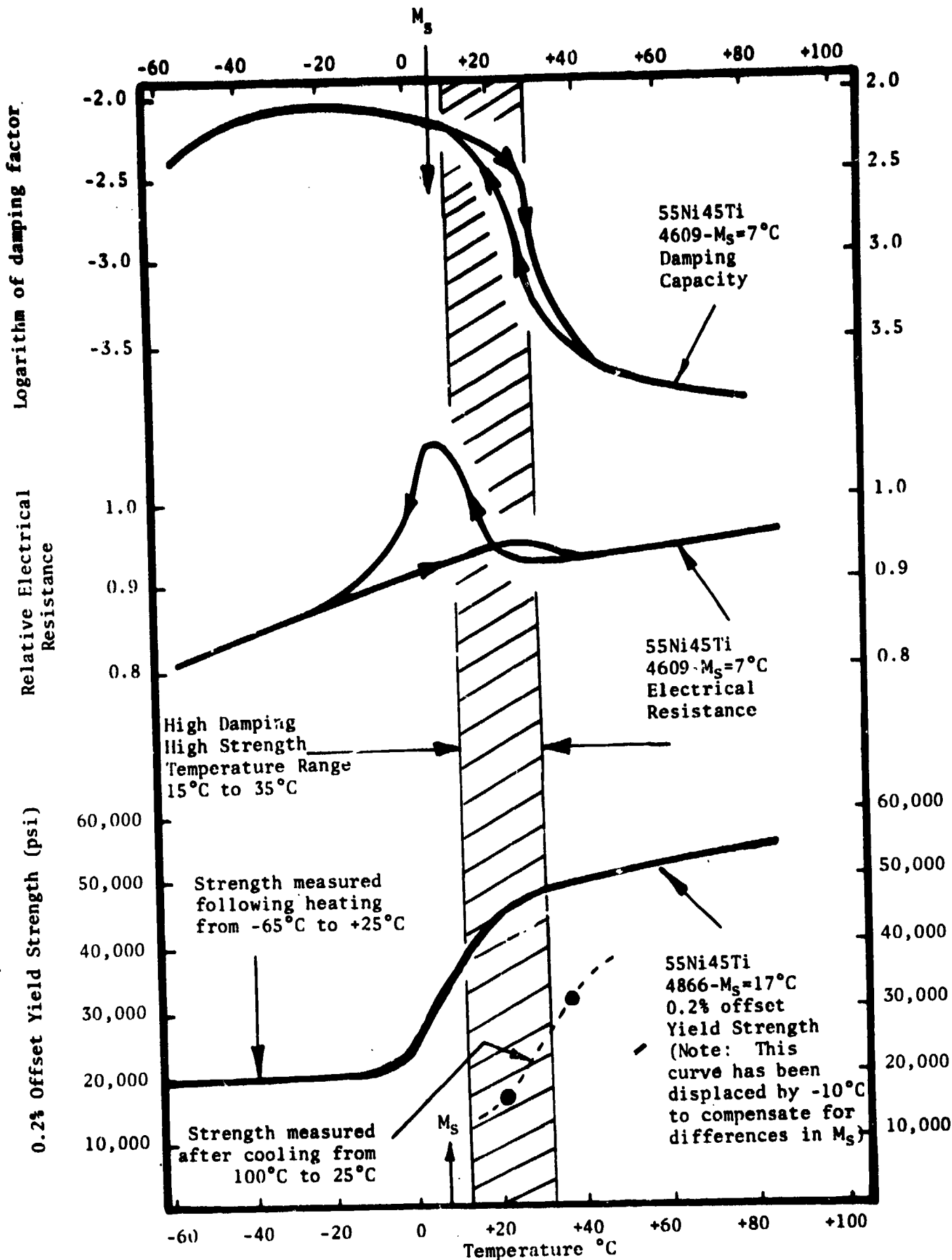
Figure 47. Damping Capacity, Electrical Resistance and 0.2% Offset Yield Strength for 55Ni45Ti as a function of temperature after Multiple Cycling Treatment.

-71-

those shown in Figure 47. Measurements of the damping behavior
and yield strength of plastically deformed samples were carried
out in order to test this hypothesis.

Figures 48 through 57 show the results which were ob-
tained on tensile testing the 55 w/o Ni-45 w/o Ti alloy after cold
working. In all cases, the samples were cycled and tested after
heating to room temperature. The results for the samples obtained
by 3% and 7% cold reduction in thickness, which are displayed in
Figures 48-53, show a decrease in strength as compared to the sam-
ples which were not cold worked. However, the samples which re-
ceived a 15% cold reduction in thickness were considerably stronger,
exhibiting 0.2 percent offset yield strengths in the 60000-70000
psi range between 0°C and 83°C.

In view of the low modulus of the 55 w/o Ni-45 w/o Ti
alloy disclosed by the tensile tests, an attempt was made to ob-
serve anelastic behavior by performing "load-unload tests" which
were interrupted to observe relaxation or "elastic memory behav-
ior." Figure 58 shows the results of such a test where a sample
of the material which had received a 3% cold reduction was mechan-
ically cycled. The observed stress-strain curve follows the enve-
lope shown in Figure 48 where no load cycling was applied. The
results indicate an increase in elastic modulus on loading with
increasing number of stress cycles. Thus the modulus increases by
20% in the twelfth cycle as compared to the initial cycle. There
is an appreciable increase in mechanical hysteresis with increas-
ing plastic strain. Upon unloading to a low stress level and
holding for thirty minutes, the amount of anelastic strain recovery
was about 0.02%. The data on yield strength and electrical re-
sistance are combined with data on damping capacity for the 55 w/o
Ni-45 w/o Ti alloy with 3%, 7% and 15% cold reduction. The results,
shown in Figures 59-61, are counterparts to the overall comparison
displayed in Figure 47. These results indicate that the best com-
bination of properties can be achieved by a 15% cold reduction which
generates yield strengths in the 60000-70000 psi range over the
0°C-80°C temperature range in combination with loss factors of Q^{-1}
equal to 100×10^{-4} at 25°C and at temperatures down to -60°C. At
60°C the loss factor drops to 30×10^{-4}.

-72-
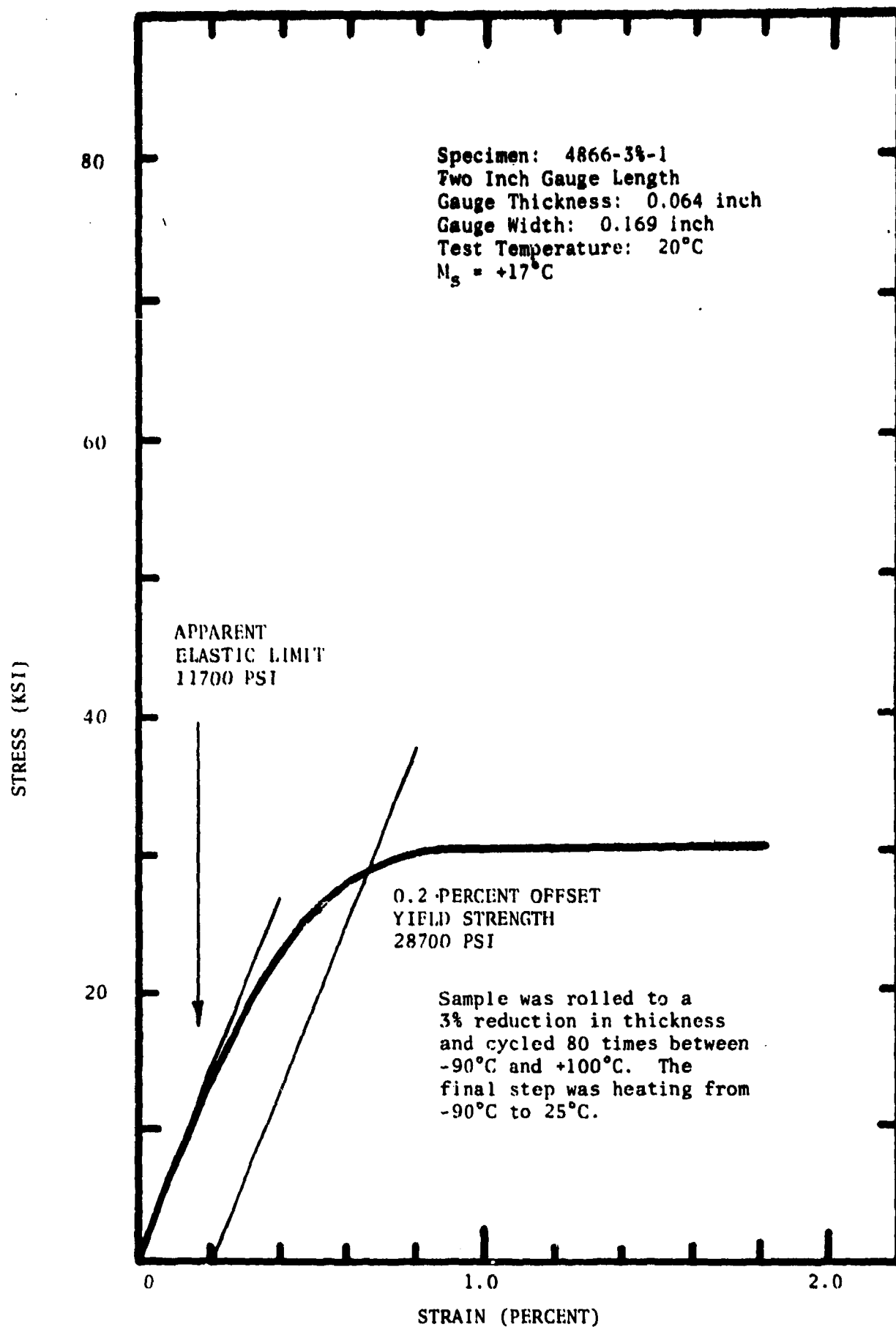
Figure 48. Stress-Strain Curve for 55 w/o Ni-45 w/o Ti at 20°C after Cold Work and Cycling.

-73-

STRESS (KSI)

80

60

40

20

0

Specimen: 4866-3%-2
Two Inch Gauge Length
Gauge Thickness: 0.065 inch
Gauge Width: 0.169 inch
Test Temperature: 40°C
M_s = +17°C

APPARENT
ELASTIC LIMIT
12200 PSI

0.2 PERCENT OFFSET
YIELD STRENGTH
23900 PSI

Sample was rolled to a
3% reduction in thickness
and cycled 80 times between
-90°C and +100°C. The final
step was heating from -90°C
to 25°C.

0   1.0   2.0

STRAIN (PERCENT)
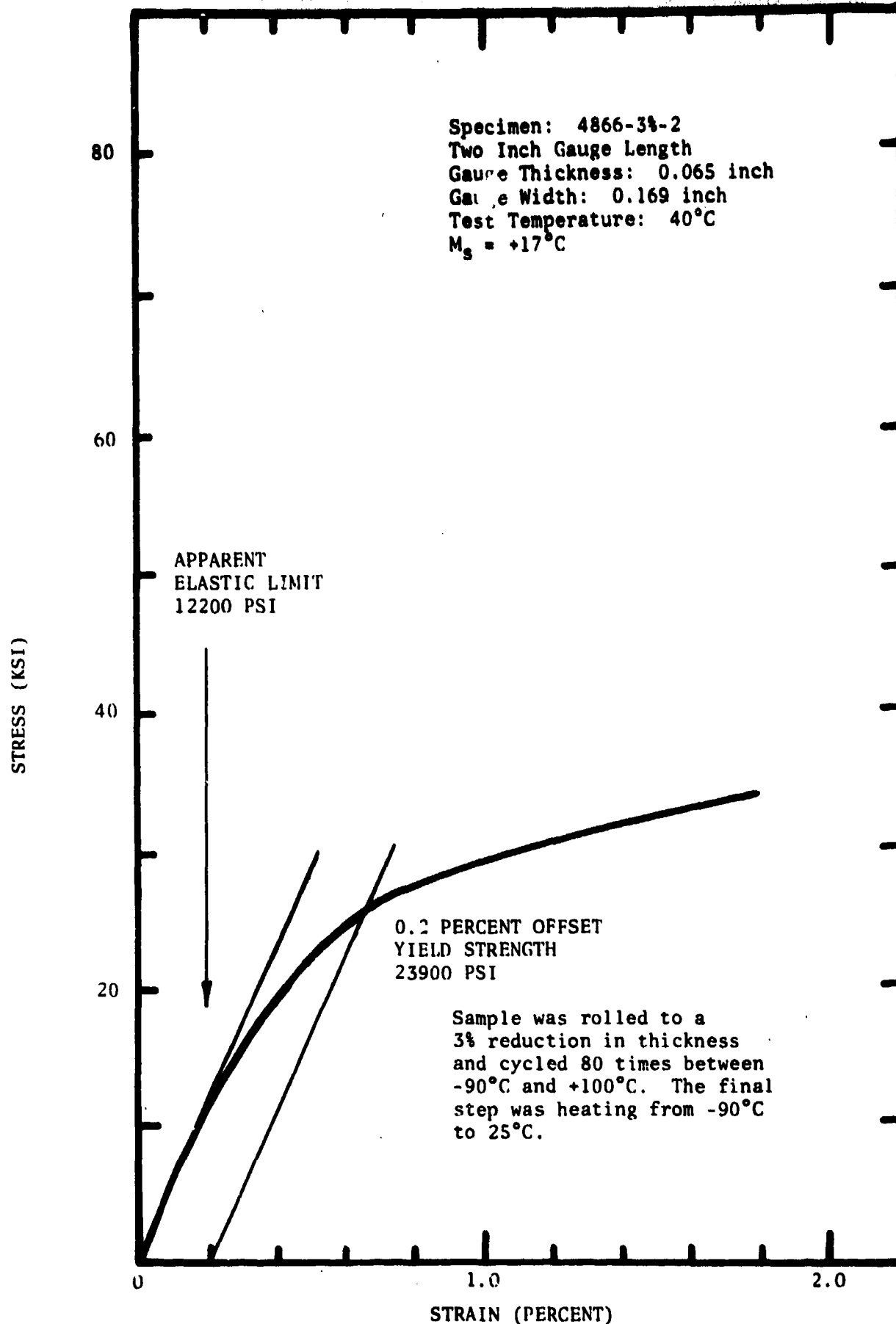
Figure 49. Stress-Strain Curve for 55 w/o Ni-45 w/o Ti at 40°C
after Cold Work and Cycling.

-74-
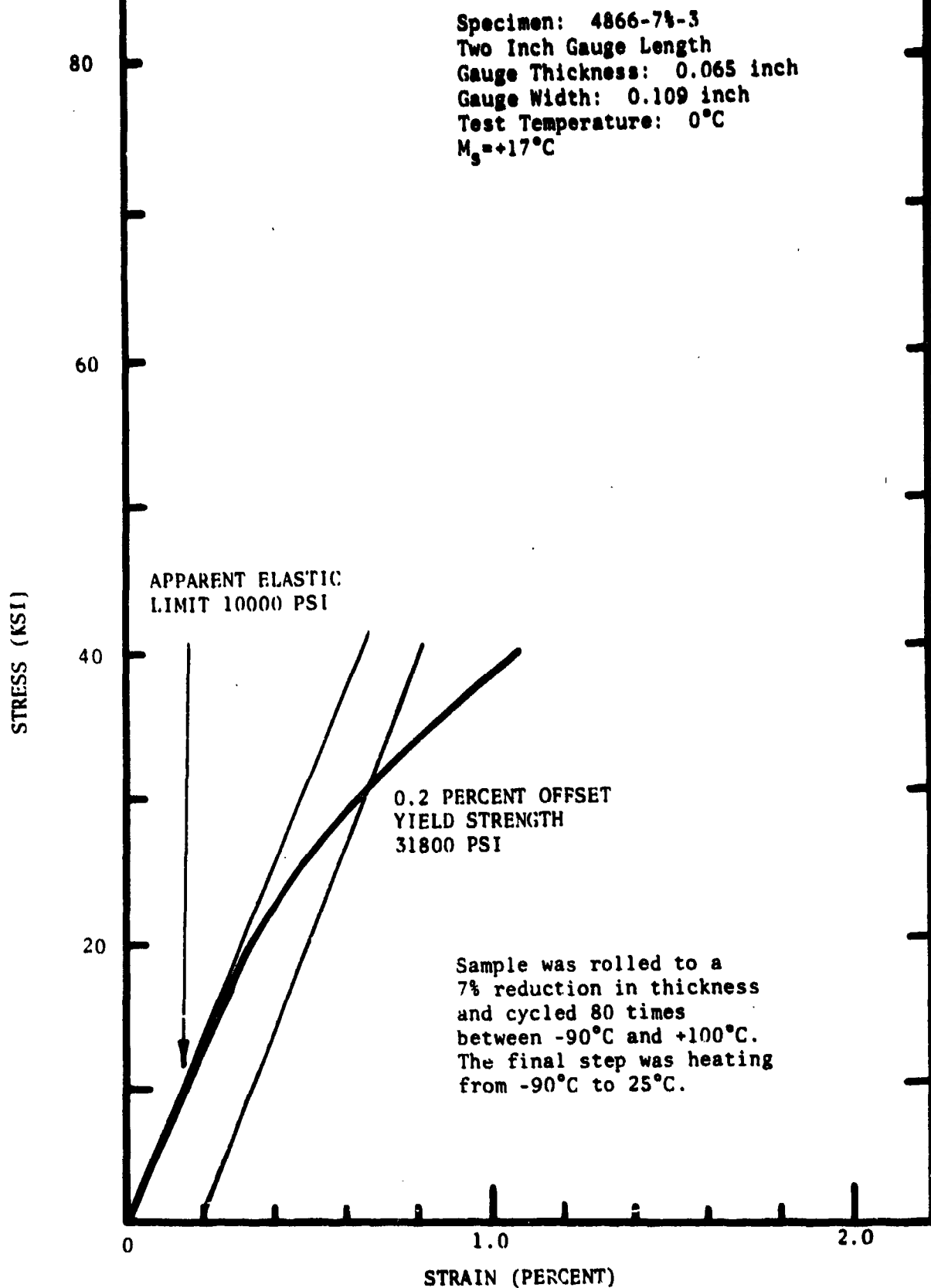
Figure 50. Stress-Strain Curve for 55 w/o Ni-45 w/o Ti at 0°C after Cold Work and Cycling.

-75-
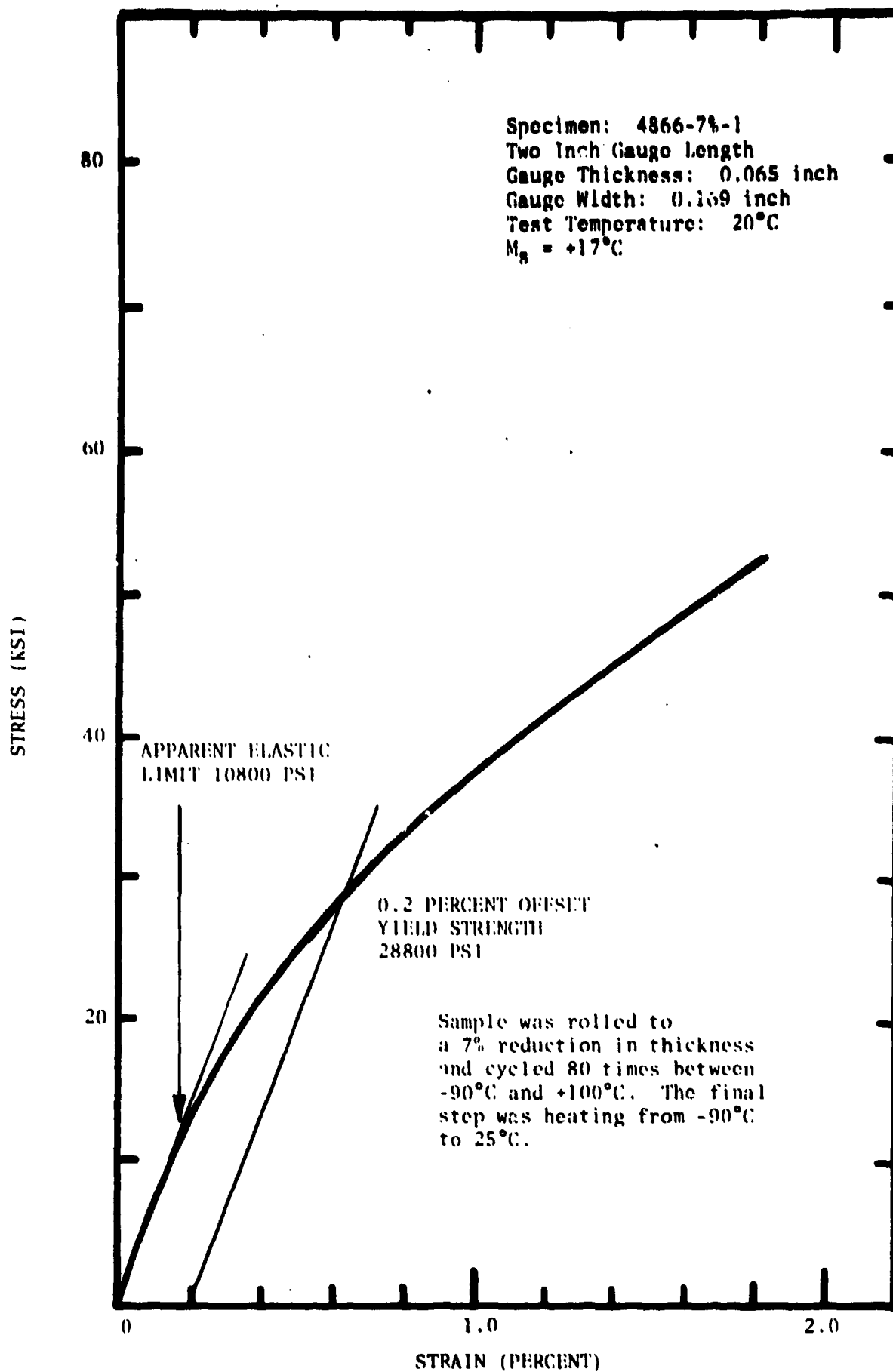
Figure 51. Stress-Strain Curve for 55 w/o Ni-45 w/o Ti at 20°C after cold work and cycling.
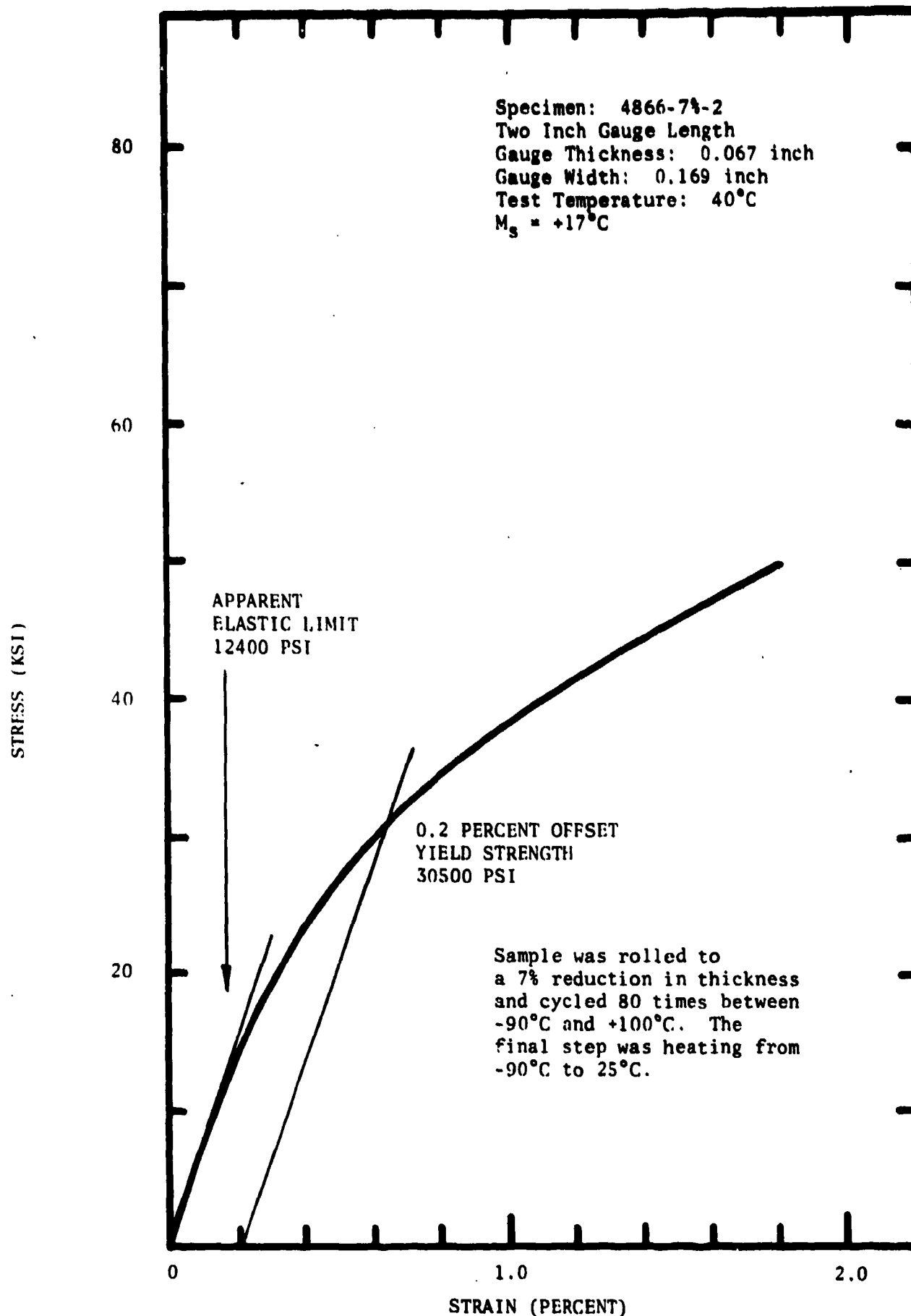
Figure 52. Stress-Strain Curve for 55 w/o Ni-45 w/o Ti at 40°C
after cold work and cycling.

-77-
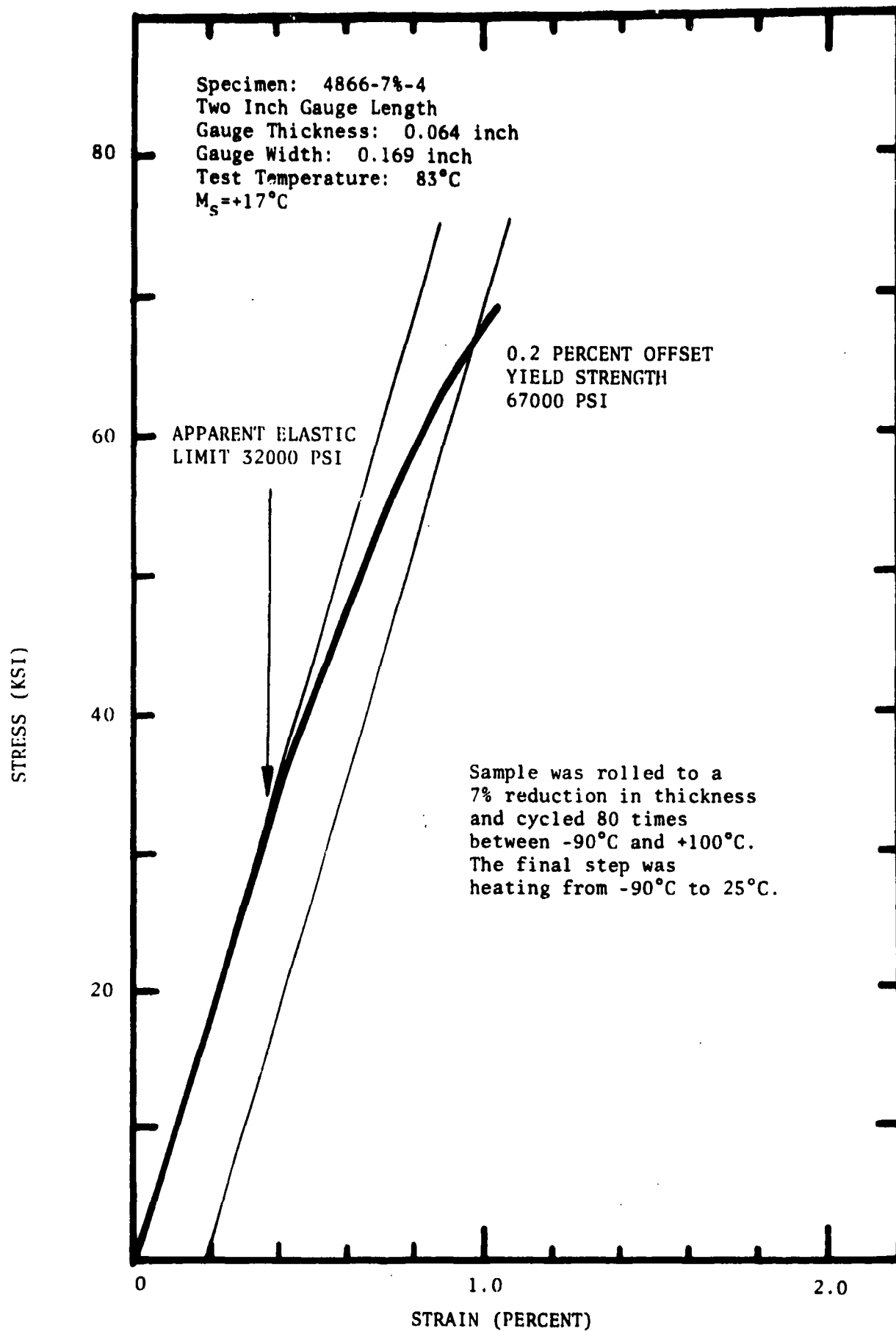
Figure 53. Stress-Strain Curve for 55 w/o Ni-45 w/o Ti at 83°C after Cold Work and Cycling.

-78-

STRESS (KSI)

80

60

40

20

Specimen: 4866-15%-3
Two Inch Gauge Length
Gauge Thickness: 0.065 inch
Gauge Width: 0.170 inch
Test Temperature: 0°C
$M_s = +17°C$

APPARENT ELASTIC
LIMIT 30000 PSI

0.2 PERCENT OFFSET
YIELD STRENGTH
68000 PSI

Sample was rolled to at
15% reduction in area and
cycled 80 times between
-90°C and 100°C. The
final step was heating
from -90°C to 25°C.

0   1.0   2.0

STRAIN (PERCENT)
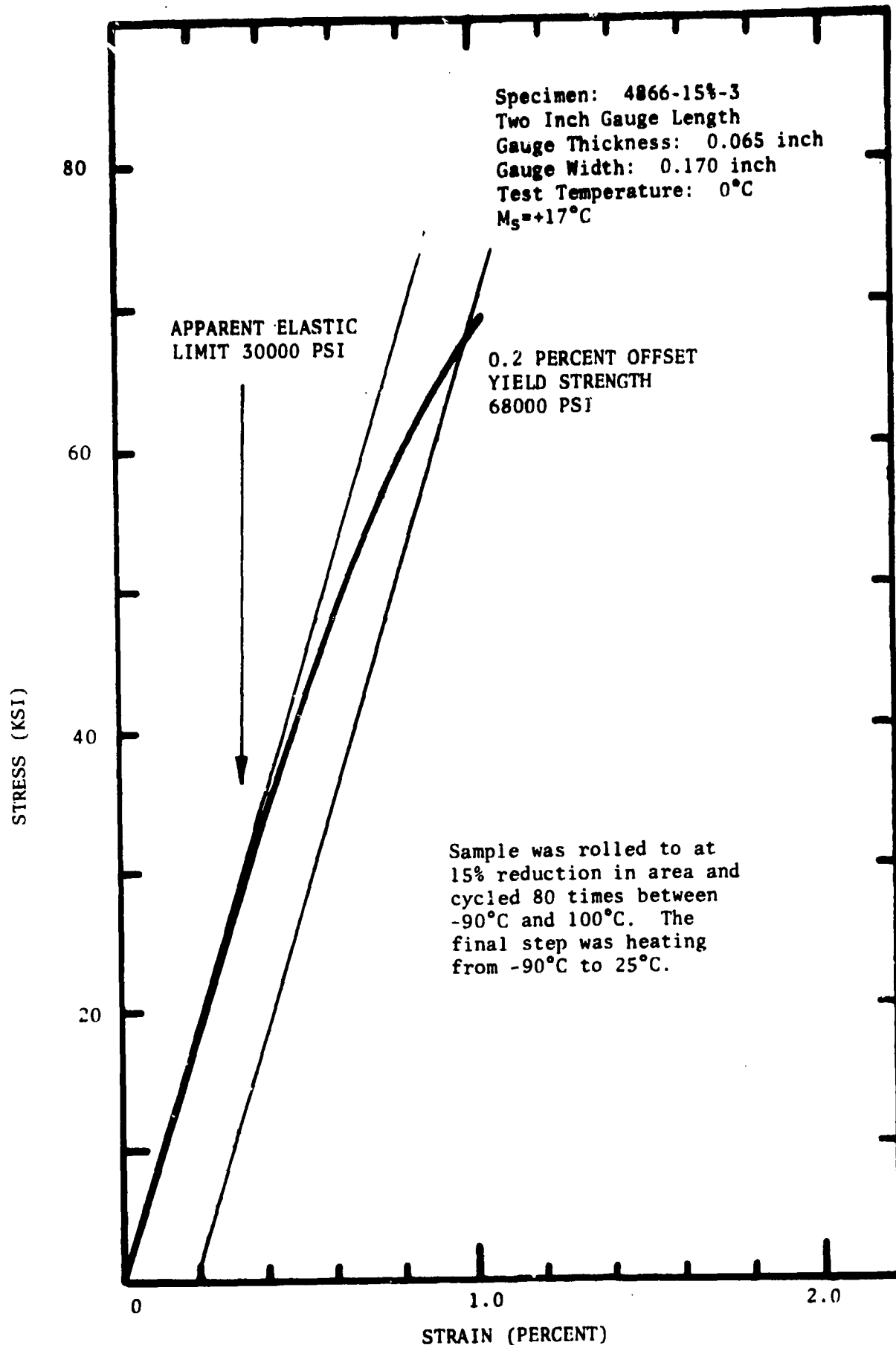
Figure 54. Stress-Strain Curve for 55 w/o Ni-45 w/o Ti at 0°C
after Cold Work and Cycling.

-79-
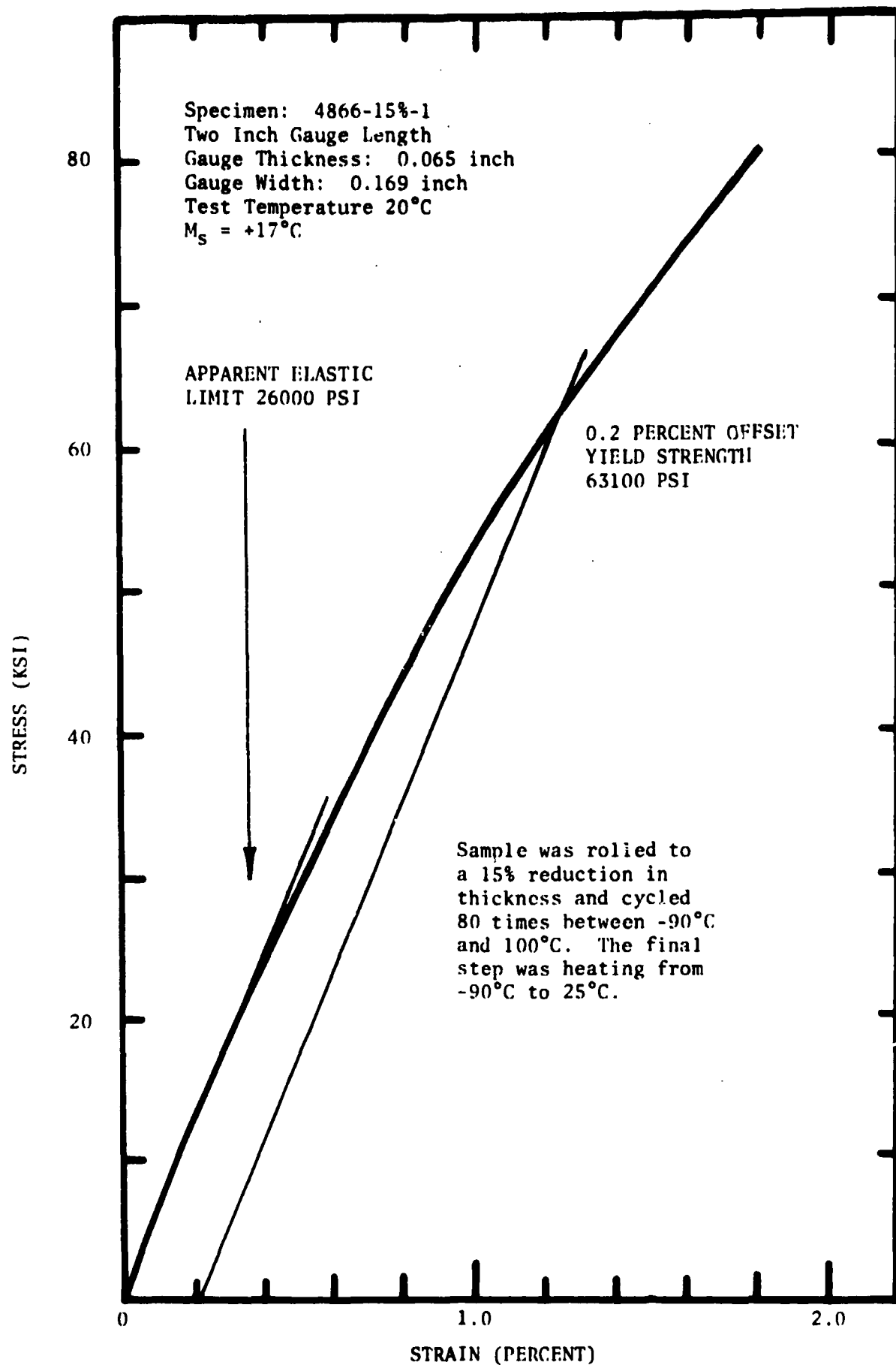
Figure 55. Stress-Strain Curve for 55 w/o Ni-45 w/o Ti at 20° C after Cold Work and Cycling.

-80-
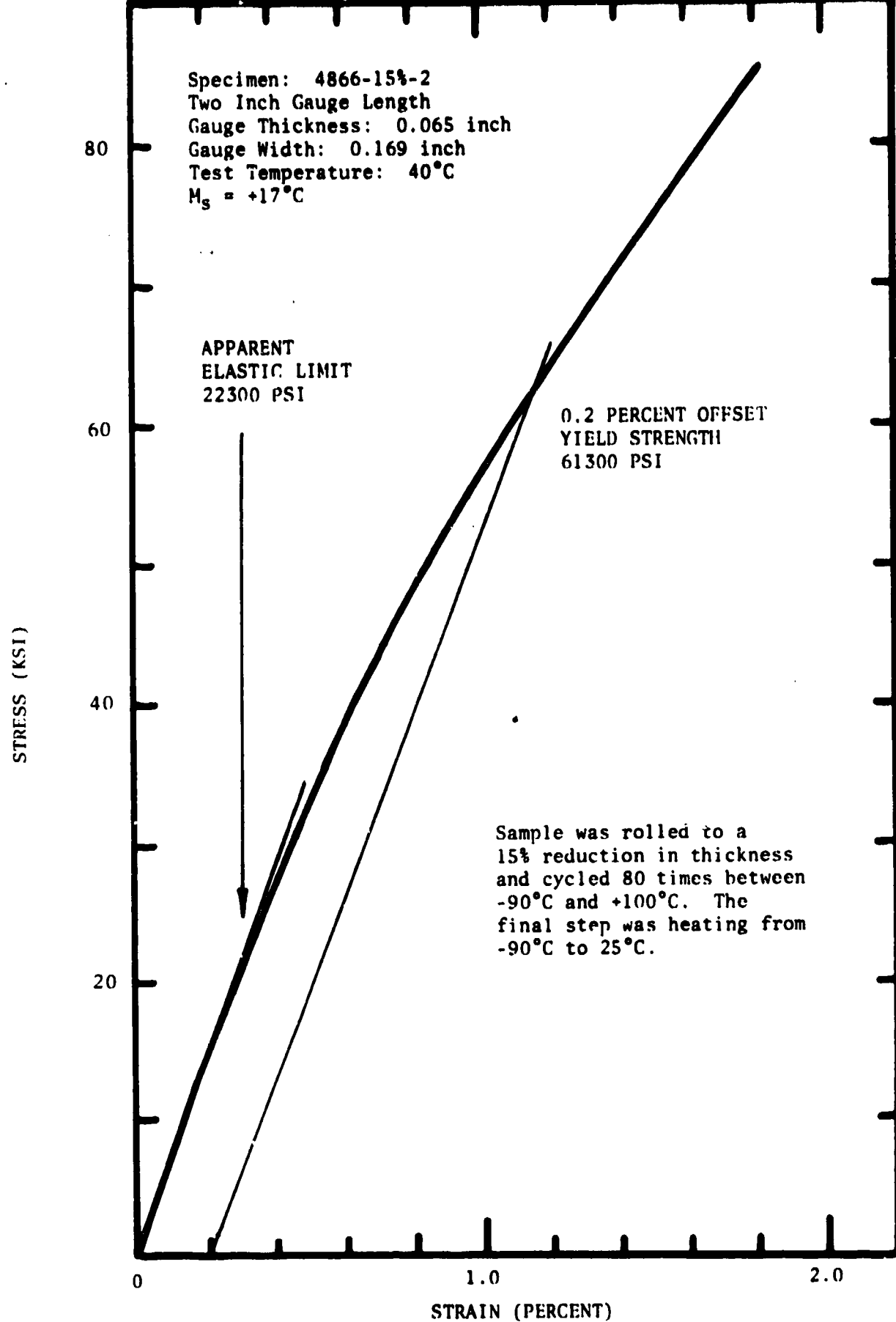
Figure 56. Stress-Strain Curve for 55 w/o Ni-45 w/o Ti at 40°C after Cold Work and Cycling.

-81-

Specimen: 4866-15%-4
Two Inch Gauge Length
Gauge Thickness: 0.064 inch
Gauge Width: 0.169 inch
Test Temperature 83°C
$M_S = +17°C$

0.2 PERCENT OFFSET
YIELD STRENGTH
70000 PSI

APPARENT ELASTIC
LIMIT 28000 PSI

Sample was rolled to a
15% reduction in thickness
and cycled 80 times
between -90°C and +100°C.
The final step was heating
from -90°C to 25°C.
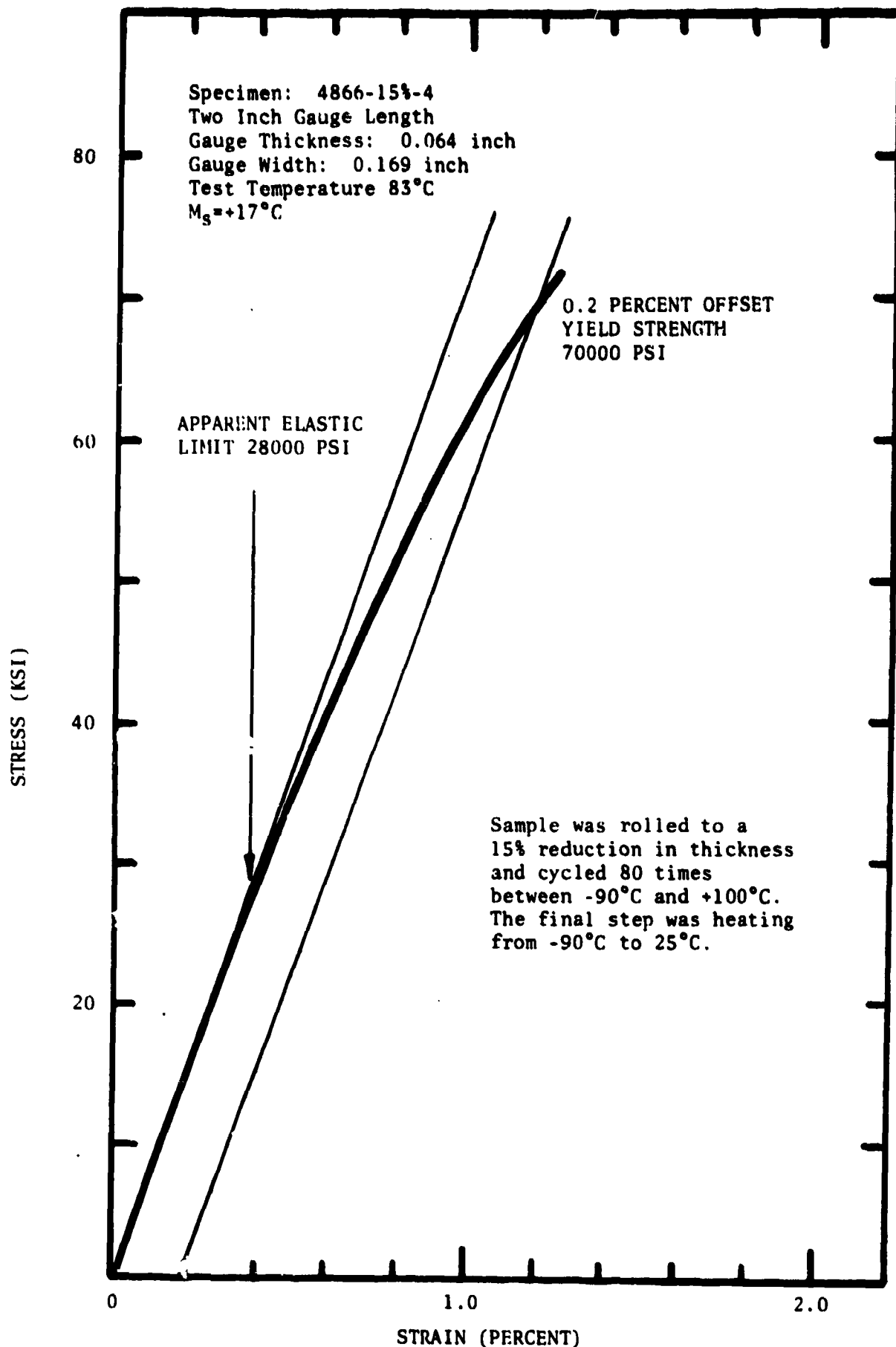
Figure 57. Stress-Strain Curve for a 55 w/o Ni-45 w/o Ti at 83°C
after Cold Work and Cycling.

-82-
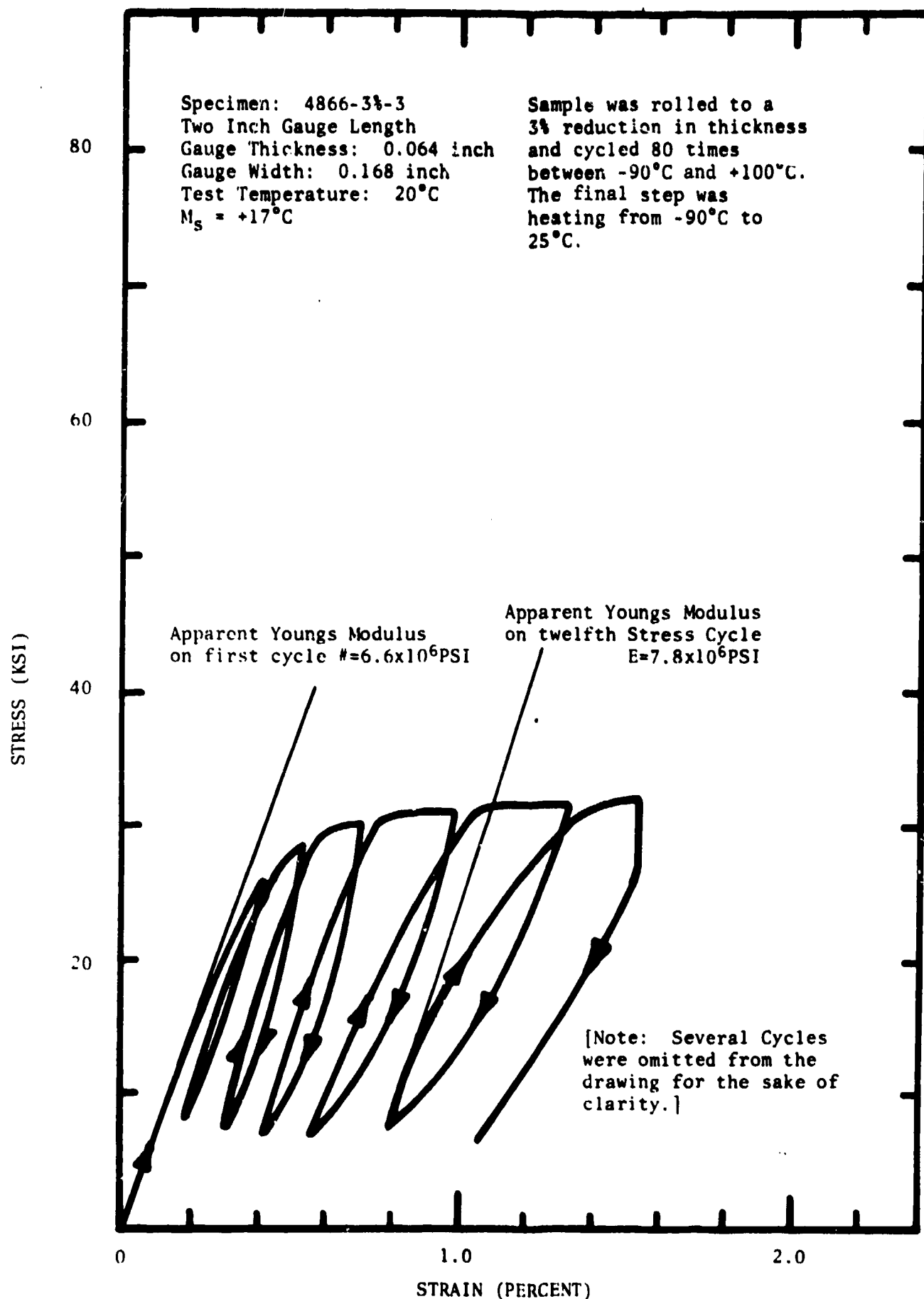
Figure 58. Stress-Strain Curve for 55 w/o Ni-45 w/o Ti at 20°C after Cold Work and Cycling.

-83-
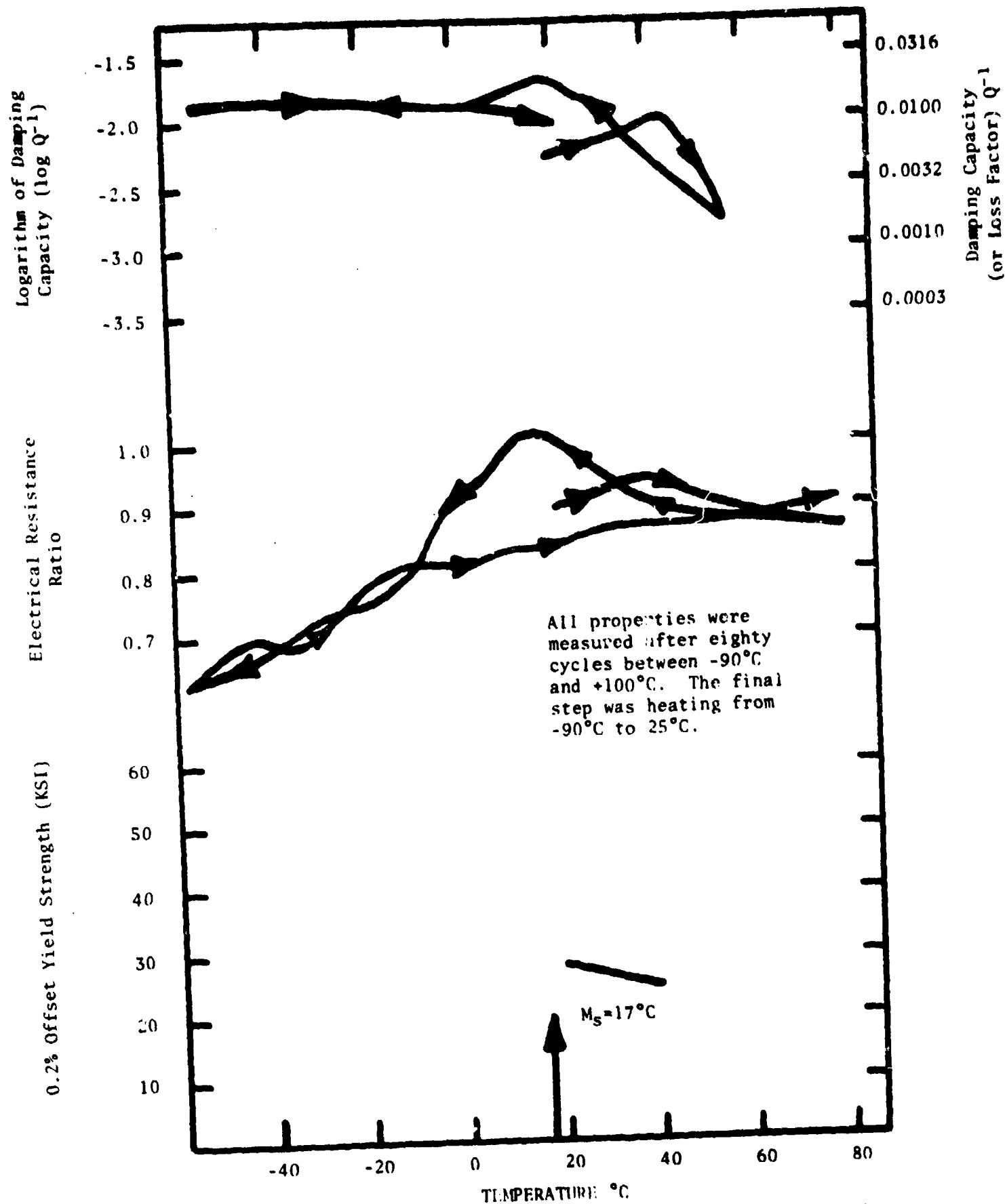
Figure 59. Damping Capacity, Electrical Resistance and 0.2% Offset Yield Strength for 55 w/o Ni-45 w/o Ti versus Temperature after 3% Cold Reduction and Cycling Treatment.

All properties were measured after eighty cycles between -90°C and +100°C. The final step was heating from -90°C to 25°C.

$M_S = 17°C$

-84-
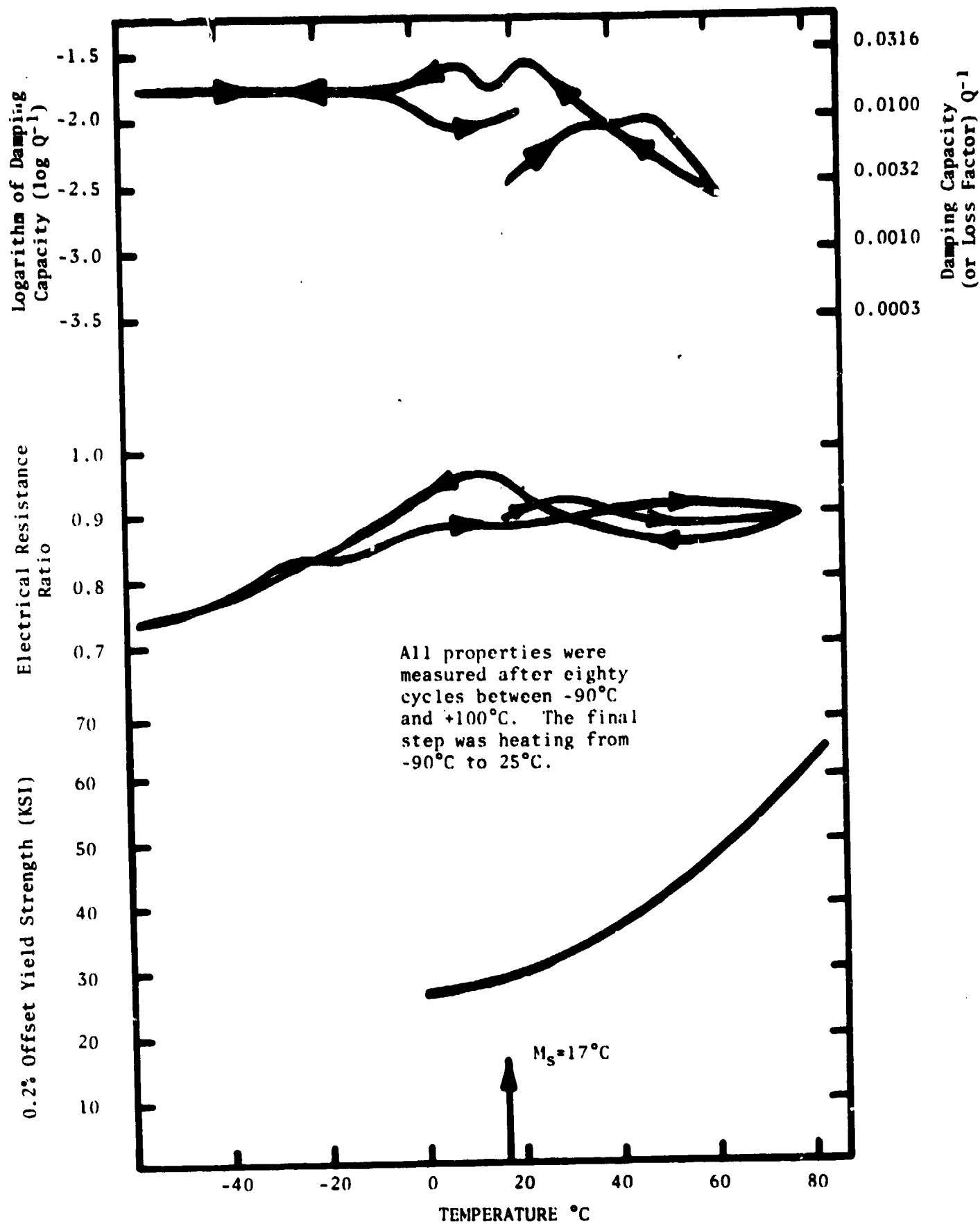
Figure 60. Damping Capacity, Electrical Resistance and 0.2% Offset Yield Strength for 55 w/o Ni-45 w/o Ti versus Temperature after 7% Cold Reduction and Cycling Treatment.
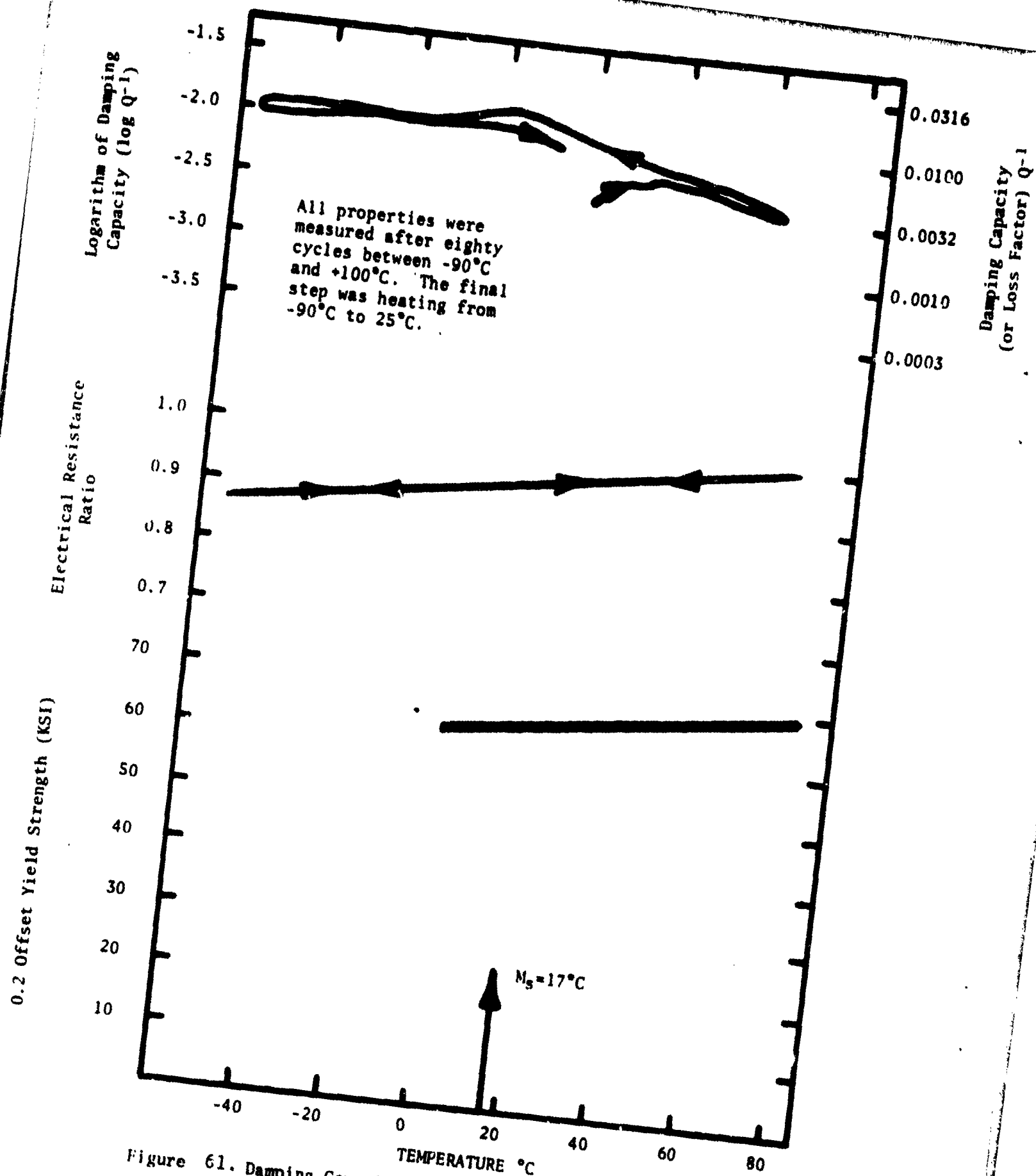
Figure 61. Damping Capacity, Electrical Resistance and 0.2% Offset Yield Strength for 55 w/o Ni-45 w/o Ti versus Temperature after 15% Cold Reduction and Cycling Treatment.

-86-

IV. MEASUREMENT OF THE DAMPING BEHAVIOR AND STRENGTH OF COBALT BASE ALLOYS

1. Work of Cochardt

The damping behavior of nickel and several cobalt base alloys has been discussed by Cochardt (6). We have measured some of these alloys and the results for the 70 w/o Co-30 w/o Ni sample are shown in Figure 62. The sample shows damping even above the M_s temperature which occurs at about 30°C (18). Figure 63 shows the results of the damping test on pure (approximately 99.9%) Ni. From other work done on Ni (20) and CoNi alloys (6) it appears that a significant amount of the damping in these materials is due to magnetic damping (i.e., from magnetic domain motion), however in several of these alloys there is a martensitic phase transformation (from fcc to hcp) and it was of considerable interest to determine if a material could be developed which would produce damping by both magnetic domain motion and by thermoelastic martensite formation.

One method for attaining these features simultaneously is to consider the fcc/hcp transformations in cobalt rich Co-Ni alloys like the 70 w/o Co-30 w/o Ni discussed above. This alloy has a very high magnetic Curie Point and a fcc/hcp transition near room temperature. Cochardt (6) reported a logarithmic decrement of 0.18 at 25°C, a frequency of one cycle/sec and a stress of 2000 psi for a 65 w/o Co-35 w/o Ni alloy. The logarithmic decrement is the product of π times Q^{-1}. Thus

$$\zeta = \pi Q^{-1} \tag{9}$$

and if $\zeta = 0.18$ then $Q^{-1} \approx 0.06$. This value is approximately fifteen times larger than the value shown in Figure 62. However, the latter values were observed at 200 Hertz (200 cycles/sec) and 2000 psi rather than 1 cycle/sec and 2000 psi stress. Cochardt also
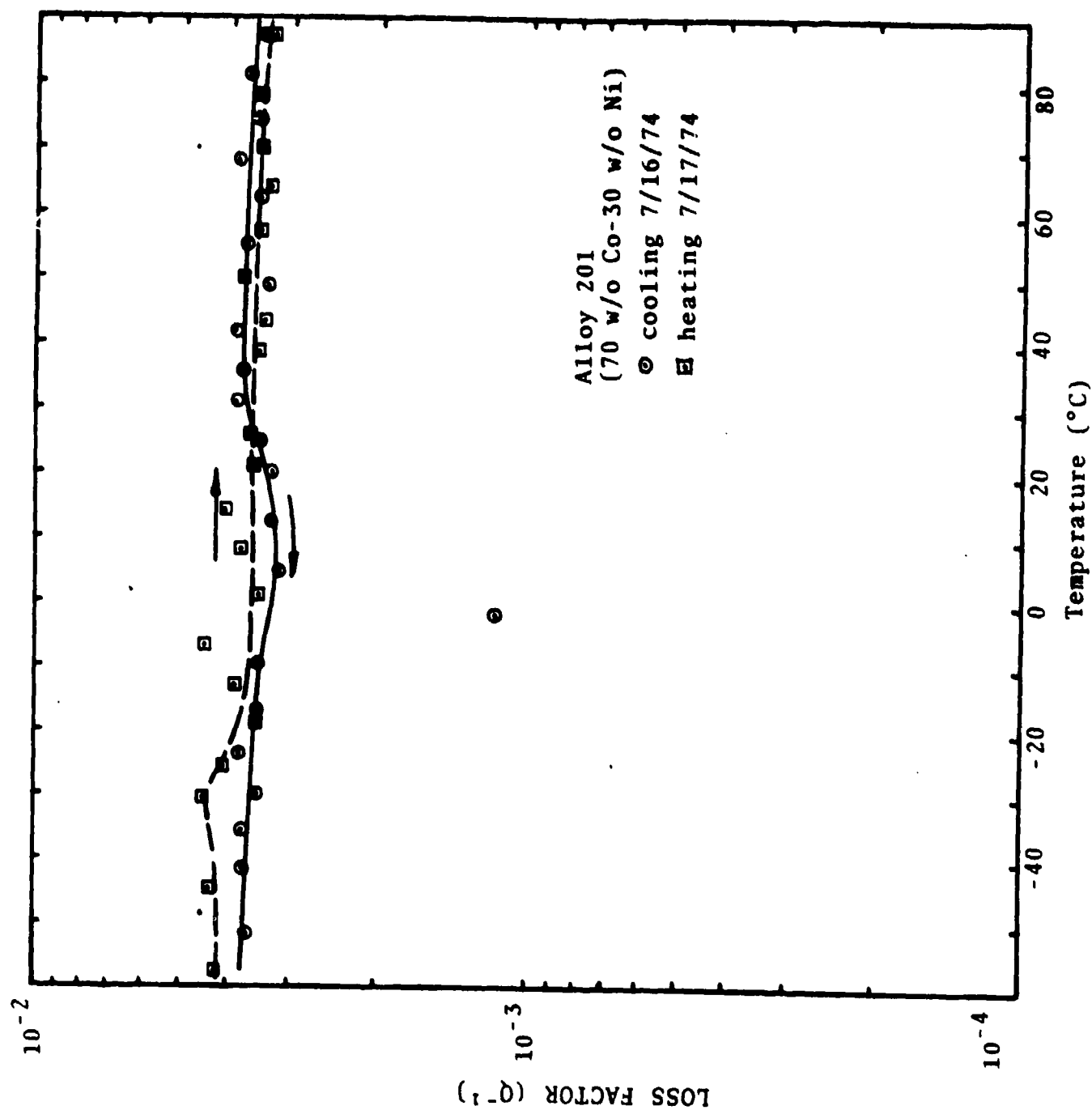
Figure 62. Damping behavior of alloy 201 (70 w/o Co-30 w/o Ni).

Alloy 201
(70 w/o Co-30 w/o Ni)

⊙ cooling 7/16/74
⊟ heating 7/17/74

Temperature (°C)

LOSS FACTOR (Q⁻¹)
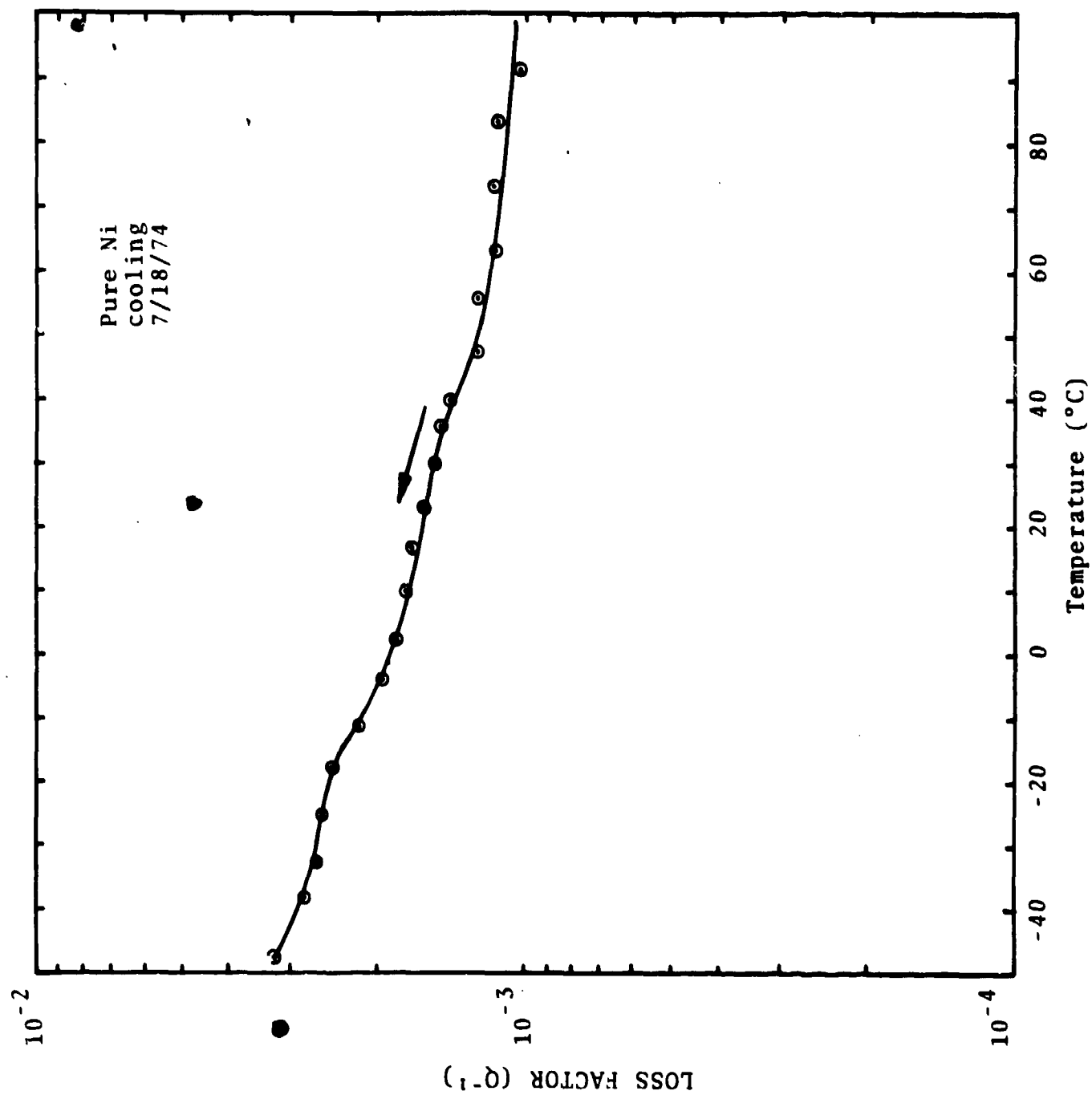
Figure 63. Damping behavior of pure nickel (approximately 99.9%).

reported on a 80 w/o Co-20 w/o Fe alloy which exhibited ζ = 0.09
(i.e., Q^{-1} = 0.03) at 1 cycle/sec and 2000 psi and 25°C. This
alloy also has a high Curie temperature. However, in the condi-
tion as fabricated by Cochardt (6), this alloy has a stable
bcc structure which was probably ordered with no chance for
transformation. The processing sequence followed by Cochardt
called for homogenization at 1100°C for two hours. Figure 64
shows that the alloy was in the fcc field at this temperature
(1373°C). Subsequently the alloy was annealed for two hours
at 900°C (1173°K). Figure 64 shows that at this temperatue the
alloy was still in the stable fcc field but just about to enter
the two phase fcc+bcc field. The final step in the processing
sequence employed by Cochardt was a slow cool to room temperature
at the rate of 120°C/hour. During this treatment the sample enters
the region where the bcc phase is stable and coexists with a fcc
phase enriched in cobalt. In addition, the bcc orders below 800°C
as is seen in Figure 64. Unfortunately Cochardt did not discuss
the structure of his 80Co-20Fe alloy. However, based on his heat
treatment schedule, it is likely that his alloy was largely bcc.

   2. CoFe Alloys
       Figure 64 also shows a curve labeled $T_o^{FCC/BCC}$ which describes
the locus of points along which the fcc and bcc Co-Fe alloys have
equal free energies. This curve has been computed using a thermo-
chemical description of the fcc and bcc phases derived earlier.
Figure 65 shows the free energy difference between the fcc and dis-
ordered bcc phases as a function of temperature and composition.
The curve labeled $\Delta F^{BCC \to FCC}$=0 is the same as that shown in Figure
64. The remaining curves show the locus of points corresponding
to various free energy differences between disordered fcc and bcc
phases. As the free energy difference becomes larger, the bcc be-
comes more stable relative to the fcc phase for a given composi-
tion. In the case of iron base alloys (i.e., Fe-Ni and Fe-C alloys),
the fcc phase can be retained by rapid cooling until the "driving
force" for transformation to the bcc form reaches the vicinity of
300 cal/g.at. (i.e., the free energy of the bcc phase is 300 cal/g.at.

-90-
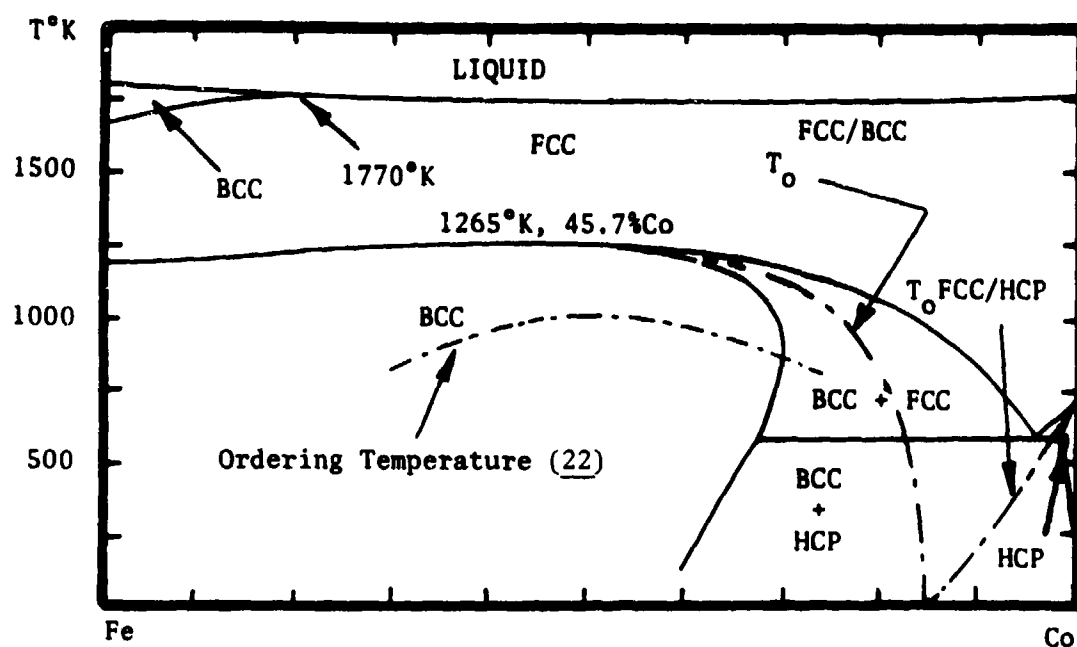
Figure 64. Calcul..ted Iron-Cobalt Phase Diagram Showing Locus of Curve for T_o(FCC/BCC) where FCC and BCC Phases of Same Composition Have Equal Free Energies (21,22).

ATOMIC PERCENT IRON
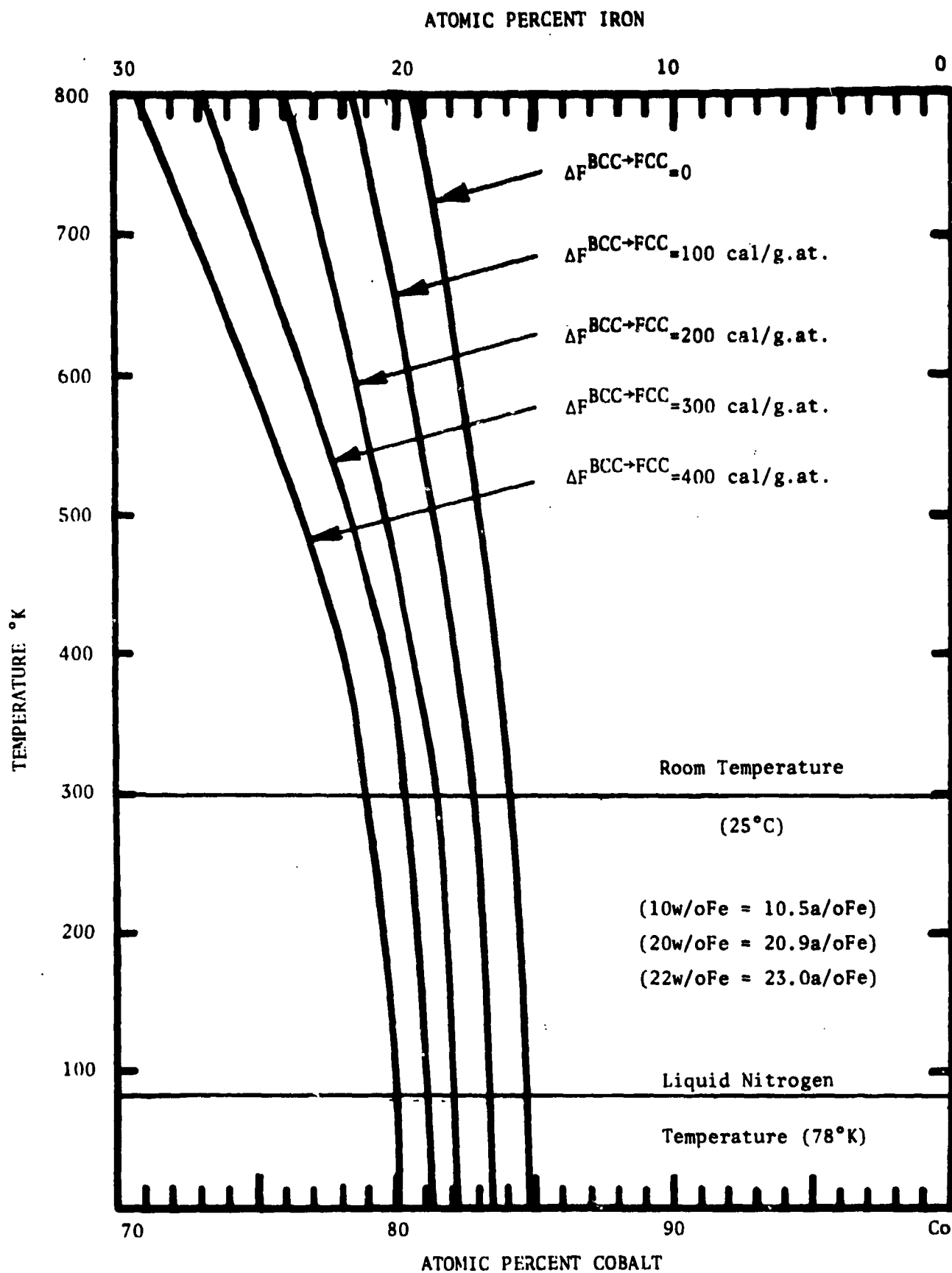
Figure 65. Calculated Temperature and Composition of the Free Energy Difference between FCC and BCC Iron Cobalt Alloys.

less than the fcc phase). Figure 65 suggests that this situation should prevail at room temperature in an alloy with 80 a/o Co-20 a/o Fe (80.9 w/o Co-19.1 w/o Fe). Alloys containing less than 20 a/o Fe could be expected to remain fcc while alloys with greater than 20 a/o (19.1 w/o) Fe would be expected to transform to the bcc phase on cooling from 1000°C. In order to test this prediction, a series of cobalt-iron alloys was prepared and air cooled from 1000°C. Figures 66-69 show the resulting microstructures. The first two photomicrographs show typical austenitic fcc structures obtained by air cooling the 82 w/o Co-18 w/o Fe and 90 w/o Co-10 w/o Fe alloys. On the other hand, Figure 68 shows the martensitic bcc structure obtained on air cooling the 78 w/o Co-22 w/o Fe alloy. The crystal structure of these alloys was verified by X-ray diffraction using CrKα radiation. Inclusions shown in Figures 65-69 are oxide particles which are present in the Ferrovac E iron used to make the alloy by combination with electrolytic cobalt.

Figure 69 shows the microstructure of the 80 w/o Co-20 w/o Fe alloy which contained some surface martensite formed during the polishing. This was established by annealing the specimen at 1000°C, air cooling it and taking an X-ray pattern from the surface without polishing. This pattern showed no bcc diffraction lines. However, polishing the surface produced strong bcc peaks. This result suggests that the 20 w/o Fe alloy (19.1 a/o Fe) is close to transforming at room temperature. This result is in keeping with the predictions of Figure 65.

An attempt was made to produce martensite in this alloy by cooling it in liquid nitrogen (i.e. to 77°K). However, no bcc phase formed. This may be due to the steep free energy difference versus temperature curve which does not yield very many more cal/ g.at. of driving force as the temperature is lowered from 300°K to 77°K.

The results shown in Figures 65-69 are in keeping with earlier studies of the Co-Fe system (23-25) which showed a lowering of the fcc/hcp transition temperature of cobalt by the addition

-93-
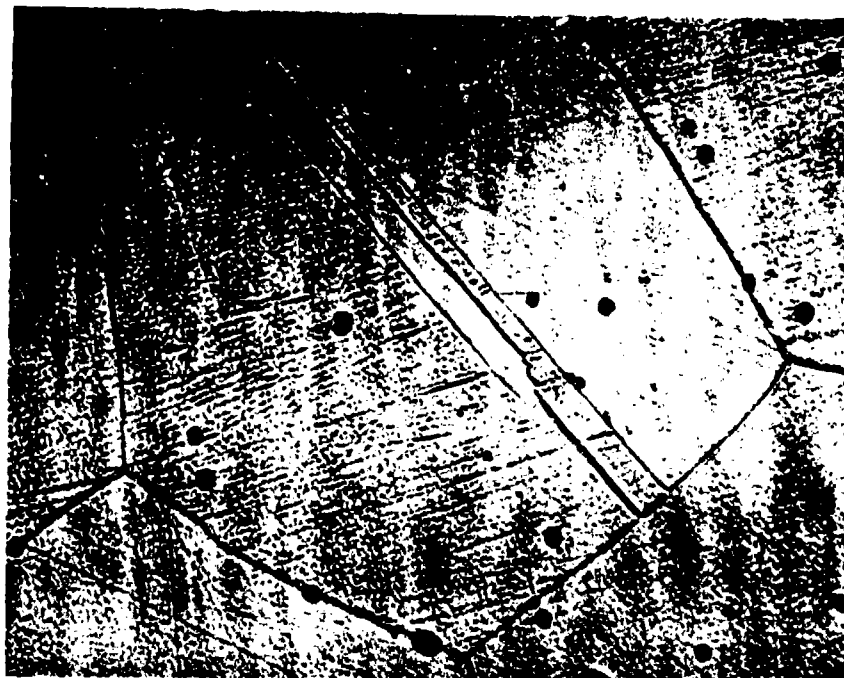
Plate No.
10486

Figure 66. 82 w/o Co-18 w/o Fe Alloy Annealed at 1000°C Air
Cooled to 25°C. Etched in 5% Nital. Photomicrograph
Shows Twinned Austenitic Structure (X1000).
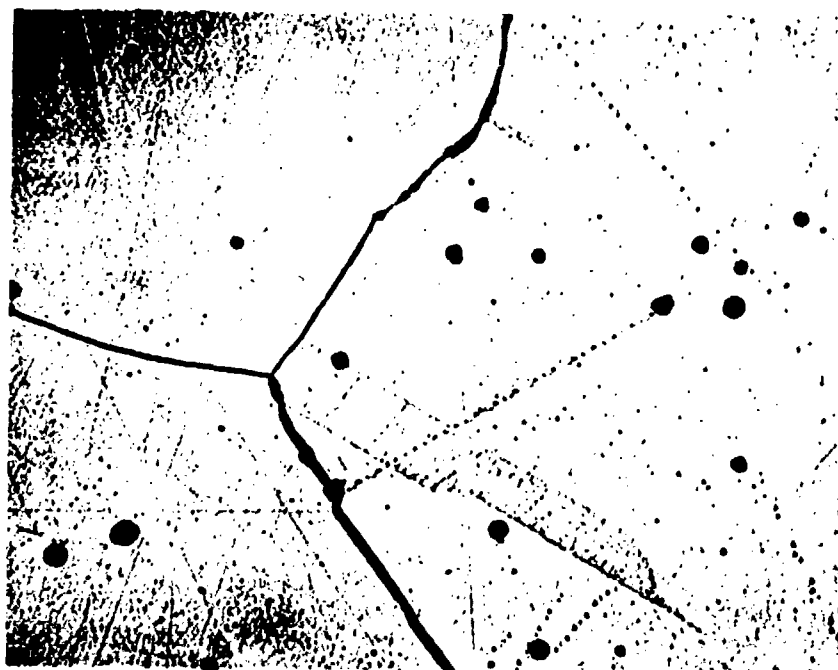
Plate No.
10489

Figure 67. 90 w/o Co-10 w/o Fe Alloy Annealed at 1000°C Air
Cooled to 25°C. Etched in 5% Nital. Photomicrograph
Shows Twinned Austenitic Structure (X1000).

Plate No.
10483

Figure 68. 78 w/o Co-22 w/o Fe Alloy Annealed at 1000°C Air
Cooled to 25°C. Etched in 5% Nital. Photomicrograph
Shows Structure of BCC Phase (X1000).
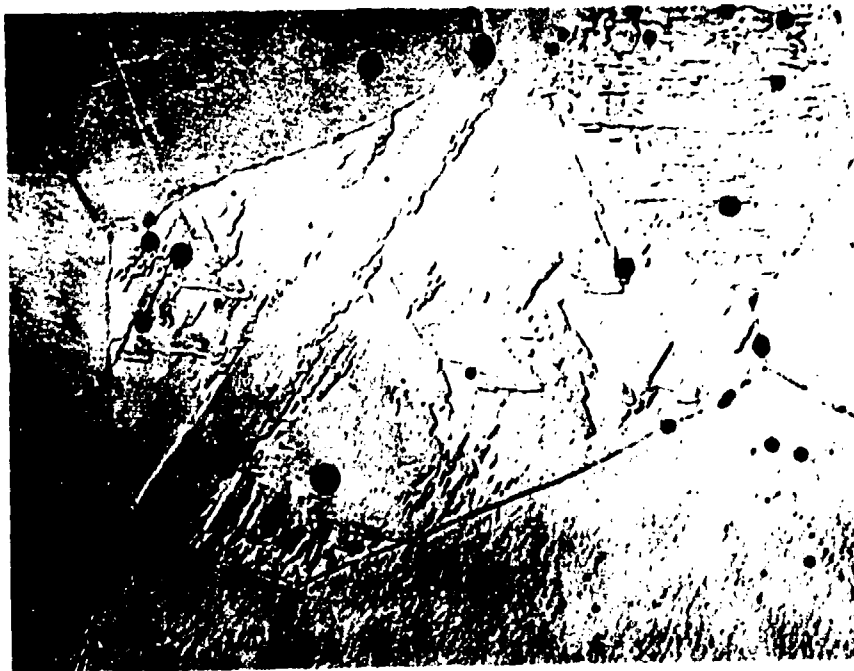
Plate No.
10484

Figure 69. 80 w/o Co-20 w/o Fe Alloy Annealed at 1000°C Air
Cooled to 25°C. Etched in 5% Nital. Central Grain
Shows Surface Martensite (BCC) Formed during Polish-
ing in an Austenite (FCC) Matrix (X1000).

-95-

of iron. Addition of 5 a/o Fe to cobalt reduced T_o from 733°K to 503°K (24,25). Alloys with 7.5, 10.0, 12.5 and 15 a/o Fe cooled to 25°C (298°K) by water quenching after two hours at 1100°C were found to be completely fcc (23). Plastic deformation in liquid nitrogen by hammering to effect a 17% deformation produced hexagonal phase in the 7.5 a/o Fe alloy and some bcc phase in the 15 a 'o alloy. However the 10.0 and 12.5 a/o Fe alloys were found to remain fcc.

Thus, the Co-Fe alloys shown in Figures 66 and 69 with 18 and 20 w/o iron fall in exactly the range required to test the hypothesis, i.e. that high damping could be attained in a metastable phase with a high magnetic Curie point. The Curie point for the fcc appears to be near 950°C (1223°K) (25).

Accordingly, a series of "resonant dwell damping" bars were fabricated from alloys in this series and tested at 25°C along with an additional set of alloys at a stress level near 2000 psi. The geometry of the samples resulted in natural frequencies in the 190-270 Hertz range. The results for the original set of samples are shown in Table 1. This group of samples labeled 51-64 were prepared by annealing alloy stock, machining the damping bars and then making the measurements.

Subsequently, the damping bars were X-rayed. It was found that samples 57, 58, 59 and 60 (i.e. 80 w/o Co-20 w/o Fe and 82 w/o Co-18 w/o Fe) exhibited fcc and bcc diffraction lines. This was apparently due to the surface deformation which occurred during machining. Consequently, these four samples were reannealed at 1000°C and oil quenched. These samples yielded completely fcc X-ray patterns. Subsequent measurement of the loss factor yielded values of 280 to 500 x 10^{-4} as shown by samples 57A, 58A, 59A and 60A in Table 1. Following this experience, the remainder of samples 51-64 were reannealed and oil quenched and the loss factor at 25°C measured once again. The results are shown in Table 2. The reannealing did not affect the loss factors of the 78 w/o Co-22 w/o Fe samples very much. These were 14 and

-96-

TABLE 1

SUMMARY OF RESONANT DWELL DAMPING MEASUREMENTS AT 25°C

Sample No. Composition (weight percent)	Resonant Frequency (Hz.)	Dynamical Youngs Modulus (PSIx10^{-6})	Peak Stress (PSI)	Loss Factor (Q^{-1}x10^4)	Comments on Test
51(70Co-30Ni)	265	28.0	2190	66	All Samples
52(47.2Fe-52.8Pt)	185	15.7	1290	28	Annealed at
53(47.2Fe-52.8Pt)	214	19.2	1660	25	1000°C--Air
54(46.2Fe-53.8Pt)	191	14.7	1290	69	Cooled--Then
55(78.0Co-22.0Fe)	259	26.6	2050	14	Machined
56(78.0Co-22.0Fe)	251	26.3	1980	16	"
57(80.0Co-20.0Fe)	237	24.2	1790	92	"
58(80.0Co-20.0Fe)	251	24.3	1900	68	"
59(82.0Co-18.0Fe)	245	23.1	1800	81	"
60(82.0Co-18.0Fe)	237	22.8	1740	64	"
61(90.0Co-10.0Fe)	264	27.8	2140	8	"
62(90.0Co-10.0Fe)	264	28.1	2140	14	"
63(65Co-28Fe-7Ni)	240	23.2	1770	17	"
64(70Fe-20Co-10Cr)	276	29.9	2410	6	"
57A(80.0Co-20.0Fe)	238	24.4	1810	280	All Samples
58A(80.0Co-20.0Fe)	243	25.5	1990	450	Annealed at
59A(82.0Co-18.0Fe)	236	21.4	1670	480	1000°C and
60A(82.0Co-18.0Fe)	242	23.8	1810	500	Oil Quenched

TABLE 2

SUMMARY OF RESONANT DWELL DAMPING MEASUREMENTS AT 25°C

Sample No. Composition (weight percent)	Resonant Frequency (Hz.)	Dynamical Youngs Modulus (PSIx10⁻⁶)	Peak Stress (PSI)	Loss Factor (Q^{-1}x10⁴)	Comments on Test
55A(78.0Co-22.0Fe)	253	25.4	1960	20	All Samples
56A(78.0Co-22.0Fe)	252	26.5	2000	13	Annealed at
61A(90.0Co-10.0Fe)	266	28.2	2170	7	1000°C--Then
62A(90.0Co-10.0Fe)	272	29.8	2270	7	Oil Quenched
63A(65Co-28Fe-7Ni)	244	24.0	1830	28	"
72A(79.0Co-21.0Fe)	249	24.3	1900	19	"
73A(79.0Co-21.0Fe)	264	27.8	2140	10	"
75A(80.0Co-20.0Fe)	249	24.3	1900	24	"
76A(80.0Co-20.0Fe)	251	26.3	1980	274	"
77C(81.0Co-19.0Fe)	232	21.2	2000	11	Machined in 33%
78C(80.5Co-19.5Fe)	248	24.3	2000	12	Cold Worked Condition
79 NIVCO	275	28.3	2000	14	As Received from
79 NIVCO	272	28.2	5000	26	Westinghouse
80C(81.5Co-18.5Fe)	245	23.1	2000	12	Machined--Cold Worked
73B(79.0Co-21.0Fe)	263	27.0	2100	9	Annealed--Water Quench.
77A(81.0Co-19.0Fe)	257	24.8	2000	31	Annealed 1000°C--Then
78A(80.5Co-19.5Fe)	248	24.4	2000	320	Oil Quenched
80A(81.5Co-18.5Fe)	247	24.3	2000	110	"

16 x 10^{-4} (Numbers 55 and 56) before the reannealing and 20 and
13 x 10^{-4} (Numbers 55A and 56A) after reannealing. The diffrac-
tion patterns both showed substantial quantities of the bcc
phase. Similarly, the reannealing had little effect on the
90 w/o Co-10 w/o Fe alloys. Thus samples 61 and 62 exhibited $Q^{-1}=$
8 and 14 x 10^{-4} before reannealing and 7 and 7 x 10^{-4} after
annealing. Both sets of X-ray patterns showed completely fcc
structures. Thus the results show a marked peak in the loss
factor in the vicinity of 80 w/o Co-20 w/o Fe providing the alloy
is all fcc. This is not dependent on the magnetic Curie tempera-
ture since both the fcc and bcc phases have high Curie temperatures
which are near 1000°C.

Table 2 shows additional results for other Co-Fe alloys
with compositions in the vicinity of 80 w/o Co-20 w/o Fe which
were made and tested in order to establish the effects of composi-
tion, structure and degree of cold work on the loss factor. These
preliminary results show that the high damping behavior can be
reproduced in other alloys but it is eliminated by cold work.

Table 2 also contains the results of damping tests on
NIVCO, which is a commercial alloy developed by Cochardt at
Westinghouse (6). It was kindly furnished by Dr. Lou Willertz of
Westinghouse Research Laboratories. According to Cochardt's de-
scription, NIVCO is 72 w/o Co-23 w/o Ni and the balance titanium
and aluminum which are added to provide strength by precipitation
hardening. Cochardt reports values of the logarithmic decrement
of 0.02 and 0.05 at room temperature for this alloy at shear
stresses of 2000 psi and 5000 psi (Figure 1 of Reference 6).
Since Q^{-1} is equal to the decrement divided by π, Cochardt's
results would correspond to loss factors of 0.007 and 0.017 or
70 x 10^{-4} and 170 x 10^{-4} respectively at 25°C and stresses of 2000
psi and 5000 psi. These values are much higher than those shown
in Table 2. The values measured in the present tests, i.e. 14x10^{-4}

at 2000 psi and 26 x 10^{-4} at 5000 psi, are five times smaller than Cochardt's results. The main difference is that the frequency of the present measurements at 230-270 Hz is in the audible range while that used by Cochardt was near 1 cycle/sec (1 Hertz).

Thus, the current results indicate that loss factors of Q^{-1} = 500 x 10^{-4} are attainable in the 80 w/o Co-20 w/o Fe alloys which are two to three times higher than observed in Nitinol (i.e., 55 w/o Ni-45 w/o Ti) and fifty times higher than NIVCO. Measurements of the loss factor of 80 w/o Co-20 w/o Fe were carried out between -80°C and +80°C for comparison with Nitinol. (Detailed results are presented below). Preliminary results showed almost no change in each of the audible "ring" at liquid nitrogen or +200°C. Thus it was anticipated that the Q^{-1} value would not change significantly in this temperature range.

The other advantages the Co-Fe alloy has in relation to the Ni-Ti alloy are a higher modulus of 25 million psi (Tables 1 and 2) versus 8 million psi and ease of fabrication.

In order to evaluate the strength of the 80 w/o Co-20 w/o Fe composition, a set of tensile bars were fabricated of annealed material. Subsequent tests were expanded to test swaged rod. These were compared with tensile results measured for NIVCO. Figures 70-78 display the results. The 82 w/o Co-18 w/o Fe and 80 w/o Co-20 w/o Fe alloys show reproducible 0.2 percent offset yield strengths of 17000-18000 psi in the annealed condition in Figures 70-74. This is the strength level of the samples which exhibited loss factors of Q^{-1} = 500 x 10^{-4}.

Figures 75-77 show the yield strength obtained for samples of the 18.5 w/o Fe, 19 w/o Fe and 19.5 w/o Fe alloys in a cold worked condition following a 33% reduction in diameter by cold swaging. Reference to Table 2 shows that these alloys exhibited loss factors of 11 to 14 x 10^{-4} in the cold worked condition. Annealing raised the loss factor of the 19.5 w/o Fe sample to 320 x 10^{-4} as shown in Table 2.

Figure 78 shows the results of a tensile test on NIVCO. The measured 0.2 percent yield strength of 108,900 psi is in good
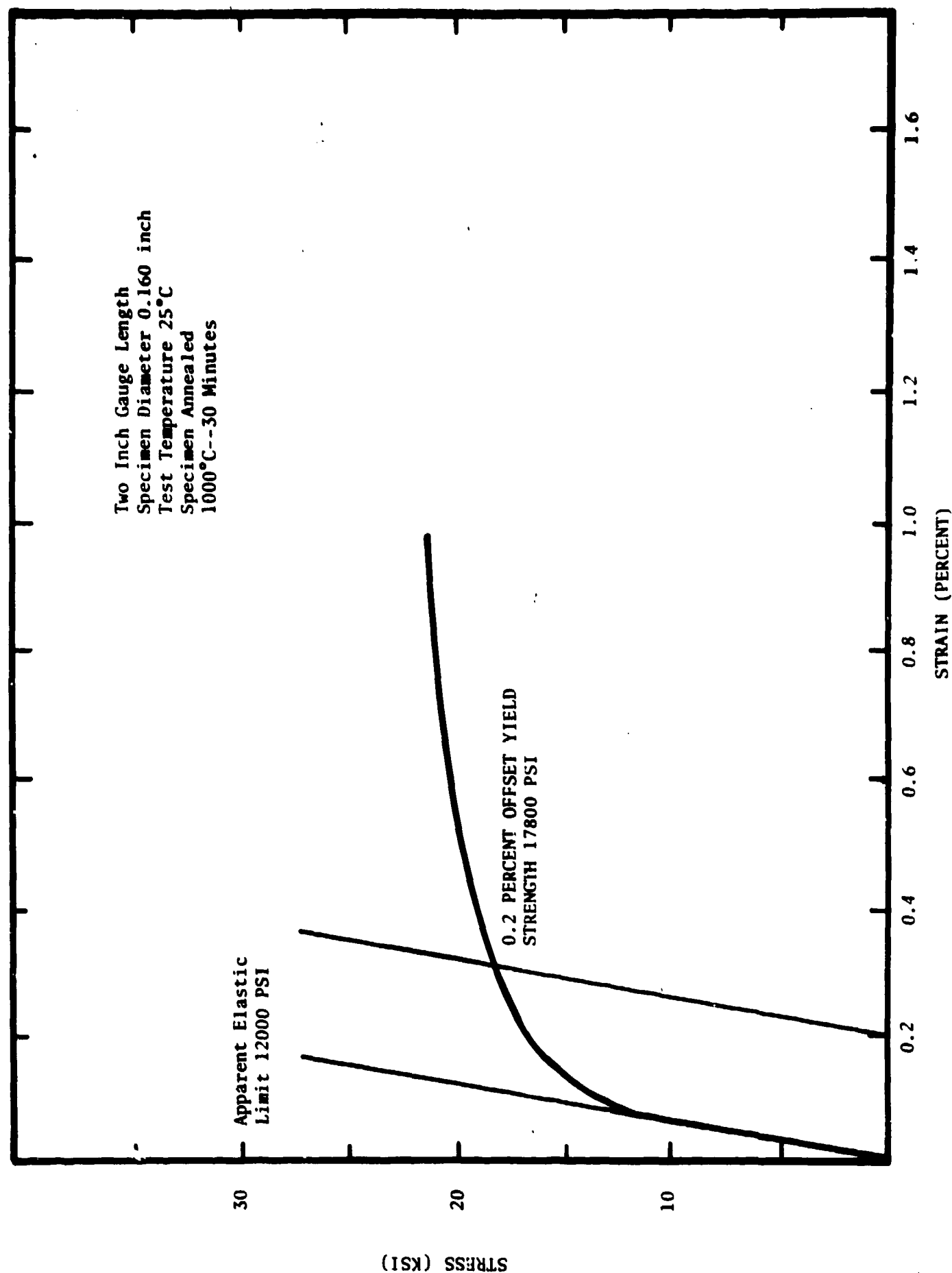
Figure 70. Stress-Strain Curve for a 82%Co-18%Fe Alloy at 25°C.

Two Inch Gauge Length
Specimen Diameter 0.160 inch
Test Temperature 25°C
Specimen Annealed
1000°C--30 Minutes

0.2 PERCENT OFFSET YIELD
STRENGTH 17800 PSI

Apparent Elastic
Limit 12000 PSI

STRAIN (PERCENT)

STRESS (KSI)
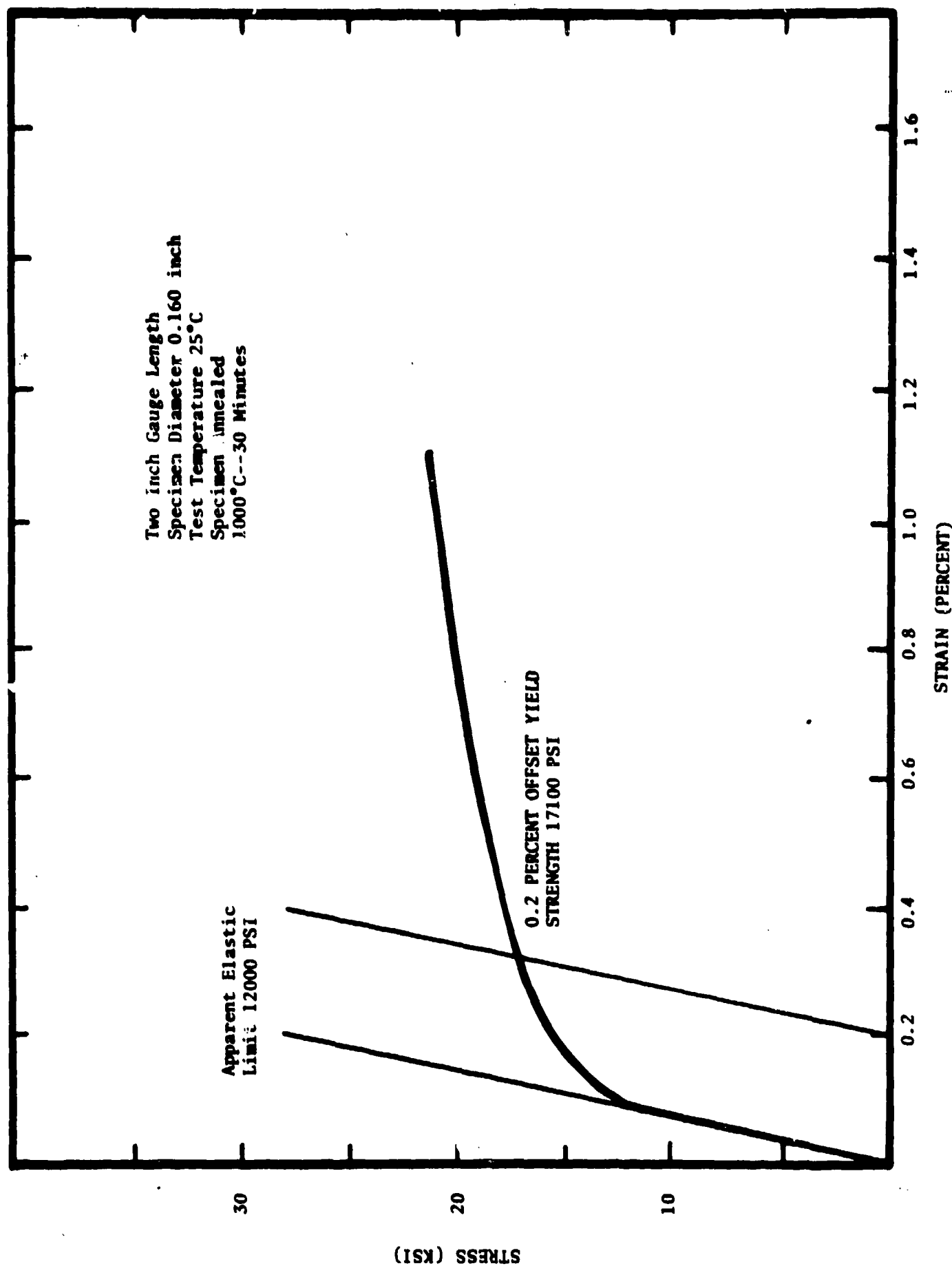
Figure 71. Stress-Strain Curve for a 82%Co-18%Fe Alloy at 25°C.
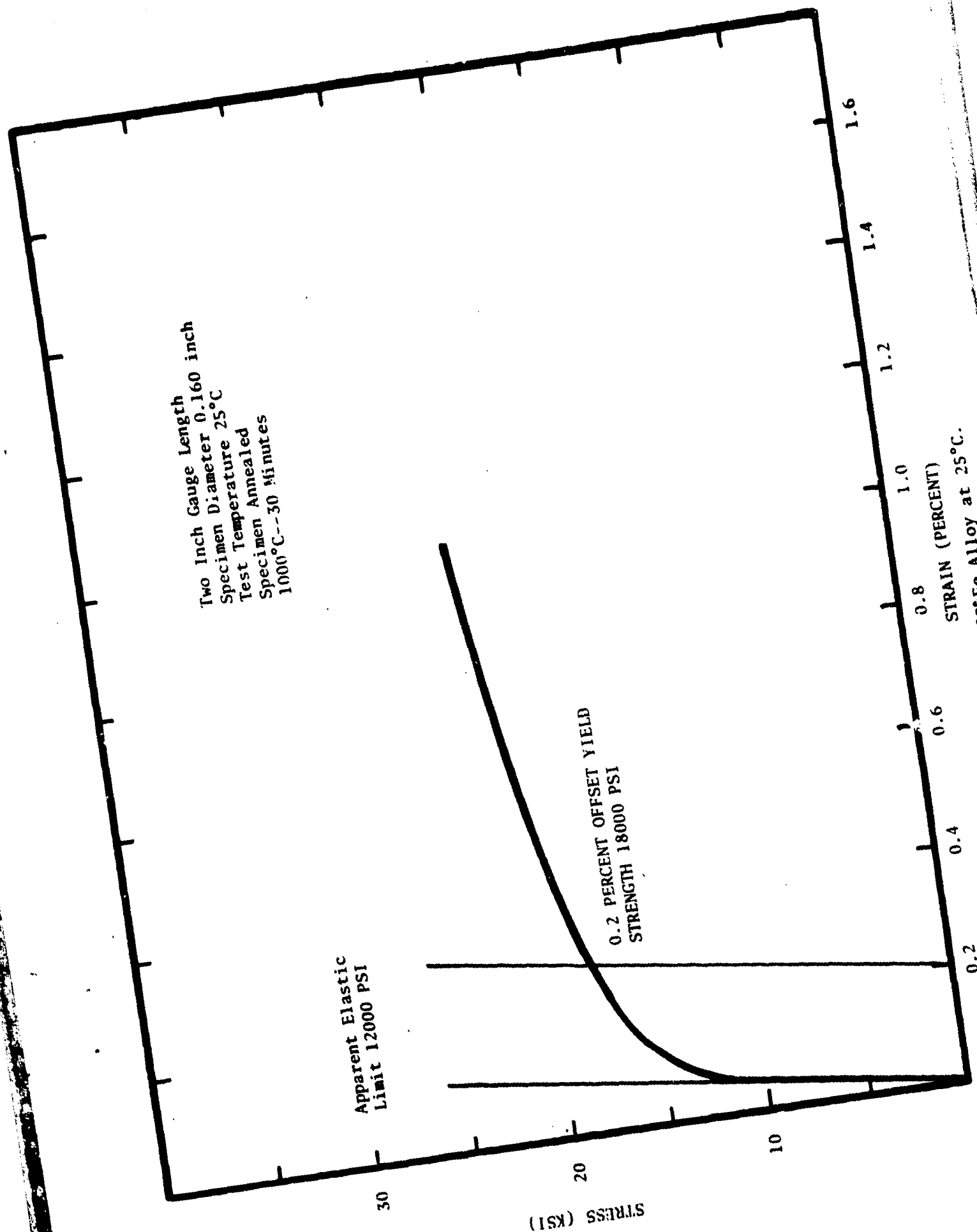
Figure 72. Stress-Strain Curve for a 80%Co-20%Fe Alloy at 25°C.

Two Inch Gauge Length
Specimen Diameter 0.160 inch
Test Temperature 25°C
Specimen Annealed
1000°C--30 Minutes

0.2 PERCENT OFFSET YIELD
STRENGTH 18000 PSI

Apparent Elastic
Limit 12000 PSI

STRAIN (PERCENT)

STRESS (KSI)

-103-
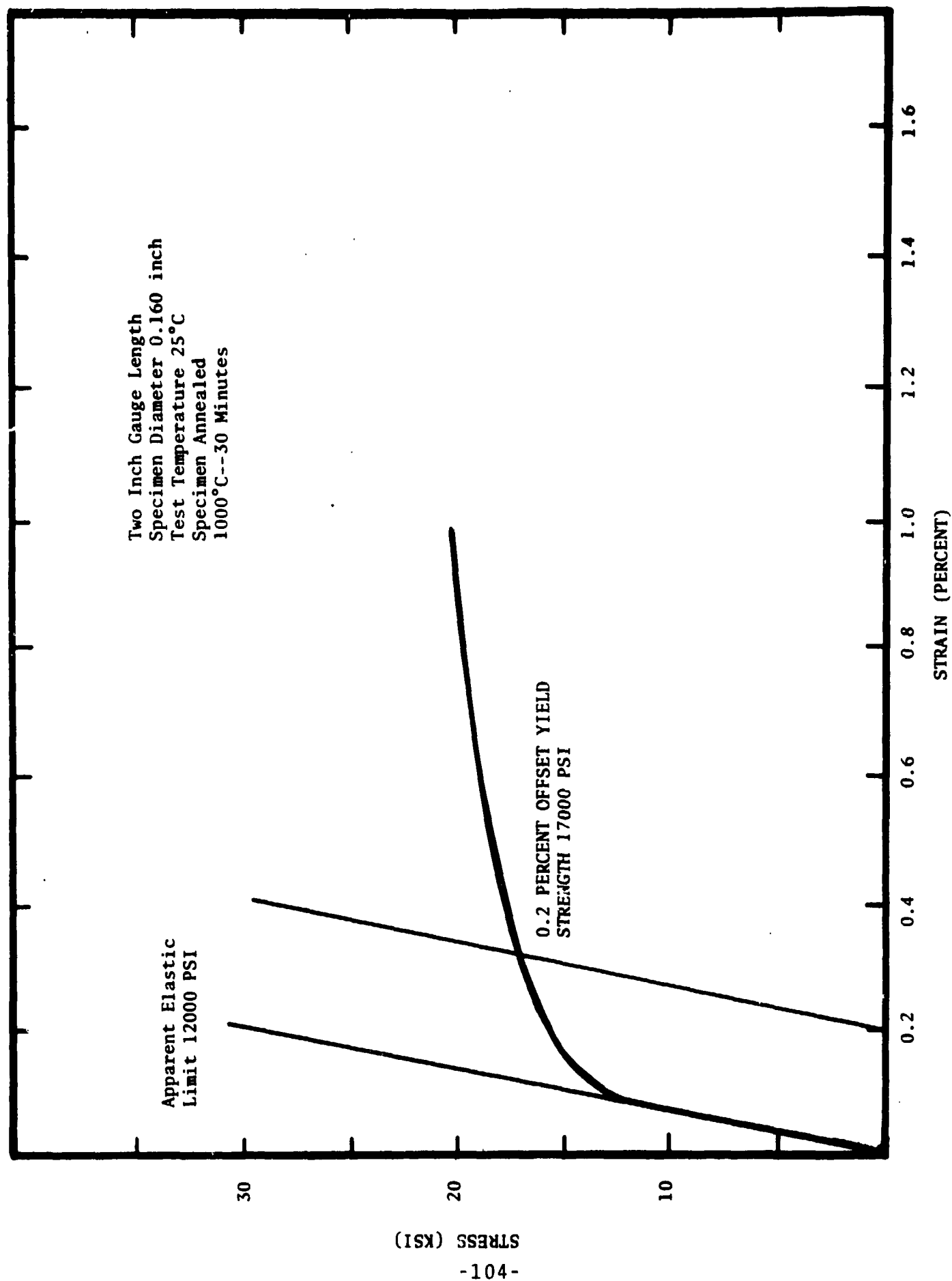
Figure 73. Stress-Strain Curve for a 80%Co-20%Fe Alloy at 25°C.

Two Inch Gauge Length
Specimen Diameter 0.160 inch
Test Temperature 25°C
Specimen Annealed
1000°C--30 Minutes

0.2 PERCENT OFFSET YIELD
STRENGTH 17000 PSI

Apparent Elastic
Limit 12000 PSI

STRAIN (PERCENT)

STRESS (KSI)

-104-
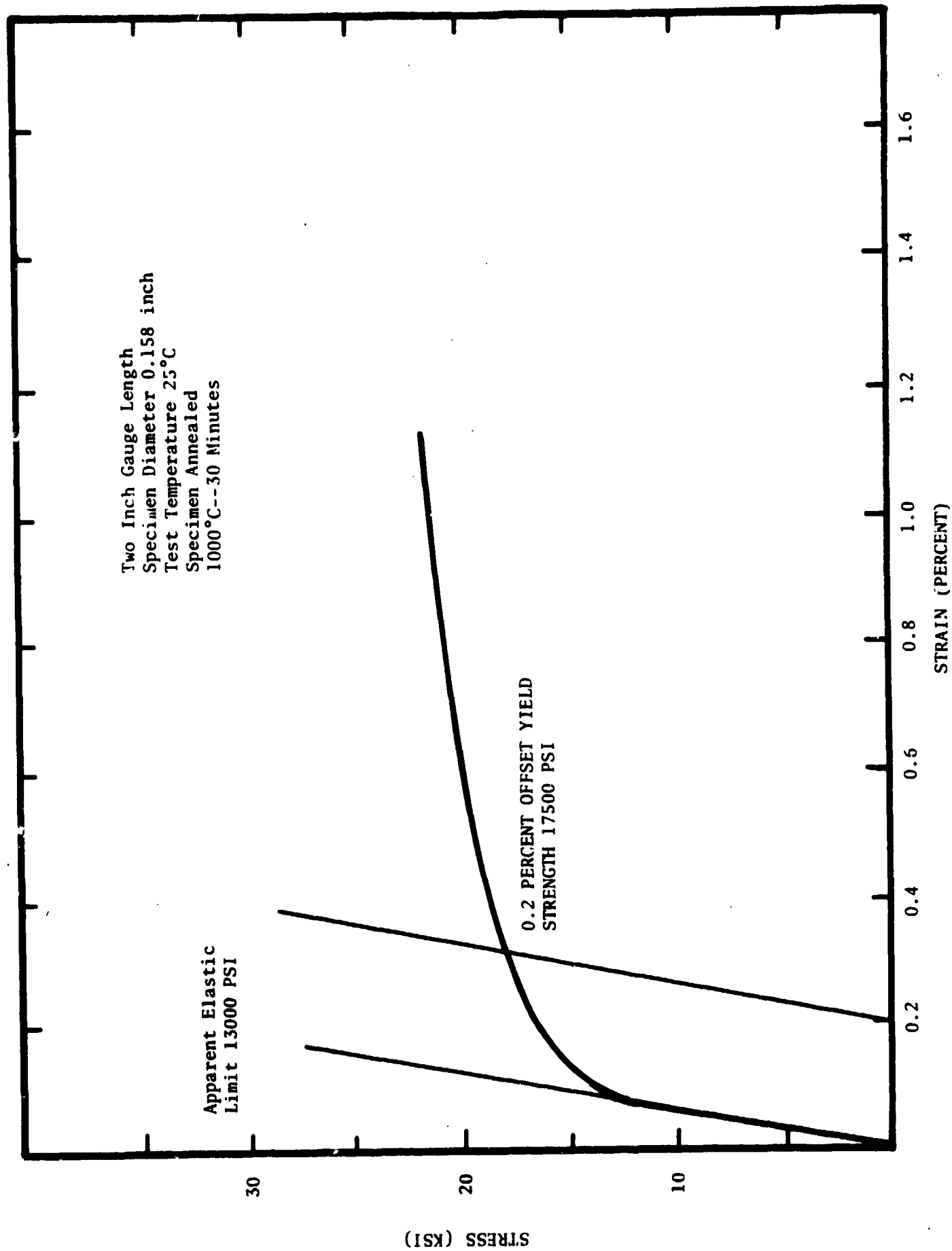
Figure 74. Stress-Strain Curve for a 80%Co-20%Fe Alloy at 25°C.

Two Inch Gauge Length
Specimen Diameter 0.158 inch
Test Temperature 25°C
Specimen Annealed
1000°C--30 Minutes

0.2 PERCENT OFFSET YIELD
STRENGTH 17500 PSI

Apparent Elastic
Limit 13000 PSI

STRAIN (PERCENT)

STRESS (KSI)
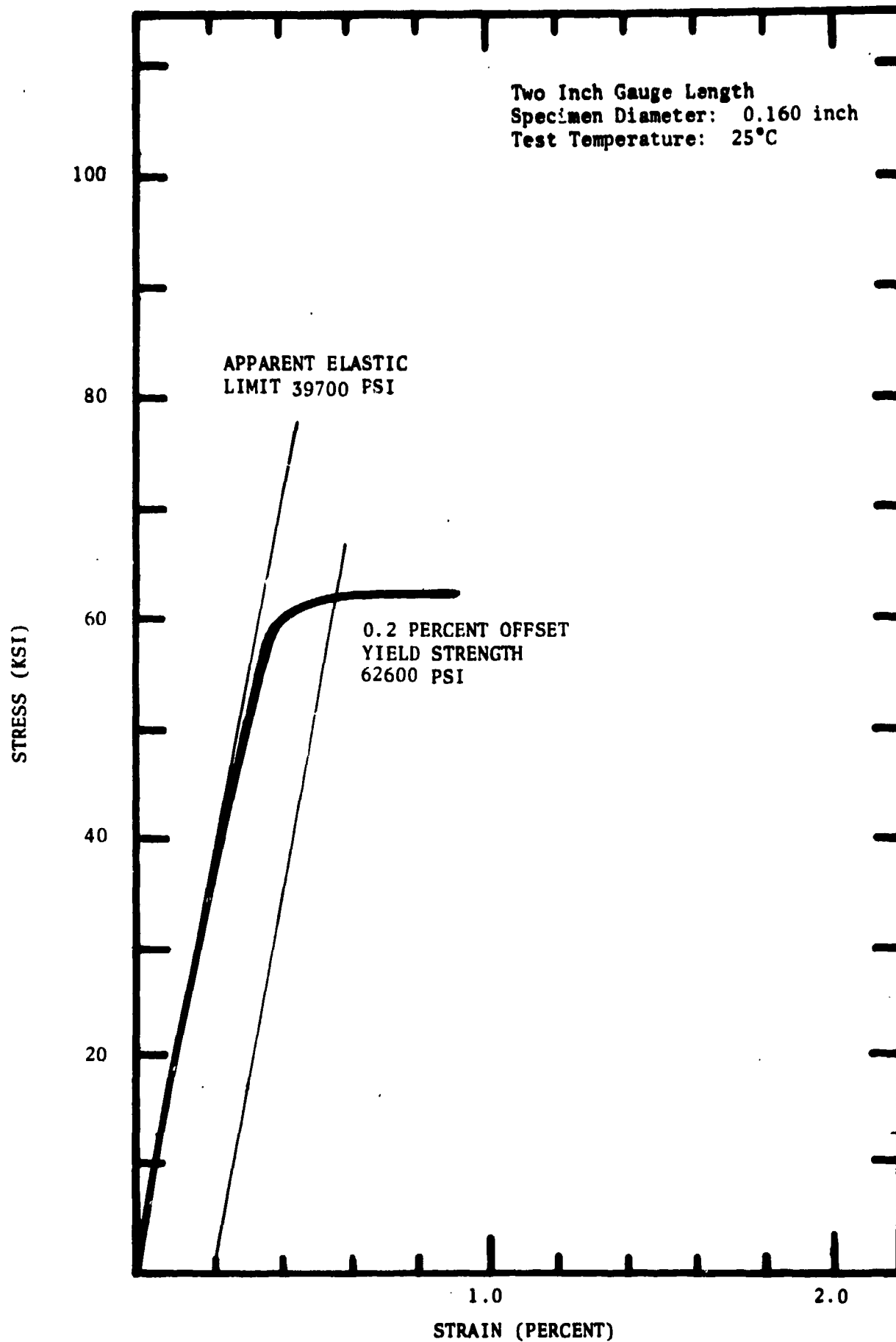
Figure 75. Stress-Strain Curve for a 81.5 w/o Co-18.5 w/o Fe
Alloy Tested in the Cold Worked Condition at 25°C.
Cold reduction of thirty-three percent (diametral)
by swaging.
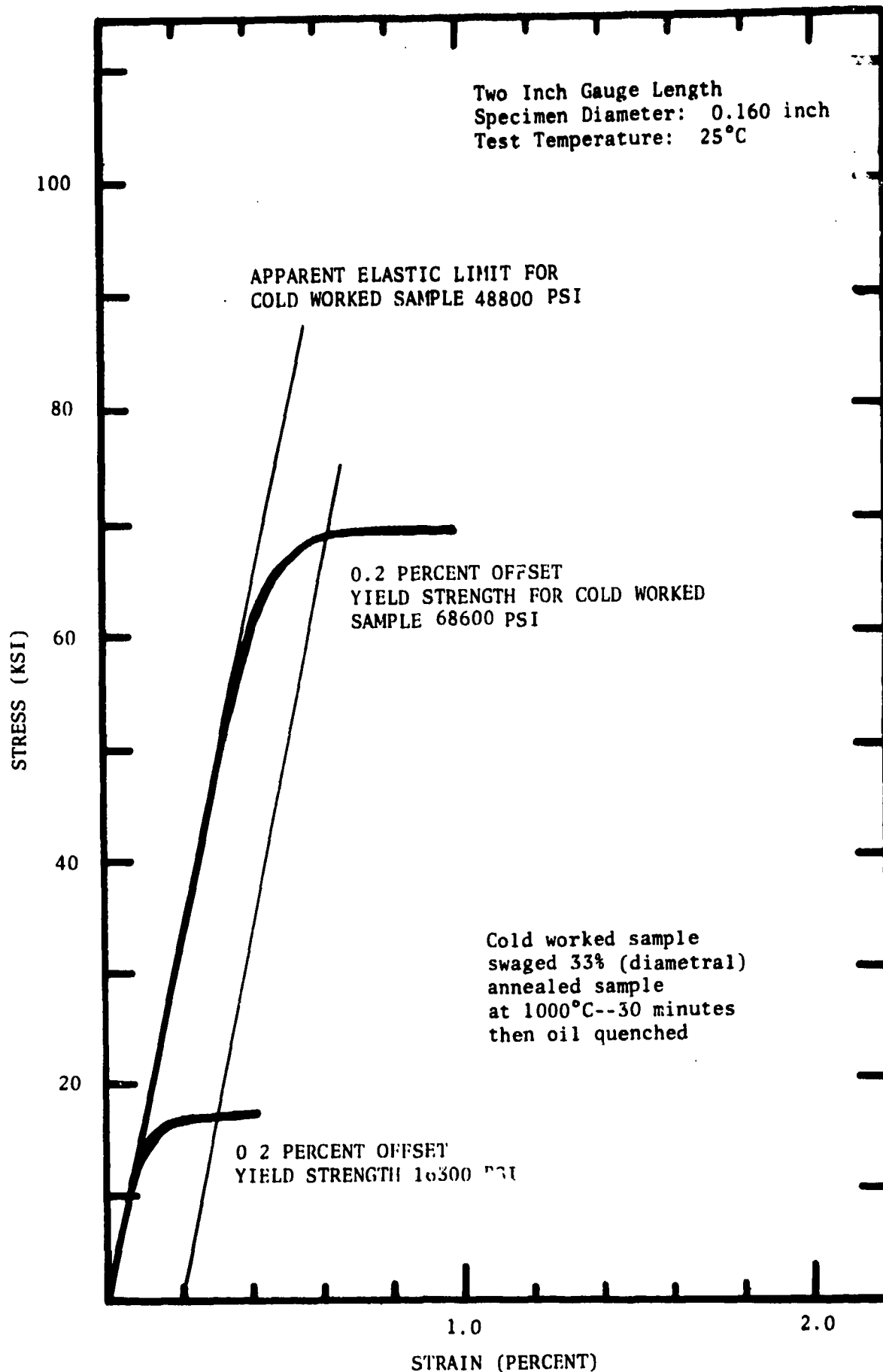
Figure 76. Stress-Strain Curves for 81 w/o Co-19 w/o Fe Alloy in the Cold Worked and Annealed Condition at 25°C.

-107-

Two Inch Gauge Length
Diameter: 0.160 inch
Test Temperature: 25°C

Apparent Elastic
Limit for Cold Worked
Sample 32000 PSI

Elastic Limit for
Annealed Sample
15700 PSI

Cold Worked by Swaging 33% (diametral)
0.2 Percent Offset Yield Strength
71500 PSI

Annealed--1000°C--30 minutes
Oil Quench

0.2 Percent Offset Yield Strength
22500 PSI

STRESS (KSI)

STRAIN (PERCENT)
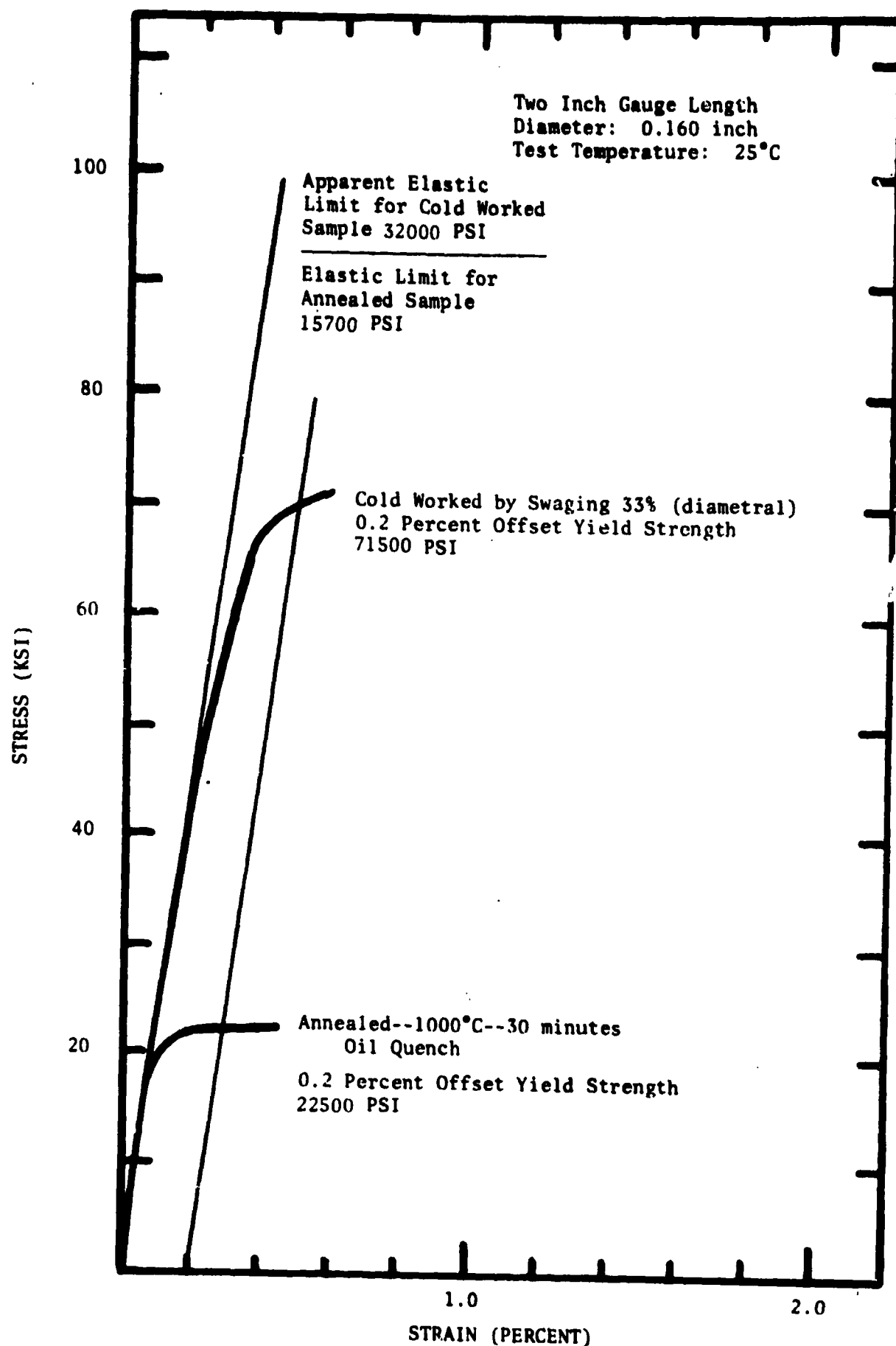
Figure 77. Stress-Strain Curves for 80.5 w/o Co-19.5 w/o Fe Alloy
in the Cold Worked and Annealed State at 25°C.

-108-
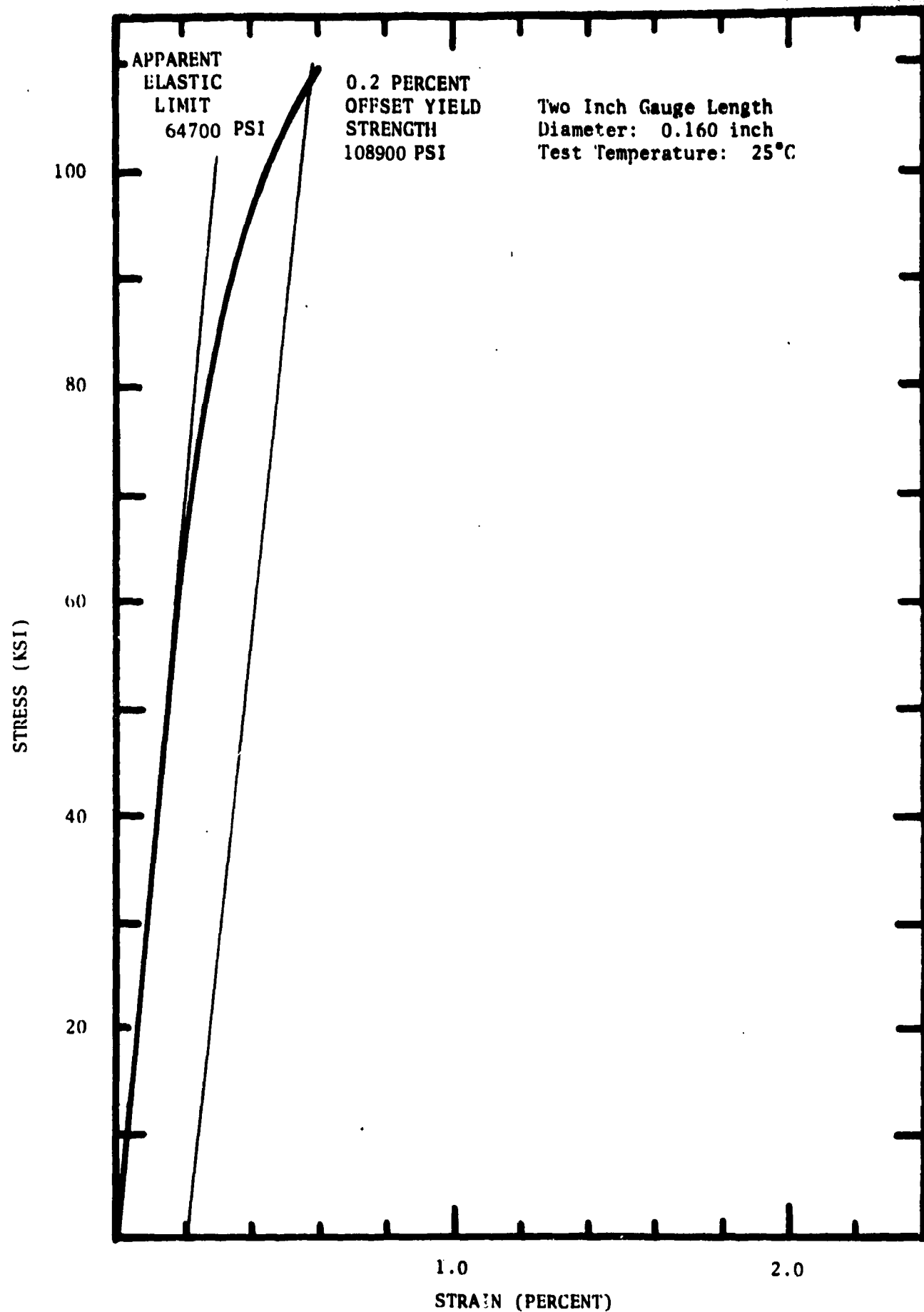
Figure 78. Stress-Strain Curve for NIVCO (Westinghouse) at 25°C.

agreement with Cochardt's reported value of 110,000 psi (6).

These values of the yield strength were combined with the measured loss factors observed at a stress level of 2000 psi in the range 150 to 250 Hz for NIVCO, 80 w/o Co-20 w/o Fe and 55 w/o Ni-45 w/o Ti and are displayed in Figure 1. The comparison shows the relatively high damping capacity (and low strength) of the Co-Fe alloy to the other two materials. However, this shortcoming in strength can be overcome through alloying as shown further in this section.

3.   The Work Ability of Co-Fe

Three ten-pound heats of the 80 w/o Co-20 w/o Fe alloy were vacuum melted and cast into two inch diameter moulds. The ingots were subsequently forged to 3/4 inch bars and then (cold) swaged to 1/2 inch rod. Intermediate anneals of 1000°C were employed. The final product was sixty inch long rod. However, it was found that this structure was a mixture of bcc and fcc phases (see earlier discussion) and the rod "rang" when struck, indicating poor damping. However, the high damping characteristics were readily restored by proper heat treatment above 1000°C followed by air cooling. The x-ray analysis of the material disclosed a fully austenitic (fcc) structure, and the high damping characteristic of the rod was regenerated.

A second demonstration of the ease with which the 80 w/o Co-20 w/o Fe alloy can be fabricated was the reduction of as-cast 1/2 inch thick slab to 50 mil foil. This was carried out in a series of 20% reductions with intermediate anneals. The reductions were quite moderate and the ease with which they were made indicates that even larger reductions could be successfully carried out. This would certainly appear to be possible if the reductions were carried out by hot rolling. The final treatment of the fifty mil foil consisted of a 1000°C anneal for 30 minutes which yielded soft foil which "rang like lead."

These results indicate that the 80 w/o Co-20 w/o Fe alloy can be reaily formed if it is in the fcc condition. More-

-110-
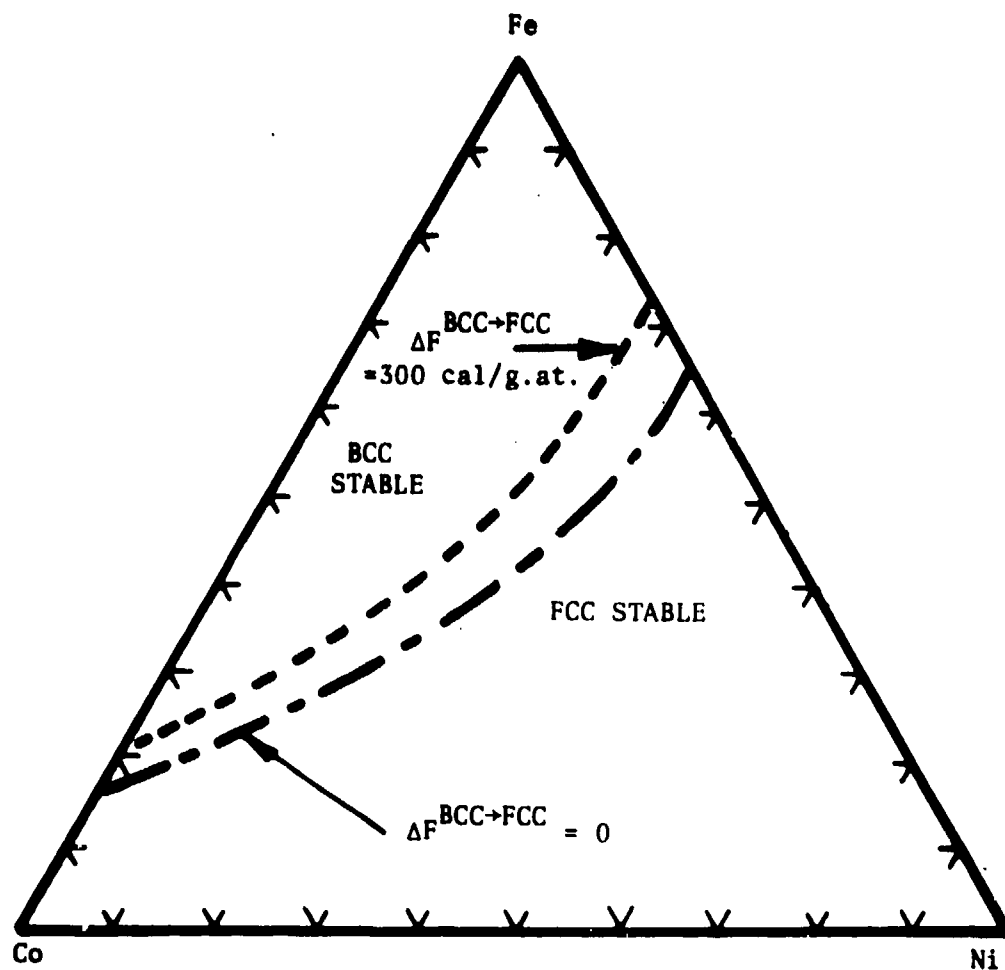
Figure 79. Calculated Regions of BCC and FCC Stability for Fixed Compositions at 25°C in the Iron-Nickel-Cobalt System.

over it can be heat treated to yield this structure quite readily. Although it has been established that the two phase (fcc + bcc) structure does not exhibit outstanding damping characteristics, it is probable that rather high strengths could be attained with this strcuture if it were attained by formation of an ordered bcc phase. This alloy (80 w/o Co-20 w/o Fe) could be readily formed in the fcc structure (as demonstrated above) and then aged to high strength by ordering the bcc phase. In fact, small carbon additions might even be incorporated into such a structure to enhance the strength by conferring some tetragonality into the bcc phase in analogy with ferrous martensites.

4. Temperature Dependence of Damping in Co-Fe

Before turning to the alloying studies conducted on the 80 w/o Co-20 w/o Fe alloy, it is useful to recount the temperature dependent studies undertaken to establish the data shown in Figure 2. The tests were conducted under the direction of Dr. John Heine of Bolt Beranek and Newman using the techniques detailed earlier in Section II.

Figures 79 and 80 show loss factor versus temperature curves for samples of a 80.5 w/o Co-19.5 w/o Fe and 81.5 w/o Co-18.5 w/o Fe alloy between -60°C and +80°C. Additional samples which were tested between 25°C and 130°C yield the results shown in Figure 2.

5. Incramute

For comparison, an additional set of data on a high damping commercial alloy (Incramute) was generated on a sample obtained from Mr. Eugene Thiele of the Copper Developing Association, Inc. A square plate 5-1/2 inches x 5-1/2 inches x 1/4 inch thick was obtained in the heat treated condition designed to yield maximum damping. This plate was employed to fabricate resonance dwell damping bars and tensile bars. Figure 81 shows the results of the damping measurements conducted on the Incramute (55 w/o Co-43 w/o Mn-2 w/o Al) alloy between -60°C and 100°C. Tensile tests

-112-

conducted at 25°C resulted in a 0.2% offset yield strength of
45,300 psi. These data are shown in Figures 1 and 2.

It is interesting to note that the copper-manganese
alloy system, upon which Incramute and several other commercial
damping alloys are based was predicted to have a metastable
fcc miscibility gap in 1969 (26). Recent experimental studies
by Vitek and Warlimont (27) and by Ye. Z. Vintaykin and coworkers
(28) have verified this prediction and Figure 82 shows that the
metastable miscibility gap in the fcc phase of this system
provides the basis for attaining high damping in Incramute and
other Cu-Mn alloys via heat treatment. This alloy is actually
face-centered tetragonal below its anti-ferromagnetic N'eel
temperature. The high damping is associated with this tetra-
gonality.

6. Third Element Additions to Co-Fe

The seond phase of the study of damping in the 80 w/o
Co-20 w/o Fe alloy was the evaluation of alloying additions on
damping and strength and demonstrated that substantial increases
in strength could be obtained. The strength of NIVCO is not due
to the properties of the 72 w/o Co-23 w/o Ni matrix, which is
comparable to the 80 w/o Co-20 w/o Fe material. The strength
is due to the presence of precipitates formed by the Al and Ti
additions. A similar effect can be expected in the Co-Fe alloy.
One possible source of strengthening is additional solid solution
hardening which might be effected by addition of nickel. The
nickel additions would be controlled so as to maintain the
"metastable condition" of the fcc phase. This is illustrated in
Figure 83 which shows the ternary Fe-Ni-Co counterpart of
Figure 65 calculated on the basis of the thermochemical descrip-
tion published previously (21). Therefore, it was believed that
these alloys should be metastable in the fcc form at 25°C and if
fabricated in this state, they might develop high Q^{-1} values
comparable to 80 w/o Co-20 w/o Fe and higher yield strengths than
the 17,500 psi level exhibited by the 80/20 Co-Fe alloys.

-113-
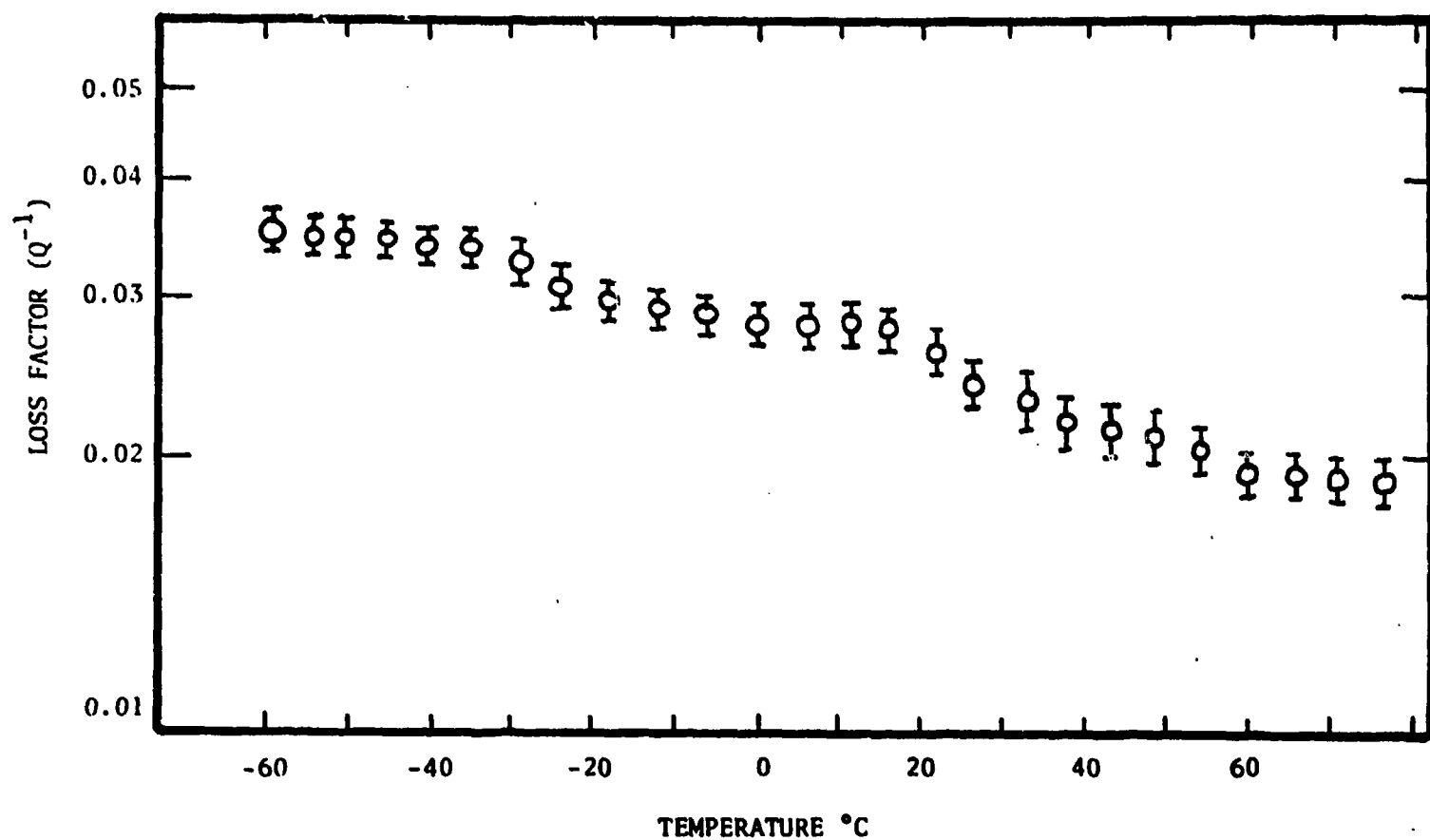
Figure 80. Loss Factor vs. Temperature Curve for a Sample of 80.5 w/o Co-19.5 w/o Fe measured at 240-250 Hertz and a stress of 2000 psi. The dynamical Young's Modulus measured over the same temperature range varied from 24 million psi at -60°C to 23 million psi at +80°C. The sample was annealed at 1000°C and air cooled.

-114-
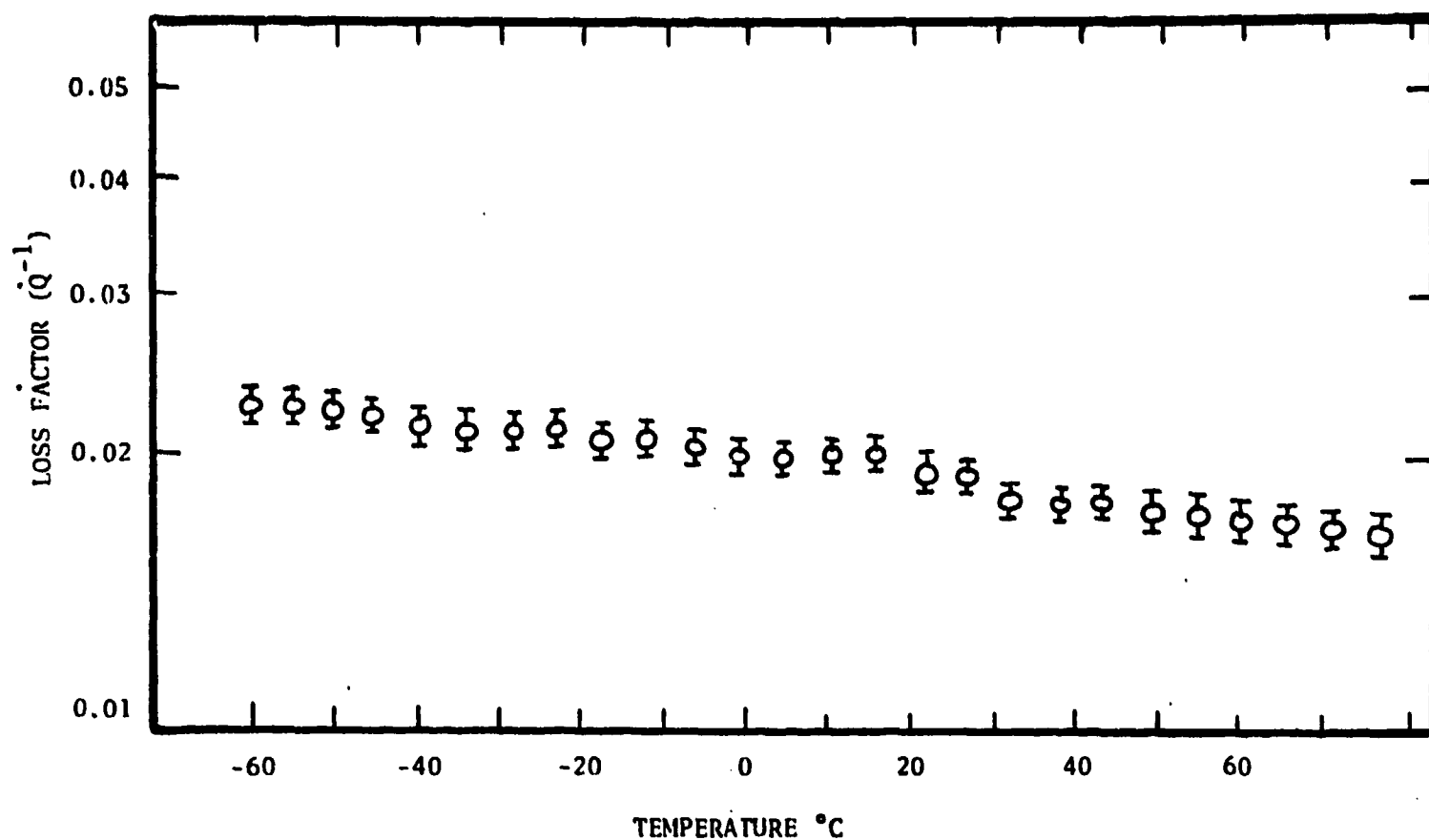
Figure 81. Loss Factor vs. Temperature Curve for a Sample of 81.5 w/o Co-18.5 w/o Fe measured at 240-250 Hertz and a stress of 2000 psi. The dynamical Young's Modulus measured over the same temperature range varied from 24 million psi at -60°C to 23 million psi at +80°C. The sample was annealed at 1000°C and air cooled.
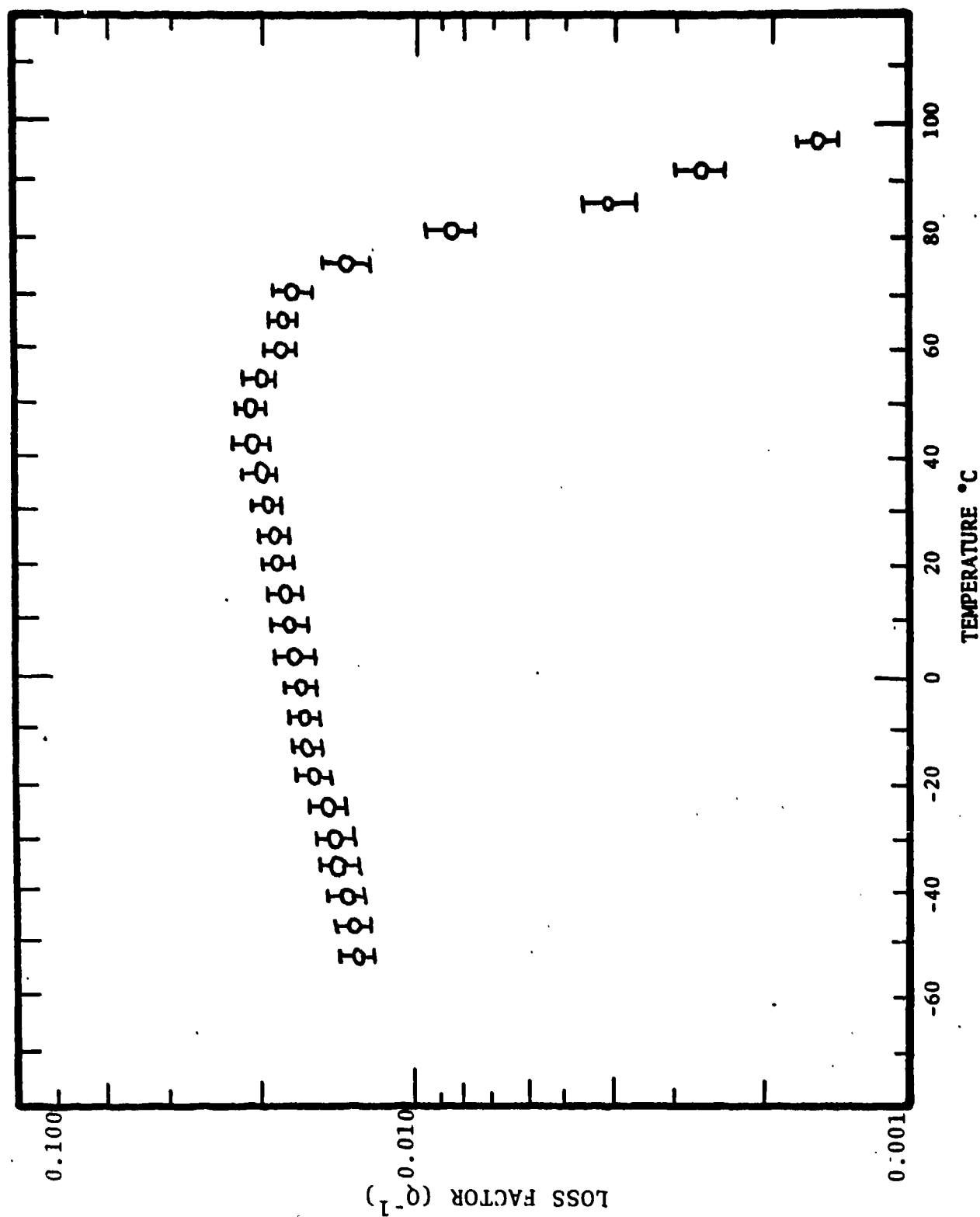
Figure 82. Loss Factor vs. Temperature for a Sample of Incramute I (Nominal Composition 55 w/o Cu-43 w/o Mn-2 w/o Al) heat treated for maximum damping characteristics and measured at 180-220 Hertz at a peak stress of 2000 psi. The dynamical Youngs Modulus varied from 12.5 Million psi at 100°C to 15.5 Million psi at -60°C.
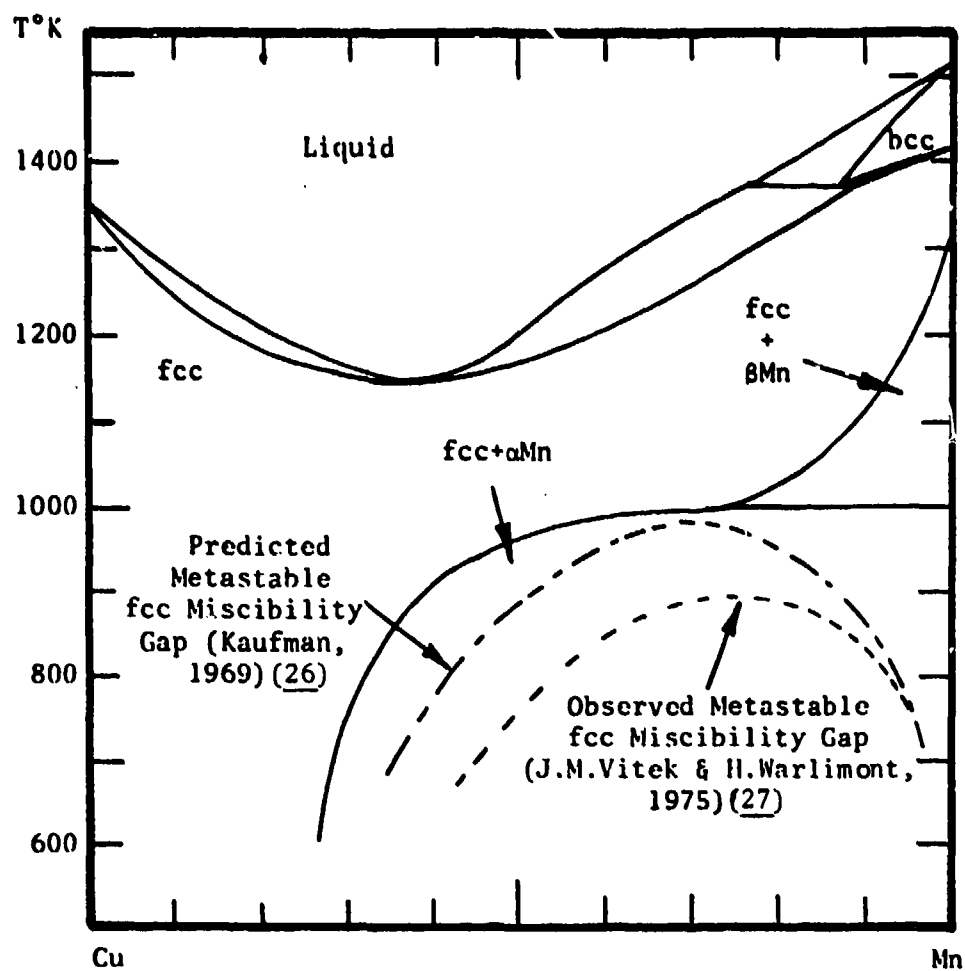
Figure 83. Predicted (26) and Observed (27) Metastable Miscibility Gaps in the Cu-Mn System.

Unfortunately, the additions of nickel did not permit retention of the high damping properties. Table 3 shows the results which have been obtained. This compilation shows results of alloy synthesis, damping, and tensile test of eight alloys based on the Co-Fe composition with substantial additions of nickel or small additions of manganese or aluminum. These results were employed in construction of the bar graph shown in Figure 1.

The results obtained thus far indicate that the additions of nickel do not offer any substantial improvement in strength. However, very substantial increases in strength have been attained with aluminum and manganese. These improvements have been accompanied by a decrease in damping capacity. Nevertheless, it is interesting to note that sample number 102 (76 w/o Co-19 w/o Fe-5 w/o Mn) exhibited twice the damping capacity of NIVCO at a comparable strength level (see Figure 1) while sample 99 (76 w/o Co-19 w/o Fe-5 w/o Al) exhibited a yield strength of 182,000 psi versus 110,000 psi for NIVCO at the same level of damping capacity which NIVCO exhibits (6).

Table 4 further summarizes the results of damping and mechanical property measurements conducted on cobalt-iron and cobalt-iron base alloys to which additions of manganese, chromium and aluminum have been made. In each case, evaluation of the damping and yield strength have been made on samples which were cold worked by rolling (to 10% reduction in thickness) as well as on companion samples annealed at 1000°C and air cooled.

The results obtained with sample composition 111 and 112 indicate a very abrupt change in behavior when the aluminum content is increased from 2.5 w/o (i.e., samples 97 and 98 in Table 3) to 3 w/o (i.e., samples 111 and 112 in Table 4). As was noted previously (6) aluminum additions result in subtantial increases in the tensile strength of the cobalt-iron which are accompanied by similar decreases in the loss factor. The compositions corresponding to 111 and 112 represented an attempt

TABLE 3

SUMMARY OF 0.2 PERCENT OFFSET YIELD STRENGTH AND

RESONANT DWELL DAMPING MEASUREMENTS AT 25° (Peak Stress 2000 PSI)

(ALL SAMPLES WERE MACHINED THEN ANNEALED

AT 1000°C AND AIR COOLED)

Sample No. Composition	Resonant Frequency	Dynamical Youngs Modulus	Loss Factor	0.2 Percent Offset Yield Strength
(weight percent)	(Hz.)	(PSI x 10^{-6})		(PSI)
85-(60Co-28Fe-12Ni)	243	24.0	0.0026	23100
86-(60Co-28Fe-12Ni)	246	24.6	0.0056	32400*
87-(50Co-32Fe-18Ni)	243	24.0	0.0026	30000
88-(40Co-38Fe-22Ni)	225	20.6	0.0016	29800
94-(72Co-18Fe-10Mn)	264	28.3	0.0011	53700
95-(72Co-18Fe-10Mn)	275	30.7	0.0008	87700*
97-(78.5Co-19Fe-2.5Aℓ)	255	26.4	0.0015	25000
98-(78.5Co-19Fe-2.5Aℓ)	240	23.4	0.0029	29900*
99-(76Co-18Fe-6Al)	273	30.3	0.0013	182000
100-(76Co-18Fe-6Al)	268	29.2	0.0011	157000*
101-(76Co-19Fe-5Mn)	262	27.9	0.0010	83800
102-(76Co-19Fe-5Mn)	264	28.3	0.0027	105700*
103-(77Co-19Fe-4Al)	271	30.1	0.0015	145000
104-(77Co-19Fe-4Al)	269	29.4	0.0011	152000*

*Cold Worked

TABLE 4

SUMMARY OF 0.2 PERCENT OFFSET YIELD STRENGTH AND

RESONANT DWELL DAMPING MEASUREMENTS AT 25°C (Peak Stress 2000 PSI)

(SAMPLES WERE MACHINED IN THE COLD WORKED CONDITION AND TESTED

DIRECTLY OR ANNEALED AT 800°C or 1000°C (AN800, AN1000) AND AIR COOLED

BEFORE TESTING)

Sample No. Composition (weight percent)	Condition	Resonant Frequency (Hz.)	Dynamical Young's Modulus (PSI x 10⁻⁶)	Loss Factor	0.2 Percent Offset Yield Strength (PSI)
106A-(78Co-20Fe-2Mn)	AN1000	248	24.2	0.0400	18000
106B-(78Co-20Fe-2Mn)	CW	250	24.3	0.0020	45000
107 -(72Co-18Fe-10Cr)	AN1000	238	23.8	0.0078	20000
108 -(72Co-18Fe-10Cr)	CW	237	23.8	0.0040	26000
109 -(80Co-20Fe)	AN1000	243	24.0	0.0040	17400
110 -(80Co-20Fe)	CW	249	24.3	0.0090	25000
111 -(77Co-19Fe-3Aℓ)	AN1000	267	27.9	0.0009	78000
112 -(77Co-19Fe-3Aℓ)	CW	270	28.5	0.0008	113000
113 -(77.2Co-19.2Fe-3.6Mn)	AN1000	247	24.2	0.0270	18000
114 -(77.2Co-19.2Fe-3.6Mn)	CW	247	24.2	0.0042	24800
115 -(76.4Co-19.2Fe-4.4Mn)	AN1000	254	26.2	0.0009	67000
116 -(76.4Co-19.2Fe-4.4Mn)	CW	255	26.3	0.0008	106000

to effect an increase in strength without experiencing a decrease in damping by operating at a composition close to that of samples 97 and 98. Unfortunately however, the desired increase in strength (to 78,000 psi) in the annealed condition was accompanied by a drop in damping.

Although the studies of aluminum additions have been disappointing in the sense that an alloy combining high damping and high strength has not been identified, the observation that small additions of aluminum result in substantial strength and corresponding increases in hardness (Rockwell "B" 30 for 0 w/o Al to Rockwell "C" 44 for 4 w/o Al) in the annealed condition may be of practical value. In particular, in the event an application demanding high damping and high hardness should present itself, it might be possible to "aluminize" an 80 Co-20 Fe alloy and obtain a wear resistant surface on a component with a high loss factor.

The results obtained with additions of chromium to the base cobalt-iron composition as disclosed by sample composition 107 and 108 suggest modest increases in strength accompanied by substantial decreases in loss factor. Accordingly, no further studies of chromium additions were made.

On the basis of the considerations presented above, additions of manganese seem to provide an avenue for increasing the strength of the cobalt-iron alloys. Table 4 also includes manganese alloys. These results, which are shown graphically in Figure 84 suggest that a "trade-off" between strength and damping can be optimized at about 4 w/o Mn.
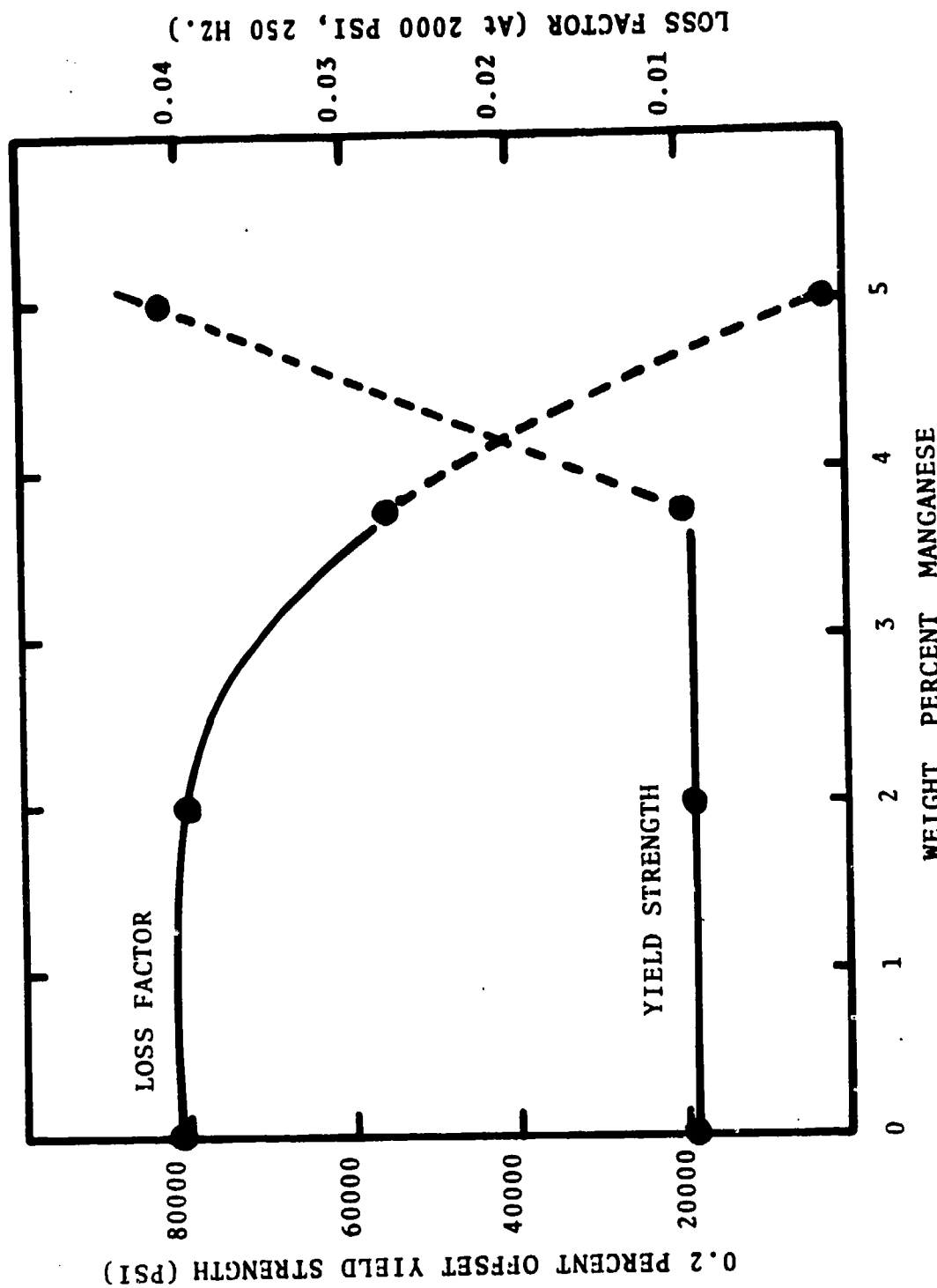
Figure 84. Loss Factor and 0.2 Percent Offset Yield Strength vs Manganese Content for a series of Cobalt-Iron-Manganese Alloys.

V.   INVESTIGATION OF IRON - CHROMIUM ALLOYS FOR APPLICATION AS HIGH DAMPING STRUCTURAL MATERIALS

One of the main short comings of the cobalt - base alloys as potential structural materials with high damping capacity is the cost per pound. Since cobalt is currently in the $3 to $4 per pound range, the finished cost for wrought cobalt parts can be as high as $5 per pound even if large quantity use were projected. In order to evaluate the potentials offered by iron base alloys as damping materials for structural applications at a lower cost per pound (i.e., $0.50/lb.) several iron - chromium base alloys have been examined.

This work was stimulated by the reports distributed by Toshiba Electric Co. (29) on a proprietary Fe-Cr-Aℓ alloy and the existence of a ·miscibility gap in the Fe - Cr system shown in Figure 85 just as there is in the Cu - Mn case shown in Figure 83. Although the mechanism responsible for the damping in Fe - Cr - Aℓ has not been established, the misicibility gap in both systems is a common feature.

Accordingly, samples of Fe - Cr - Aℓ alloys and Fe - Cr - C alloys corresponding to several commercial steels were prepared and tested. The results are summarized for Samples 117-125 shown in Table 5, and Figures 86 and 87. It was found that the optimum temperature for heat treatment was 800°C (1073°K). Heat treatment at higher temperatures (i.e., above 1000°C) (1273°K) within the gamma loop lead to low damping. This may be related to the transformation structure in the resulting bcc phase following the fcc→bcc transition on cooling. Heat treatment at 600°C (873°K) did not yield results which were as satisfactory as those obtained at 800°C.

Reference to Table 5 shows that attractive damping capacity and yield strength characteristics can be obtained in the 85 w/o Fe - 12 w/o Cr - 3 w/o Aℓ alloy as well as the 86 w/o Fe - 14 w/o Cr - 0.05 w/o C alloy. The latter corresponds in

-123-
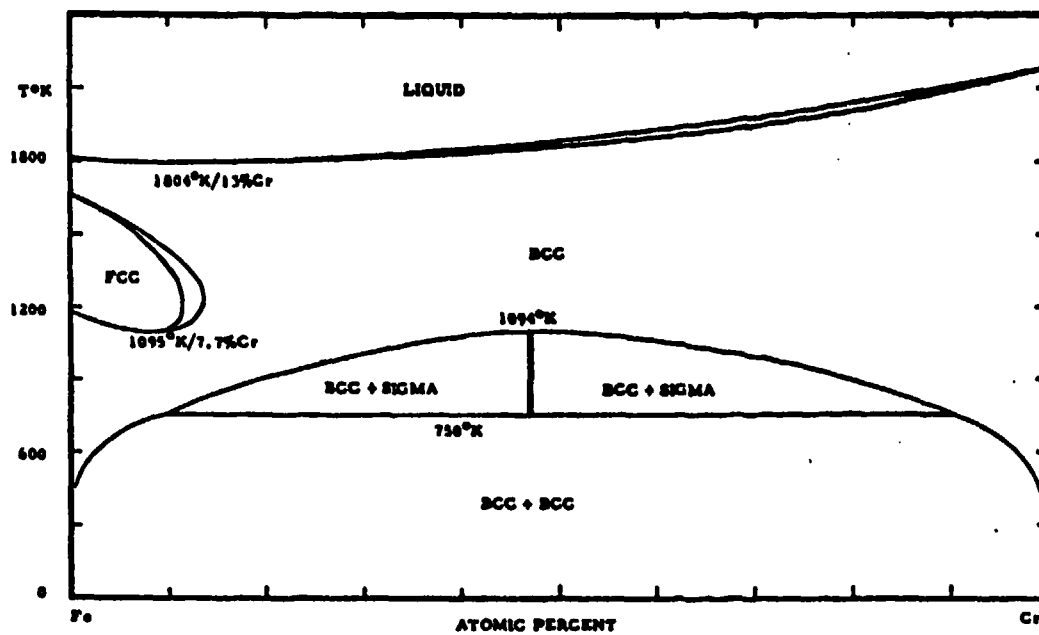
Figure 85. Iron-Chromium Phase Diagram.

TABLE 5

SUMMARY OF 0.2 PERCENT OFFSET YIELD STRENGTH AND

RESONANT DWELL DAMPING MEASUREMENTS AT 25°C (Peak Stress 2000 PSI)

(SAMPLES WERE MACHINED IN THE COLD WORKED CONDITION AND TESTED

DIRECTL.. OR ANNEALED AT 800°C OR 1000°C (AN800, AN1000) AND AIR COOLED

BEFORE TESTING)

Sample No. Composition (weight percent)	Condition	Resonant Frequency (Hz.)	Dynamical Young's Modulus (PSI x 10^{-6})	Loss Factor	0.2 Percent Offset Yield Strength (PSI)
117-(85Fe-12Cr-3Aℓ)	AN800	258	26.5	0.0360	37900
118-(85Fe-12Cr-3Aℓ)	CW	260	26.6	0.0030	42000
119-(85Fe-12Cr-3Aℓ)	AN600	256	26.4	0.0030	32500
120-(85Fe-12Cr-3Aℓ)	CW	257	26.5	0.0030	39000
121-(88Fe-12Cr-0.12C)	AN800	290	31.8	0.0028	40000
122-(88Fe-12Cr-0.12C)	CW	292	32.2	0.0010	49000
123-(88Fe-12Cr-0.08C)	AN800	288	31.3	0.0042	54000
124-(88Fe-12Cr-0.08C)	CW	290	31.8	0.0015	84000
125-(86Fe-14Cr-0.05C)	AN800	292	32.2	0.0180	42000
126-(86Fe-14Cr-0.05C)	CW	303	34.3	0.0008	49000
TESTED AT A PEAK STRESS OF 500 PSI					
109-(80Co-20Fe)	AN1000	250	24.3	0.0202	17400
TESTED IN A MAGNETIC FIELD UNDER CONDITIONS OF SATURATION					
109-(80Co-20Fe)	AN1000	243	24.0	0.0170	17400
117-(85Fe-12Cr-3Aℓ)	AN800	258	26.5	0.0230	37900
125-(87Fe-13Cr)	AN800	294	32.6	0.0065	42000
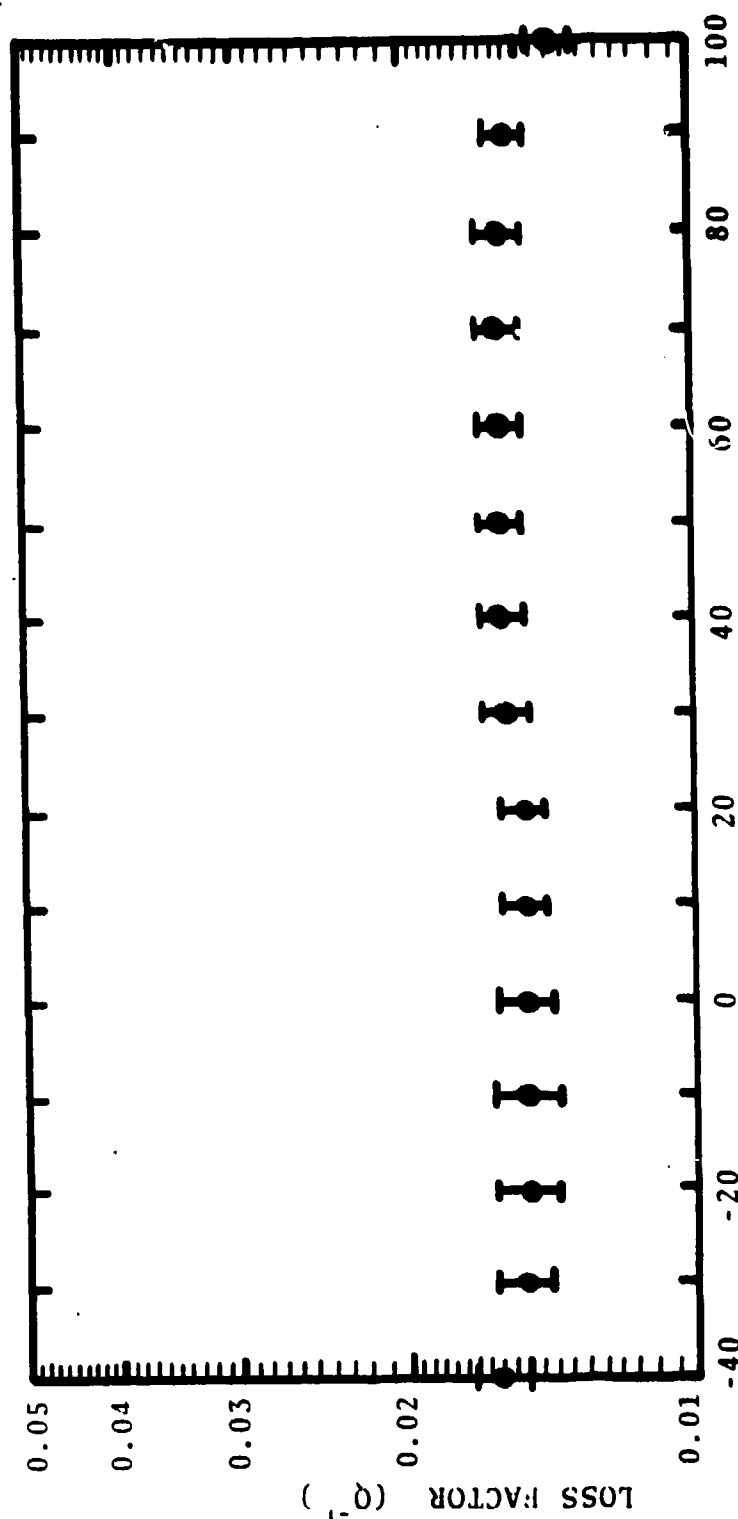
Figure 86. Loss Factor vs. Temperature Curve for a Sample of 85 w/o Fe - 14 w/o Cr - 0.05 w/o C Measured at 290 - 300 Hertz and a Stress of 2000 psi.
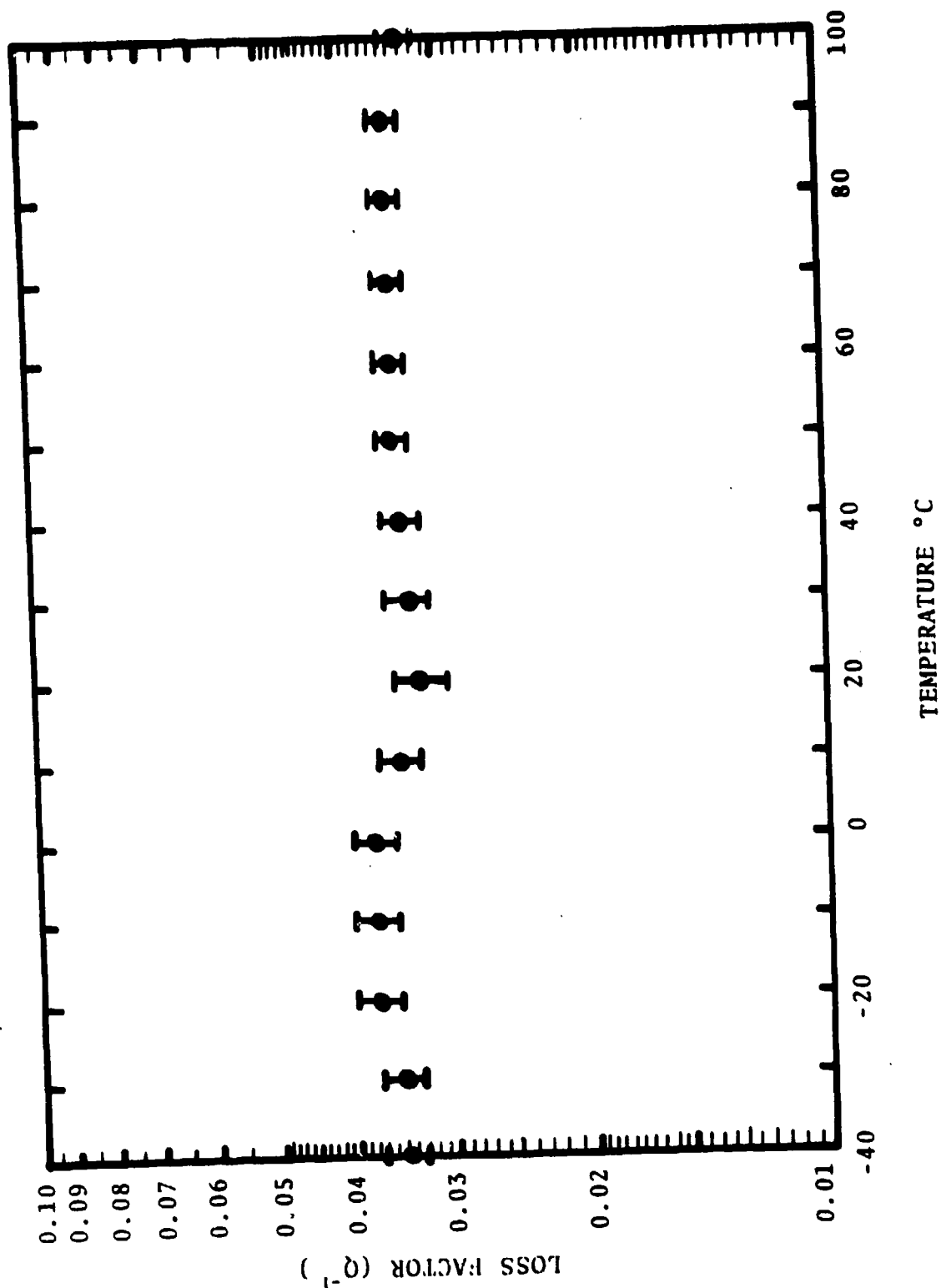
Figure 87. Loss Factor vs. Temperature Curve for a Sample of
85 w/o Fe - 12 w/o Cr - 3 w/o Aℓ measured at 250-260
Hertz and a Stress of 2000 psi.

in composition to type 405 stainless steel (i.e., samples 125, 126). Samples 121, 122, 123 and 124 correspond to types 410 and 403 stainless steel respectively. The results indicate that combinations of 4000 psi yield strength, loss factors of 0.02 - 0.04, good corrosion resistance and a cost per pound of $0.50 - $0.80/lb., can readily be attained in alloys of the iron - chromium system. However, optimization of properties will undoubtedly depend on third alloying element additions as well as heat treatment as indicated by Table 5.

Figures 86 and 87 indicate that the damping is insensitive to changes in temperature up to 100 °C. These results were obtained on samples 125 and 111 which are shown in Figures 86 and 87 respectively. The results of similar studies at Toshiba Electric suggests that the loss factor is insensitive to temperature up to 300°C. Table 5 also contains some results on the 80 w/o Co - 20 W/o Fe alloy at a lower stress (500 psi) as well as the 80 w/o - 20 w/o Fe and the iron - chromium alloys in a saturating field.

The former result at 500 psi indicates a loss factor of about 2% for the Co - Fe alloys as compared with a loss factor of 4% for this alloy at 2000 psi. This is in keeping with the general finding that the loss factor is proportional to stress to the one half power.

Measurement of the loss factor at 2000 psi in a saturating magnetic field indicated at 15% decrease in loss factors of the cobalt-iron alloy and the iron-chromium base alloy. These results indicate that only some of the damping behavior is due to magnetic domain walls. Nevertheless, the measured values of the loss factors in a saturating field remained high enough to indicate that other mechanisms may be contributing to the damping behavior in these alloys.

-128-

VI. CONSIDERATION OF POTENTIAL APPLICATIONS AND TESTING OF HIGH DAMPING ALLOYS

A survey of potential applications of high damping alloys to problems of noise and vibration control was conducted in order to examine problem areas in military and civilian systems which could benefit from advances in damping materials technology. Tables 6A and 6B list some of the results of this survey. In this listing, general and specific items are noted. Each entry is also accompanied by material properties which are required in addition to damping. For the cases listed in Tables 6A and 6B, high damping characteristics would be a desirable feature since add-on noise or vibration treatments are inappropriate or too expensive.

On the basis of this survey, it appears that three potential applications merit particular consideration. These are ship or torpedo propellers, body panels of military reconnaissence vehicles, engine oil pans and valve covers. In each case, improvement in the damping properties may be expected to lead to significant reductions of radiated noise and hence, in acoustic detectibility and/or tolerance. Subsequent parts of this section summarize the results of tests that have been conducted on hardware fabricated from high damping iron-chromium-aluminum and cobalt-iron alloys to demonstrate the efficacy of such alloys in reducing the noise levels in military reconnaissence vehicles and torpedo blades.

Although the tests reported here are certainly of a preliminary nature and could benefit by further refinement and extension, they show clearly the advantages offered by high damping alloys.

1. High Damping Alloys for Armoured Personnel Carriers

Recent measurements performed by Bolt, Beranek and Newman Inc., under contract No. DAAE07-74-C-0002 on a 1/6 scale dynamic model of an M-113 armoured personnel carrier (APC) indicated that the exterior and interior noise of an APC depends significantly on the damping of the APC hull. The 1/6 scale dynamic model M-113 vehicle, which is shown in Figures 88(a)-(e) has been instrumented

TABLE 6A

POTENTIAL APPLICATIONS OF HIGH DAMPING ALLOYS IN NOISE CONTROL

ITEM	APPLICATION	PRIMARY PROPERTIES
Propellers	Military Ship Propulsion	Corrosion Resistance Surface Fatigue Strength
Gears	Ship & Helicopter Power Train	Fatigue Strength Stiffness
Hull Plating and Engine Oil Pans and Valve Covers	Military Reconnaissance Vehicles	Formability
Mufflers and Ducts	Air Compressors	Fatigue Strength
Damped Springs & Suspensions	Land Vehicles	Fatigue Strength
Perforated Plates for Test Cells	Engine Test Cells	High Temperature
Cams and Cam Followers Relays & Ratchets	Machinery & Control Systems	Fatigue Strength Stiffness
Machinery Stops	Production Machines Automatic Weapons	Fatigue Strength Stiffness
Saw Blades	Fabrication Machinery	Fatigue Strength Abrasions Resistance
Impact Bits	Jack Hammers	Abrasions Resistance Fatigue
Grinders & Pelletizers	Material Preprocessing (e.g. plastics)	Abrasions Resistance
Wheel Squeal	Rail Vehicle Wheels and Retarders	Abrasion Resistance
Material Transfer & Handling	Food & Chemical Processing	abrasion Resistance Resistance to Chemicals Formability

TABLE 6B

POTENTIAL APPLICATIONS OF HIGH DAMPING ALLOYS IN VIBRATION AND FATIGUE CONTROL

ITEM	APPLICATION	PRIMARY PROPERTIES
VIBRATION CONTROL		
Engine Crank Shafts	Piston Engines	Fatigue
Electronic Chasses	Vehicle-Borne Electronics	Fatigue
Machine Tool Holders	Production Machinery	Strength
Machinery Stops	Production Machinery Automatic Weapons	Stiffness Fatigue Strength
Cam & Cam Followers, Rely & Ratchet Devices	Machinery & Control System (e.g., high speed printers)	Fatigue Strength Stiffness
FATIGUE CONTROL		
Turbine Blades	Turbo Machinery	High Temperature Strength Low Density
Aircraft Components	Surface Structures and Equipment Near Engines and Armaments	Fatigue Strength
Light Bulb Filaments	Bulbs for all Vehicles	Luminescence Electrical Resistance High Temperature Fatigue Strength
Nuclear Reactor Components	Gas Cooled Reactors	Compatibility with Reactor Environment
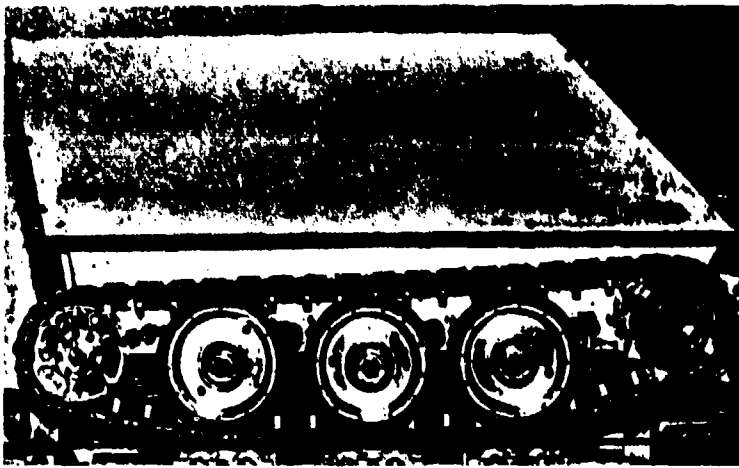
Figure 88a. Side View of 1/6 Scale Model of Armoured Personnel Carrier (Courtesy of Bolt, Beranek, Newman Contract DAAE07-74-C-0022).
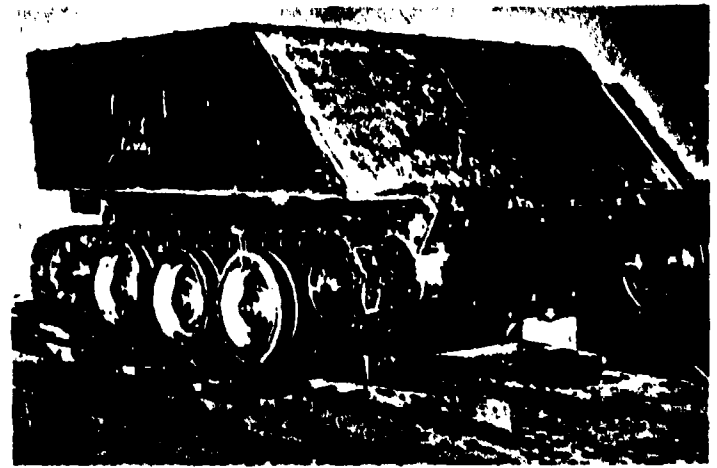
Figure 88b. Front View of 1/6 Scale Dynamic Model.
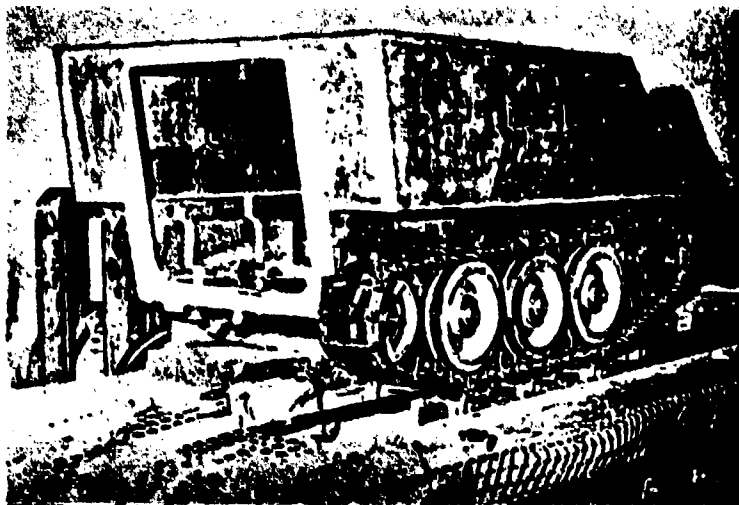
Figure 88c. Rear View of 1/6 Scale Dynamic Model of Armoured Personnel Carrier (Courtesy of Bolt, Beranek, Newman Contract DAAE07-74-C-002).
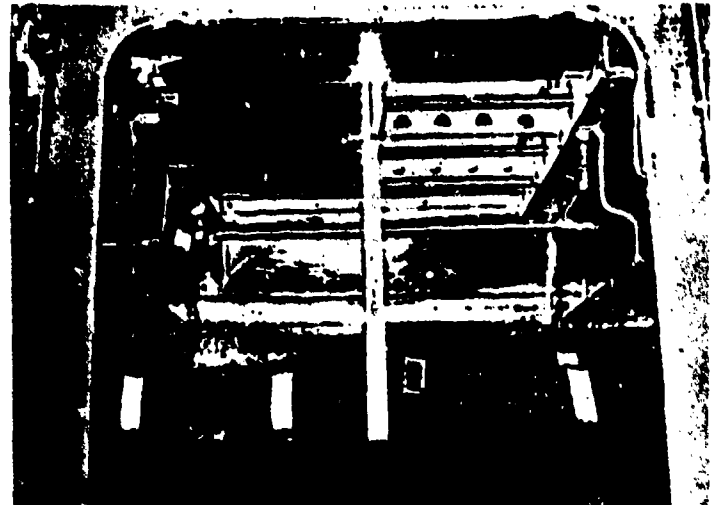
Figure 88d. Close-up of 1/6 Scale Model Rear View.
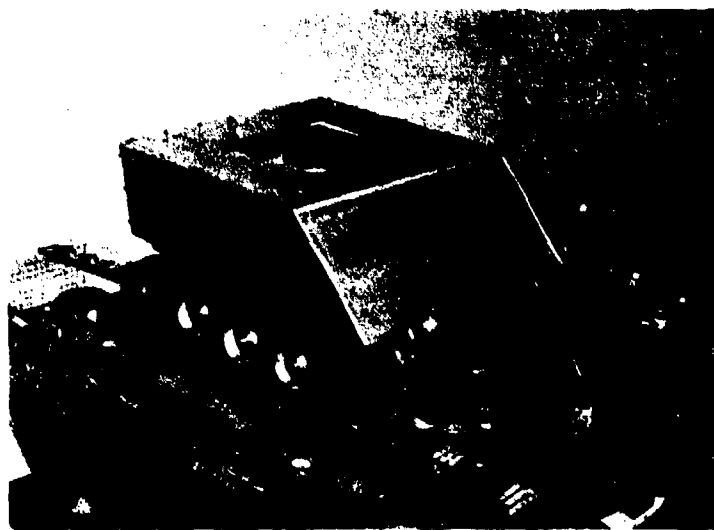
Figure 88e. Aluminum Scale Model M-113 Vehicle, Front Vi On Motor Driven Steel Belt Running Surface.
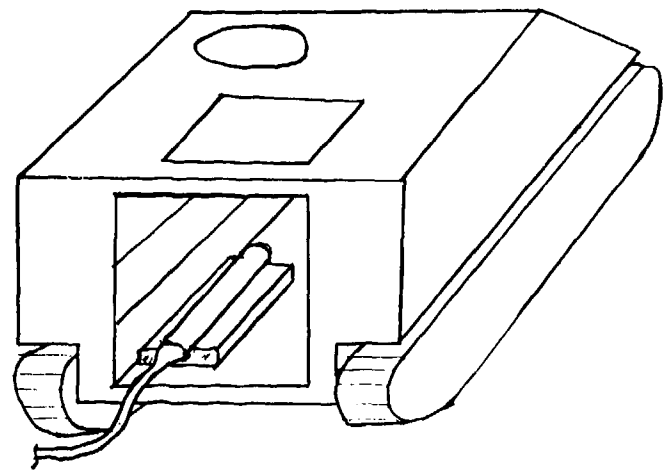
Figure 88f. Iron-Chromium-Aluminum Alloy M-113 Vehicle, Aft View, With "Soft Mounted" Microphone.

-131-

in order to provide detailed measurements of interior and exterior radiated noise (30). Figure 88f shows the location of a soft mounted microphone in the M-113 vehicle. In order to evaluate the effect of material damping characteristics on the noise levels generated in the APC scale model, a hull was constructed of the iron-15 chromium-3 aluminum alloy described in Section V for comparison with a standard hull made of aluminum plate. The dimensions of the hulls were identical. The loss factor of the iron-chromium-aluminum alloy which was measured as 0.036 (see Table 5) was 36 times larger than the aluminum alloy. Testing was conducted on an electric motor driven device which uses an endless, moving steel belt to simulate the terrain going along under a single track. The models are one-sixth size in all dimensions and deflections and model speeds are identical with full size vehicle speeds (30). The tests were conducted on 10-12 November 1976 by Tom Norris (Consultants in Accoustics) and witnessed by Peter Rentz (Bolt, Beranek and Newman) and Dr. Richard J. Weiss (AMMRC).

The one sixth scale model personnel carrier was run at speeds of 6,20,30 and 50 miles per hour (Model and full scale linear track speeds are identical). Track tension was adjusted so that the track just cleared the roadwheels--this is a lower than ususal setting, but it lessened the chance of a breakdown. The slightly lowered tension has little effect on noise. The downward force on the roadwheels was set to 5 lbs.; higher forces would require that the hull be firmly mounted and anchored. Based on experience, such a mounting would provide considerable damping that would cover up the effects that we hoped to observe. For similar reasons, and to assure that the interior acoustic buildup (reverberation) was identical for both hulls, all hatches were re ved (driver hatch, cargo hatch, and rear personnel hatch). For these reasons, the treadplates were also removed. Track speed was indicated by an optical tachometer operating directly off of the sprocket shaft. After the aluminum hull test, the suspenion was removed and then

attached to the alloy hull. The microphone was shock mounted with 2 inches of soft, closed cell neoprene foam, which was taped to the floor beams. This positioned the microphone facing forward and 2-1/2 inches above treadplate level (the treadplate was not present).

The acoustic test apparatus consisted of; B & K 4220 pistonphone, B & K 4133 1/2 inch microphone, B & K 1/2 to 1 inch adaptor, B & K AO 0033 3 meter extension cable, B & K 2203 Sound Level Meter, Nagra III magnetic tape recorder, Ampex 641 "Professional" tape, B & K 1613 Octave Band Filter Set, and B & K 2305 Graphic Level Recorder. Recordings were made during sweeps from 6 to 20, 6 to 30, and 6 to 50 miles per hour. The duration at top speed in each case was approximately 5 seconds or more. In addition, hammer blows were recorded with the microphone inside and outside the hull for reverberation time measurements. All tape recordings were made at 15 inches per second. Steady speed noise data reductions were made by playing the tape back through the Sound Level Meter and 1613 Octave Filter Set and into the Graphic Level Recorder. The sound levels shown in Figures 89(a)-89 (d) were read from these paper tapes of the noise time histories. The reverberation times (T_{60}) were determined by playing the magnetic tape backwards at 1/4 of recorded speed, and by setting the graphic level recorder writing speed to 1000 mm per second. This technique was judged to have a sufficiently rapid response for even the shortest RT measured, which was 0.04 seconds. Comparative octave band internal sound levels for vehicle speeds of 6, 20, 30 and 50 miles per hour are shown in Figures 89(a)-(d). These figures also show calculated A-weighted sound levels for the full sized vehicle. This is considered an important parameter for comparison. The results show a steady improvement in dB(A) with increasing speed plus a corresponding reduction in the levels at the peak vibration frequency, 1000Hz, (167Hz full scale). The maximum reductions were realized at 50 mph with 6dB(A) and 10dB at 1000Hz.

-133-
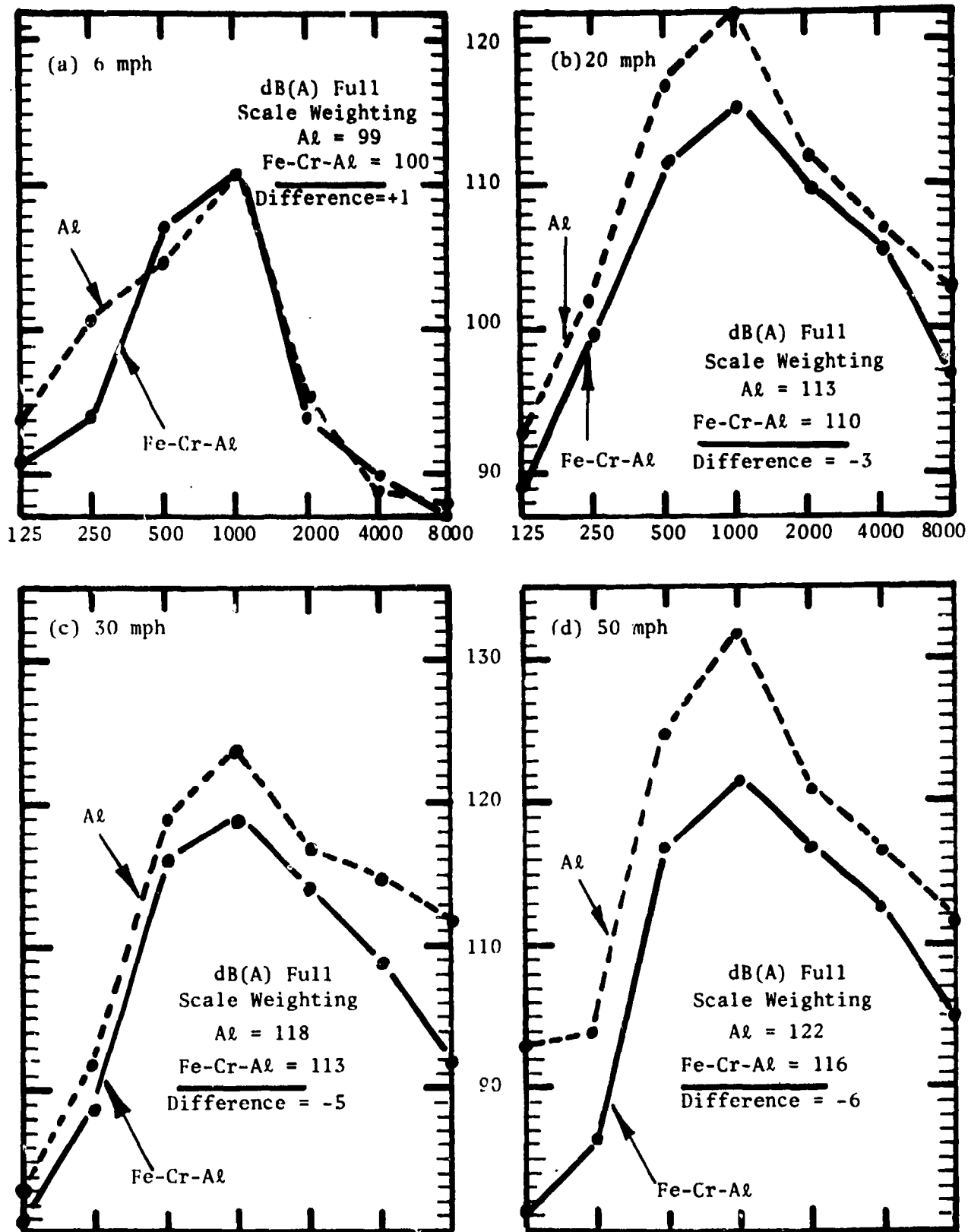
OCTAVE BAND CENTER FREQUENCIES IN HERTZ (cps)

Figure 89. Interior Sound Levels, Aluminum (Aℓ) and Iron-Chromium-Aluminum (Fe-Cr-Aℓ) Alloy One-Sixth Model M-113 Vehicles as a Function of Forward Speed.

-134-

The interior noise levels for the two models could be expected to differ because the iron-chromium-aluminum alloy has a loss factor (0.036) which is 36 times that of the aluminum alloy. On the other hand, the noise level reduction could be due entirely to the fact that the density of the iron alloy (and hence the mass of the iron model) is about 2.8 times that of the aluminum. The expectation for reduction of internal noise levels due to the increased mass depends on the characteristics of the vibratory source. If the track interaction with the sprocket, idler, and road wheels result in a constant force spectra being applied to the hull, the hull vibration and resulting interior sound pressure would decrease in proportion to mass, or approximately 9 dB. If, on the other hand, the input to the hull is constant velocity in nature, then hull vibration and resulting interior noise would be unchanged. Since the measured noise levels are essentially identical at 6 mph, Figure 89a, it is concluded that the input is constant velocity in nature. Physical justification for this conclusion is beyond the scope of this study. The suspension members would have to have a higher mechanical impedance than the hull, and this is not obvious. Nevertheless, the constant velocity conclusion will be used, but with caution. The interior noise level would be expected to be reduced with increased internal damping. The amount of the decrease depends on the ratio of total damping, before and after. (This assumes that the radiated noise is due to resonant motion of the plates, which is probably not true for the plates near the suspension attach points). For the aluminum hull, the damping is provided mainly by the attached track, not the internal friction of the materials. Therefore, the sound pressure level decrease would be less than indicated by the ratio of material loss factors. Decay rate measurements of the noise following hammer blows did not show significant differences between the two models. However, the stress levels were not known, and the measurements are considered inconclusive. In order to separate the effects of mass and damping, it is necessary to look at the speed dependence.

Increased speed means increased stress levels and higher loss factor values in the iron-chromium-aluminum alloy. Therefore, since the measured noise reduction increases with speed, the improvement is attributed to the damping of the material.

2. High Damping Materials for Military Ship and Torpedo Propellers

The performance of cobalt-18^W/o iron torpedo propellers has been evaluated in the Bolt, Beranek, Newman Reverberant Tank by N. A. Brown and J. C. Colaruotolo in January 1977 as part of a program conducted for the Naval Underwater Systems Center, Newport Laboratory in Newport, Rhode Island 02840. Mr. T. Davis is the technical monitor for this work. The cobalt-iron alloy propeller was compared to a geometrically similar aluminum propeller by measuring the force-to underwater radiated noise transfer functions of both the aluminum and cobalt-iron propellers. Figure 90(a) shows a schematic for the energy flow associated with hydrodynamic exitations of a propeller of the type outlined axially in Figure 90(b). Two exitation mechanisms are shown in Figure 90(a), turbulence ingestion and vortex shedding, which generates continuous forces in the blades.

These forces, acting through the mechanical admittance of the propeller blades along their leading and trailing edges, excite vibration of the blades. The energy of this vibration is concentrated in frequency bands containing the resonances of the blades. Conservation of energy requires that the power input to the blades be dissipated in equal amounts.

This dissipation takes several forms; the undesirable one here, though not necessarily the largest, being acoustic radiation from the vibrating blades and the attached structure. Other dissipation mechanisms include hydrodynamic damping and internal structural or applied damping - treatment losses. It is, of course, the latter two which we are trying to increa e with the high loss material. For a fixed vibrational power input, any increase in structural damping losses will result in an equal decrease in acoustic radiation, other factors kept constant.
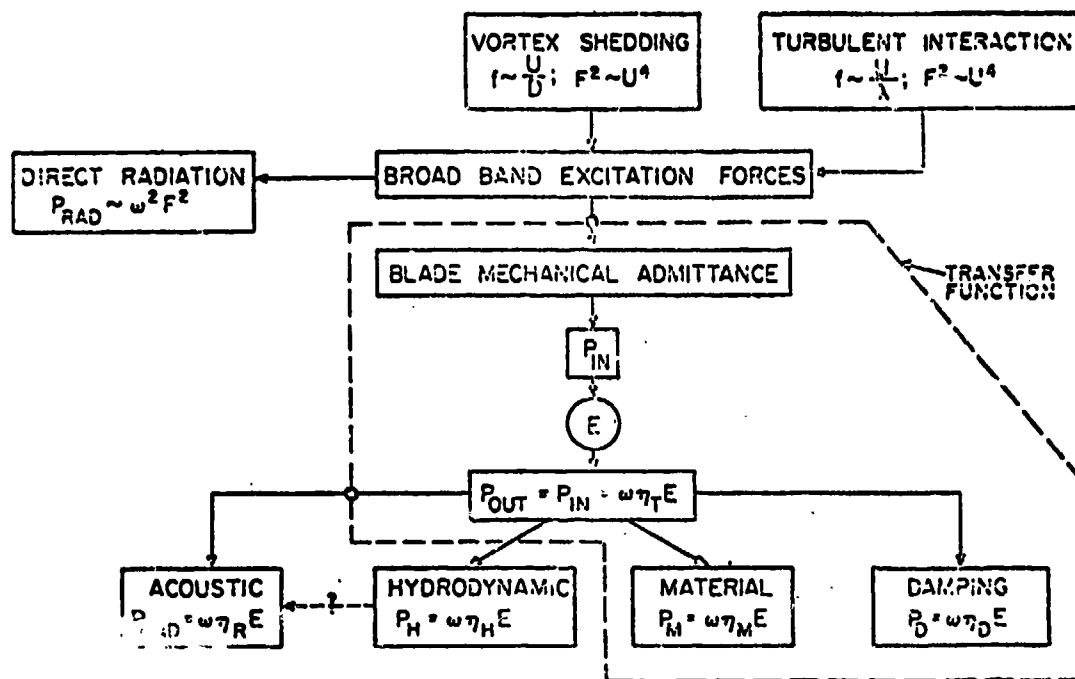
Figure 90a.   Schematic Power Flow for Blade Model Radiation.
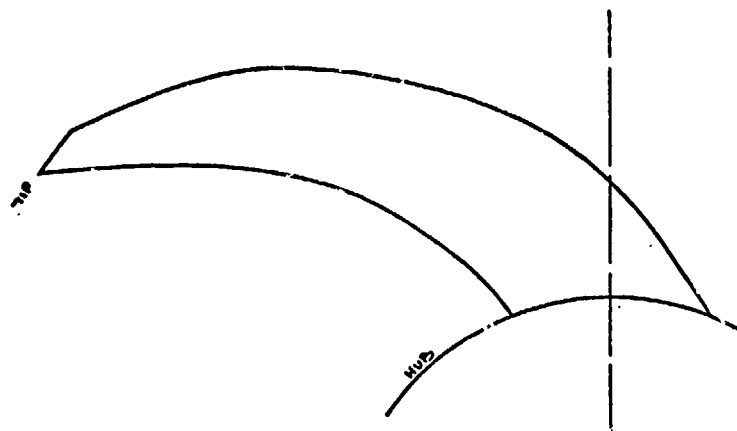
Figure 90b.   Axial View of Propeller Blade Outline.

-137-

It is neither practical nor necessary to measure or estimate all the various components shown in Figure 90(a). The overall transfer function between applied forces and the resulting radiation, shown by the dotted block in the schematic, can be rather simply measured. Any beneficial effects of damping will appear directly in this transfer function.

Actual measurment of the transfer functions need not require mechanical excitation of the blades, which is awkward. Rather, a reciprocal technique is used where the propeller is immersed in a diffuse sound field of known pressure and the resulting acceleration levels of the blades are measured. The ratio of acceleration-to-incident pressure is equal to that of radiated pressure-to-applied force. The latter ratio is the desired transfer function.

The baseline propeller has four blades with fairly high skew (blade sweepback in the peripheral directio..,. Blade sections are of airfoil shape. The diameter is 18 inches. The blades are made separately and are bolted securely to a cylindrical hub 7 inches in diameter and 3 inches long. An axial view of the outline of both blades is shown in Figure 90(b). Two views of the assembled propellers are shown in Figures 91(a) and 91(b).

An extra blade was machined of aluminum to serve as a pattern for the casting of the high damping alloy blades. When received, these alloy blades were found to be somewhat warped and very much thicker than desired; apparently shrinkage had been greatly over-compensated for.

The alloy blades were straightened in an arbor press to improve their fit to an existing check which had been molded to the face of the aluminum blade. Supported on this check, the backs of the alloy blade were machined to reduce their thickness on a tracer milling machine using the pattern for the orginal blades. The orignal aluminum blades were made entirely by this method. The alloy blades were cleaned up by hand filing and then returned to the supplier for a second heat treatment.

Neither time nor funds allowed a more careful rework of
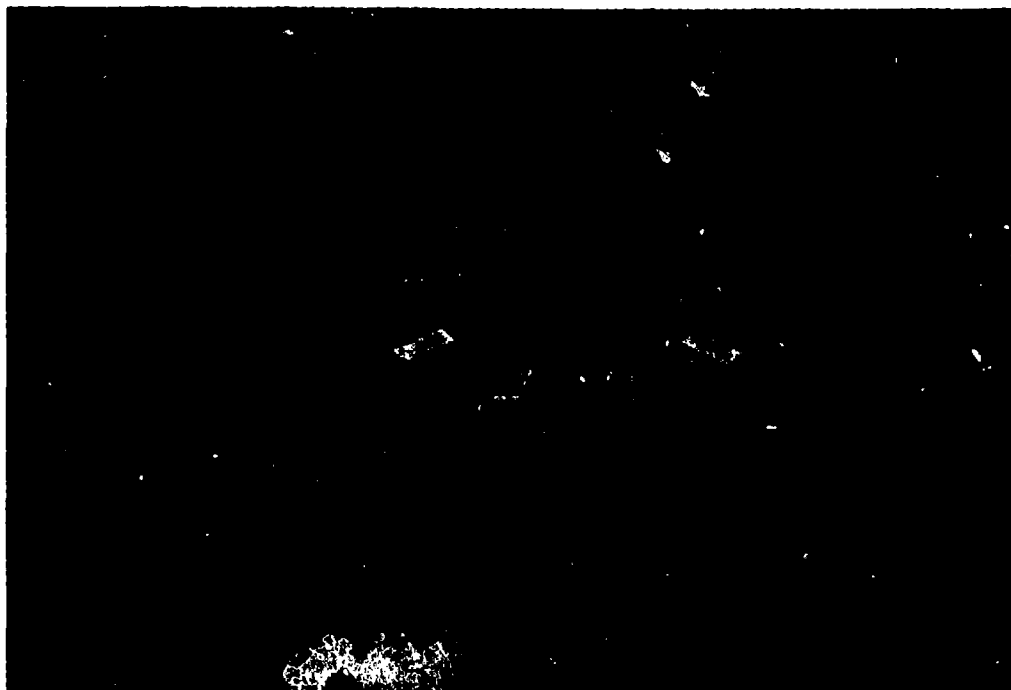
Figure 91a. Aluminum Propeller with Accelerometer and Pads.
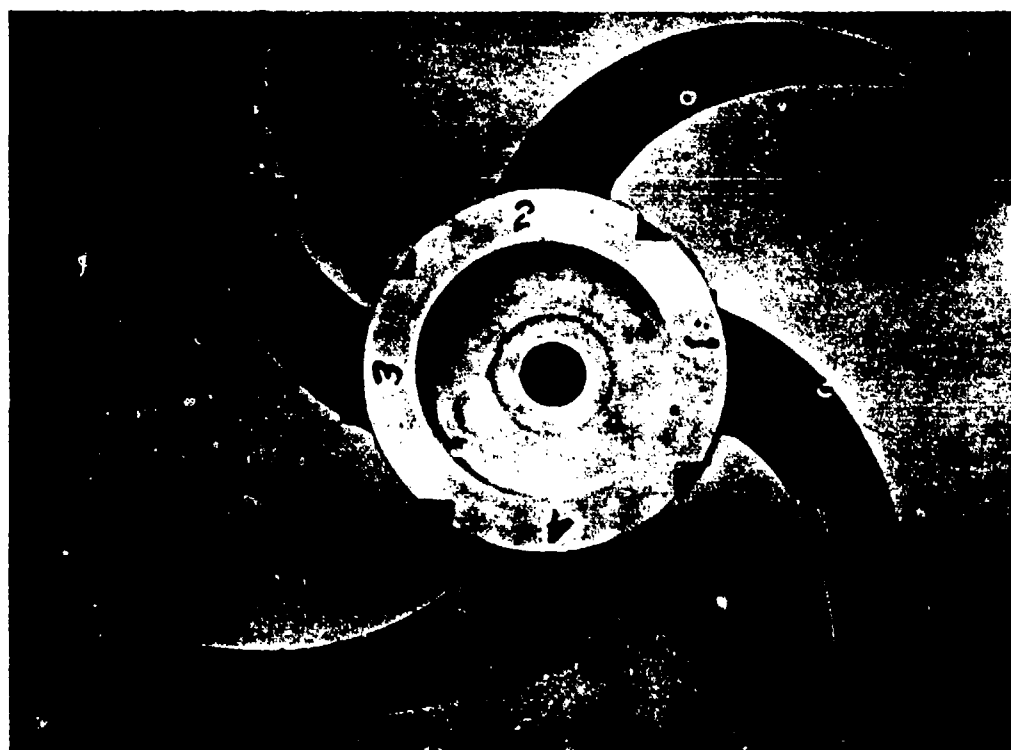
Figure 91b. Propeller with Accelerometer and Pads (Cobalt-Iron Alloy).

these blades than that described. As a result, their thickness
is still too great in comparison with the aluminum blades; see
Figure 92. Since the extra thickness results in both increased
bending stiffness and blade mass, it has some (unknown) affect
on the transfer functions; a factor which should be considered
in comparing the results.

The alloy blades were bolted to another aluminum hub
indentical to that of the aluminum propeller. The propeller
with high-damping alloy blades is shown in Figure 91(b). Discolor-
ation of the blades is a result of the heat treatment.

Each of the propellers was mounted on a heavy, highly
damped shaft, as shown in Figure 93. This provides an im edance
to the propeller hub similar to that of a torpedo hull. Each
propeller was immersed in the reverberant acoustic water tank
to a depth of about six feet. The BBN water tank facility is
shown in Figure 94. A diffuse sound field, broad band in
frequency, was generated in the tank and its position-average
pressure level measured. Acceleration levels in the direction
normal to the blade surfaces were measured at ten positions
over the blade radius. Sound pressures and accelerations were
spectally analyzed in one-third octave bands from 300 Hz to
20 kHz and transfer functions calculated.

A block diagram of the acceleration measurment system
is given in Figure 95. The system consists of an accelerometer,
an amplifier, a one-third octave band analyzer and a x-y plotter.
The accelerometer is a BBN Model 501 accelerometer which has been
sealed and treated for underwater use. The sensitivity is - 43
dBv/g, and the frequency response is flat (±0.5 dB) from 3 Hz to
20 kHz. The nominal mounted resonance of the accelerometer is
above 90 kHz. The system is calibrated.

The acoustic measurement system (Figure 96) consists of
three hydrophones, amplifiers, a multiplexer, a one-third octave
band analyzer and an x-y plotter. The hydrophones, (Model LC-10)
have a sensitivity of -110 dBv/µbar, and the frequency response
is essentially flat (±1 dB) from 10 Hz to 25 kHz. The hydrophones

-140-
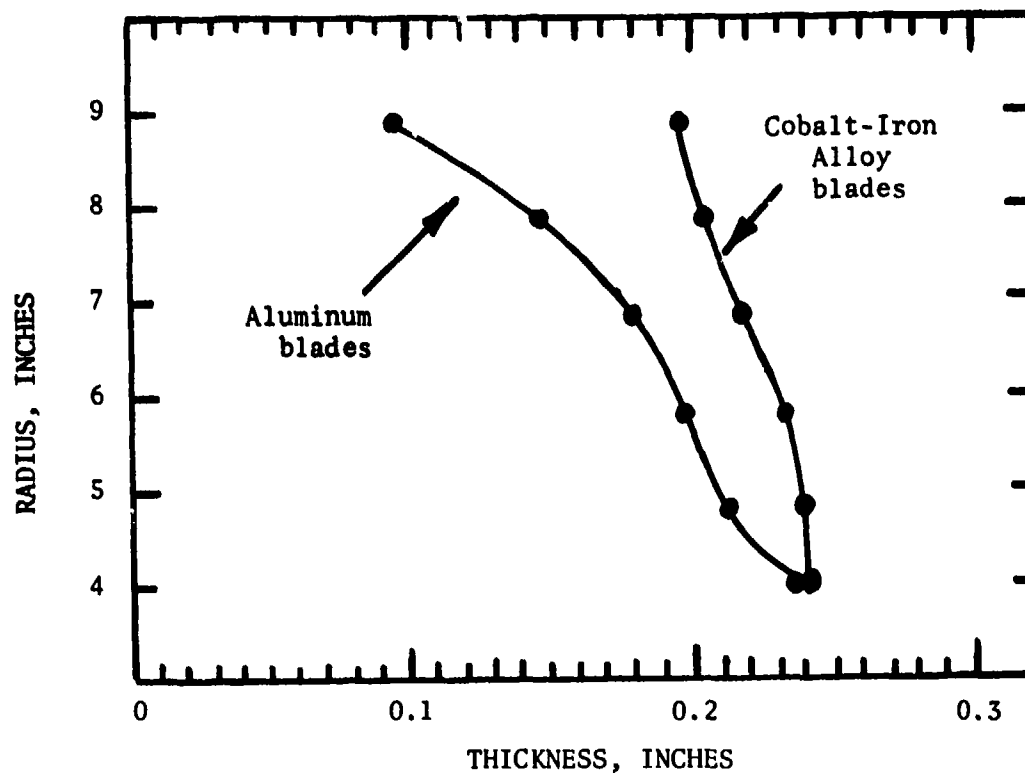
Figure 92. Thickness distributions of propeller blades.

Figure 93. Propeller mounted on heavy shaft, ready for acoustic tank.

-141-
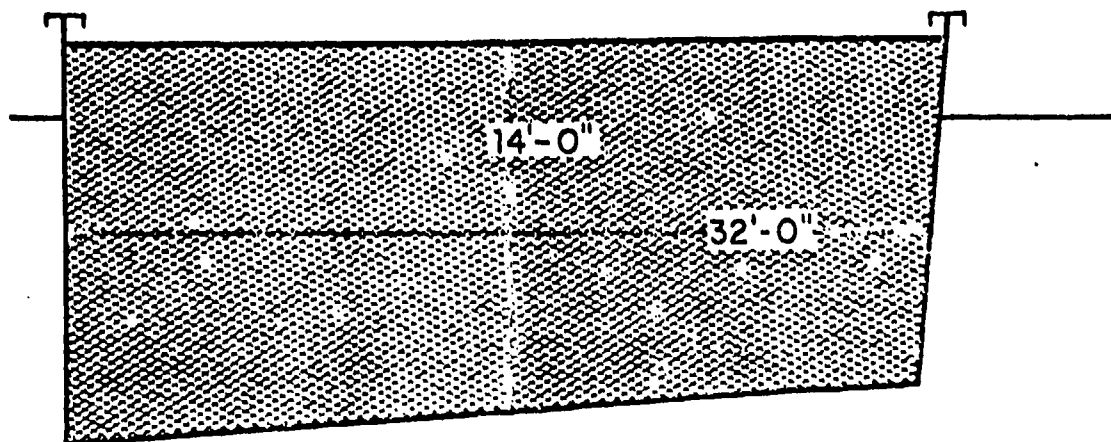
CENTERLINE DIMENSIONS	14'-0"x 23'-0"x 32'-0"
VOLUME	11,000 CU. FT.
LOWEST USEABLE 1/3 OCTAVE	320 Hz
ACOUSTIC LINING	PRESSURE RELEASE α = 0.05
CRANE CAPACITY	2 TONS
HOIST	20 FT

Figure 94

- BBN REVERBERANT-TANK CHARACTERISTICS
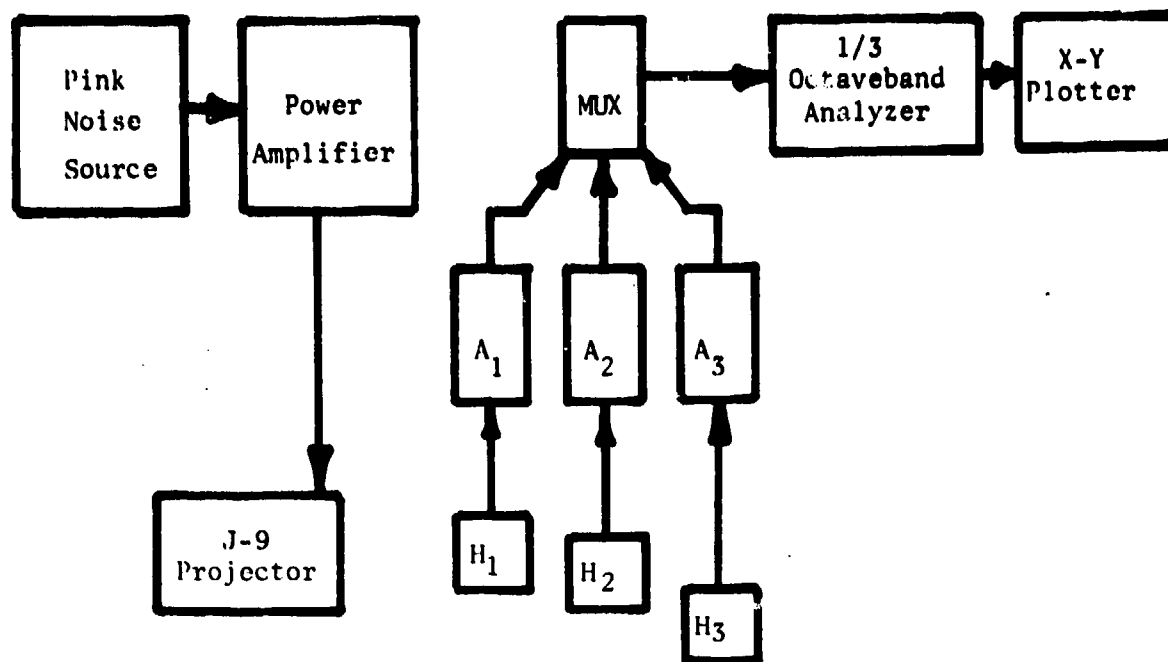
Figure 95.   Block Diagram of Sound Source and Multiplexed
             Hydrophones.
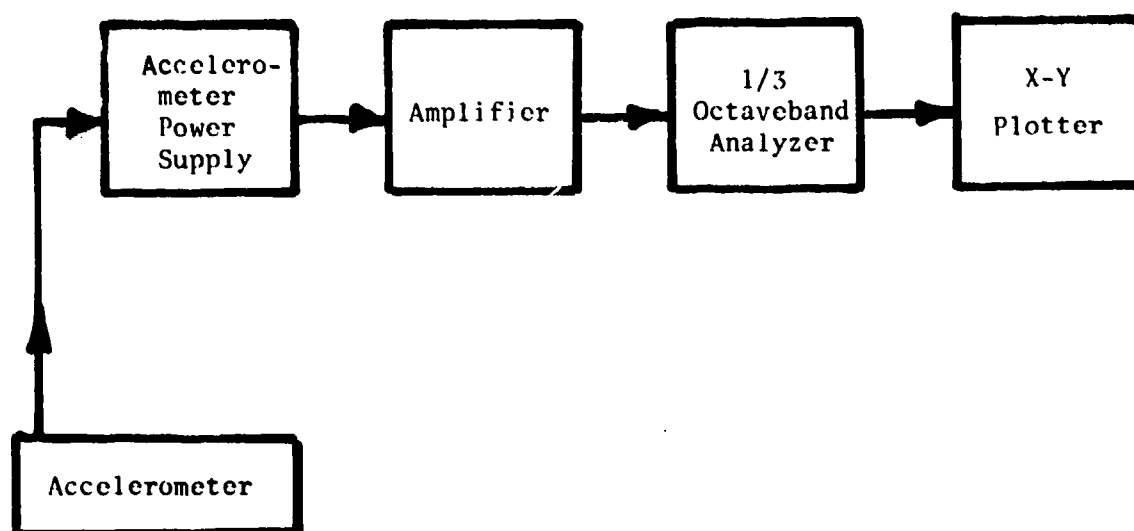
Figure 96.   Block Diagram of the Acceleration Measuring System.

signals are amplified and sequentially sampled by the multiplexer
at a rate of 15 samples per second. The sampled signals are
filtered with one-third octave band filters, detected with a
true RMS detector and averaged in the one-third octave band
analyzer. This analysis technique provides a measurement of
the spatial average of the sound field in the tank. The
system is calibrated, and the sound pressure level is plotted
in dB re 1 μbar in one-third octave bands. The transfer func-
tion is computed for each one-third octave band and each
accelerometer position as follows:

$$\text{TF, dB}//(\mu\text{bar} \times \text{yd.}/\text{lb.})^2 = adB - SPL + 111.6 \text{ dB,} \qquad (10)$$

where

adB = the measured one-third octave band acceleration
level in $dB//(1\ g)^2$, and

SPL = the measured position averaged sound pressure
level in $dB//(1\ \mu\text{bar})^2$

The transfer function is expressed in terms of source
level per pound of excitation force. The source level is the
standard form for representing the underwater radiated noise
output, namely, the sound pressure level which would be measured
at a distance of one yard from the source if it were reduced to
a point. For spherical spreading in a limitless ideal fluid, the
acoustic pressure - distance product is constant.

The constant on the right hand side of the equation is
a function only of the units involved.

Averaging of the transfer functions, or equivalently of
the accelerations for constant incident sound pressure, is done
as follows:

$$\overline{adB} = 10\ \log\left(\frac{\sum_{i=1}^{N} \log^{-1}\left(\frac{adB_i}{10}\right)}{N}\right) \qquad (11)$$

where $\overline{adB}$ is the average acceleration level in dB, adB_i is an
individual level, and N is the number of positions over which
the average is taken.

-144-

The use of an incoherent average such as this for the transfer functions is appropriate for estimating the radiated noise when the hydrodynamic forces applied to the blades are uncorrelated at the radial intervals used.

Average transfer functions of the aluminum and high damping alloy blades are shown and compared in Figures 97(a) and 97b for the leading edge (inner radii) and trailing edge (outer radii) measurement positions, respectively. Table 7 lists the radial positions of these measurement points.

With some typical force spectra, as measured for skewed propellers operating behind a torpedo, these transfer functions can be applied to yield underwater radiated noise levels. The leading edge average functions are applied to turbulence ingestion forces and the trailing edge functions to vortex shedding forces. The excitation force spectra are presumed independent of the propeller material. When this is done, and the two contributions are added together in each case, relative radiated noise spectra such as those of Figure 97(c) are produced. Finally, in Figure 97(d), the noise reduction due to the high damping alloy, as implied by the comparison of Figure 97(c) is shown.

The apparent noise reduction is quite substantial. Reductions of about 10 dB are common in the low and mid frequency bands, with selected bands showing considerably larger values. At the higher frequencies, the noise reduction is reduced, perhaps reflecting the presence of a relatively large value of acoustic radiation damping for both propellers.

Moreover, the noise reduction is significant in that the larger reductions apply in those frequency ranges where the propeller noise is greatest. The smaller improvements apply at the higher frequencies and the propeller radiated noise levels are already quite low; in fact they may be unimportant relative to other, non-propeller, sources of noise. The occasional frequency band which shows a negative noise reduction (an increase in noise) are not considered to be important. If Figure 97(c) is examined,
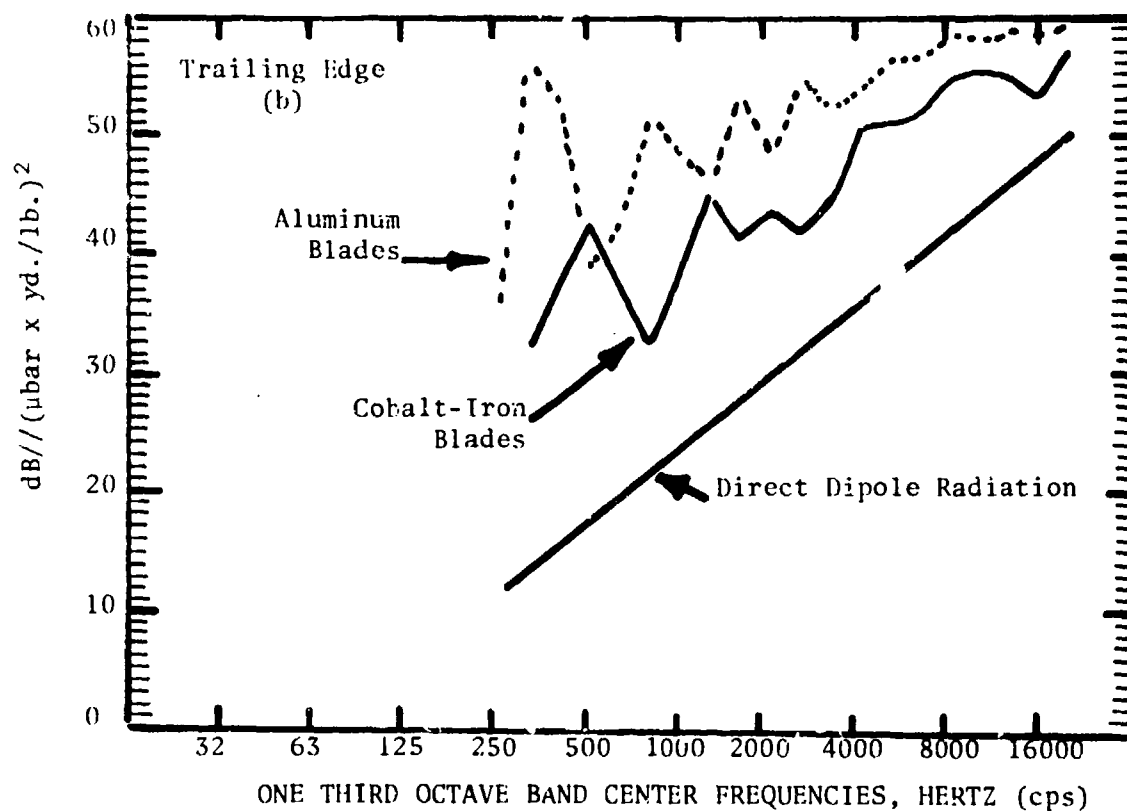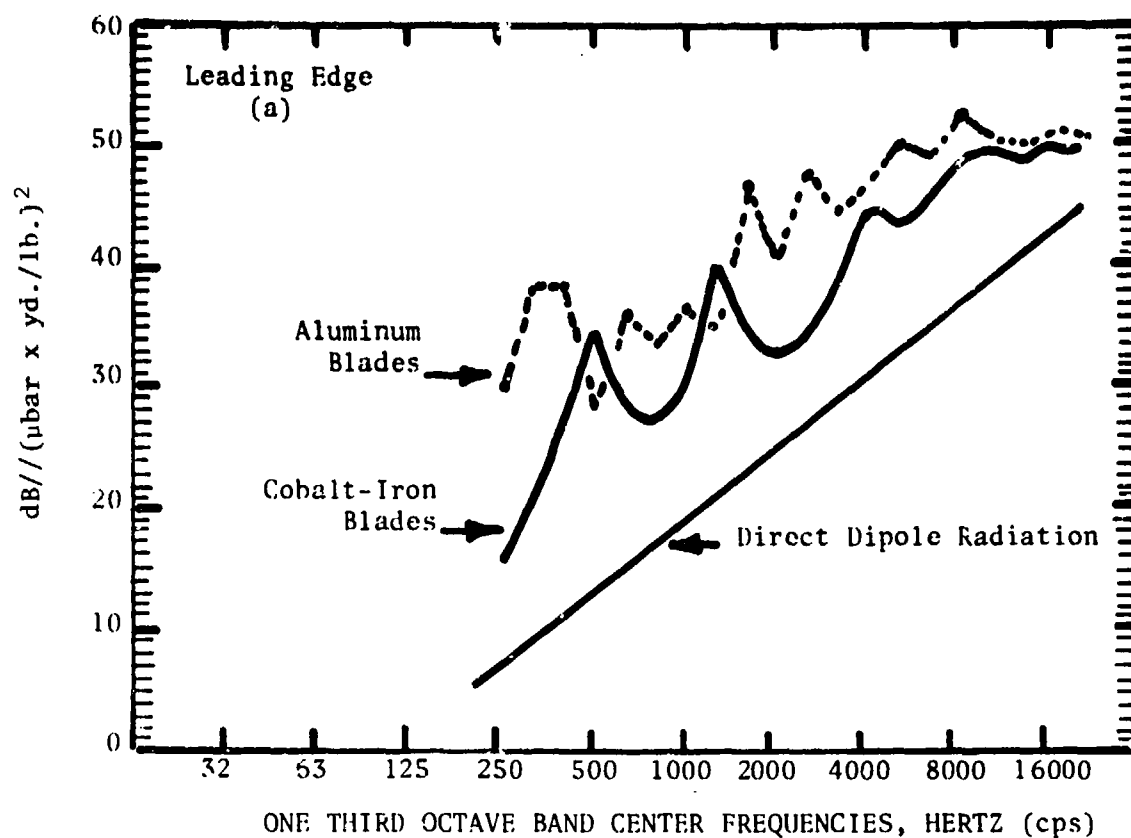
Figure 97(a),(b).   Average Transfer Function for Leading (a)
and Trailing (b) Edge Positions.

-146-

TABLE 7

ACCELEROMETER POSITIONS

POSITION NO.	LOCATION	RADIUS, INCHES	
		ALUMINUM	DAMPED ALLOY
1	Trailing Edge	8.9	8.8
2		8.3	8.2
3		7.6	7.5
4		6.8	6.7
5		5.9	5.9
6	Leading Edge	6.7	6.6
7		6.0	5.9
8		5.4	5.3
9		4.7	4.7
10		4.2	4.1

it will be seen that these occur in the frequencies bands where the
aluminum propeller's radiated noise levels are unusually low. If
the spectra were smoothed before drawing the noise reduction, such
negative values would not occur.

Some of the differences, both up and down, between the
propellers' transfer functions are due to changes in their modal
structure. These results from the different densities and Young's
moduli of the two materials as well as the increased thickness of
the damped alloy blades. For purposes of this comparison, the two
propellers were intended to have the same geometry. The geometry
of an actual propeller designed for the high damping alloy may
well be different, however, particularly in the blade thickness,
because the strength of the material will be a factor. The acoustic
performance of the high damping alloy as shown by these measurments
is very promising. Further consideration should be given to its
application in torpedo propellers.

ONE THIRD OCTAVE BAND REQUENCY, HERTZ (cps)
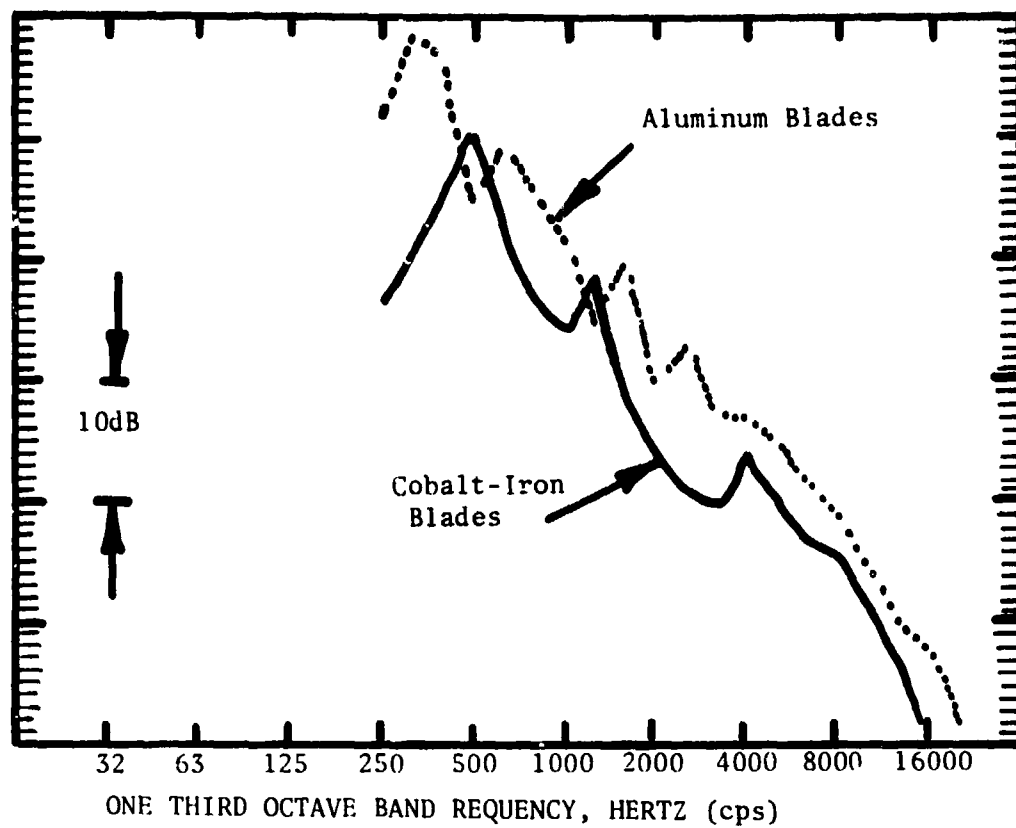
Figure 97. Relative Radiated Noise Spectra for
Aluminum and Cobalt-Iron Alloy Blades.

ONE THIRD OCTAVE BAND CENTER FREQUENCY, HERTZ (cps)
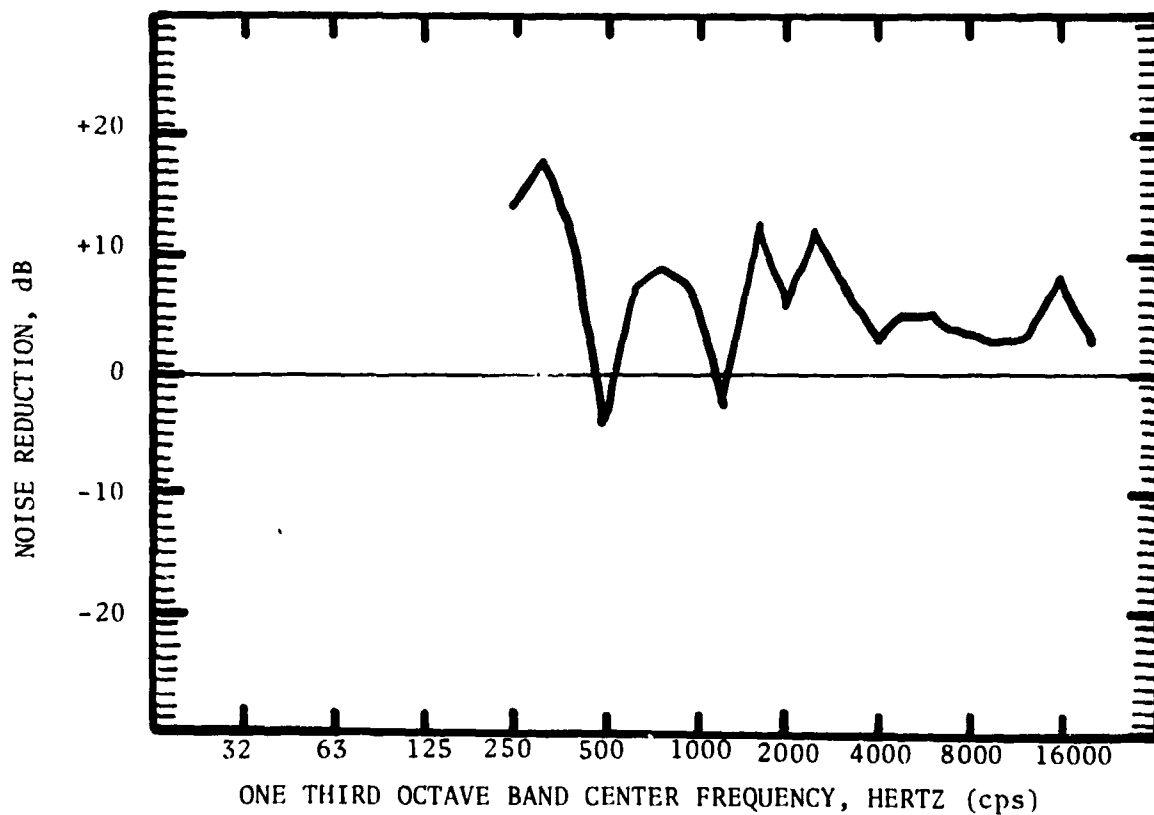
Figure 97d. Radiated Noise Reduction of Cobalt-Iron
Blades over Aluminum Blades as a Function
of Frequency.

-148-

The hydroacoustic performance of the cobalt-iron propeller has been evaluated by comparing the measured force-to-underwater radiation transfer functions of the two propellers, and by comparing their resulting estimated radiated noise levels when equal hydrodynamic exciatation spectra are applied. These excitation spectra are typical of torpedo propellers of modern design. The apparent noise reduction is quite substantial. Reduction of about 10 dB are common in the low and mid frequency bands. At higher frequencies, the noise reductions is reduced perhaps reflecting the pre-existance of important values of acoustic radiation damping in both propellers. The noise reduction is significant because the large reductions apply where the propeller radiated noise levels are highest. The acoustic performance of the propeller with the high damping alloy is very promising and further consideration should be given to the application of this material in torpedo propellers.

VII. MECHANISTIC STUDIES OF DAMPING IN Cu-Al-Ni AND Co-Fe ALLOYS

The ability of a thermoelastic martensite to "store" elastic energy is ultimately related to the capacity of that same material to continually absorb and damp out vibrational energy. If the energy-absorbing mechanism in a particular material is nonrepeatable, then the damping capacity will deteriorate with the amount of energy absorbed. However, if the energy-absorbing mechanism is repeatable, that is, it is able to return to its original state easily, then the damping capacity will not readily deteriorate. A martensitic transformation can be used to absorb mechanical vibrations, but if the transformation is nonthermoelastic (such as in the case of most steels), then it is essentially nonrepeatable and much of the strain energy of the transformation is "lost" by the formation of defects in the matrix. The strain energy in a thermoelastic martensitic transformation, however, is stored elastically in the matrix. This elastic strain energy is recoverable, and can aid the reverse transformation. Increasing the thermoelasticity of a martensitic transformation (by increasing the amount of recoverable strain energy in the matrix) improves the cyclability of the transformation and thus promotes the long-term efficiency of energy absorption in the material. The thermodynamic and microstructural studies reported here attempt to provide some insight into the mechanisms of energy absorption in Cu-Al-Ni, Co-Fe and Ni-Ti alloys.

1. Investigation of the Transformation Characteristics in Cu-Al-Ni Alloys

Much of the recent interest in thermoelastic martensitic alloys has been directed towards the study of the unusual mechanical effects associated with the transformation (31). While many properties of these alloys have been measured, little attention has been paid towards developing a clear understanding of the underlying thermodynamics of the transformation. The clear understanding of the basic thermodynamics of thermoelastic martensites should properly form the basis for further research to

develop methods of exploiting the unique properties these materials exhibit.

The storage of the transformational shape change as elastic strain energy is fundamental to the concept of a thermoelastic martensite. The original term "thermoelastic" was used by Kurdjumov (32) to describe a case where there is a balance of the chemical and elastic forces which results in the growth of a martensitic particle being stopped. The balance between chemical and nonchemical forces is built up during the transformation itself because the transformational shape change is accommodated entirely by elastic displacements. The elastic accommodation of the martensite means that elastic energy is being built up which produces a force opposing the further growth of the plate. The importance of the elastic terms in the thermoelastic transformation has often been overlooked when dealing with thermodynamic properties.

The temperature T_o is defined as the temperature where the chemical free energies of the parent and martensitic phases are equal. It is important to recognize that T_o refers to the temperature where the change in chemical free-energy between the parent and martensitic phases is zero (i.e., $G_{chem}^{P \to M} = 0$), and as such may be different from temperatures at which the total change in free-energy (both chemical and nonchemical) between the two phases is zero.

In nonthermoelastic martensitic transformations, it is usual to place T_o halfway between M_s and A_s (i.e., $T_o = 1/2$ $(M_s + A_s)$ where M_s is the martensite-start temperature and A_s is the start of the reverse transformation) (18). This treatment is reasonable because of the relative absence of stored elastic strain energy; the initial transformation (parent to martensite) and the reversion (martensite back to parent) are each nucleated, and it is assumed that the chemical driving force necessary to start the parent-to-martensite transformation is about equal to the driving force necessary to start the transformation of the martensite back to the parent. In a thermoelastic transformation, however, elastic strain energy is stored in the alloy (martensite plus parent),

and this stored elastic energy can significantly affect the transformation temperatures of a thermoelastic martensitic reaction. Tong and Wayman (33) recognized that stored elastic strain energy can affect M_f (the finish temperature of the martensitic transformation) as well as A_s; in particular, they noted that A_s can lie below T_o. However, the contribution of strain energy was considered by Tong and Wayman to be negligible at M_s as well as at A_f (the finish temperature for the martensite-to-parent reaction). By assuming the elastic contributions to the free energy to be minimal in this range, Tong and Wayman placed T_o between M_s and A_f.

The contribution of strain energy to the transformation behavior has been shown by Olson and Cohen (34) to be an important factor during the entire transformation. Specifically, if a single martensitic plate is formed in thermoelastic equilibrium, then this plate will revert at a temperature below T_o. Therefore, not only A_s, but also A_f will be below T_o for the case of ideal thermoelastic equilibrium. There are, however, two factors which can cause A_f to move above T_o in an otherwise highly thermoelastic alloy. First, the interface between the martensite and the parent phase may have a significant frictional stress associated with its motion, and the finite stress required to move this interface can cause a deviation from thermoelastic equilibrium. If the frictional stress is large enough, A_f may be displaced above T_o. Another deviation from ideal thermoelasticity arises when the shape change associated with the transformation is not stored elastically in the system. This may result because of some degree of plastic accommodation (extensive plastic accommodation of the transformational shape change will lead to nonthermoelastic martensites as exhibited by many ferrous systems). The transformational shape change may not be elastically accommodated in at least one other important situation; that of the single-interface transformation in a single crystal. In the single-interface transformation, the macroscopic shape of the crystal is not constrained, and thus the transformation strain is not elastically stored, but rather the entire external shape of the crystal is changed. The amount of strain energy stored in a sample may be similarly reduced in large-grained polycrystalline samples.

The effects of stored elastic-strain energy can be eliminated in a material which would normally undergo a thermoelastic martensitic transformation by causing a single crystal to undergo a single-interface transformation. Cu-14w/oAl-3w/oNi transforms from β_1 (a DO_3 structure) to γ_1' (a 2H structure) at a temperature close to room temperature. A single crystal of this alloy (prepared by the Bridgman technique) was heat treated at 950°C in an argon atmosphere for one hour and water quenched. The single crystal was then cooled so as to transform it by a single-interface; specifically, the sample was transformed in a temperature gradient. Thermocouples were spot-welded at various points to the surface of the single crystal so that the temperature could be monitored throughout the transformation. During the single interface transformation, the temperature at which the interface passed each thermocouple was measured and was found to be the same at each thermocouple location as the P/M interface* passed. The temperature for growth of the forward transformation (T_g) was measured as well as the temperature for the reverse motion of the interface (T_r). The motion of the interface during forward growth was not smooth and uniform; the interface got "hung up" at different places in the sample and at these points more undercooling was necessary to cause the interface to break free and growth to continue. However, the temperature at which the interface passed each thermocouple (moving smoothly and uniformly in that region) was found to be constant. It proved to be substantially more difficult to obtain a single-interface reversion, because nucleation of the parent (in the martensitic matrix) usually occurred nearly simultaneously at several points. On those occasions when a single-interface reversion was accomplished, the behavior was much the same as that described for the single-interface growth, the most important feature being that T_r was the same as the interface passed each thermocouple.

The same single crystal was also cooled in a manner which caused it to undergo a multiple-interface transformation; that is, the sample was cooled uniformly and this resulted in a number of different martensitic variants being formed during the transformation.

---

* Interface between the parent and martensitic phases.

-153-

The same series of thermocouples was used to determine the temperatures M_s, M_f, A_s, and A_f. These critical temperatures in the hysteresis loop were determined by visually observing the sample under a low power microscope. Figure 98 shows how the two different transformations occur as a function of temperature. The lowering of M_f and A_s in the multiple-interface transformation shows the effect of the elastic strain-energy storage. A_f (from the multiple-interface reversion) is very nearly equal to T_r (in the single-interface reverse transformation) because the final plate to revert in the multiple-interface reversion has no stored elastic energy to affect it.* The A_f temperature is thus primarily determined by the heating above T_o necessary for growth. The difference between M_s and T_g (for the multiple-interface and single-interface transformations respectively) is small, and this indicates the undercooling below T_o necessary for nucleation is close to that necessary for growth (after nucleation has already been accomplished). T_o can unambigously be

---

*This need not always be the case: in other samples of this material cut in the shape of thin (0.05 mm) discs, the reverse transformation did not proceed as the orderly "unzipping" process normally observed in thermoelastic alloys. The reverse transformation usually proceeds such that the last plates to form are the first to revert. The "normal" sequence then implies that the final plate to revert was the first formed and in a single crystal this plate is not affected by strain energy. Further, in the normal, well behaved reverse transformation, it requires only a small change in temperature to cause this last remaining plate to revert completely. In the "abnormally" behaving samples, the reversion of the final plate (or the "single plate" in a single-interface transformation) took place by the parent phase being nucleated at several places, and a large change in temperature was then required to cause the parent to grow over the entire martensitic plate. It is not clear why the large driving force for complete reversion is sometimes required, but it is evident that the A_f thus obtained is significantly greater than the A_f observed for a "normal" reversion.
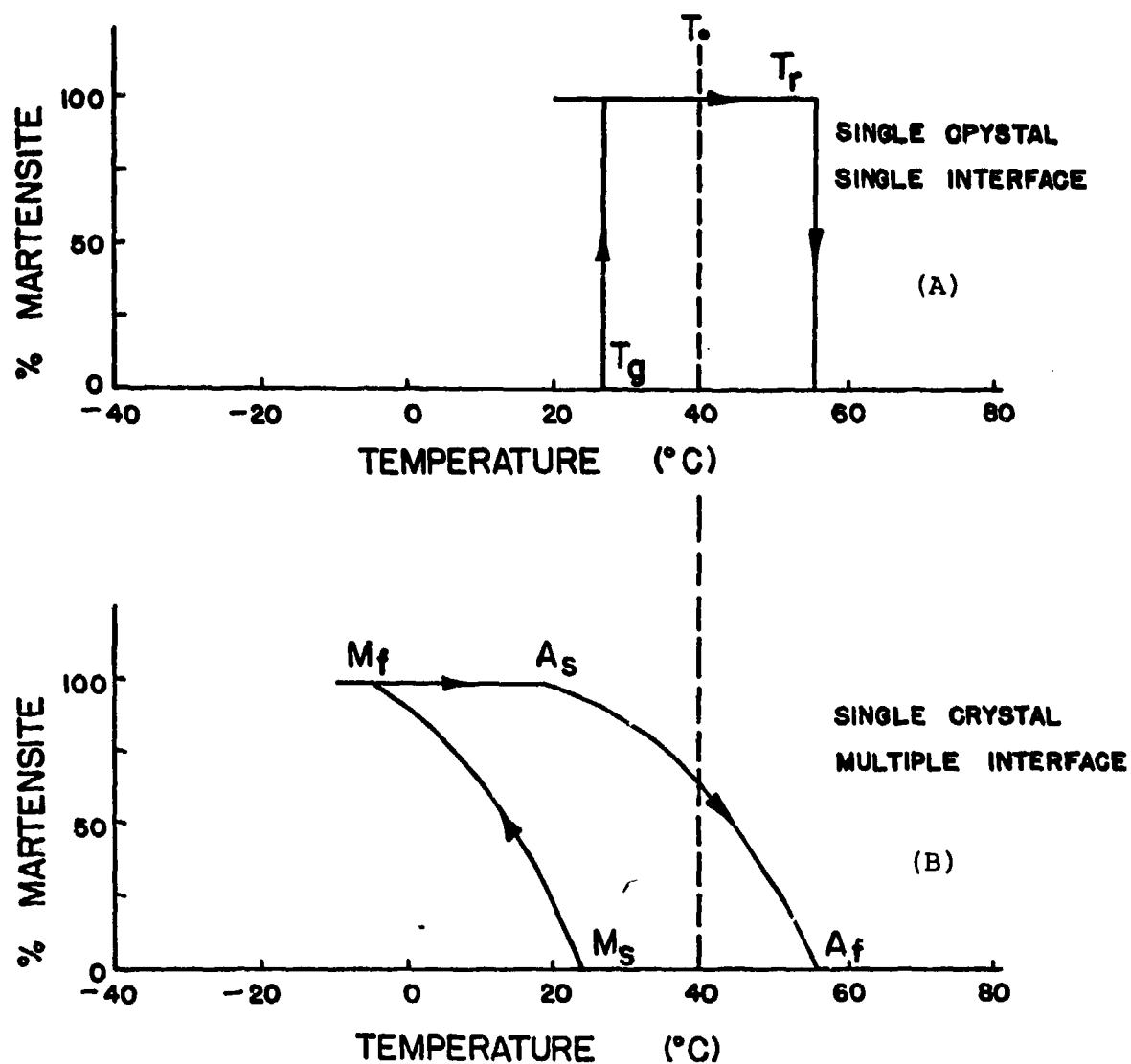
Figure 98.   Transformation Hysteresis Curves for a Single
Crystal Cu-14.0Al-3.0Ni.   (A) Single-Interface
Transformation, and (B) Multiple-Interface
Transformation.

bracketed between T_g and T_r for the single-interface transformation
and reversion. Further, by assuming that the friction stress which
must be overcome by the interface growing in the forward direction
(i.e., P→M) is the same as the friction stress which must be over-
come by the interface growing in the reverse direction (i.e. M→P),
then T_o may be placed halfway between T_g and T_r (i.e., $T_o = 1/2$
$(T_g + T_r)$). The temperatures M_s and A_f for the multiple-interface
transformation in the <u>single crystal</u> must also bracket T_o because
of the absence of the effects of strain energy both at M_s and A_f.
In the present alloy, the values of M_s and A_f for the multiple-
interface transformation are nearly equal to T_g and T_r respec-
tively for the same sample transformed via single-interface, and
thus the setting of T_o equal to $1/2 (T_g + T_r)$ is approxi-
mately equal to the determination of T_o as being equal to $1/2$
$(M_s + A_f)$. It is emphasized that the above discussion deals only
with single crystals, and can not be extended to polycrystalline
samples as will presently be shown.

In order to show the effect that grain boundaries have
on the storage of elastic strain energy, samples of Cu-14Al-3Ni
with differing grain size were examined. The polycrystalline
samples underwent the same heat treatment as the single crystal
that is, it was held at 950°C (in argon) for one hour and then
water quenched. Samples of differing grain size (the average
grain diameter, D, varying from .5mm to 4.0mm) were subsequently
viewed under a light microscope while being heated and cooled in
order to determine the transformation temperatures. The results
are shown in Figure 99 (a,b,c). It is, of course, recognized that
at least some of the differences observed in the hysteresis loops
of the various samples can be explained by small compositional
variations from sample to sample (and even from grain to grain
within the same sample). In order to unabiguously show the effect
of grain boundaries on the transformation, the grain from the
coarsest-grained sample previously examined (see Figure 99C) was
spark-machined away in order to determine the transformation
hysteresis loop. The differences in the hysteresis loops of the
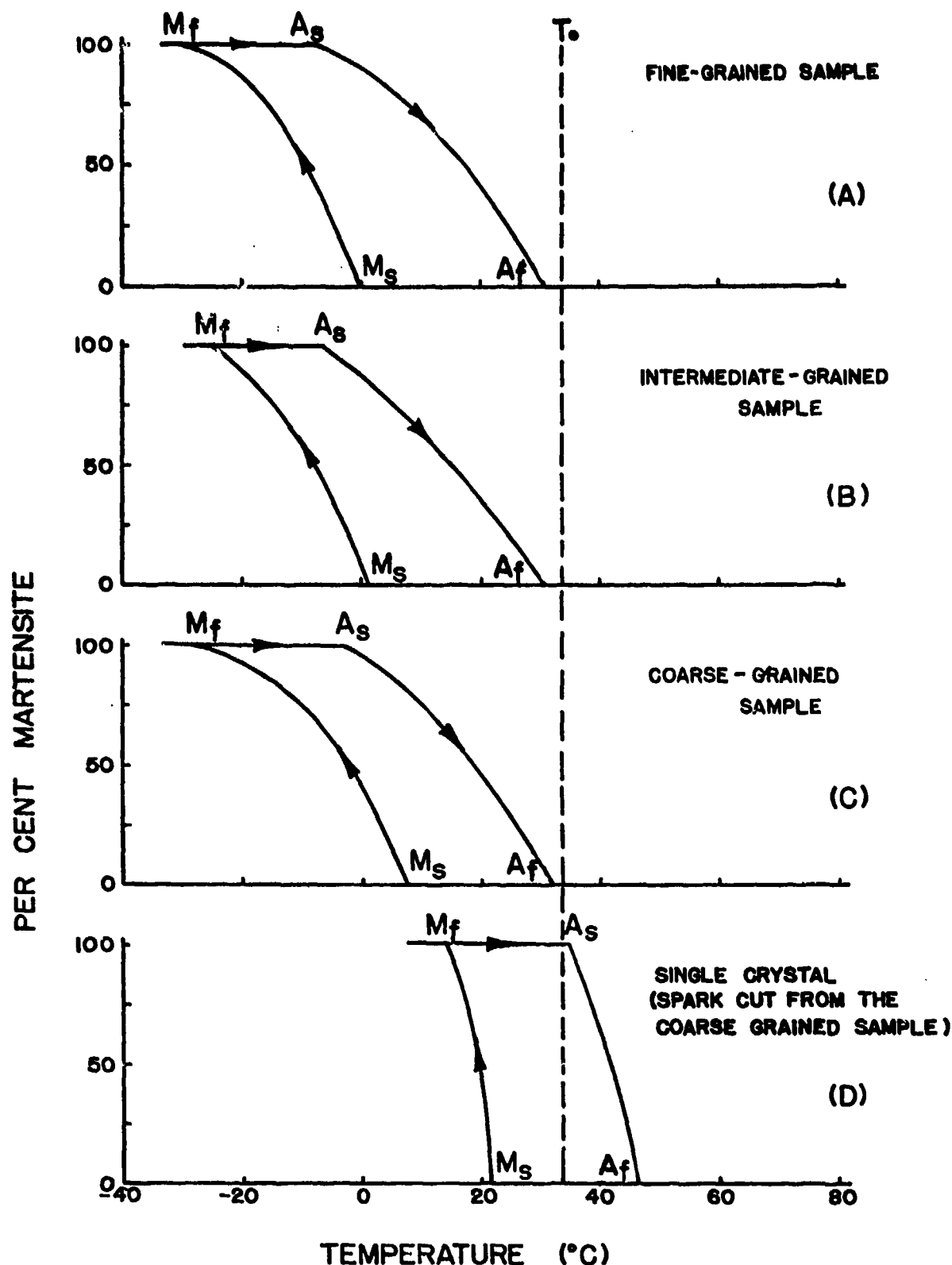
Figure 99.   Transformation Hysteresis Curves for Cu-14.0Al-3.0Ni
             as a Function of Grain Size. (A)   Fine Grained
             (G.S.=40 grains/in²), (B)   Intermediate Grained
             (G.S.=60 grains/in²), (C)   Coarse Grained (G.S.=
             in²), and (D)   Single Crystal (cut from the
             coarse-grained sample).

coarsest-grained sample and single-crystal sample (shown in Figures 99c and 99d respectively) are due entirely to the effects of the grain boundaries and are not due to any compositional changes or differences in heat treatment. Figure 99 shows that the hysteresis loop is depressed with decreasing grain size. A_f is depressed in going from the single crystal to the polycrystal, but is only slightly affected by decreasing grain size over the narrow range of grain size tested. M_s is more strongly affected by decreasing grain size than is A_f, and this indicates that the effect of elastic constraint is significant even in the initial growth of martensite.

The single-crystal sample whose hysteresis loop is shown in Figure 99d (nonsingle-interface transformation) had a negligible amount of stored elastic strain energy both near M_s and A_f, that is, it was "well behaved" (see the footnote at the bottom of page 154). Thus, T_o can be bracketed by M_s and A_f as was shown previously. Using the assumption that T_o is exactly halfway between M_s and A_f* for the single crystal, a value of 33°C for T_o is obtained. However, if the same scheme is used for polycrystalline samples (as suggested by Tong and Wayman), the values for T_o would range from 15 to 19°C depending on the grain size of the sample tested. This results in an error of from 14 to 19°C in the approximation of T_o; this error is certainly significant since the width of the hysteresis loops of these samples is only about 20 to 30°C. Further, an error of 14 to 19°C has a fairly large effect on the calculation of the chemical driving force. The error involved in putting T_o equal to $1/2$ $(M_s + A_f)$ for a polycrystalline sample may also become considerably greater in finer-grained specimens where it may be possible to store a larger amount of elastic strain energy.

The effects of polycrystalline constraints on transformation behavior are also shown qualitatively in Figure 100. In a given polycrystalline specimen, within a small area, a variation in grain size could be seen. A small (D=0.5mm) interior grain

---

* The difference in the T_o's measured for the single crystals whose transformation characteristics are shown in Figures 98 and 99 respectively are most probably the result of slight compositional changes and/or small differences in the quenching rates of the two samples.

(i.e., away from edges and corners) was examined, and its M_s and A_f were compared to an interior grain of larger diameter (D=1.5mm). These results can also be compared with less-constrained grains of about the same size adjacent to the edges of the sample. Figure 100 shows that when the grain is less constrained, the M_s is raised significantly, and to a lesser extent the A_f is also raised. The increase of the A_f (with decreasing amount of constraint) may be explained by the corresponding decrease in stored elastic energy. The even stronger effect on M_s is somewhat surprising, but is undoubtedly associated with the effect of elastic constraints on the growth of the martensite.

Electrical resistivity has been measured as a function of temperature, and can be used as an alternate method of determining M_s, M_f, A_s, and A_f. Figure 101a shows the resistivity versus temperature curve for a Cu-14.0Al-3.0Ni single crystal. The transformation temperatures cannot be compared quantitatively with the single-crystal hysteresis loops in Figures 98 and 99 because even the minor differences in quenching rate from the solutionizing temperature of 950°C can change the degree of long-range order and this affects the transformation temperatures. However, it was noted that the temperatures where the color changes occurred coincided with the points of resistivity inversion, thus confirming the validity of determining the transformation temperatures on cooling and heating by the optical (color change) method.

The resistivity versus temperature curve of the single-crystal specimen (Figure 101a) shows M_s to be -1°C and A_f to be 37°C. The temperatures for M_f and A_s cannot be determined accurately from the curve because of the relatively gradual changes in slope near both M_f and A_s. Certainly the bulk (greater than 90%) of the transformation has been completed by -5°C on cooling and similarly the reversion is underway between 20 and 25°C on heating. It is important to note, however, that the temperatures of importance for present purposes (i.e., M_s and A_f) can be determined fairly precisely from the resistivity curves.

The single crystal (with resistivity leads and thermocouple still attached) was cleaned and a thin layer (less than 0.001 in. thick as measured by a micrometer) of Ni was electro·

-159-
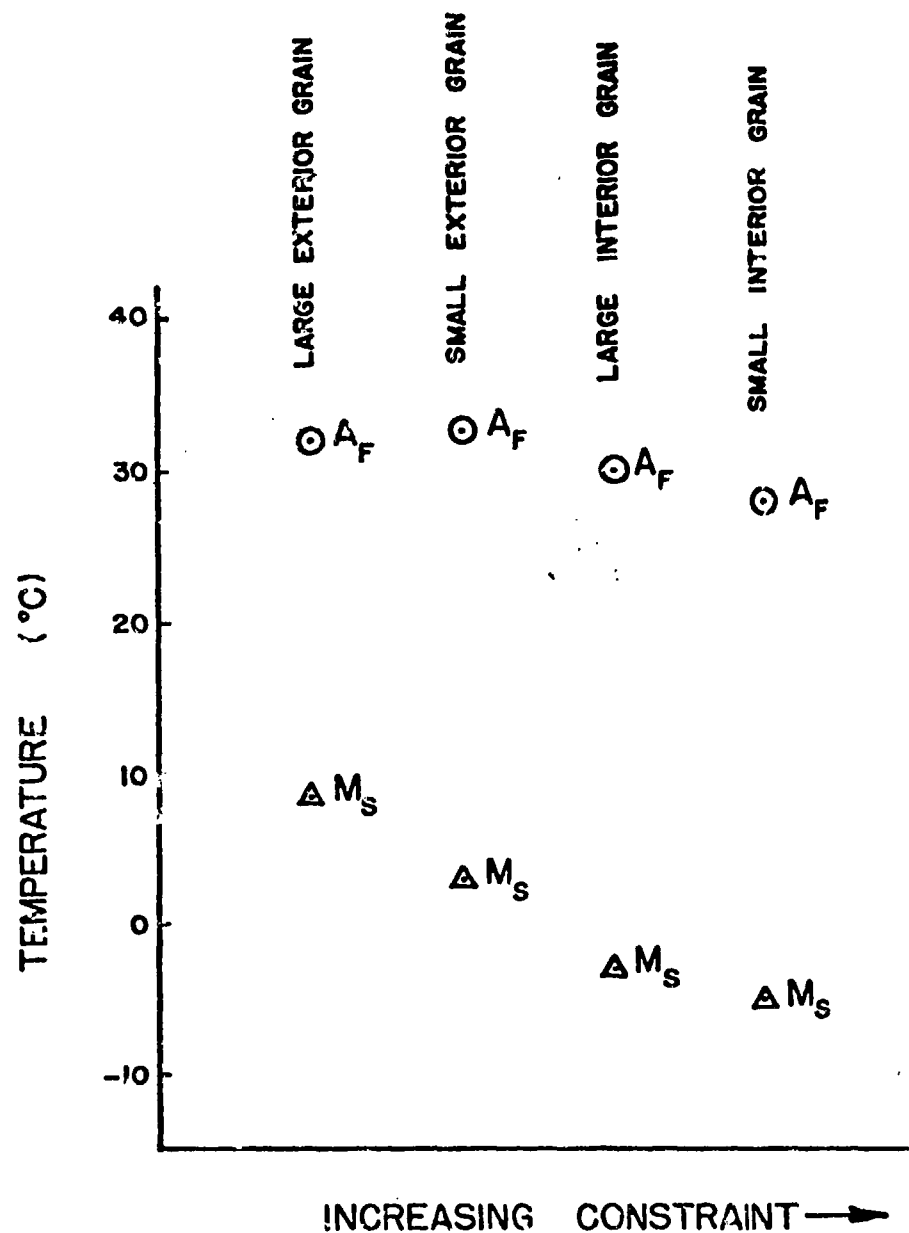
Figure 100. M_s and A_f Temperatures as a Function of Increasing Constraint on the Grain.
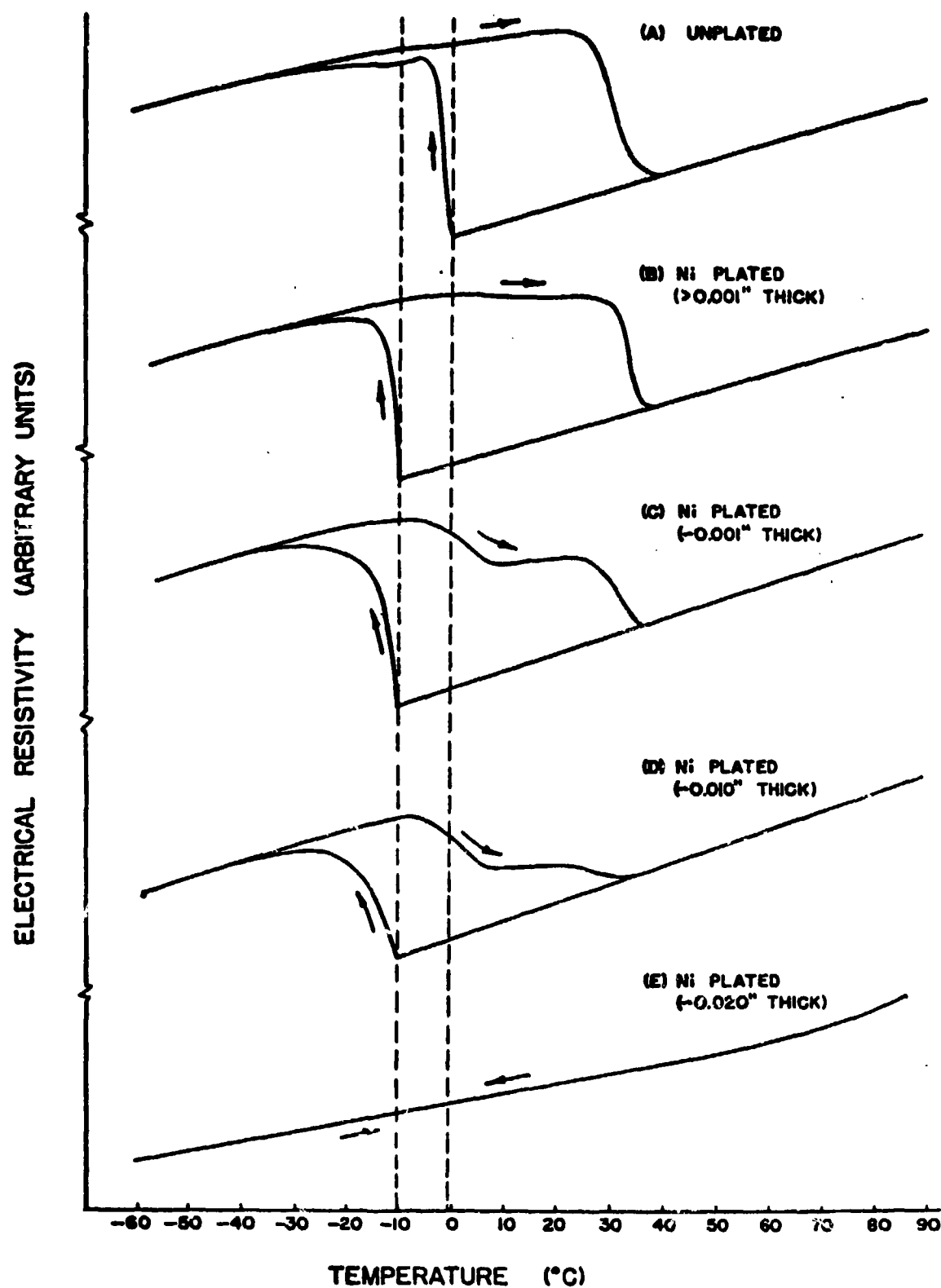
Figure 101. Transformation Hysteresis Curves for a Cu-14.0Aℓ-3.0Ni Single Crystal with Different Thickness of Ni-Plating on the Specimen Surface.

-161-

lytically plated on the specimen. The electrical resistivity was
then measured as a function of temperature (Figure 101b). The M_s
has been depressed to approximately -10°C (as compared to the M_s
of -1°C) for the unplated specimen. The A_f, however, remains
at 37°C. The M_f and A_s values are less easily defined; that is,
the portion of the curve that would indicate M_f on cooling has
become more rounded off than it was for the nonplated sample.
This is also true for the portion of the heating curve (near 20°C)
which is used to yield the (approximate) value for A_s. The in-
crease in "blurring" of M_f and A_s over what it was for the non-
plated sample is probably due to the reduced size to which the ini-
tially-formed martensitic plates can grow (because of the con-
straints imposed by the Ni-plating). The reduced size of the
first-formed plates results in a larger volume fraction of the
sample that must be transformed by still smaller plates "filling
in" between the initial plates. These small plates require more
super cooling in order to form because of the increased elastic
strain energy that must be stored in the system due to the more
complex geometry of the aggregate of plates.

Another layer of Ni was added to the surface of the
specimen and the resistivity versus temperature was again mea-
sured (Figure 101c). The M_s remains unchanged at -10°C while
A_f has been lowered slightly to about 34°C (from the previous value
of 37°C). The "blurring" of the M_f portion of the curve (around
-20°C on cooling) is greater than in the previous runs. On heat-
ing, the resistivity displays a dip that starts at about -10°C.
When more Ni is added to the plating (about 0.010 inch), the
resistivity curve (Figure 101d) shows an enhancement of the
effects exhibited by the curve of Figure 101c. In other words,
M_s and A_f remain approximately constant at -10°C and 34°C res-
pectively, but the curve (on cooling) rounds off even more in
the vicinity of M_f and the dip on heating (starting at about
-10°C) becomes still more pronounced.

A thick Ni-layer was finally applied to the surface and
the resulting resistivity is shown in Figure 101e. This final

Ni-plating was about 20 mils thick. The resistivity curve becomes nearly a straight line, and does not indicate any transformation occurring in the temperature range observed. Samples with Ni-plating of thickness intermediate between those reported in Figures 101d and 101e showed basically the same behavior as the curve in Figure 101d.

The curves in Figure 101 represent rather unusual behavior for thermoelastic martensitic material; this behavior as presently understood will be described below. The first Ni-plating seems to have depressed M_s by suppressing the <u>surface</u> nucleation of the martensite (i.e., the free surface is, in effect, removed by the Ni-plating). The M_f and A_s are less well-defined because of the increased number of smaller plates forming (which previously were able to grow to almost the entire volume of the specimen). As the Ni-plating is increased in thickness, the M_s and A_f remain relatively unchanged. The M_f portion of the curve becomes increasingly rounded-off, indicating that a larger part of the sample volume is being taken up by smaller plates. The transformation is thus rendered more thermoelastic - - that is, the Ni-plating causes a greater amount of elastic strain energy to be stored in the matrix and this has the effect of making the transformation of the single crystal occur via a greater number of plates and variants than was previously observed in the unplated condition. The elastic strain energy stored in the Ni-plated sample can be used to promote the reverse transformation on heating - this seems to be the cause of the early dip in the heating curve, which increases in magnitude as the thickness of the Ni-plating is increased. If this is the case, then at some Ni-plating thickness, the amount of strain energy stored in the Ni-plated sample should be sufficient to cause the reversion of the sample to be complete before the A_f of the unplated sample. This behavior was not demonstrated in the present set of experiments, the most probable reason being that the conductivity of the thick Ni-plating becomes sufficiently large to obscure any resistivity changes due to the transformation itself.

Subsequently, the specimen with the thick Ni-plating

was electropolished to remove the Ni. The resistivity curve
of this sample (unplated) was then re-measured and is shown
in Figure 102A. The M_s increased to $-2°C$ (very close to the
M_s of $-1°C$ for the unplated specimen). This demonstrates
that the effect of the Ni-plating is reversible and that
removing the Ni-plating causes the return of M_s to $-10°C$,
with little or no influence of the A_f.

Stored elastic strain energy can also importantly
affect the evaluation of other thermodynamic quantities,
specifically enthalpy and entropy. The elastic strain energy
increases during the forward transformation in order to bring
about a thermoelastic balance. The condition for thermoelastic
equilibrium has been determined by Olson and Cohen (34) and
Tong and Wayman (33) to be:

$$\Delta G_{chem} + n\Delta G_{elas} = \frac{heating}{cooling} \pm \Delta G_{frict} \qquad [12]$$

where ΔG_{chem} is the change in chemical free energy, ΔG_{elas} is
the change in elastic free energy, ΔG_{frict} is the energy regis-
tered to overcome lattice friction (i.e., the inherent lattice
resistance to the motion of the P-M interface), and n is a con-
stant. The value of n must be greater than or equal to one; from
the First Law of Thermodynamics, it is not possible to "store"
more energy elastically than is made available to the system by
the change in chemical free energy produced by the transformation.
For the case of a single isolated plate of martensite formed in
thermoelastic equilibrium, n has been calculated by Olson and Cohen
to have a value of two. Because the chemical and elastic terms are
of opposite sign, it is anticipated that the elastic enthalpy con-
tribution will cause a substantial reduction in the magnitude of
the measured net enthalpy change when the transformation proceeds
in a thermoelastic manner. A quantitative interpretation of the
calorimetric measurements of polycrystalline samples is not at
all straightforward, but it is clear that these measurements
do not determine the chemical enthalpy change of the trans-

-164-
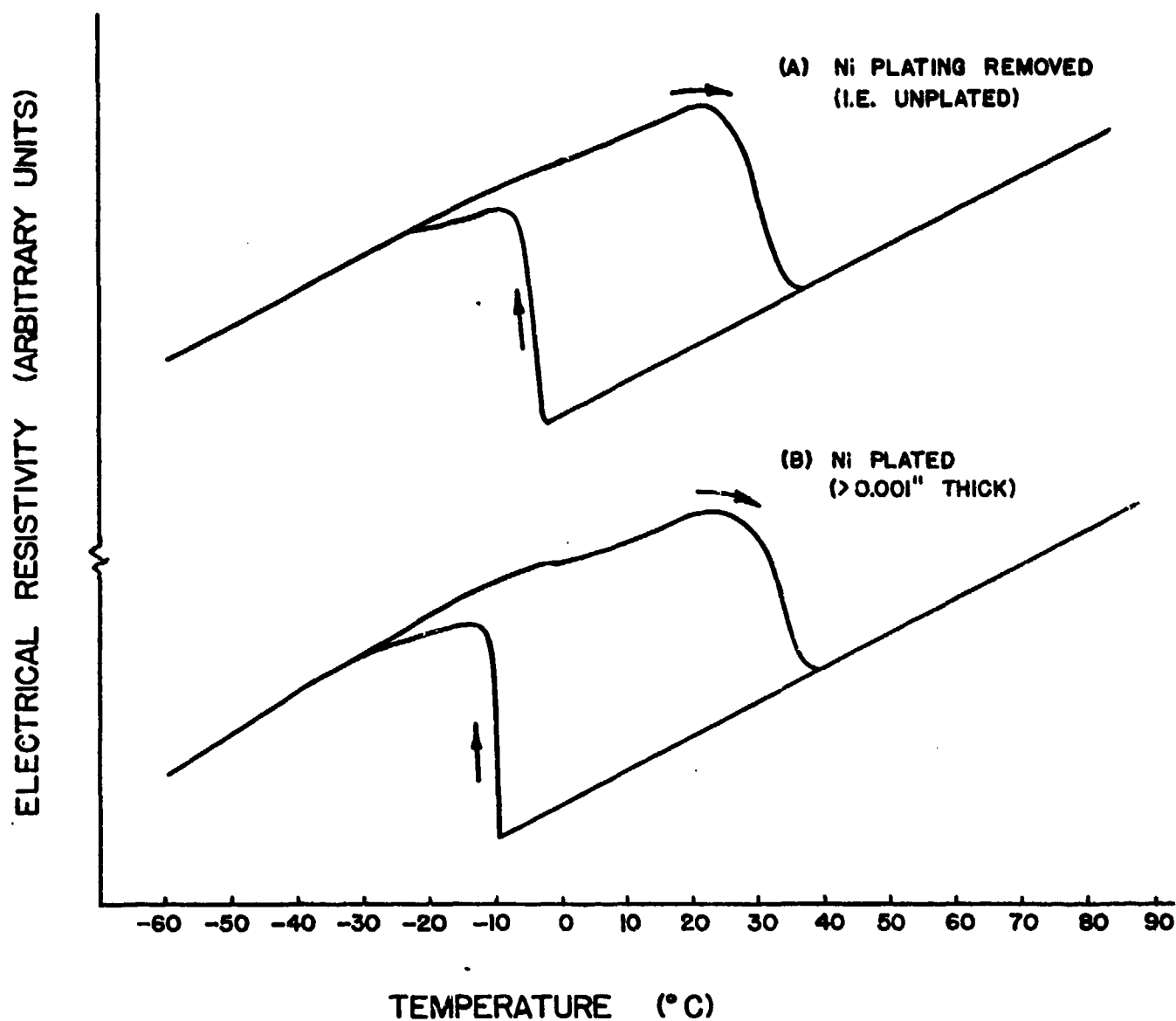
Figure 102. Transformation Hysteresis Curves for a
Cu-14.0A1-3.0Ni Single Crystal with
(A) Ni-Plating Removed, and
(B) A Thin Thin Ni-Plating Reapplied.

-165-

formation.

Recognizing that elastic strain energy affects the observed enthalpy change, the most direct way of measuring the chemical enthalpy change is to eliminate the storage of elastic strain energy in the system. As outlined previously, this can be accomplished by 1) eliminating the grain boundaries, and 2) transforming the sample via a single interface. Single-crystal samples of Cu-14Al-3Ni were prepared for testing in a D.S.C. (differential scanning calorimeter; Perkins and Elmer model). The samples were discs about 6mm in diameter by 0.2 to 1.5 mm thick, and were obtained by spark cutting from a (large) single-crystal specimen. Each disc sample was then chemically polished and examined visually while cooling under a low-power optical microscope. One of the samples consistently transformed by the motion of a single interface with no special cooling procedures. This sample (designated as Sample 1) along with two other single crystals (Sample 2 and 3) were tested in the D.S.C. along with two polycrystalline samples (Samples 4 and 5). The cooling curves from the calorimeter (i.e., for the $\beta_1 \to \gamma_1'$ transformation) for Sample 1 suggested that the transformation occurred by a single-interface mechanism. The measured peak was sharp and retained the same size and shape for cooling rates varying from 80°C/min down to 0.31°C/min. In addition, the cooling peak of Sample 1 exhibited none of the structure which was subsequently found in the calorimetric curves porduced by the other samples. The maximum difference between M_s and M_f (measured at the slowest cooling rate of 0.31°C/min) was less than 0.05°C. The other samples (both single crystals and polycrystals) produced broad peaks on cooling, which indicated that the transformation occurred by a multiple interface mechanism. The peaks from the $\beta_1 \to \gamma_1'$ transformation for Samples 2 through 5 had a width and structure which was not evident in the peak from Sample 1. Figure 103 shows examples of the transformation peak exhibited by each of the samples (cooling rate of 40°C/min). Table 8 shows the net enthalpy change measured for each sample (i.e., the area under the peak). The values listed in the table are the averages of at least

-166-

TABLE 8

NET ENTHALPY CHANGE FOR THE $\beta_1 \rightarrow \gamma_1'$ TRANSFOR-
MATION IN SINGLE-CRYSTAL AND POLYCRYSTALLINE
SAMPLES OF Cu–14 w/o Al–3 w/o Ni.

SAMPLE	$\Delta H_{cooling}$ (cal/mole)	$\Delta H_{heating}$ (cal/mole)
SAMPLE 1 (single-interface) single crystal– 32.8 mg.	–123	128
SAMPLE 2 (multiple-interface) single crystal– 71.0 mg.	–113	120
SAMPLE 3 (multiple-interface) single crystal– 85.8 mg.	–106	121
SAMPLE 4 polycrystal– 37.7 mg. (D ≐ 1.0 mm.)	–113	120
SAMPLE 5 polycrystal– 93.2 mg. (D ≐ 1.0 mm.)	–113	112

D is the average grain diameter.
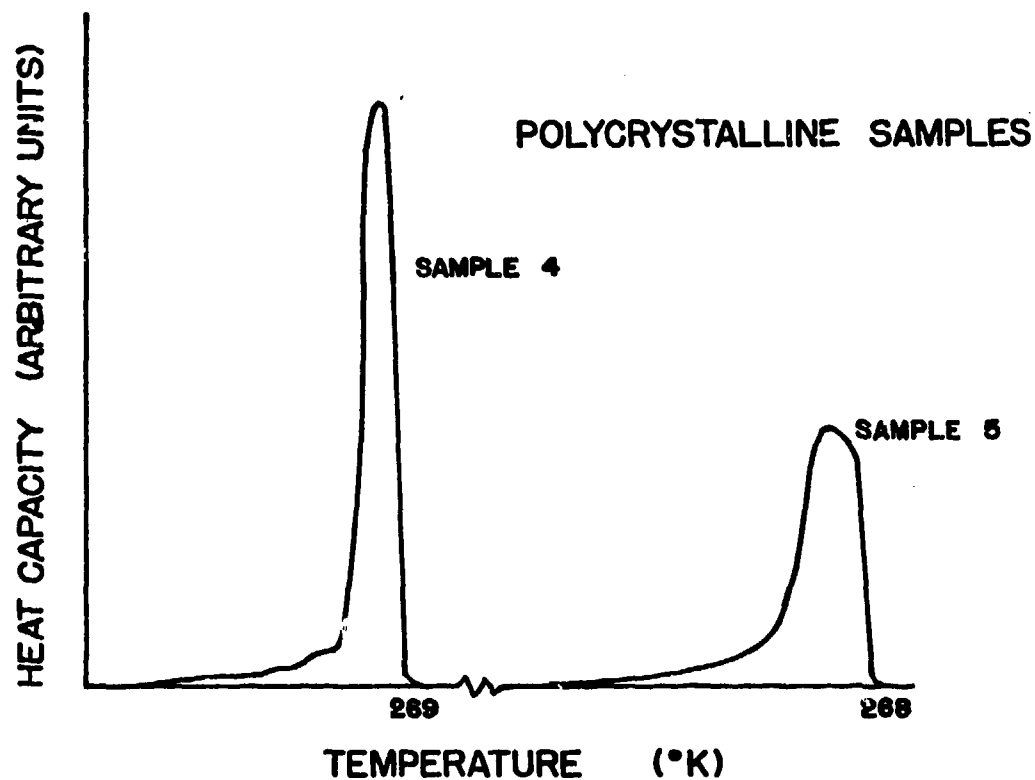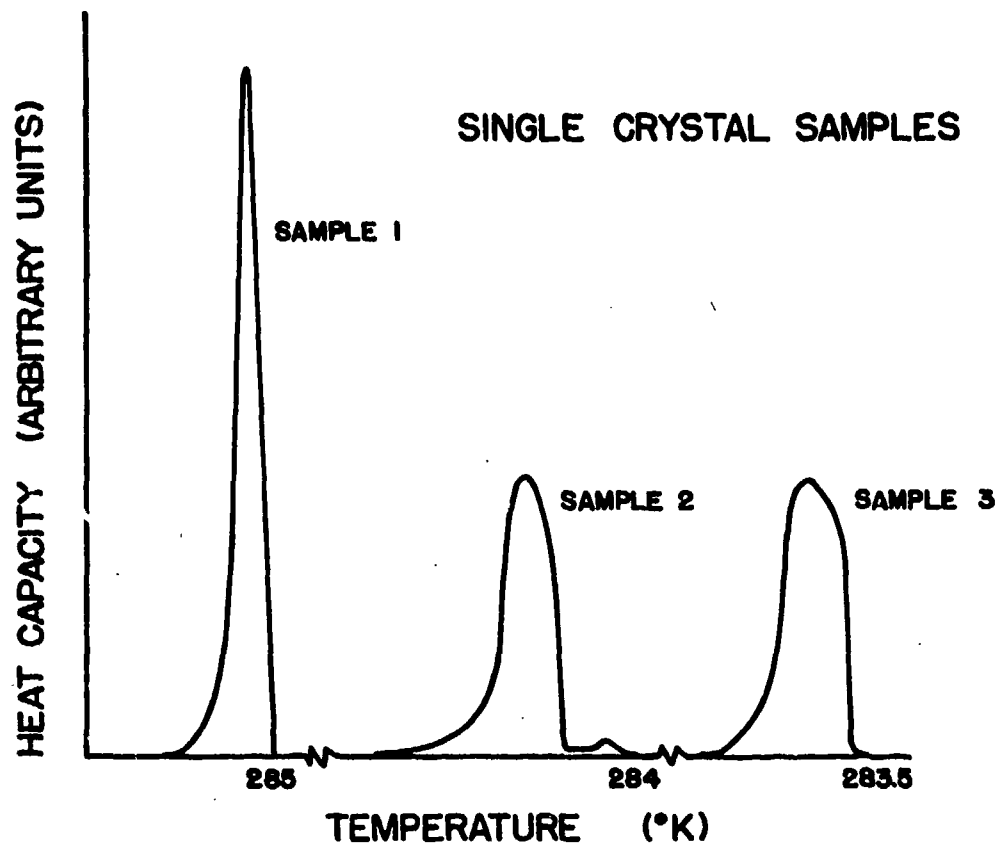
Figure 103. Differential Scanning Calorimeter Curves for Samples of Cu-14Al-3Ni (cooling rate of 40°K/min.).

three runs on each sample and show that the single-interface trans-
formation (Sample 1) is free from the contribution of elastic strain
energy (the measured change in enthalpy is equal to the chemical
enthalpy change for the $\beta_1 \rightarrow \gamma_1'$ transformation). Further, the contri-
bution of elastic strain energy to the multiple-interface transfor-
mations acts to decrease the absolute value of the measured enthalpy
change as predicted by the fundamental theoretical considerations
treated earlier. The absolute values of the measured enthalpy
changes of Samples 2 through 5 are at least 10 cal/mole less than
the absolute value of the net enthalpy change measured for Sample 1.
The actual value of ΔH_{net} is, of course, dependent on the amount of
strain energy actually stored in the sample -- the amount of strain
energy can vary from sample to sample depending on grain size, de-
fect substructure (dislocation density for example), second phase
(amount and distribution), degree of long-range order, and external
constraints on the crystal.

As was shown earlier, a thin plating (less than 0.001 inches
thick) of nickel on Cu-14Al-3Ni depresses the M_s of the sample by
about 10°C without affecting the A_f temperature. Nickel plating also
has the effect of causing a single-crystal sample to transform to
a larger number of fine martensitic plates than it transformed to in
the absence of the nickel plating. This implies that the strain
energy should be larger due to the increase in the "multiple-interface"
character of the transformation (the interface between the martensite
plates can provide barriers to the growth of other plates and act to
constrain the shape of the sample). Also, the depression of the trans-
formation increases the chemical driving force, and thus by Equation
12, the magnitude of the elastic strain energy must also be increased.

The samples previously tested were lightly chemically po-
lished, weighed, and plated with a thin layer of nickel. These
nickel plated specimens were tested in the calorimeter, and for
those samples on which the nickel plating kept its integrity (i.e.,
it did not flake off after the samples were transformed and revert-
ed), the M_s and the average transformation temperature of the samples

-169-

were depressed. The average transformation temperature used here
is the temperature at which the center-of-mass of the calorimetric
curve (on cooling) is located.

Sample 1, which previously, when unplated underwent a
single-interface transformation, displayed a ΔH transformation
curve which showed much structure and width after the sample
was nickel plated. This can be seen in Figure 104. The change
in peak size, width, and shape strongly indicates a change from
a single-interface transformation to a multiple-interface trans-
formation in the same sample. Subsequent metallographic exami-
antion showed (after the nickel was chemically polished away)
that the sample had indeed transformed to many individual marten-
site plates (i.e., a multiple-interface transformation) when the
sample was nickel plated. The sample was then reverted to the
single-crystal parent phase, polished, and upon cooling (on a
cold stage under an optical microscope), the sample again trans-
formed via single interface.

The absolute values of the net change in enthalpy on
cooling were decreased in going from unplated to plated samples,
and this is shown in Table 9. The absolute value of the measured
enthalpy change was decreased from 123 cal/mole to 101 cal/mole
for Sample 1 (single-interface). The absolute values of the
measured enthalpy changes for the nickel-plated polycrystals are
also smaller than for the unplated samples.

In summarizing the calorimetric measurements, it is quite
evident that elastic effects can contribute importantly to
measured enthalpy terms. The elastic contributions to the enthalpy
change in the present set of experiments affected the measurement
of the net enthalpy changes up to about 20%. [The effects of
strain energy, which can be eliminated by a single-interface transfor-
tion, can be interpreted in a straightforward manner as will
presently be described].

It is clear that the enthalpy term obtained from the
single-interface transformation is a measure of the chemical en-
thalpy change of the $\beta_1 \rightarrow \gamma_1'$ transformation. Specifically, there
is no elastic contribution to the measured enthalpy change in the
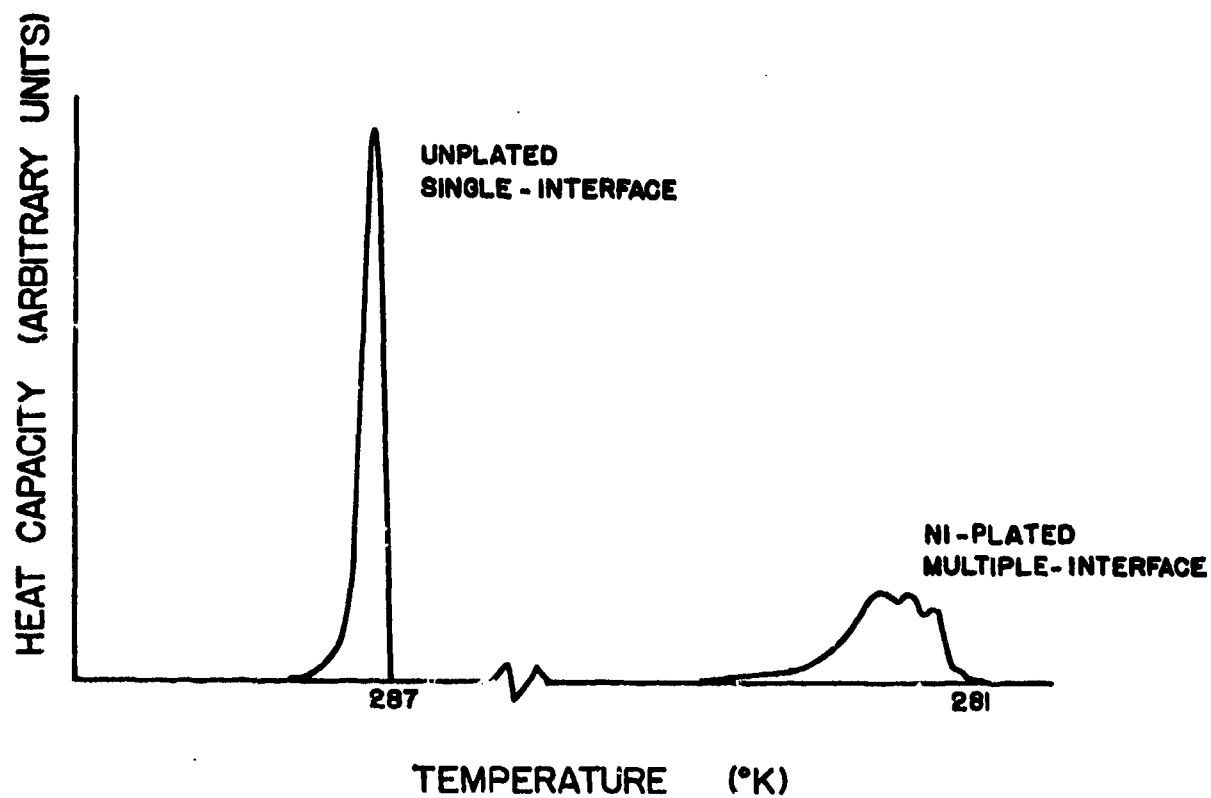
Figure 104. Differential Scanning Calorimeter Curves for a Single Crystal of Cu-14Al-3Ni in the Unplated and Ni-Plated Conditions (cooling rate of 40°K/min).

-171-

TABLE 9

NET ENTHALPY CHANGE FOR THE $\beta_1 \to \gamma_1'$ TRANSFORMATION IN NON-PLATED AND Ni-PLATED SAMPLES OF Cu-14 w/o Al-3 w/o Ni.

SAMPLE	$\Delta H_{cooling}$ (cal./mole)	M_s (°K)	$\bar{T}$ (°K)
SAMPLE I			
UNPLATED (single-interface)	-123	287	285
Ni-PLATED	-101	281	272
SAMPLE 4 (polycrystal – D ≐ 1.0 mm)			
UNPLATED	-113	274	270
Ni-PLATED	-101	257	255
SAMPLE 5 (polycrystal – D ≐ 1.0 mm)			
UNPLATED	-113	270	265
Ni-PLATED	-105	257	254

$\bar{T}$ is the average transformation temperature.
D is the average grain diameter.

single-interface transformation, leaving only the chemical term. The enthalpy change measured for the single-interface transformation of Cu-14Al-3Ni indicates that $\Delta H_{chem}^{\beta_1 \to \gamma_1'}$ is equal to -123 cal/mole.

Since $\Delta G_{net}^{\beta_1 \to \gamma_1'} = \Delta G_{chem}^{\beta_1 \to \gamma_1'} = 0$ for the single-interface transformation at T_o, it follows that:

$$\Delta S_{chem}^{\beta_1 \to \gamma_1'} = \frac{\Delta H_{chem}^{\beta_1 \to \gamma_1'}}{T_o} \qquad [13]$$

where $\Delta S_{chem}^{\beta_1 \to \gamma_1'}$ is the chemical entropy change for the $\beta_1 \to \gamma_1'$ transformation. T_o, as was previously shown, can be placed between T_g and T_r for a sample which undergoes a single-interface transformation on cooling but not on heating (see footnote on page 154). Further, from the single-interface transformation in a gradient, (described earlier), it was determined that, for these Cu-14Al-3Ni alloys, T_g equals approximately M_s + 2°C and that T_r equals approximately A_s. From measurements both in the calorimeter and under an optical microscope, M_s and A_s are found to be 14°C and 46°C respectively. T_g and T_r are thus 16°C and 46°C respectively, and since T_o is approximated as being halfway between T_g and T_r, T_o is found to be 31°C. Using the appropriate values of $\Delta H_{chem}^{\beta_1 \to \gamma_1'}$ and T_o in Equation 13, a value of -0.405 cal/mole°K is calculated for $\Delta S_{chem}^{\beta_1 \to \gamma_1'}$. The chemical free-energy change at M_s for the single-interface transformation is then given by:

$$\Delta G_{chem}^{\beta_1 \to \gamma_1'} \quad (\text{at } M_s) = (T_o - M_s)\Delta S_{chem}^{\beta_1 \to \gamma_1'} \qquad [14]$$

and $\Delta G_{chem}^{\beta_1 \to \gamma_1'}$ (at M_s) is then found to be -6.9 cal/mole (i.e., the chemical driving force at M_s is equal to 6.9 cal/mole).

For the single-interface transformation, the effects of elastic strain energy are eliminated, and to a good approximation the entire hysteresis involved in moving an existing parent-martensite interface is caused by the existence of a frictional resistance to its motion. That is, a sufficient chemical driving

-173-

force must be built up (by cooling below T_o for the forward trans-
formation) to overcome the "resistance" of the lattice friction. Thus,
the interface friction contribution to the change in free energy
can be estimated (for the large interface moving in the single-
interface transformation) by finding the undercooling necessary
to move the existing interface. For the single-interface trans-
formation Equation 12 becomes:

$$\Delta G_{chem}^{\beta_1 \rightarrow \gamma_1'} (T_g) = -\Delta G_{frict} \quad \text{(for cooling)} \qquad [15]$$

and

$$\Delta G_{chem}^{\beta_1 \rightarrow \gamma_1'} (\text{at } T_g) = \Delta S(T_o - T_g) \qquad [16]$$

The contribution of the friction term to the change in free energy
thus is 6.1 cal/mole (for the foward or $\beta_1 \rightarrow \gamma_1'$ transformation).

The chemical thermodynamic terms for the $\beta_1 \rightarrow \gamma_1'$ transfor-
mation in Cu-14Al-3Ni can be calculated unambiguously from the
data known for the single-interface transformation. Table 10
gives a summary of the chemical thermodynamic terms calculated
in this work.

After establishing the chemical thermodynamic terms, it
is possible to gain a significant understanding of the effect that
elastic strain energy has on the thermodynamics. It is evident
from the calorimetric results that stored elastic energy lowers
the magnitude of the measured net enthalpy. Further, the magni-
tude of the measured enthalpy is decreased as the average trans-
formation temperature is lowered. The average transformation tem-
perature of a single-interface transformation in a single crystal
can be lowered by transforming the sample via a multiple-interface
mechanism. By sample preparation (control of grain size, nickel
plating, etc.), the transformation can be caused by proceed as a
finer and finer multiple-interface transformation which simultan-
eously causes the effect of strain energy to become larger and
larger.

TABLE 10

CHEMICAL THERMODYNAMIC QUANTITIES FOR Cu-14Al-3Ni
CALCULATED FROM CALORIMETRY DATA OF SINGLE-
INTERFACE TRANSFORMATIONS.

$$M_s = 14 \ ^\circ C$$

$$T_g = 16 \ ^\circ C \ ^*$$

$$A_s = 46 \ ^\circ C$$

$$T_0 = 31 \ ^\circ C$$

$$\Delta H_{chem}^{\beta_1 \to \gamma_1'} = -123 \ (cal/mole)$$

$$\Delta S_{chem}^{\beta_1 \to \gamma_1'} = -0.405 \ (cal/mole-^\circ K)$$

$$\Delta G_{chem}^{\beta_1 \to \gamma_1'} = -6.9 \ (cal/mole) \qquad (NUCLEATION)$$

$$\Delta G_{chem}^{\beta_1 \to \gamma_1'} = -6.1 \ (cal/mole) \qquad (GROWTH)$$

* FROM THE SINGLE-INTERFACE GRADIENT EXPERIMENT
$T_g - M_s \doteq 2 \ ^\circ C.$

-175-

Experimentally measured changes in enthalpy plotted as a function of the average transformation temperature are shown in Figure 105. The data points are measured enthalpy changes for the $\beta_1 \to \gamma_1'$ transformation in Cu-14Al-3Ni single-crystal chips spark cut from the same initial (large) single crystal sample. Included in this figure are enthalpy changes from Samples 2 and 3, and the nickel-plated Sample 1. The chemical enthalpy change (from the nonplated Sample 1) was found to be -123 cal/mole in the foregoing. The chemical enthalpy change was placed at the forward growth temperature, T_g, for the $\beta_1 \to \gamma_1'$ interface. The difference between the growth temperature and T_o reflects the driving force necessary to overcome the friction term. The approximate temperature for T_g (equal to M_s+2°C) was obtained for the previously described experiments on the growth of a single interface in a temperature gradient. The absolute number for the difference between T_g and M_s is small in this case, and indeed is about equal to the experimental error. However, the difference between T_g and M_s will be used because of the important conceptual distinction between the two temperatures.

The elastic entropy change can be related to the change of some appropriate modulus as a function of temperature. Specifically

$$\frac{\Delta S_{elas}}{\Delta G_{elas}} = \frac{-1}{M} \frac{dM}{dT} \qquad [17]$$

where M is some particular modulus (depending on the stress state created by the shape change of the transformation). Data for Young's modulus (35) and for the shear modulus (36) show $\frac{-1}{M} \frac{dM}{dT}$ to be about 2.5 x 10⁻⁷°C for Cu-Al-Ni specimens which undergo the $\beta_1 \to \gamma_1'$ transformation on cooling. Using this value of $\frac{-1}{M} \frac{dM}{dT}$, ΔS_{elas} (as a function of temperature) can be calculated if ΔG_{elas} (as a function of temperature) is known. Previously, the balance of free energy at a thermoelastic equilibrium was expressed as:

-176-
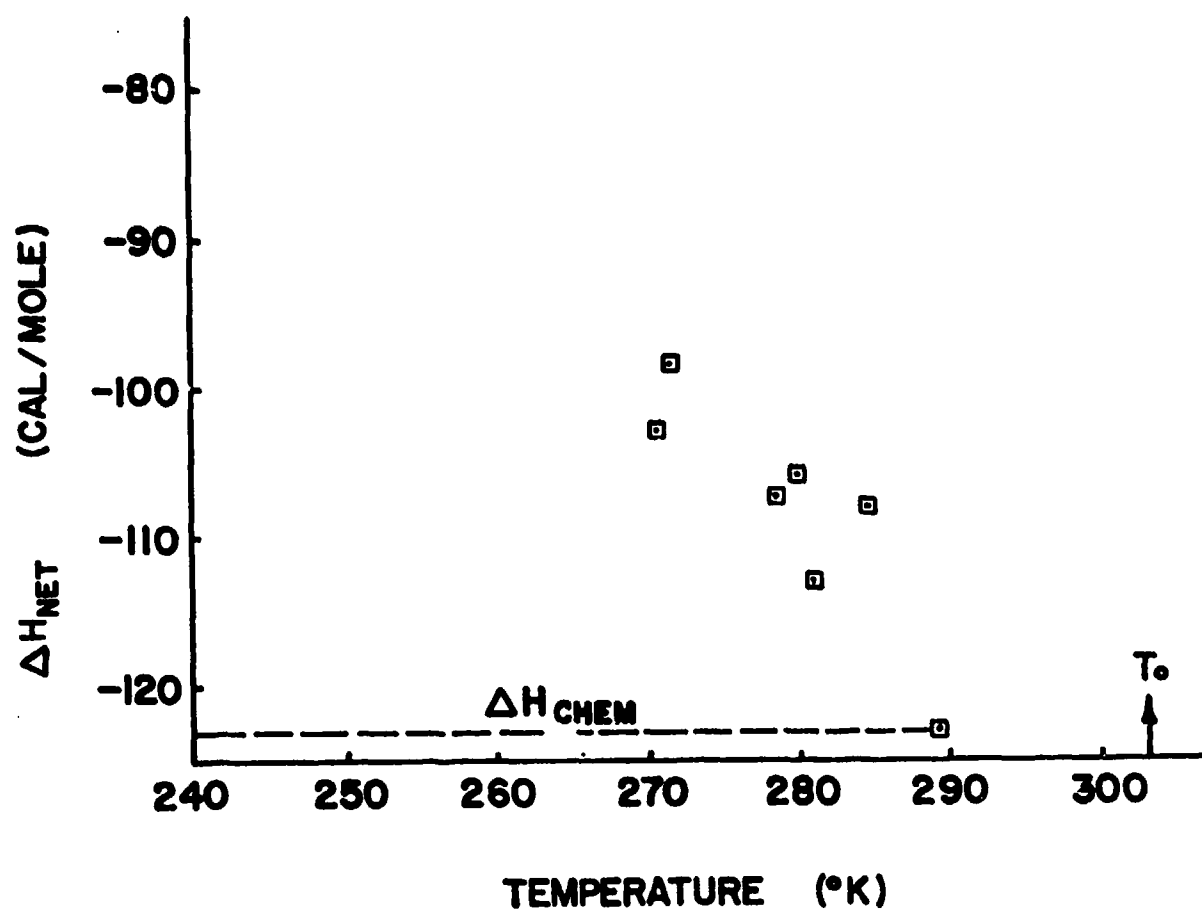
Figure 105.   Measured Change in Enthalpy Versus Average
Transformation Temperature for Single Crystals
of Cu-14Al-3Ni.

$$\Delta G_{chem} + n\Delta G_{elas} \approx -\Delta G_{frict} \qquad \text{(on cooling)} \qquad [18]$$

and since ΔG_{chem} can be calculated from

$$\Delta G_{chem}(\text{at } T) = \Delta S_{chem}(T_o - T) \qquad [19]$$

ΔG_{elas} can be calculated at each temperature if n and ΔG_{frict} are known. In the following calculations, a value of n equal to one has been used because it predicts the largest effect of strain energy and thus provides the best fit to the experimental data. The difference between T_o and T_g can be used to calculate the friction term for the motion of large interfaces (such as the single-interface transformation or the large initial plates of a multiple-interface transformation). The calculated value for ΔG_{frict} for the single-interface transformation is equal to 6.1 cal/mole. However, experimentally it has been shown that the last plates which form during the transformation often have a much smaller hysteresis between the temperatures for growth and reversion than the first plates to form. This indicates that the effective friction term is not a constant and that its magnitude is lowered as the transformation proceeds. Work by Wayman and co-workers, (37-38) as well as our own observations show that the hysteresis for the final plates formed is less than a third of that for initially formed plates. In fact, the sequential micrographs of a thermoelastic transformation (and reversion) in Fe_3Pt (37) indicate that there is an order of magnitude difference in the hysteresis between the temperatures for growth and shrinkage of various plates. This information suggests that the friction free energy term may vary during the course of the transformation. Hence, in the following calculations, two extremes are adopted relating to the maximum and minimum magnitudes between which the friction term is likely to vary during the transformation. The maximum magnitude used is the value of 6.1 cal/mole determined from the thermal hysteresis of moving the single interface back and forth. The minimum value used in the calculations is zero,

that is, the magnitude of the friction term appears negligible as the transformation approaches completion. With these extreme values of the friction term (and $n=1$), two functions of ΔG_{elas} (vs. temperature) can be calculated (from Equation 18). This, in turn, then leads to two functions of ΔS_{elas} with temperature (from Equation 17), and these can be used to calculate changes in ΔH_{elas} with temperature (again two functions) from the following relation:

$$\Delta H_{elas} = \Delta G_{elas} + T\Delta S_{elas} \qquad [20]$$

Finally, two ranges of ΔH_{net} as a function of temperature are found from

$$\Delta H_{net} = \Delta H_{elas} + \Delta H_{chem} = \Delta H_{elas} - 123 \text{ cal/mole} \quad [21]$$

Figure 106 shows the calculated values of ΔH_{net} (dashed lines) which correspond to using maximum and minimum values of the frictional term. As shown in Figure 106, some of the data lie outside of the predicted band. The width of the calorimeter peak is included for each point. Thus it is reasonable to assert that the average transformation temperature should really be used as an upper limit for the functional dependence of ΔH_{net} on temperature. This is because most of the elastic energy (specifically in the case of single-crystals, the data of which is reported in Figure 106) is generated in the sample as the multiple-interface transformation approaches completion. As the transformation proceeds, the martensitic plates impinge upon, and constrain, each other, and this impingement and constraint becomes highest (i.e., more strain energy is stored per unit volume) near the end of the transformation. The actual temperature dependence of ΔH_{net} should then probably be biased more toward the lower end of the transformation peak than to the center of mass (i.e., the average transformation temperature) of the peak.

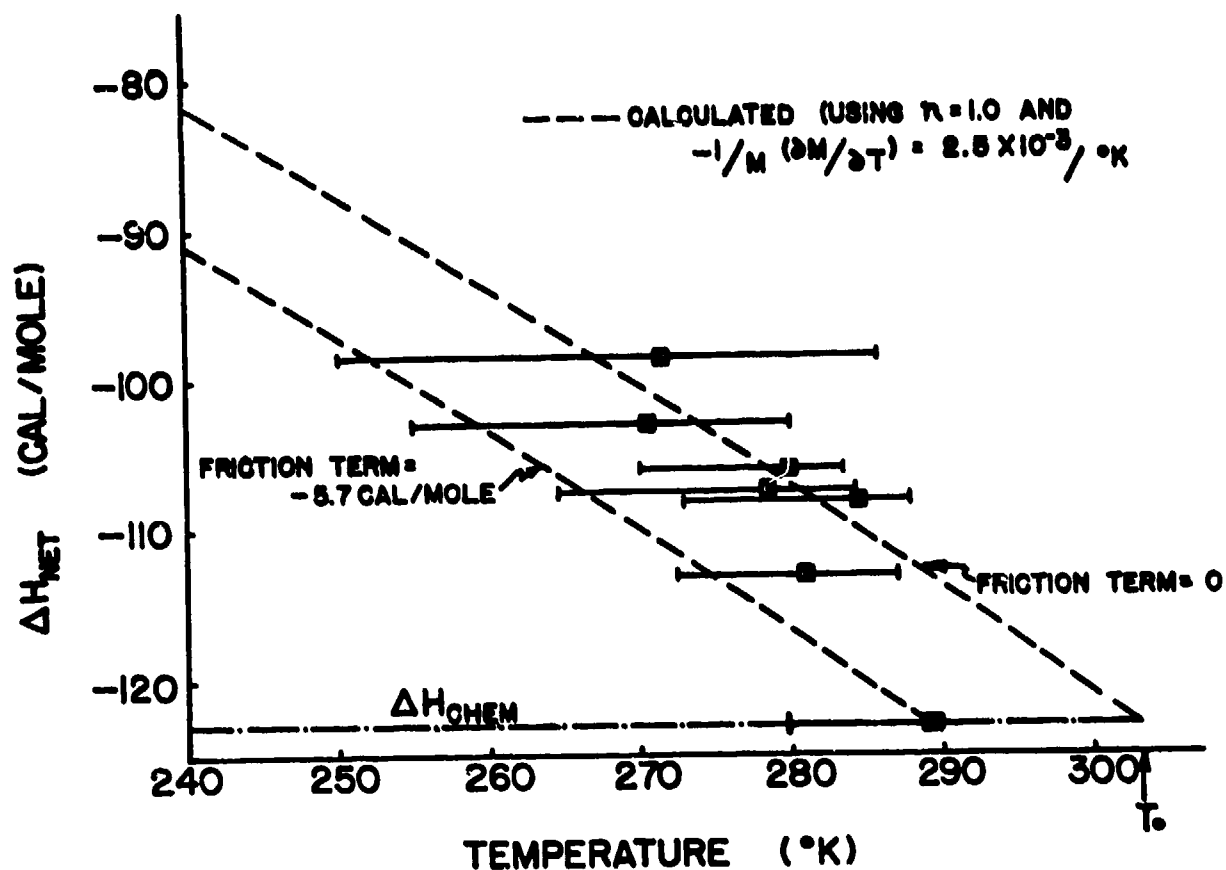Any remaining difference between the experimental points

-179-

Figure 106. Comparison of Calculated Versus Measured Values
of ΔH_{net} as a Function of Temperature.

and the band calculated from the modulus data could possibly be
due to a significant increase in the amount of interfacial area
due to twins (and/or stacking faults) as the martensitic plates
become finer and finer. In this work it has been found that the
number of martensitic plates increases and, correspondingly, the plate
size decreases as the average transformation temperature is lowered.
It has further been reported in the Cu-Al system (which undergoes
the same transformation from β_1 to γ_1' that the twin spacing de-
creases with the size of the martensite plate (39). In alloys
of Cu-Al-Ni which undergo the $\beta_1 \rightarrow \gamma_1'$ transformation, it has also
been reported that the width of the twins varies significantly
from one plate to another; but no correlation was made with overall
plate size (40). Replicas of the alloys studied in this work do
however, suggest a tendency of the twin spacing to decrease with
plate size.

The contribution of twin boundaries to the net change in
enthalpy (ΔH_{TB}) is given approximately by:

$$\Delta H_{TB} = \gamma V_M \frac{1}{d} \qquad [22]$$

where γ is the boundary interfacial energy (which is on the order
of 30 ergs/cm^2), V_M is the molar volume (7.46 cm^3/mole), and d
is the twin spacing. In order for the increase in twin boundary
area (or stacking-fault area) to account for the discrepancy in
Figure 106 (of up to 3 cal/mole), the spacing between the twins
(or stacking faults) in the last plates to form would have to be
on the order of 250Å. On the other hand, the interface spacing
(of twins and/or stacking faults) would have to be above about
1500Å in the initial large plates in order that the contribution
to the enthalpy change from interfacial energy be negligible. The
information available on the microstructure of Cu-Al-Ni shows that
the twin spacing of the γ_1' martensites can range from below 500Å to
as high as about 10,000Å. It is also apparent that stacking faults
can form with a fine spacing in some γ_1' martensitic plates, but
this unfortunately has not been correlated with the size of the
martensitic plates. Further experiments would have to be made to

quantify the contribution of interfacial energy to the measured enthalpy change, and to determine whether or not this can explain why some experimental data fall outside of the calculated band.

To summarize, the calorimetric data of Cu-14Al-3Ni shows that elastic contributions are not negligible. Further, calculations have shown that the experimental data can be fitted fairly well by using reasonable values of n, $\frac{-1}{M}\frac{dM}{dT}$, and ΔG_{frict}.

2. Damping in Thermoelastic Cu-Al-Ni Alloys

Previous reports (1-5) as well as articles in the literature (35-45) have identified Cu-Al-Ni alloys which undergo the $\beta_1 \rightarrow \gamma_1'$ transformation as a high damping material. Several methods have been employed to measure the damping in thermoelastic martensites, and in many cases, the actual damping curve is quite complicated. A schematic representation of measured damping curves can however be presented which divides the damping behavior into three regions. This schematic illustration is shown in Figure 107. In region I, the damping is relatively low and can adequately be accounted for by dislocation damping (35-42) The damping in region I is not directly connected with the martensitic transformation and thus will not be considered further. The high damping in regions II and III appears to be associated with the nature of the thermoelastic martensitic transformation. The damping in region II has been attributed to the energy loss associated with parent-martensite (P-M) interface motion (35-44). The fairly substantial damping often found in region III (for the thermoelastic martensites) has been ascribed to the motion of defects within the fully martensitic structure. The particular defects proposed as being most important are twin boundaries and martensite-martensite (M-M) interfaces.

Important aspects of the damping behavior in region II will now be presented and discussed. Figure 108* presents strong

---

* Figure 108 is a schematic representation of data in references (35-45).
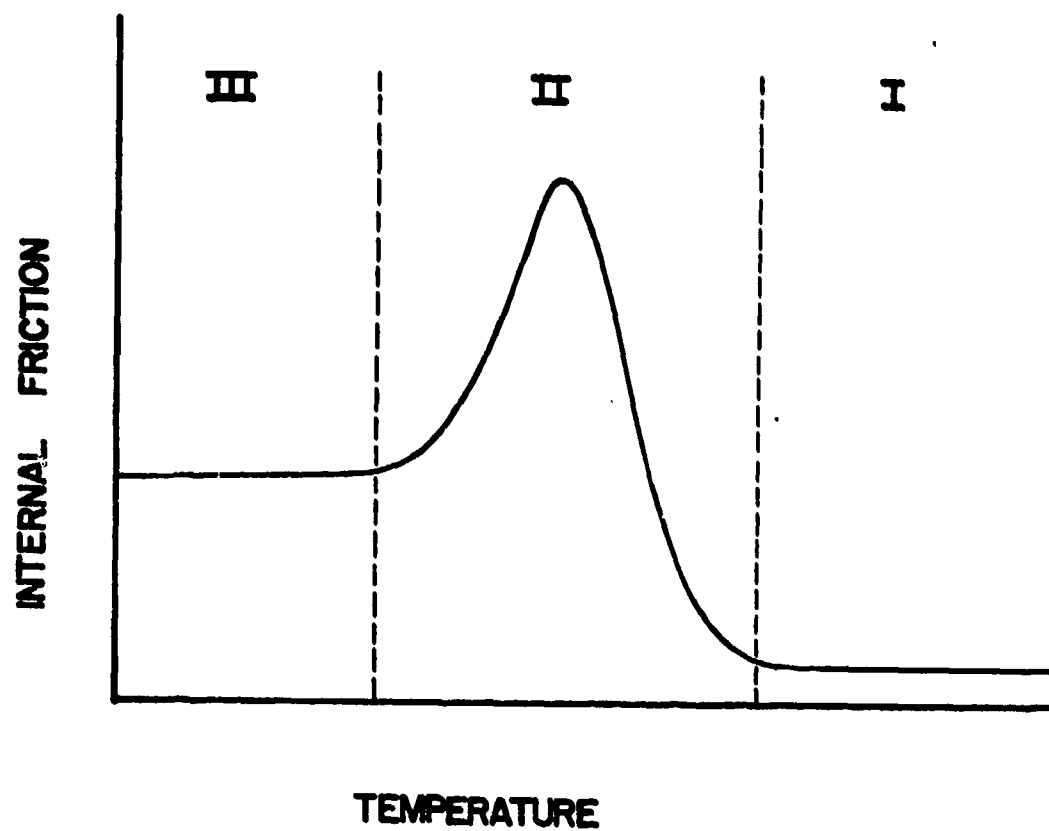
Figure 107.   Schematic Illustration of the Internal Friction
in Thermoelastic Martensites.

evidence for considering the motion of P-M interfaces to be the
most important damping mechanism in region II. The damping
shown in Figure 108 peaks when the transformation is approxi-
mately 50% complete. The damping is a function of the amount
of P-M interface present, and thus the damping increases as the
amount of P-M interface increases up to the point where the vol-
ume of the martensite approximately equals that of the parent.
When the transformation increases beyond this point, the marten-
sitic plates increasingly impinge on one another meaning that the
P-M interfaces are no longer as free to move. Then the interfaces
cease to damp as effectively. The damping in region II has also
been shown to be amplitude dependent (36-45) and frequency indep-
dent, (34-45). This behavior is expected for damping caused by
the motion of P-M interfaces.

For most practical applications of damping materials,
it is important that the mechanism causing the vibrational energy
dissipation not be exhausted after some number of cycles. In the
present example, this means that the P-M interface should be able
to be moved in either direction with little hysteresis in either
stress or temperature. This indicates that it is important for
the martensitic transformation to possess a high degree of thermo-
elasticity if it is to have good continuous damping properties.
A graphic example of this is seen when the damping behavior of a
thermoelastic martensite is compared to the damping behavior of
a nonthermoelastic martensite (44). Figure 109 shows the damp-
ing behavior of a thermoelastic Cu-Al-Ni alloy. The dashed curve
in Figure 109A shows the measured damping exhibited by the alloy
on continuous cooling (at 3°C/min). The solid curve in Figure
109A shows the "stable" damping behavior which was obtained by
measuring the damping after holding the sample at each temperature
for ten minutes. The isothermal damping curves as a function of
time at a particular temperature are shown in Figure 109b. In
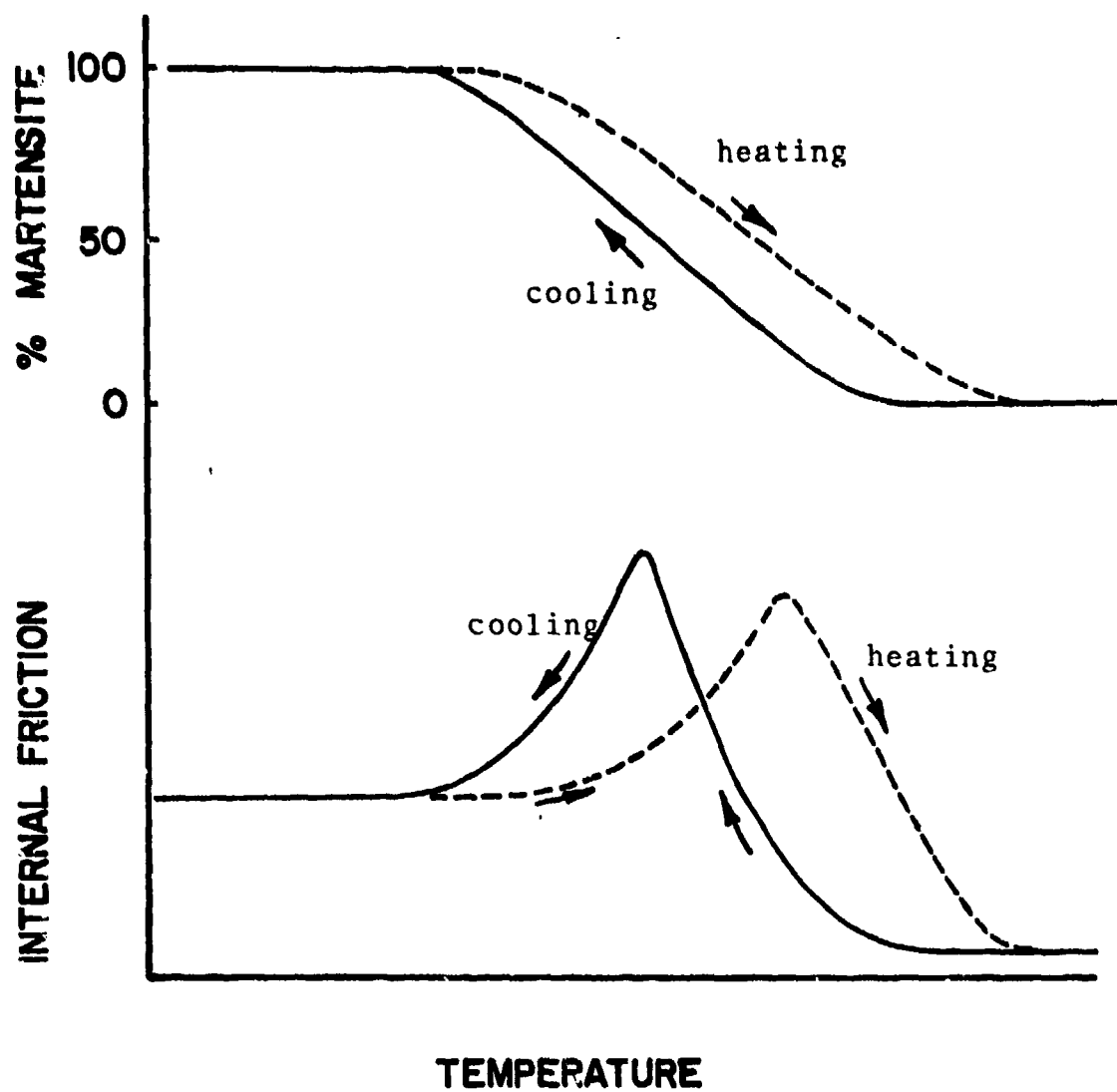this figure, it is clearly demonstrated that the damping at vari-

Figure 108.   Transformation Curve and Damping Curve
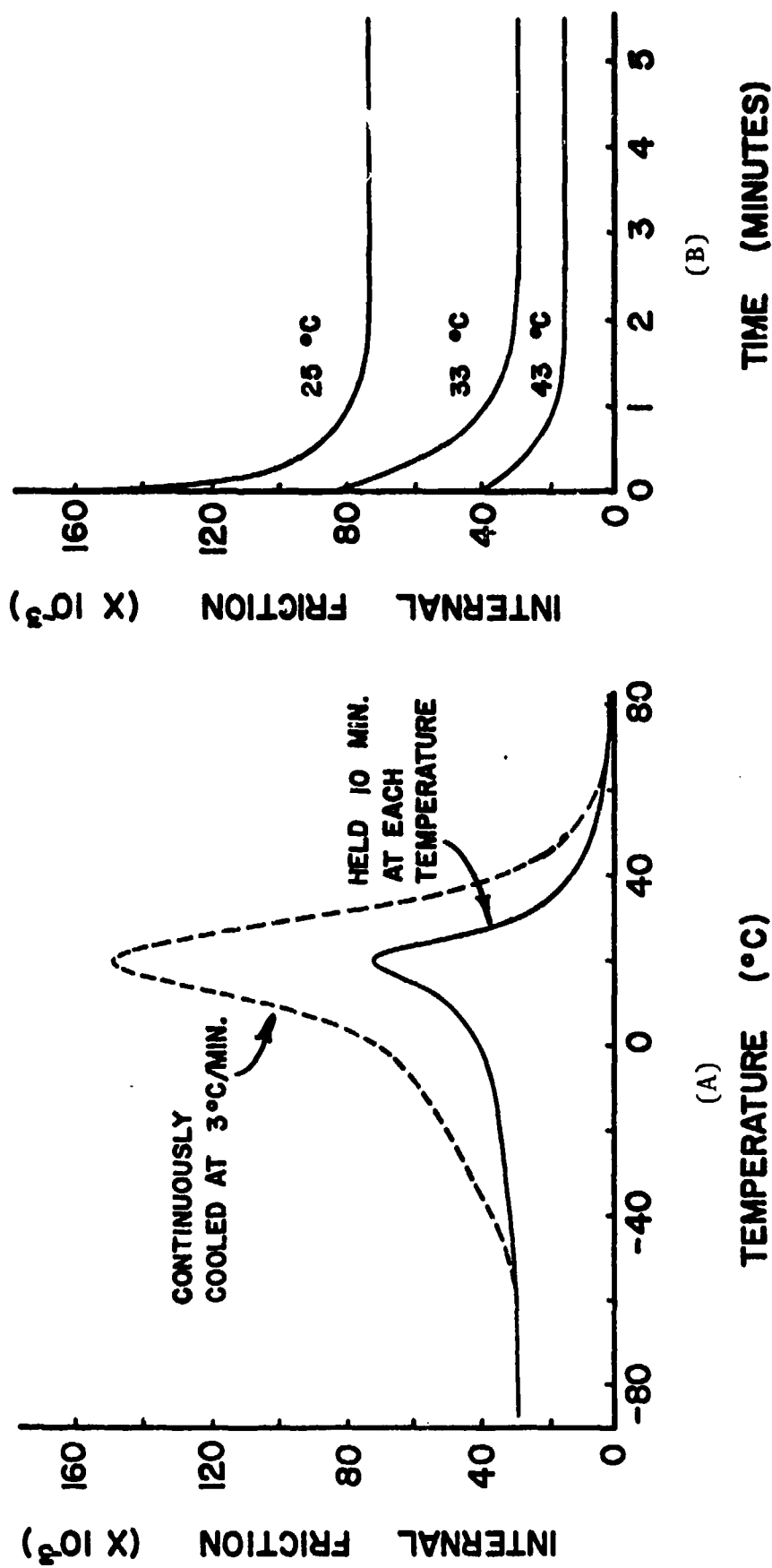as Functions of Temperature (from
Reference 4).

Figure 109. A) Stable and Unstable Internal Friction Curves for the Thermoelastic Cu-Al-Ni Alloy.
B) Internal Friction as a Function of Time During Isothermal Soaking (from Reference 44).

-186-

ous temperatures decreases with time until stable behavior is attained. The stable peak-damping value for the thermoelastic Cu-Al-Ni still remains at a very high level, demonstrating that some damping mechanism continues to operate effectively through many cycles. In contrast to the thermoelastic damping behavior shown in Figure 109, the damping characteristics of a nonthermo-elastic martensite are shown in Figure 110. Again, the dashed cu ve (Figure 110A) shows the damping measured when the alloy was continuously cooled (at 4°C/min) and the solid line shows the "stable" damping measured after holding the sample at each temperature for five minutes. The decay with time of the damping measured isothermally is shown in Figure 110b. Thus, in contrast to the thermoelastic martensite, the damping behavior of the nonthermoelastic martensite shows that the damping falls to the background level (established in region I) after a few minutes at all temperatures. This demonstrates the importance of having a repeatable mechanism to cause the damping. In the case of a martensitic transformation, it is quite important that the transformation have a large amount of thermoelasticity. When the thermoelastic nature is complete, (i.e., there is no irrever-sible plastic accomodation of the transformational shape change), the interface between the parent and the martensite can move in either direction with only a relatively small amount of hysteresis (in either stress or temperature). The motion of the P-M inter-face in response to the vibrational stress is thus able to cause damping of the static hysteresis type (46).

Microstructural evidence for the P-M damping mechanism is given by the optical micrographs shown in Figures 111 and 112. These micrographs show that P-M interfaces can move forward with stress and revert with little hysteresis and no time delay. Ten-sile stresses on the order of 5000 psi were applied to samples being held at constant temperature. In Figure 111, the sample was at a temperature of 40°C which is about 35°C above M_s.

-187-

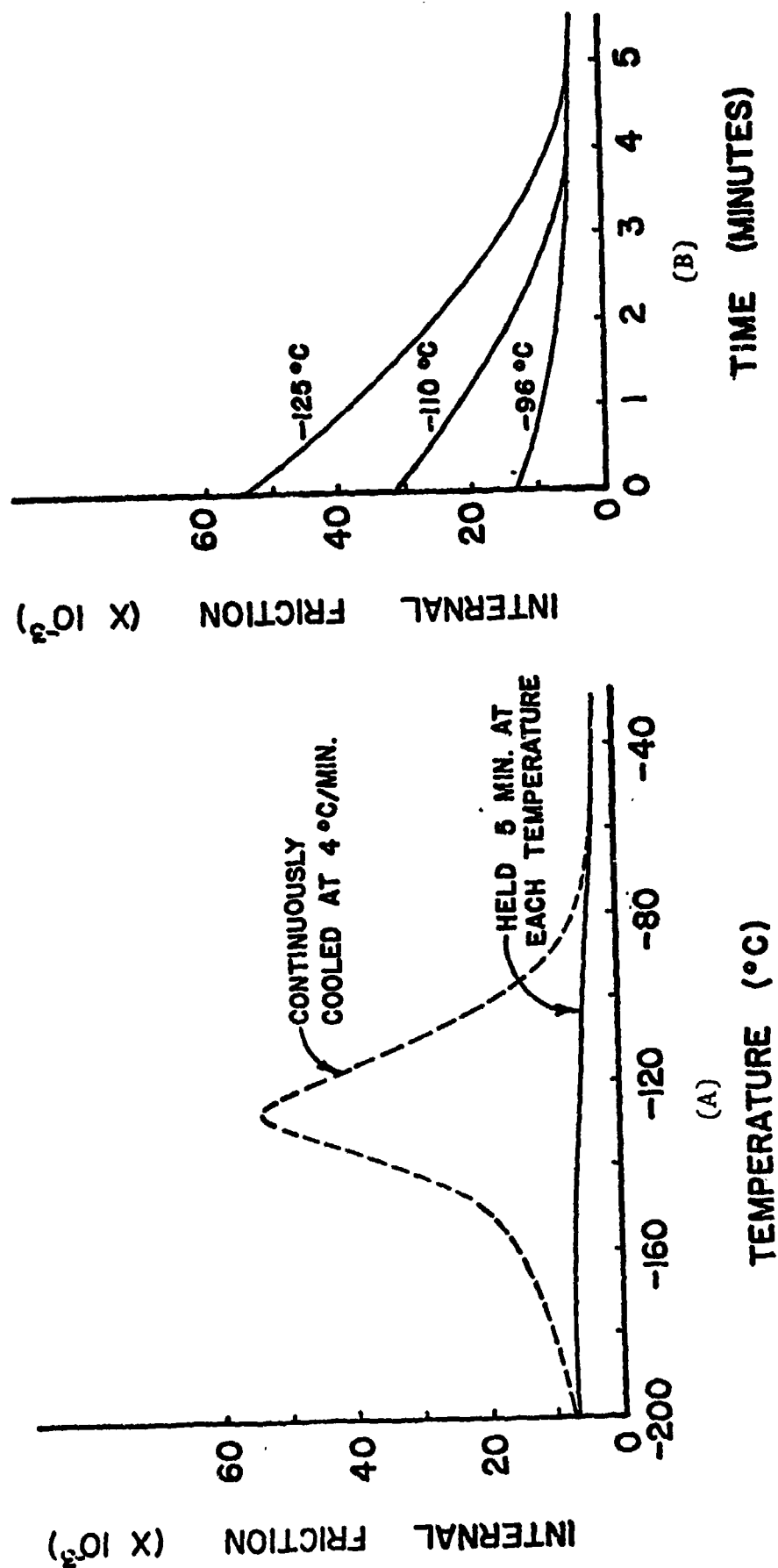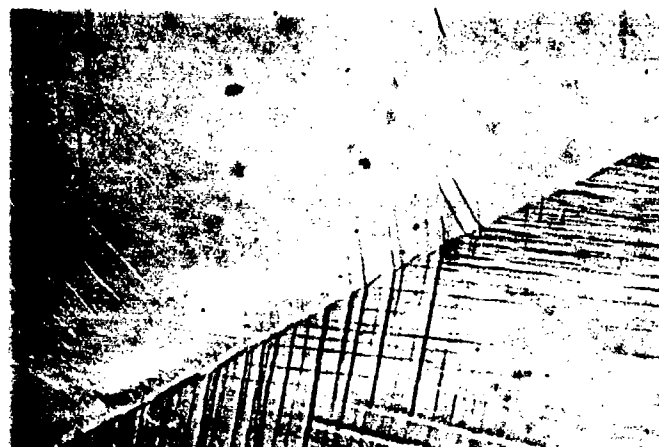Figure 110. A) Stable and Unstable Internal Friction Curves for the Nonthermoelastic Cu-Sn Alloy.
B) Internal Friction as a Function of Time During Isothermal Soaking (from Reference 44).

-188-

(A)

(B)

(C)

Figure 111. Optical Micrograph (Magnification 50X) of Cu-14Al-3Ni
          At a Temperature 36°C above M_S. (A) Unstressed,
          (B) Applied Stress of 5000 psi, and (C) Stress
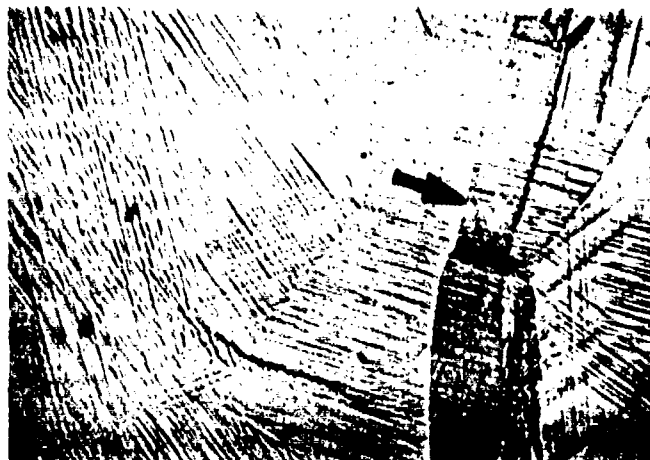   Released.

-189-

Figure 111A is the microstructure with no stress applied,* and in Figure 111B a stress (of approximately 5000 psi) was applied. Note that the number and width of the acicular martensitic units have increased. In Figure 111C the stress was again returned to zero, and the microstructure has been reverted to very close to the first microstructure shown in 111a. The acicular martensite formed by stressing the matrix well above M_s has been identified by Otsuka and Shimizu (47) as being of the β_1' (or 9R) type compared to the thermally formed γ_1' (or 2H) type.

As the temperature is moved close to M_s, the stress-induced martensite is the same as that thermally formed (γ_1' or the 2H). Figure 112A shows the Cu-14Al-3Ni sample just below M_s; the thermally formed martensite is platelike designated by the arrows in the micrograph. In Figure 112B with a stress applied (again roughly 5000 psi), existing plates have increased in both thickness and length (see arrows) and new plates of γ_1' have been formed. As in the previous example, when the stress is released (Figure 112C), the microstructure returns substantially to that of the unstressed state (Figure 112A).

These results show that for stresses on the order of those employed in testing the damping of the samples (2-5 ksi) that P-M interfaces can indeed move. Further, they are glissile in both directions and are not necessarily prevented from returning to their original position when the stress is released (or the sample is stressed in the opposite sense).

The damping in region III (see Figure 107) has been ascribed to the motion of twin boundaries and/or the martensite-martensite (M-M) boundaries. As was found in region II, the damping in region III is amplitude dependent as well as frequency in-

---

* Earlier in the sample's history, however, stress had been applied which induced the nonreverted acicular-type martensite seen in in the micrograph.

(A)
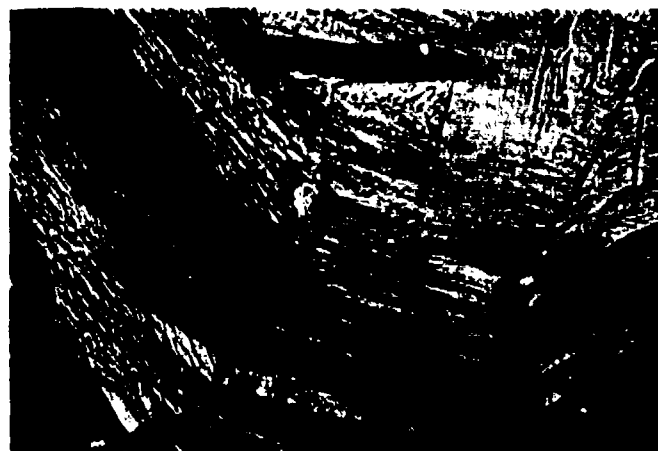
(B)

(C)

Figure 112. Optical Micrograph (Magnification 50X) of Cu-14Al-3Ni at a Temperature Just Below M_s. (A) Unstressed, (B) Applied Stress of 5000 psi, and (C) Stress Released.

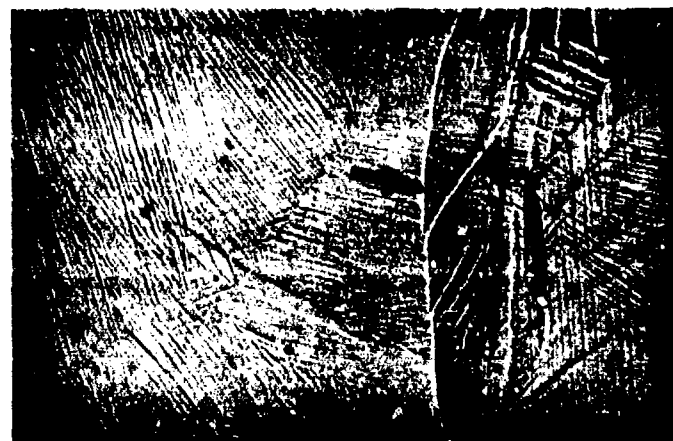dependent ($\underline{35}$-$\underline{45}$). Again, this is consistent with the proposed
damping mechanism (i.e., the motion of twin or M-M interfaces).
Referring again to Figures 109 and 110, a substantial difference
of the damping in region III is seen between the thermoelastic
and nonthermoelastic martensites. The damping of the nonthei-
moelastic martensite at temperatures where the sample is entirely
martensite is not substantially above the background level of
region I (where the sample is all parent phase). The stable
damping of the martensite is low because the transformation
strain is not stored elastically in the lattice, but rather there
is a large amount of nonrecoverable plastic accomodation of the
transformation strain. This nonrecoverable plastic accomodation
prevents the reversible motion of twin boundaries and/or M-M
interfaces and cannot itself be used effectively in damping. In
contrast, the damping level in region III of the thermoelastic
alloy is substantially above the background level in region I. It
is well known ($\underline{40}$-$\underline{48}$) that the γ_1' martensite in Cu-Al-Ni contains
substantial numbers of twins and that there is little non-
recoverable plastic accomodation of the transformation. This
implies that motion of twin interfaces and M-M boundaries in
response to a stress should not be obstructed by a large amount
of dislocation debris. Electron microscopy work ($\underline{48}$) performed
on γ_1' Cu-Al-Ni martensites has demonstrated the mobility of twins
under stress. Figure 113 shows optical micrographs where the
reversible motion of twin boundaries on application of a tensile
load to the specimen is recorded. This then provides microstruc-
tural evidence that twin boundaries are glissile and therefore
their stress-induced motion can cause static hysteresis-type
damping.

The microstructure of fully martensitic samples which
have been loaded (in tension and/or compression) is often very com-
plicated, and it becomes difficult to identify the individual fea-
tures as being twins within a single martensite variant or twin-
related martensitic variants. Under certain conditions, there are
several different sets of nearly parallel microstructural features

(A)
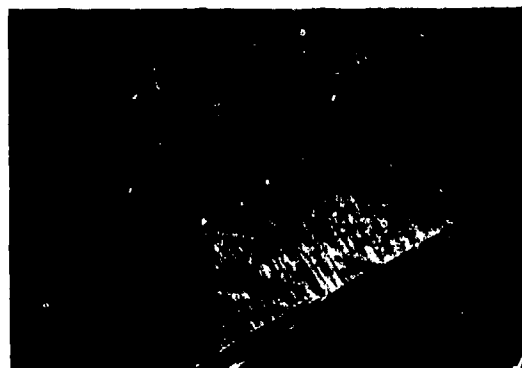
(B)

(C)

Figure 113. Optical Micrographs (Magnification 80X) of a
Cu-14Al-3Ni Single Crystal at a Temperature
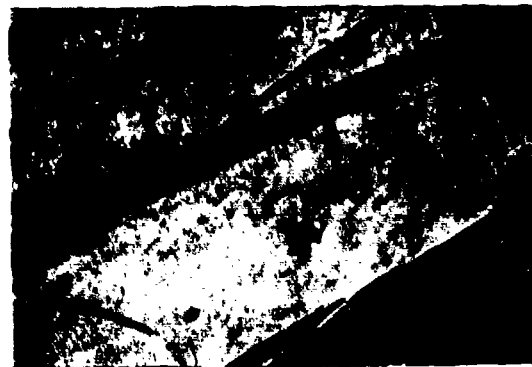Below M_f.

A) Tensile Stress Applied (to about 2 ksi).
B) Tensile Stress Released.
C) Tensile Stress Applied (to about 3 ksi).

-193-

which can move reversibly in response to stress and can thus be considered as capable of causing damping. An M-M interface which can be very clearly identified and seen to move in response to a stress is shown in Figure 114. In Figure 114A the thermally-formed fully martensitic structure is shown, and when a tensile load is applied, the martensite variant denoted by the arrow becomes successively more narrow and shrinks in size (Figure 114B and 114C). However, upon release of the stress or upon application of a stress of oppostie sign, the variant marked in Figure 114 did not widen or grow (i.e., the M-M interface did not move in the opposite direction). This behavior was observed in several instances; specifically, the reversible motion of definite M-M interfaces was never observed. This would seem to cast doubt as to whether M-M motion is an important damping mechanism. It is important to note, however, that these M-M boundaries were observed in a single crystal and the M-M interfaces may not have moved in the reverse direction because of the lack of sufficient stored elastic strain energy (due to absence of grain boundary constraints on sample shape). It is also possible that the correct stress to move the observed M-M interfaces in the opposite direction could not be applied because of sample geometry. Attempts to observe the motion of features in the micro structure of fully transformed polycrystalline samples were not successful due to intergranular fracture at fairly low loads.

A single martensitic variant with very few apparent microstructural features, formed by applying a tensile load is shown in Figure 115A. Figure 115B shows the typical complicated microstructure often observed; the structure in Figure 115B was formed by releasing the tensile stress and applying a compressive load to the sample. It is not readily apparent from studying the microstructure at this magnification (80X) as well as magnifications up to 500X whether the parallel features are twins within a single variant or are twin-related variants of martensite.

-194-

(A)

(B)

(C)

Figure 114. Optical Micrographs (Magnification 80X) of a
Cu-14Al-3Ni Single Crystal at a Temperature
Below M_f.
A) Initial microstructure (fully martensite
under no load).
B) Tensile Stress Applied (about 1 ksi).
C) Increased Tensile Stress Applied (about
5 ksi).

-195-

(A)

(B)

(C)

(D)

(E)

Figure 115. Optical Micrographs (Magnification 80X) of a Cu-14Al-3Ni Single Crystal at a Temperature Below M_f.

A) Single Variant (formed by application of a tensile load).
B) Compressive Stress Applied and Released.
C) Tensile Stress (to about 1 ksi).
D) Tensile Stress Increased (to about 3 ksi).
E) Tensile Stress Increased (to about 6 ksi-single variant).

-196-

When a tensile stress is applied, many of the microstructural twin-like features move and some grow at the expense of others (Figures 115C and 115D),and at a high enough tensile load, the microstructure is essentially featureless (Figure 115E). That is, one twin-like orientation has become favored enough to eliminate the other. The sequence shown in Figure 115 shows the reversible motion of the twin-like features first formed by a compressive load.

Strong evidence has thus been presented that the motion of twin boundaries gives rise to the relatively high damping in region III. The microstructural support for the reversible motion of M-M interfaces is not as clear. The growth under stress of some variants at the expense of others has been observed in several cases; however, this growth did not reverse when a stress of opposite sign was applied (at least in the case of a single crystal). In many cases involving a complicated microstructure, however, it has not been established if the parallel microstructural features (which do move reversibly with stress) are twins within a single martensite variant or are twin-related variants of martensite. If some of the parallel features in Figure 115 are twin-related martensitic variants, the observed reversible motion of these features (then classified as the motion of M-M interfaces) would provide evidence for damping due to a M-M interface mechanism.

3. Brittleness in Cu$_3$Al-Base Alloys

The problem of brittleness in polycrystalline Cu$_3$Al-based alloys is of considerable importance in developing a useful alloy. The phase diagram of the Cu-Al system indicates that the equilibrium structure of the alloy under study lies in the $\alpha + \gamma_2$ phase field, and γ_2 has a brittle hcp structure. In the foundry industry, Cu-Al alloys with more than 10w/o Al are avoided because of extreme brittleness

caused by the γ_2 phase. It has also been claimed (49) that the retained β_1 phase is instrumental in causing brittleness in Cu-Al alloys. When nickel is added to the Cu-Al alloys, further difficulties may be encountered because of brittle Ni-Al inter-metallic compounds. In Cu-Al-Ni polycrystalline samples, the embrittlement is so severe that essentially no plastic deformation can be induced prior to intergranular fracture. By optical examination, the main problem seems to be the formation of a precipitate at the grain boundaries. Accordingly, a typical solution would be to increase the grain-boundary area and to break-up the continuity of the grain-boundary precipitate; this result is often accomplished in various alloy systems by hot working.

Samples of the Cu-Al-3.0Ni alloy containing from 12 to 14.2 w/o Al were hot rolled at temperatures from 550 to 900°C, the reduction usually being greater than 50% (after several passes). A small but noticeable increase in ductility in alloys of 12.6 w/o Al and 13.8 w/o Al was achieved by hot rolling at 800°C (80% in 5-10 passes) and water quenching directly from the rolls. The increase in ductility was, however, not large enough to be of practical interest. A sample 1/15 inch thick about 3 inches long could only be bent to a radius of curvature of about 15 inches. These thermomechanical treatments of the Cu-Al-Ni alloys had a negligible effect on the grain size (the average grain size stayed at about D=0.5 mm throughout the processing) The major effect of the hot rolling and quenching seemed to lie in the breaking-up of the precipitates at the grain boundaries (as seen in the optical microscope).

To refine the grain size of cast Cu-Al alloys in practice, the most common element added is iron. Mn is also used in some cases. The additions of Fe and Mn are also known to depress the M_s in Cu-Al alloys (Ni was added to the Cu-Al alloys in order to depress the M_s from about 150-300°C to near room temperature). Thus, the additions of Fe and/or Mn to replace Ni in the Cu-Al alloys were

hoped to have two beneficial effects. The first was that the Fe and Mn would refine the grain size and thereby present more grain-boundary area to any brittle precipitate-enough to make it non-continuous at the grain boundaries. Secondly, the replacement of Ni by Fe and Mn might rid the system of any troublesome Ni-Al precipitates.

A series of samples of Cu-14.0Al with additions of 2 to 6 w/o Mn and 3 to 5 w/o Fe were induction-melted under a partial argon atmosphere and cast into an iron mold. The samples were solutionized at 950°C and quenched; those containing 4 to 6 w/o Mn cracked on quenching. The as-quenched samples of 2 and 3 w/o Mn (at room temperature) showed an equiaxed structure (retained β_1) with clear evidence of precipitates at the grain boundaries. The 3 to 5 w/o Fe alloys were fully transformed to martensite at room temperature and also showed evidence of grain-boundary precipitation as well as fine precipitates dispersed throughout the matrix. Table 11 summarizes the effects of Mn and Fe additions on the grain size of the cast Cu-Al alloys. The Mn lowered the M_s to below room temperature (in the 3 w/o Mn alloy the M_s was below -20°C, and in the 6 w/o Mn alloy the M_s was below the liquid-nitrogen temperature). The Fe helped refine the grain size but seemed to have little effect in reducing M_s (heating the 5 w/o Fe sample to about 100°C caused no reversion).

The Cu-Al alloys containing Mn and Fe were hot rolled at 800°C; however, the hot rolling yielded no appreciable improvement in the ductility. The brittleness, therefore, seems to be little affected by the presence of Ni. There now remain two probable causes for the brittleness of the Cu-Al alloys. First, the alloys of Cu-Al which contain greater than about 10 w/o Al have an equilibrium structure which is two-phase $(\alpha + \gamma_2)$ at room temperature, and it seems as though the formation of the brittle γ_2 phase at grain boundaries cannot be fully suppressed even with fairly fast quenching from the β_1 field (i.e., quenching into iced brine from

-199-

TABLE II

THE EFFECT OF Mn AND Fe ADDITIONS ON THE
GRAIN SIZE OF Cu-14 w/o Al.

ADDITION (w/o)	GRAIN SIZE (Grains / in^2)
2 % Mn	30-35
3 % Mn	35-40
4 % Mn	45
5 % Mn	55
6 % Mn	70
3 % Fe	50
4 % Fe	65
5 % Fe	200

950°C).

Secondly, compression tests on the β_1 phase of Cu-14.1Al-3.0Ni single crystals by Shepard (50) indicate that normal slip is very difficult (at best) in this alloy. The single crystal samples of (100) orientation were stressed to 100 ksi with no indication on non-recoverable plastic flow (i.e., plastic flow caused by slip yielding). The only exception was the development of kink bands in some single-crystal orientations. These results suggest that, when stress-induced transformations take place in polycrystalline Cu-Al-Ni alloys, the compatibility requirement that five independent deformation systems must operate in each individual grain can only be met by having at least five martensitic variants form within each grain. The stress (within the grain) needed to induce the formation of variants oriented nonpreferentially to the macroscopically-applied stress may be sufficiently high to cause fracture at the grain boundaries. The combination of the brittle intermetallics at the grain boundaries and the lack of dislocation-caused plasticity in this case seem to work together to make Cu-Al alloys lack any appreciable ductility. Solutions to this problem would seem to involve first the removal of the brittle precipitates at the grain boundary,(thus making the grain boundary more ductile), and second to lower the dislocation flow stress. Lowering the dislocation flow stress would allow the proper stress compatibility conditions to operate at the grain boundaries.

4. Studies of Cobalt-Iron Alloys

Certain Co-Fe-based alloys have been found to possess high damping capacities (see section IV), and specifically, compositions near 80Co-20Fe seem to have the highest damping. A series of micrographs of the 80Co-20Fe alloys are shown in Figures 116 through 120. The starting material was a rod which had been swaged to about 60% of its starting diameter. The microstructure is shown in Figure 116. Two samples were then encapsulated in Vycor and heat treated at 1000°C for one hour--one sample was water quenched (capsule was broken), and the other

-201-

was air cooled in the capsule. Micrographs are given in Figures
117 and 118. They indicate that (1) no martensite was formed
on being cooled to room temperature, and (2) no martensite
formed as a result of the polishing. Further cooling in
liquid nitrogen also gave no evidence of any phase transforma-
tion occurring in either the water-quenched or slowly-cooled
samples.

Figure 117A shows an area of the sample which underwent
considerable grain growth during heat treatment, where as 117B
is another section of the same surface in which a smaller amount
of grain growth was observed. The microstructure of the air-
cooled (encapsulated) sample is shown in Figure 118. Again
there were areas with a large amount of grain growth (Figure
118A) and other areas where the grain growth was significally
smaller (Figure 118B).

A goal of this part of the investigation was to
identify the damping mechanisms in potential structural
materials which exhibit high damping capacities. The
mechanisms thought to cause the major portion of the damping
in the relevant materials are of the static hysteresis type.
The operative mecahnism is thought to involve the motion of
twin boundaries, stacking faults, magnetic domain boundaries,
and the interfaces between parent and martensitic phases.
Damping caused by the motion of interfaces is characterized
by being amplitude (or stress) dependent, and by being
essentially frequency independent. The amplitude dependence
of the Co-Fe alloy, which is considered to be a main candidate
material, has been shown in prior reports (3-4-5).· The
frequency dependence of the high damping Co-Fe alloys has
not yet been measured.

Because of the strong probability that magnetic domain-
wall motion contributes significantly to the damping in Co-Fe
alloys, the magnetic-domain structure of 80Co-20Fe was investigated

Figure 116. Structure of Heavily Swaged 80Co-20Fe (200x).

(A)

(B)

Figure 117. (A) Grain Growth of 80Co-20Fe Annealed One Hour at
1000°C and Water Quenches (200x).

(B) Area of Same Sample Showing Little Grain Growth
(200x).

-204-

(A)

(B)

Figure   118.   (A) Grain Growth of 80Co-20Fe Annealed One Hour
                   at 1000°C and Air Cooled (in Vycor Capsule)
                   (200x).

               (B) Area of Same Sample Showing Little Grain
                   Growth (200x).

-205-

using a colloidal suspension of magnetic particles. Figure 119
shows the domain pattern associated with the water-quenched
80Co-20Fe alloy, and Figure 120, the domain structure of the
same alloy after air cooling. The domain size of the water-
quenched sample seems to be somewhat larger than that of the
air-cooled sample.

It has been described in a previous section (Section IV)
how the Co-Fe alloys with a composition near 80 w/o Co-20 w/o Fe
are close to undergoing a fcc-bcc transformation at room tempera-
ture. Also the 80Co-20Fe alloy has a Curie temperature which is
quite high -- near 950°C. The experimentally determined damping
in various Co-Fe alloys (with compositions near 80Co-20Fe) shows
a very strong dependence on whether the alloy is completely fcc
(high damping) or is bcc or some mixture of fcc and bcc (lower
damping). Since the Curie temperature in both the fcc and bcc
phases is very high, it was thought that magnetic domain wall
motion damping could cause of only a portion of the total
damping. It has been shown in the damping tests that the damping
of a suitably heat treated 80Co-20Fe sample was reduced by approxi-
mately 55% when a saturating magnetic field was applied during
testing. This indicates that although magnetic domain wall
damping is important, it is not the sole damping mechan-
ism. Because the 80Co-20Fe alloy displays the highest damping
when the alloy is all fcc (and seemingly about to transform to
bcc), it was proposed that much of the damping is caused by the
alloy being in a metastable phase condition. The exact nature
of the mechanism causing the high damping was, however, not
specified. With the intention of identifying additional possible
damping mechanisms, a study of the microstructure by trans-
mission electron microscopy was initated.

The 80Co-20Fe alloy was rolled (with intermediate
anneals at 1000°C) to a sheet of approximately 1.5 mils thickness,
then annealed at 1150°C (in a quartz capsule backfilled with argon)
for two hours. Samples were then either air-cooled (in the unbroken

Figure 119 Magnetic Domain Structure of 80Co-20Fe Annealed at
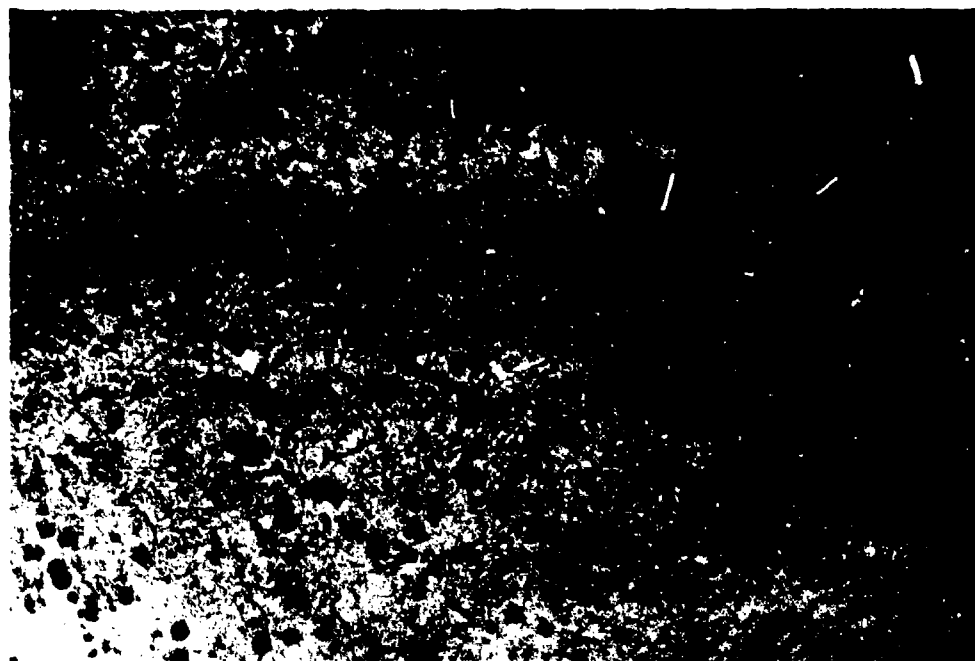1000°C for One Hour and Water Quenched (200x).

-207-

Figure 120. Magnetic Domain Structure of 80Co-20Fe Annealed at
1000°C for One Hour and Air Cooled (in Vycor Capsule)
(200x).

-208-

capsule) or water quenched (with the capsule broken). Electron transparent foils were obtained by electropolishing the thin annealed sheet in a solution of 80 methanol-20 perchloric acid at -40°C and about 15 volts. The polish of the heat-treated sheet was very uneven -- thinnest portions of the sample were perforated with a large number of fine holes. The samples behaved as though they were composed of a two-phase mixture with one of the phases being preferentially attacked in the electrolytic thinning.

A T.E.M. micrograph of the air-cooled sample is shown in Figure 121. The matrix was essentially devoid of major faults, including stacking faults, dislocation arrays, etc. The thin area had an overall mottled appearance. This microstructural feature may be caused by a fine two-phase mixture, but the diffraction patterns were of insufficient quality to confirm this. The diffraction patterns did, however, show the matrix to be fcc. It is also of interest to note that, using the Lorentz technique for imaging ferromagnetic domains, the samples failed to show any magnetic-domain structure.

Figure 122 shows T.E.M. micrographs of a sample of 80Co-20Fe which was water quenched. The general appearance of most of the thin area is shown in Figure 122A-- that is, it is a coarsely mottled structure. This again may be due to a coherent two-phase structure, but the diffraction patterns were not of high enough quality to support this. The matrix was indexed as fcc. Underfocussing of the image in Figure 122A yields the micrograph shown in Figure 122B which displays the magnetic domain structure of the sample. Figure 122C shows some of the thin areas of the water-quenched sample -- they give the appearance of stacking faults, but in this examination the faults were not fully identified.
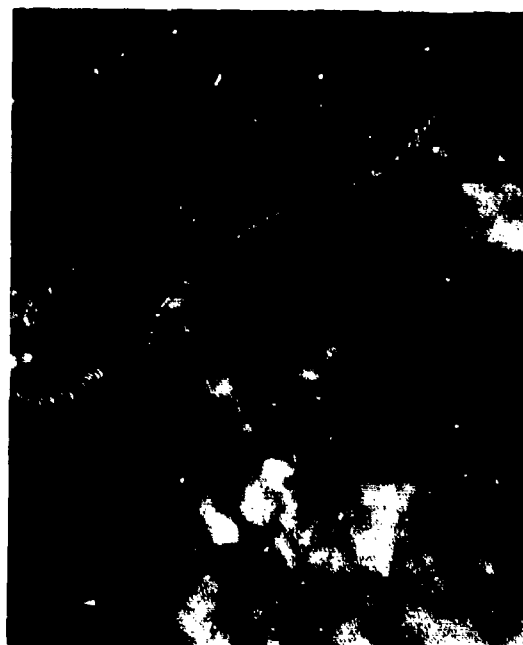
The primary results of the electron microscopy of air-cooled and water-quenched 80Co-20Fe indicate that (1) the air-

Figure 121. Transmission Electron Micrograph of Air Cooled
80Co-20Fe (Magnification 45000X)

(A)

(B)

(C)

Figure 122. Transmission Electron Micrographs of Water Quenched
80Co-20Fe (Magnification 45000X) (A) General Matrix
Appearance, (B) Underfocussed Image Showing Magnetic
Domain Structure, and (C) Straight Lined Faults in
the Matrix.

-211-

cooled samples examined contained no major faults or interfaces (including almost no dislocations), and (2) the water-quenched sample on the other hand did show some faults and also exhibited a magnetic-domain structure. However, the total number of faults seen was very small and it is very unlikely that these few faults could contribute significantly to the total damping. Thus, the source of an additional damping mechanism (i.e., besides magnetic-domain motion) in the 80Co-20Fe alloy has not been identified by electron microscopy. However, because of the large variation in damping with composition and thermo-mechanical treatment, the mechanism causing the damping seems to be intimately connected with the fcc-bcc transformation in these alloys.

REFERENCES

1. S. A. Kulin, L. Kaufman, and P. P. Neshe, "Noise Abatement and Internal Vibrational Absorption in Potential Structural Materials," AMMRC CTR 75-4, Contract DAAG46-74-C-0048, ARPA Order-2555, December 1974, ManLabs, Inc., Cambridge, Massachusetts 02139.

2. L. Kaufman, S. A. Kulin and P. P. Neshe, "Noise Abatement and Internal Vibrational Absorption in Potential Structural Materials," AMMRC CTR 75-4, Contract DAAG46-74-C-0048, ARPA Order 2555, March 1975, ManLabs, Inc., Cambridge, Massachusetts 02139.

3. L. Kaufman, S. A. Kulin and P. P. Neshe, "Noise Abatement and Internal Vibrational Absorption in Potential Structural Materials," AMMRC CTR 75-4, Contract DAAG46-74-C-0048, ARPA Order 2555, Sept. 1975, ManLabs, Inc., Cambridge, Massachusetts 02139.

4. L. Kaufman, S. A. Kulin and P. P. Neshe, "Noise Abatement and Internal Vibrational Absorption in Potential Structural Materials," AMMRC CTR 75-4, Contract DAAG46-74-C-0048, ARPA Order 2555, March 1976, ManLabs, Inc., Cambridge, Massachusetts 02139.

5. L. Kaufman, S. A. Kulin, and P. P. Neshe, "Noise Abatement and Internal Vibrational Absorption in Potential Structural Materials," AMMRC CTR 75-4, Contract DAAG46-74-C-0048, ARPA Order 2555, Sept. 1976, ManLabs, Inc., Cambridge, Massachusetts 02139.

6. A. Cochardt, Magnetic Properties of Metals and Alloys, A.S.M., Cleveland (1959) 251-279., Tr. A.I.M.E. (1956) 206 1295.

7. J. C. Fister and S. Shapiro, "Improved High Damping Copper-Base Alloys," International Copper Research Association Project 221, Final Report, September 1974, Olin Metals Research Laboratories, New Haven, Connecticut 06504.

8. J. Perkins, G. R. Edwards and N. Hills, "Materials Approaches to Ship Silencing," June 1974, NPS-59PS74061, Naval Post Graduate School, Monterey, California.

9. J. F. Nachman, J. C. Napier and A. N. Hammer, "Development of Cu-Mn Base Alloys with High Damping Properties," International Copper Research Association Report No. 152, Final Report March 1970, Solar Division, International Harvester Corporation, San Diego, California 92112.

10. J. F. Nachman, J. C. Napier and A. N. Hammer, "Development of Cu-Mn Base Alloys with High Damping Properties," International Copper Research Association Project No. 152A, Final Report, March 1971, Solar Division, International Harvester Corporation, San Diego, California 92112.

11. J. C. Heine, "The Stress and Frequency Dependence of Material Damping on Some Engineering Alloys," Ph.D. Dissertation, Massachusetts Institute of Technology (1966).

12. L. Cremer, M. Heckl and E. E. Ungar, Structure-Borne Sound, Springer-Verlag, New York, Chapter III (1973).

13. E. E. Ungar, "Damping of Panels," in Noise and Vibration Control, Ed. Leo L. Beranek, McGraw-Hill, New York (1971).

14. E. E. Ungar, "The Status of Engineering Knowledge Concerning the Damping of Built-up Structures," J. Sound & Vib. 26 (1) 141-154 (1973).

15. G. D. Sandrock, Met. Tr. (1974) 5 299.

16. G. D. Sandrock, A. J. Perkins and R. F. Heheman, Met. Tr. (1971) 2 2769.

17. K. Otsuka, T. Sawamura, K. Shimuzu and C. M. Wayman, Met. Tr. (1971) 2 2583.

18. L. Kaufman and M. Cohen, Progress in Metal Physics, Volume 7 (1958) p. 165, Pergamon Press, London.

19. T. Takeuchi and M. Honma, Science Reports of the Research Institute of Tohaku University, A9 (1957) p. 492.

20. B. K. Basu, Applied Physics Letters (1973) 15 961.

21. L. Kaufman and H. Nesor, Zeit. Metallkunde (1973) 74 249.

22. K. C. Mills, M. J. Richardson and P. J. Spencer, "Thermodynamic Properties and Phase Diagram of the Fe-Co and Ni-Pt System," Faraday Society Symposium (1973) (to be published).

23. H. Schumann, "Cobalt" (1968) 40 156.

24. U. Hashimoto, J. Japanese Inst. of Metals (1937) 1 177.

25. K. Ishida and T. Nishizawa, Tr. Jap. Inst. of Metals (1974) 15 225.

26. L. Kaufman, Metallurgical Transactions (1969) 245 91.

27. J. M. Vitek and H. Warlimont (1975) (Submitted for publication in Metal Science).

28. Y. Z. Vintaykin, D. F. Litvin and V. A. Udorenko, Fiz. Metal, Metall., 37 No. 6 1974, 1228.

29. Toshiba Electric Co., R and D Center, Kawasaki City, Kanagawa, 210 Japan.

30. T. R. Norris, "Tracked Vehicles: Model Study on the Effect of Track Parameter Changes on the Acoustic Signature, Seismic Signature and Interior Noise", Bolt, Beranek and Newman Inc., Report No. 3031, submitted to U. S. Army Tank-Automotive Command, Warren Michigan (1975), (Contract DAAE07-74-C-0002).

31. J. Perkins, ed., Shape Memory Effects in Alloys, Plenum Press, New York, (1975).

32. G. V. Kurdjimov, Journal of Metals, 11, 449, (1959).

33. H. C. Tong and C. M. Wayman, Acta Met., 22, 887, (1974).

34. G. B. Olson and M. Cohen, Scripta Met., 9, 1247, (1975).

35. K. Sugimoto, T. Mori, K. Otsuka, and K. Shimizu, Scripta Met., 8, 1341, (1974).

36. V. A. Teplov, V. A. Paulov, K. A. Malysheu, Fiz. Met. Metalloved, 27, 339, (1969).

37. D. P. Dunne, and C. M. Wayman, Met. Trans., 4, 137, (1973).

38. K. Otsuka, K. Shimizu, I. Cornelis, and C. M. Wayman, Scripta Met., 6, 377, (1972).

39. A. B. Greninger, Trans., A.I.M.E., 133, 204, (1939).

40. K. Otsuka and K. Shimizu, Trans., J.I.M., 15, 109, (1974).

41. V. S. Postnikov, I. M. Sharshakov, and U. G. Komarov, Fiz. Met. Metalloved, 33, 222, (1972).

42. W. DeJonghe, R. DeBatist, L. Delaey, and M. DeBonte, Shape Memory Effects in Alloys, Jeff Perkins, ed., Plemum Press, New York, 451, (1975).

43. V. A. Teplov, K. A. Malysheu, and V. A. Paulov, Fiz. Met. Metalloved, 34, 166, (1972).

44. I. A. Arbuzova, V. S. Gavrilyuk, and G. L. Khandros, Fiz. Met. Metalloved, $\underline{30}$, 181, (1970).

45. I. A. Arbuzova, V. S. Gavrilyuk, and G. L. Khandros, Fiz. Met. Metalloved, 27, 1126, (1969).

46. C. Zener, Elasticity and Anelasticity of Metals, Univ. of Chicago Press, Chicago, Ill., (1948).

47. K. Otsuka, and K. Shimizu, Phil. Mag. $\underline{24}$, 481, (1971).

48. K. Otsuka, J. of Applied Physics, $\underline{10}$, 571, (1971).

49. B. Heyer, Engineering Physical Metallurgy, Van Nostrand, New York, (1939).

50. L. Shepard, Shape Memory Effects in Alloys, Jeff Perkins, ed., Plenum Press, New York, 419, (1975).

DISTRIBUTION LIST

No. of Copies	To
1	Office of the Director, Defense Research and Engineering, The Pentagon, Washington, D. C. 20301
12	Commander, Defense Documentation Center, Cameron Station, Building 5, 5010 Duke Street, Alexandria, Virginia 22314
1	Metals and Ceramics Information Center, Battelle Columbus Laboratories, 505 King Avenue, Columbus, Ohio 43201

Chief of Research and Development, Department of the Army,
Washington, D. C. 20310
2 ATTN: Physical and Engineering Sciences Division

Commander, Army Research Office, P. O. Box 12211, Research
Triangle Park, North Carolina 27709
1 ATTN: Information Processing Office

Commander, U. S. Army Materiel Development and Readiness Command,
5001 Eisenhower Avenue, Alexandria, Virginia 22333
1 ATTN: DRCDE-TC

Commander, U. S. Army Electronics Command, Fort Monmouth, New Jersey 07703
1 ATTN: DRSEL-GG-DD
1   DRSEL-GG-DM

Commander, U. S. Army Missile Command, Redstone Arsenal, Alabama 35809
1 ATTN: Technical Library
1   DRSMI-RSM, Mr. E. J. Wheelahan

Commander, U. S. Army Armament Command, Rock Island, Illinois 61201
2 ATTN: Technical Library
1   DRSAR-SC, Dr. C. M. Hudson
1   DRSAR-PPW-PB, Mr. Francis X. Walter

Commander, U. S. Army Tank-Automotive Research and Development Command,
Warren, Michigan 48090
2 ATTN: DRDTA, Research Library Branch

Commander, White Sands Missile Range, New Mexico 88002
1 ATTN: STEWS-WS-VT

Commander, Aberdeen Proving Ground, Maryland 21005
1 ATTN: STEAP-TL, Bldg. 305

Commander, Frankford Arsenal, Philadelphia, Pennsylvania 19137
1 ATTN: Library, H1300, Bl. 51-2
1   SARFA-L300, Mr. J. Corrie

No. of Copies	To

Commander, Picatinny Arsenal, Dover, New Jersey 07801
1 ATTN: SARPA-RT-S

Commander, Redstone Scientific Information Center, U. S. Army Missile Command, Redstone Arsenal, Alabama 35809
4 ATTN: DRSMI-RBLD, Document Section

Commander, Watervliet Arsenal, Watervliet, New York 12189
1 ATTN: SARWV-RDT, Technical Information Services Office

Commander, U. S. Army Foreign Science and Technology Center, 220 7th Street, N. E., Charlottesville, Virginia 22901
1 ATTN: DRXST-SD2

Director, Eustis Directorate, U. S. Army Air Mobility Research and Development Laboratory, Fort Eustis, Virginia 23604
1 ATTN: Mr. J. Robinson, SAVDL-EU-SS

Librarian, U. S. Army Aviation School Library, Fort Rucker, Alabama 36360
1 ATTN: Building 5907

Naval Research Laboratory, Washington, D. C. 20375
1 ATTN: Dr. J. M. Krafft - Code 8430

Chief of Naval Research, Arlington, Virginia 22217
1 ATTN: Code 471

Air Force Materials Laboratory, Wright-Patterson Air Force Base, Ohio 45433
2 ATTN: AFML/MXE/E. Morrissey
1   AFML/LC
1   AFML/LLP/D. M. Forney, Jr.
1   AFML/MBC/Mr. Stanley Schulman

National Aeronautics and Space Administration, Washington, D. C. 20546
1 ATTN: Mr. B. G. Achhammer
1   Mr. G. C. Deutsch - Code RR-1

National Aeronautics and Space Administration, Marshall Space Flight Center, Huntsville, Alabama 35812
1 ATTN: R-P&VE-M, R. J. Schwinghamer
1   S&E-ME-MM, Mr. W. A. Wilson, Building 4720

Wyman-Gordon Company, Worcester, Massachusetts 01601
1 ATTN: Technical Library

Defense Advanced Research Projects Agency, 1400 Wilson Boulevard, Arlington, Virginia 22209
5 ATTN: Dr. E. C. van Reuth

No. of Copies	To

National Science Foundation, 1800 G Street, Washington, D. C. 20550
1 ATTN: Dr. Robert Reynik

General Electric Company, Corporate Research and Development, Schenectady, New York 12301
5 ATTN: Mr. F. X. Gigliotti, Jr.

Hitchiner Manufacturing Co., Inc., Elm Street, Milford, New Hampshire 03055
5 ATTN: Mr. G. D. Chandley

Abex Corporation, Research Center, Mahwah, New Jersey 07430
5 ATTN: H. R. Larson

Massachusetts Institute of Technology, Dept. of Metallurgy and Materials Science, Cambridge, Massachusetts 02139
5 ATTN: Dr. Merton C. Fleming

TRW Equipment, TRW Inc., 23555 Euclid Avenue, Cleveland, Ohio 44117
1 ATTN: Elizabeth Barrett, T/M 3417

Deposits & Composites Inc., 1821 Michael Faraday Drive, Reston, Virginia 22090
1 ATTN: Richard E. Engdahl, President

1 Dr. Maurice Sinnott, University of Michigan, Assoc. Dir. of Engineering, Ann Arbor, Michigan 48104

1 Fred E. Ziter, Adirondack Steel Casting Co., Shaker Road, Watervliet, New York 12189

1 Dr. Raymond J. Bratton, Westinghouse Electric Corporation Research Laboratory, Pittsburgh, Pennsylvania 15235

1 W. M. Spurgeon, Director, Mfg., Quality Control & Home Systems, Program Management Center, Bendix Research Laboratories, Bendix Center, Southfield, Michigan 48075

1 S. T. Wlodek, Director of Stellite R&D, Stellite Division, Cabot Corporation, 1020 West Park Avenue, Kokomo, Indiana 46901

1 Mr. William A. Butler, Contract Administrator, Microwave Associates, Inc., Burlington, Massachusetts 01803

1 Mr. John A. Ulrich, Sr. Vice-President, Chamberlain Manufacturing Corp., Waterloo, Iowa 50705

1 A. V. Illyn, Technical Director, Babcock & Wilcox, Old Savannah Road, Augusta, Georgia 30903

No. of Copies	To
1	Mr. W. J. Welsch (Code 224), Naval Materials Industry Resources Office, N.A.E.C., Building #537, Philadelphia, Pennsylvania 19112
1	Mr. R. E. Cross, Federal Die Casting Co., 2222 Elston Avenue, Chicago, Illinois 60614
1	Captain Ebenezer F. Porter, 2618 S. Lynn Street, Arlington, Virginia 22202
1	Mr. Charles E. Bates, Head, Metallurgy Section, Southern Research Institute, 2000 Ninth Avenue, South, Birmingham, Alabama 35205
1	Mr. R. F. Kirby, Chief, Materials Engineering Dept., Dept. 93-39M, Airesearch Manufacturing Company of Arizona, 402 South 36th Street, P. O. Box 5217, Phoenix, Arizona 85010
1	Dr. Mervin T. Rowley, American Foundry Men's Society, Golf & Wolf Roads, Des Plaines, Illinois 60016
1	William R. Freeman, Jr., Howmet Corporation, Vice President and Technical Director, Technical Center, Gas Turbine Components Group, 699 Benston Road, Whitehall, Michigan 49461
1	Dole A. Marek, General Motors Corporation, Detroit Diesel Allison, 4700 W 10th Street, Indianapolis, Indiana 46206

General Dynamics, Convair Aerospace Division, P. O. Box 748, Ft. Worth, Texas 76101
| 1 | ATTN: Mfg. Engineering Technical Library |

| 1 | Dr. Robert Mehrabian, Dept. of Metallurgy & Mining Engineering, University of Illinois, Urbana, Illinois 61801 |
| 1 | Robert McNally, Research Library, Special Metals Corporation, Middle Settlement Road, New Hartford, New York 13413 |

Director, Army Materials and Mechanics Research Center, Watertown, Massachusetts 02172
2	ATTN: DRXMR-PL
1	DRXMR-PR
1	DRXMR-AP
1	DRXMR-CT
1	DRXMR-X
1	DRXMR-ER